amU
Aix Marseille Université

NNT: XXXXXXXXX

THÈSE DE DOCTORAT

Soutenue à Aix-Marseille Université

le 24/02/2025 par

Florent TOMI

Contributions à l'amélioration de l'implantation de vis pédiculaires par la création d'une segmentation personnalisée du rachis humain

Composition du jury

Carl Eric AUBIN Pr, Polytechnique Montreal	Rapporteur
Nadia BAHLOULI Pr, Université de Strasbourg	Rapporteure
Anne-Sophie CARO-BRETELLE Pr, Institut Mines-Télécom, Mines Alès	Examinatrice
Sébastien PESENTI MD, Pr, Aix-Marseille Université	Président du jury
Pierre-Jean ARNOUX Directeur de laboratoire, Laboratoire de Biomécanique Appliquée	Directeur de thèse
Morgane EVIN Laboratoire de Biomécanique Appliquée	Co-directrice de thèse
Marie-Hélène BEAUSEJOUR Pr, Ecole de Technologie Supérieure Montreal	Membre invitée
Raphael LA GRECA PYTHEAS NAVIGATION	Membre invité

Discipline
Sciences du Mouvement Humain

École doctorale
ED 463 SCIENCES DU MOUVEMENT HUMAIN

Laboratoire/Partenaires de recherche
Laboratoire de Biomecanique Appliquée, PYTHEAS NAVIGATION

PYTHEAS NAVIGATION

LBA LABORATOIRE DE BIOMÉCANIQUE APPLIQUÉE
Sous la co-tutelle de : AIX-MARSEILLE UNIVERSITÉ UNIVERSITÉ GUSTAVE EIFFEL

1. Affidavit

I, undersigned, Florent TOMI, hereby declare that the work presented in this manuscript is my own work, carried out under the scientific supervision of Pierre-Jean ARNOUX, Morgane EVIN and Yves GODIO-RABOUTET, in accordance with the principles of honesty, integrity and responsibility inherent to the research mission. The research work and the writing of this manuscript have been carried out in compliance with both the french national charter for Research Integrity and the Aix-Marseille University charter on the fight against plagiarism.

This work has not been submitted previously either in this country or in another country in the same or in a similar version to any other examination body.

Marseille, 13/09/2024



This work is licensed under Creative Commons Attribution-NonCommercial-NoDerivatives 4.0 International Public License

2. Liste de publications et participation aux conférences

Liste des publications réalisées dans le cadre du projet de thèse :

1. Change of vertebral orientation, between the supine position and the prone position (Giorgi et al. 2023)
   Journal : Spine Deformity
   Auteurs : Hadrien Giorgi, Florent Tomi, Yann Glard, David Afonso, Lucrezia Montanari, Aymeric Faure
   Status : Accepté

2. Sliding on cortical shell: Biomechanical characterization of the vertebral cannulation for pedicle screw insertion (Leblond; Yves Godio-Raboutet, et al. 2023)
   Journal : Clinical Biomechanics
   Auteurs : Lugdivine Leblond, Yves Godio-Raboutet, Florent Tomi, Yann Glard, Raphael La Greca, Thomas Clement, Morgane Evin
   Status : Accepté

3. Vertebral Cortical Thickness and Cortical Bone Density: an automated CT assessment - Towards enhanced spine segmentation (Tomi et al. 2024)
   Journal : Computer Methods in Biomechanics and Biomedical Engineering: Imaging and Visualization
   Auteurs : Florent Tomi, Yves Godio-Raboutet, Raphael La Greca, Thomas Clement, Yann Glard, Morgane Evin
   Status : Accepté

Participation aux conférences et écoles d'été au cours de la période de thèse :

1. Présentation : Vertebral bone density investigation
   Conférence : 47ème congrès de la Société de Biomécanique (2022)

2. Abstract : Vertebral bone density investigation
   Conférence : 47ème congrès de la Société de Biomécanique (2022)

Auteurs : Florent Tomi, Lugdivine Leblond, Yves Godio-Raboutet, Raphael La Greca and Morgane Evin

3. Abstract : INTER AND INTRA VARIABILITY OF LANDMARK POSITIONNING FOR VERTEBRAE MORPHOLOGICAL CHARACTERIZATION
   Conférence : IEEE International Symposium on Biomedical Imaging (ISBI) 2021
   Auteurs : F. Tomi, M. Evin, Y. Godio-Raboutet, K. Chaumoitre, K. Plomb, R. La Greca, A. Evin

4. Poster : Cortical assessment in vertebrae: thickness and bone density investigation
   Journée de l'école doctorale SMH 2023
   Auteurs : Florent Tomi, Yves Godio-Raboutet, Raphael La Greca, Thomas Clement, Yann Glard , Morgane Evin

3. Abstract and keywords

Pedicle screw placement is critical for spinal surgery, but misplacement can lead to complications like nerve damage and extended recovery times. This thesis investigates automated spine segmentation as a method to improve the accuracy of pre-operative planning using CT scans, and it setups the groundwork for its automation.

Current pre-operative planning relies on manual segmentation, a time-consuming and subjective process. Automated segmentation offers enhanced accuracy and objectivity, potentially leading to more consistent screw placement and improved surgical outcomes. Furthermore, automation can streamline planning workflows, freeing up surgeon time for other tasks.

This research explores two automated segmentation methods aiming to prepare the groundwork for a fully automated surgery planning. The first one achieves high accuracy while processing a spine in under a minute, making it suitable for clinical settings. This method has been substantiated in clinical trials. The second one segments cortical bone in addition to the spine, providing valuable information about bone quality for screw selection and placement.

Both methods were validated on a popular spine segmentation dataset, achieving results similar to AI algorithms. They both demonstrate the potential of automated segmentation to reduce complications and improve surgical outcomes.

In order to further enhance the precision of the planning, a strong emphasis has been brought to the biomechanics of the surgery. Researches have been done towards a better understanding of the cannulation process and the patient positioning deviation between the input media (CT scan) and the OR setting. These works will bring several inputs for the automation process by expanding the overall knowledge of the surgery context.

This research has the potential to significantly improve patient safety and surgical outcomes in spinal procedures with pedicle screws.

Keywords: Spine segmentation, pedicle screw, cortical thickness, tolerance angle, patient-specificity

4. Résumé et mots-clés

Le placement précis des vis pédiculaires est crucial lors de la chirurgie rachidienne, mais un mauvais positionnement peut entraîner des complications telles que des lésions nerveuses et des temps de récupération prolongés. Cette thèse étudie la segmentation automatisée de la colonne vertébrale comme méthode pour améliorer la précision de la planification préopératoire à l'aide de scanners CT et pour préparer les bases de son automatisation.

La planification préopératoire actuelle repose sur une segmentation manuelle, un processus chronophage et subjectif. La segmentation automatisée offre une précision et une objectivité accrues, pouvant conduire à un placement plus cohérent des vis et à de meilleurs résultats chirurgicaux. De plus, l'automatisation peut rationaliser les flux de travail de planification, libérant ainsi du temps pour les chirurgiens afin qu'ils puissent se consacrer à d'autres tâches.

Cette recherche explore deux méthodes de segmentation automatisée visant à préparer le terrain pour une planification chirurgicale entièrement automatisée. La première atteint une grande précision tout en traitant une colonne vertébrale en moins d'une minute, ce qui la rend adaptée aux contextes cliniques. Cette méthode a été validée dans des essais cliniques. La seconde segmente l'os cortical en plus de la colonne vertébrale, fournissant des informations précieuses sur la qualité de l'os pour la sélection et le placement des vis.

Les deux méthodes ont été validées sur un ensemble de données populaire pour la segmentation de la colonne vertébrale, obtenant des résultats similaires à ceux des algorithmes d'IA. Elles démontrent toutes deux le potentiel de la segmentation automatisée pour réduire les complications et améliorer les résultats chirurgicaux.

Afin d'améliorer encore la précision de la planification, une grande importance a été accordée à la biomécanique de la chirurgie. Des recherches ont été menées pour mieux comprendre le processus de cannulation et la déviation du positionnement du patient entre le média d'entrée (scanner CT) et le bloc opératoire. Ces travaux apporteront plusieurs apports au processus d'automatisation en élargissant la connaissance globale du contexte chirurgical.

Cette recherche a le potentiel d'améliorer considérablement la sécurité des patients et les résultats chirurgicaux lors des procédures spinales avec vis pédiculaires.

Mots-clés: Segmentation du rachis, vis pédiculaire, épaisseur cortical, angle de tolérance, spécificité du patient

Contents

1. Affidavit 2

2. Liste de publications et participation aux conférences 3

3. Abstract and keywords 5

4. Résumé et mots-clés 6

Contents 8

List of Figures 11

List of Tables 14

Acronyms 15

Glossary 18

5. Introduction 19

6. Clinical and biomechanical context 23

6.1. Anatomy of the human spine 23

6.1.1. General considerations about spinal anatomy 23

6.1.2. Physiological spine curvature 25

6.1.3. Vertebral anatomy 26

6.1.4. Vertebral cortical thickness 32

6.2. Vertebral mechanical properties 32

6.2.1. Microstructure of the bone tissue 33

6.2.2. Mechanical characterization of the bone tissue 36

6.3. Spinal diseases and their morphological consequences 40

6.3.1. Etiology of the spinal diseases 40

6.3.2. Diagnosis of spinal diseases 42

6.3.3. Morphological consequences of spinal diseases 47

6.4. Spine surgery: pedicle screw implantation 52

6.4.1. Context 52

6.4.2. Freehand pedicle screw insertion techniques 53

6.4.3. Freehand methods: thoracic vertebrae 55

6.4.4. Freehand methods: lumbar vertebrae 57

7. Industrial context **60**
7.1. Computer Assisted Spine surgery . . . 60
7.1.1. Historical context . . . 60
7.1.2. The early stage of navigation technology . . . 61
7.1.3. The later stage of Navigation Technology . . . 62
7.1.4. Advantages and limitations of CAS . . . 66
7.2. PYTHEAS NAVIGATION *Your Guided Trajectory*: a new Medical Device based on *Inertial Measurement Units* (IMU) . . . 68
7.2.1. Brief history of PYTHEAS NAVIGATION . . . 68
7.2.2. General considerations about Image guided trajectory guidance in spine surgery . . . 68
7.2.3. General principles of the PYTHEAS NAVIGATION *Your Guided Trajectory* Medical Device . . . 69
7.2.4. Hardware . . . 72
7.2.5. Software . . . 74
7.2.6. Registration and calibration issues . . . 75
7.2.7. Challenges . . . 75
7.2.8. Prototype version: manual thresholding . . . 76

8. State of the art **78**
8.1. Image segmentation . . . 78
8.1.1. Classic segmentation methods . . . 79
8.1.2. Co-segmentation methods . . . 84
8.1.3. Segmentation based on Machine Learning (ML) . . . 84
8.2. Image segmentation in medical imaging . . . 90
8.2.1. Segmentation evaluation metrics . . . 90
8.2.2. Segmentation of the spine in CT scans . . . 93

9. Objectives **99**
9.1. Automated segmentation of the spine . . . 99
9.2. Understanding of the differences between pre-operative CT scan and surgery context . . . 101
9.3. Improvement of pedicle screw implantation: the cannulation process . 102

10.Automated segmentation of the spine **104**
10.1. Region-growing based segmentation . . . 104
10.1.1. Method . . . 104
10.1.2. Clinical trials and validation . . . 105
10.1.3. Discussion . . . 106
10.2. GMM-based segmentation . . . 106
10.2.1. Introduction . . . 106
10.2.2. Materials and methods . . . 108
10.2.3. Results . . . 115
10.2.4. Discussion . . . 120

10.2.5. Conclusion . . . 121

11. Assessment of the difference between supine and prone position (Giorgi et al. 2023) 122
11.1. Introduction . . . 122
11.2. Material and methods . . . 123
11.2.1. Dataset . . . 123
11.2.2. Data processing . . . 124
11.3. Results . . . 127
11.4. Discussion and conclusions . . . 129

12. Assessment of the limits of the surgeon maneuver (Leblond; Yves Godio-Raboutet, et al. 2023) 132
12.1. Introduction . . . 132
12.2. Assessment and validation of the incertitude of tolerance angle in synthetic bones . . . 133
12.2.1. Introduction . . . 133
12.2.2. Material and methods . . . 134
12.2.3. Results . . . 139
12.2.4. Discussion . . . 142
12.2.5. Conclusion . . . 144
12.3. Assessment and validation of the incertitude of tolerance angle in swine and cadavers . . . 145
12.3.1. Introduction . . . 145
12.3.2. Material and methods . . . 145
12.3.3. Statistical analysis . . . 150
12.3.4. Results . . . 150
12.3.5. Vertebra by vertebra results with and without pedicle perforation 152
12.3.6. Discussion . . . 153
12.3.7. Conclusion . . . 155

13. Perspectives 156
13.1. Planning automation . . . 156
13.2. Surgeon practices . . . 160
13.3. Biomechanics . . . 161

14. Conclusion 163

Appendices 165

A. Figures 166

B. Tables 175

Bibliography 185

List of Figures

6.1. Cervical vertebrae . . . 23
6.2. Thoracic vertebrae . . . 24
6.3. Lumbar vertebrae . . . 24
6.4. Sacrum . . . 24
6.5. Coccyx . . . 25
6.6. Intervertebral disc . . . 25
6.7. Spine curves . . . 25
6.8. Vertebra characterization . . . 30
6.9. 2D landmarks . . . 31
6.10. 3D landmarks . . . 31
6.11. CTh of a femur assessed on a plain AP X-Ray (Niimi et al. 2015) . . . 32
6.12. CTh of a vertebra . . . 32
6.13. Diagram of cortical bone structure . . . 33
6.14. Type I . . . 34
6.15. Type IIc . . . 34
6.16. Type IIIb, Singh 1978 . . . 35
6.17. Type IIIc, Singh 1978 . . . 35
6.18. Pedicular screw . . . 37
6.19. Example of a pullout test . . . 38
6.20. Indentation . . . 39
6.21. MRI visualization of vertebral end plate and bone marrow alteration . . . 48
6.22. CT visualisation of a L_4 spondylolysis . . . 48
6.23. Schematic visualization of degenerative stenosis in the lumbar spine . . . 49
6.24. Vertebral metastasis . . . 50
6.25. vertebral osteomyelitis . . . 50
6.26. Cobb angle . . . 51
6.27. Spine deformity examples . . . 52
6.28. Pedicle screw implantation . . . 53
6.29. Exposed vertebra during surgery. . . . 54
6.30. Pedicle screw surgery instruments . . . 54
6.31. Pedicle screw freehand insertion . . . 55
6.32. Entry point general area for thoracic vertebrae . . . 55
6.33. Y. J. Kim; Lenke, et al. 2004 . . . 56
6.34. Parker et al. 2011 . . . 57
6.35. Fennell et al. 2014 . . . 57
6.36. Magerl 1984 . . . 58
6.37. Roy-Camille; Saillant, et al. 1986b . . . 58

6.38. Weinstein et al. 1988 59

7.1. Horsley-Clarke stereotaxic apparatus 61
7.2. Watanabe et al. 1987 62
7.3. Example of electromagnetic navigation 63
7.4. FRACAS system concept 64
7.5. PYTHEAS NAVIGATION *Your Guided Trajectory* planning 70
7.6. PYTHEAS NAVIGATION *Your Guided Trajectory* navigation 71
7.7. Movella DOT 72
7.8. Angular guidance 75
7.9. Prototype GUI 76
7.10. Prototype segmentation 77

8.1. Image segmentation methods 78
8.2. Sobel-Feldman operator example 79
8.3. Canny edge detector example 81
8.4. Segmentation process of the watershed algorithm 82
8.5. Machine Learning (ML) vs. Deep Learning (DL) 85
8.6. Examples of activation functions: Sigmoid and ReLU 87
8.7. Evolution of the cost function during backpropagation 88
8.8. Example of CNN architecture 89
8.9. Typical deep neural network 90
8.10. U-net architecture 97
8.11. Segmentation 98
8.12. Segmentation process 98

10.1. Example of CT scan histogram 105
10.2. Cortical segmentation algorithm chart 109
10.3. Cortical bone segmentation - Cortical Thickness and Cortical Bone Density 112
10.4. Morphological features of the sample (a-b) and vertebral functional areas (c-f). 113
10.5. Normalized Cortical Thickness (human in-vivo sub-group) 118
10.6. Cortical Bone Density (human in-vivo sub-group) 119

11.1. Difference of vertebral orientation between the preoperative CT scan and the operating room 123
11.2. Patient in the prone position according to the AO recommendations . 124
11.3. Segmentation and entry point/pedicular direction identification 125
11.4. Distribution of vertebral levels analyzed. 127
11.5. Comparison between the two methods. 128

12.1. Cylindrical samples 135
12.2. Cannulation tool with curved tip 136
12.3. Cylinder positioned under the cannulation tool 137

12.4. Controlled rotation of the samples according to the expected computed angles. . . . 137
12.5. Cannulation procedure measurements . . . 138
12.6. Perforation or degradation of the cortical shell verified with a CT scan performed after the tests. . . . 139
12.7. Cannulation coefficient reproducibility of the measurement for 10° perforation angle for each type of samples with epoxy. . . . 140
12.8. Cannulation coefficient reproducibility of the measurement for 10° perforation angle for each type of samples with bi-foam model. . . . 140
12.9. PCF10 and PCF20 measurements. . . . 141
12.10 Principal Component analysis of the perforation tests . . . 142
12.11 Cannulation tool mounted on the MTS device. . . . 148
12.12 Typical displacement and angle command signal . . . 148
12.13 Typical force-displacement signals for perforated pedicles . . . 149
12.14 Tested β number for β threshold identification and prediction by maximal forces and torque. . . . 151
12.15 Beta angle and vertebral level influence on elastic moduli . . . 151
12.16 β angle and E ratio . . . 151
12.17 β angle and vertebral level influence on forces and torque . . . 152
12.18 E ratio . . . 152
12.19 ROC analysis for β threshold identification and prediction by maximal forces and torque. . . . 153

13.1. Planning automation . . . 157
13.2. Ehm et al. 2009 . . . 158

A.1. Spondylolisthesis grading . . . 166
A.2. AO Spine System (2013) classifications . . . 167
A.3. AO Spine System (2013) decision tree . . . 168
A.4. Processing method . . . 169
A.5. Superposition of slices of the same vertebral level . . . 170
A.6. Method 1 — Vertebral rotation variation from supine to prone . . . 171
A.7. Method 2 — Vertebral rotation variation from supine to prone . . . 172
A.8. Table showing the cannulation coefficient, the maximum resultant force, the maximum force in the z axis (load axis) and the maximum XY forces for different angles of perforation . . . 173
A.9. Mean values of trabecular and cortical elastic moduli found for human and swine samples according the vertebral level . . . 174

List of Tables

6.1. Summarized differences of the vertebra structures between region of the spine. . . . 29
6.2. 2D landmark description . . . 31
6.3. Summary of mechanical characterization techniques . . . 36
6.4. Estimated dose in the United States . . . 47
6.5. Estimated number of procedures in the United States . . . 47

7.1. Radiation dosage at the radiation source . . . 67

8.1. Confusion matrix of G and T . . . 92
8.2. Summary of classic segmentation techniques . . . 94
8.3. Summary of geometric/anatomical model- and atlas-based segmentation techniques . . . 95
8.4. Summary of deep learning segmentation techniques . . . 98

10.1. PYTHEAS NAVIGATION *Your Guided Trajectory* clinical trials . . . 106
10.2. Sample description . . . 108
10.3. Morphological characteristics of the sample . . . 116
10.4. Normalized CTh comparison . . . 117
10.5. CBD comparison . . . 117
10.6. Normalized CTh comparison . . . 117

12.1. Table of mechanical properties of the used synthetic materials given by the manufacturers materials guides . . . 135
12.2. Table of experiment on synthetic materials samples . . . 136
12.3. Design of experiment of the perforated pedicles . . . 147
12.4. Pedicle morphometric specifications . . . 150

B.1. Vertebra parameter set . . . 175
B.2. Method 1 - Sagittal angle . . . 176
B.3. Method 1 - Transversal angle . . . 177
B.4. Method 1 - Frontal angle . . . 178
B.5. Method 2 - Sagittal angle . . . 179
B.6. Method 2 - Transversal angle . . . 180
B.7. Mean values of Normalized CTh and CBD . . . 181
B.8. Normalized CTh comparison . . . 182
B.9. Primary diagnoses for spinal fusion revisions . . . 183
B.10. Examples of co-segmentation methods . . . 184

Acronyms

AI

Artificial Intelligence. 84, 156, 158

AIS

Adolescent Idiopathic Scoliosis. 100

ALARA

As Low As Reasonably Achievable. 67, 129

ASTM

American Society for Testing and Materials. 37

BMD

Bone Mineral Density. 95, 100

CAS

Computer-Aided Surgery. 9, 64, 66, 67

CBCT

Cone Beam Computed Tomography. 123, 124, 129

CBD

Cortical Bone Density. 100

CNN

Convolutional Neural Network. 12, 89, 96

CTh

Cortical Thickness. 32, 100

DL

Deep Learning. 12, 84, 85

FCN

Fully Convolutional Network. 96

FRACAS

FRActure Computer-Aided Surgery. 12, 63, 64

GAN

Generative Adversarial Network. 96

GMM

Gaussian Mixture Model. 82, 86, 94, 109

ICD-9

International Classification of Diseases, 9th revision. 183

IPEP

Ideal Pedicular Entry Point. 157

LAB

CIELAB Color space. 184

LL

Lumbar Lordosis. 130

LPS

Left-Posterior-Superior. 18

MD

Medical Device. 104, 105

ML

Machine Learning. 9, 12, 84, 85

MLP

Multi-Layer Perceptron. 88, 89

MRF

Markov Random Field. 82, 83, 184

MSE

Mean Square Error. 88

MST

Minimum Spanning Tree. 82

PCA

Principal Component Analysis. 86

PGM

Probabilistic Graphical Model. 82

PS

Pedicle Screw. 130

RNN

Recurrent Neural Network. 89

ROI

Region Of Interest. 78

SIFT

Scale Invariant Feature Transform. 184

SVD

Singular Value Decomposition. 86

SVM

Support Vector Machine. 86

TK

Thoracic Kyphosis. 130

ULDCT

Ultra Low-Dose CT. 128, 129

Glossary

Anatomical reference frame 125

The anatomical space (i.e. patient coordinate system) consists of three planes describing the standard anatomical position of a standing human:
Axial plane: parallel to the ground, separates the head (*Superior*) from the feet (*Inferior*)
Coronal plane: perpendicular to the ground, separates the front (*Anterior*) from the back (*Posterior*)
Sagittal plane: perpendicular to the ground, separates the *Left* hand from the *Right* hand.
The axis directions is what makes each reference frame unique. In the PYTHEAS NAVIGATION *Your Guided Trajectory* case, the Left-Posterior-Superior (LPS) referential has been chosen. This choice has no impact on the surgeon use of the device, and is simply a mean to interpret all the coordinates in the same frame of reference. It is typically used in DICOM images, which are the main file type output by the CT scanners.

$$\text{LPS reference frame} = \begin{cases} \text{From right towards left (X axis)} \\ \text{From anterior towards posterior (Y axis)} \\ \text{From inferior towards superior (Z axis)} \end{cases}$$

Image segmentation 78

In digital image processing, image segmentation is the process of partitioning an input N-D image into multiple image segments, which can be a whole region of the input image or sets of pixels. The goal of the segmentation is to transform the input image into a more meaningful and, most likely, easier to analyze.

5. Introduction

Pedicle screw implantation procedures are crucial for treating a wide range of spinal conditions, improving the quality of life for millions of patients globally each year. However, these procedures carry inherent risks, with one of the biggest challenges being the accurate placement of pedicle screws. These screws are inserted into the vertebrae to provide stability and support for some spinal fusion or osteosynthesis. Misplacement of these screws can lead to procedure failure, necessitating revision surgeries and potentially causing further complications.

The freehand technique, the most widely used approach for pedicle screw placement, primarily relies on the surgeon experience and skill in feeling the bony anatomy of the vertebrae. Fluoroscopy images may also be used to provide additional guidance during the procedure. In this technique, the surgeon palpates the vertebrae to determine the entry point for a small pedicle probe, which is then inserted into the pedicle. Once positioned correctly, the probe serves as a guide for drilling the hole and inserting the pedicle screw. However, the freehand technique has inherent limitations regardless of whether fluoroscopy is used. Surgeon feel can be subjective and prone to error due to variations in individual anatomy and limited access to palpate certain areas. This makes it difficult to consistently pinpoint the ideal entry point for the probe and screw, even with fluoroscopy providing some visual aid.

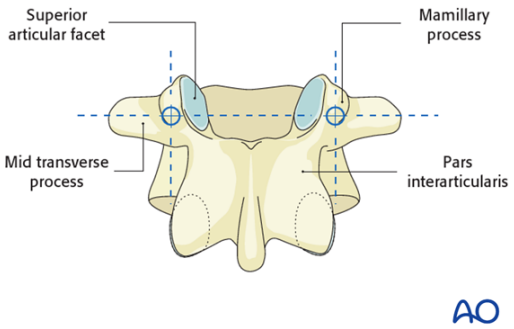

The limitations of the freehand technique, particularly the reliance on surgeon feel and two-dimensional fluoroscopy, highlight the importance of advancements in pre-operative planning. Pre-operative planning allows surgeons to meticulously analyze a patient's anatomy before surgery, potentially leading to more precise screw placement and improved surgical outcomes.

Current approaches to pre-operative planning, while helpful, still have limitations that can hinder surgeons' ability to precisely place pedicle screws. Pre-operative planning often relies on traditional methods like CT scans, which provide detailed two-dimensional slices of the anatomy. However, these methods lack the ability to create a comprehensive 3D understanding of the patient's specific anatomy. This

makes it challenging for surgeons to visualize the complex three-dimensional relationships between the vertebrae and surrounding structures. This limitation can lead to difficulties in precisely planning the trajectory of the pedicle screws, potentially increasing the risk of complications during surgery.

Additionally, interpreting CT scans can be subjective and prone to error depending on the surgeon experience. Furthermore, the manual analysis of CT scans for pre-operative planning can be a time-consuming process. Surgeons or radiologists often need to meticulously examine numerous 2D slices to create a mental 3D reconstruction, which can be tedious and prone to errors. This time-consuming process can impact workflow efficiency and potentially delay surgeries.

Software tools like *3D Slicer* (Fedorov et al. 2012) can be valuable for pre-operative planning by offering 3D visualization of the patient anatomy. However, these tools may have limitations in terms of user interface complexity or requiring extensive user input for segmentation, particularly for isolating the spine from surrounding structures. This manual segmentation can be a bottleneck in the pre-operative planning workflow, further impacting efficiency. Accurately segmenting the spine from CT scans can be challenging due to variations in patient anatomy, image quality, and the presence of overlapping structures. This manual process can be time-consuming and prone to errors introduced by human subjectivity.

These limitations in pre-operative planning can restrict surgeons' ability to precisely plan screw placement, potentially increasing the risk of complications like breaches in the cortical shell and nerve damage. These complications can lead to additional surgeries, prolonged recovery times, and increased healthcare costs. There is a clear need for a more accurate and accessible pre-operative planning tool to address these limitations and improve patient outcomes.

Another critical limitation in pre-operative planning lies in its inability to address the inherent challenges associated with the cannulation process during surgery. Cannulation, the act of guiding a drill or probe through the pedicle to create a pathway for the screw, is a crucial but subjective step that relies heavily on surgeon feel. This reliance on tactile feedback introduces limitations and potential inaccuracies. Even with a meticulously planned screw trajectory based on pre-operative imaging, deviations can occur during cannulation due to factors like variations in patient anatomy, unexpected tissue resistance, and limitations in instrument maneuverability. These deviations can compromise the safety and efficacy of screw placement, potentially leading to breaches in the cortical wall or nerve damage. While advancements in pre-operative planning offer significant improvements, addressing the limitations of cannulation itself remains a challenge. This highlights the need for a more comprehensive approach to surgical planning that integrates not only pre-operative imaging analysis but also considerations for intra-operative challenges like cannulation.

In response to these limitations in pre-operative planning, the company PYTHEAS NAVIGATION tackles these drawbacks with their device *Your Guided Trajectory*. This product offers a comprehensive workflow, including both pre-operative planning and intra-operative navigation. During the planning stage, surgeons can visualize a 3D spine model (created from a CT scan) and plan pedicle screw placement for each vertebra requiring instrumentation. *Your Guided Trajectory* then transitions to its navigation functionality in the operating room (OR). This navigation guidance assists surgeons by providing a real-time visual feedback on the orientation of the surgical instruments relative to the patient anatomy.

PYTHEAS NAVIGATION recognizes the importance of automation in streamlining the pre-operative planning process. Their next big step focuses on automating the creation of the 3D model (segmentation of the spine) and the processing of screw entry points and trajectories. The automation aims to make the product easier to learn and use, ultimately reducing both pre-operative planning time and time spent in surgery.

Accurately segmenting the spine from CT scans for pre-operative planning remains a challenge despite advancements in medical imaging. This complexity stems from several factors: variations in patient anatomy, including degenerative changes or prior surgeries, can alter the expected shape and appearance of the spine. Additionally, image quality can be impacted by factors like artifacts caused by metal implants or motion during the scan. Furthermore, the presence of overlapping structures like ribs and blood vessels can make it difficult to distinguish the spine from surrounding tissues. These factors contribute to the limitations of traditional segmentation methods, which often require significant user input and expertise.

Automation of segmentation in pre-operative planning holds immense promise for overcoming these challenges. However, developing robust and accurate automated segmentation algorithms is an active area of research. These algorithms need to be trained on large datasets of diverse patient anatomies to account for the natural variations present in the spine. Additionally, they must be able to handle potential image quality issues and differentiate between the spine and overlapping structures.

Another critical challenge in pre-operative planning is bridging the gap between the ideal and the real. While pre-operative planning relies on data gathered from CT scans, the surgical environment presents a different reality. These discrepancies between the CT scan setting and the OR setting can introduce challenges for surgeons striving to achieve optimal outcomes.

One way these discrepancies manifest is through posture changes. A patient spine is typically in a neutral position during a CT scan (supine position, face-up), while surgery often involves manipulating the spine into a different posture to access the surgical target, typically in a prone position (face-down). These posture changes can alter the spatial relationships between the vertebrae, potentially leading to discrepancies between the pre-operatively planned screw placement and the actual anatomy

during surgery. This can necessitate intra-operative adjustments, which can add to surgery time and potentially increase the risk of complications.

Addressing these discrepancies between the CT scan setting and the OR setting is a crucial area of focus in improving pre-operative planning for pedicle screw implantation procedures. This is also a critical issue to address for *Your Guided Trajectory* calibration process during the navigation step.

In conclusion, inaccurate pedicle screw placement during spine surgery can lead to serious complications, extending recovery times and increasing healthcare costs. These complications can include nerve damage, leakage of cerebrospinal fluid (CSF), and vertebral fractures. By improving screw placement accuracy, the risk of these complications can be significantly reduced. This can lead to faster recovery times, lower healthcare costs, and ultimately, improved patient outcomes following spine surgery. Additionally, improved pre-operative planning through automated spine segmentation can benefit surgeons by potentially improving surgical efficiency, reducing stress and improving decision-making, and potentially leading to enhanced patient satisfaction. This thesis explores how automated spine segmentation, using advanced imaging techniques, can improve the accuracy of pre-operative planning, potentially reducing the risk of complications and improving surgical outcomes.

6. Clinical and biomechanical context

In this chapter, we will introduce the human spine anatomy related to the pedicular screw implantation as well as the mechanical considerations. The clinical context will include a description of the pathologies and surgical treatments.

6.1. Anatomy of the human spine

6.1.1. General considerations about spinal anatomy

The human spine is made of 32 to 34 bones (Figs. 6.1 to 6.5):

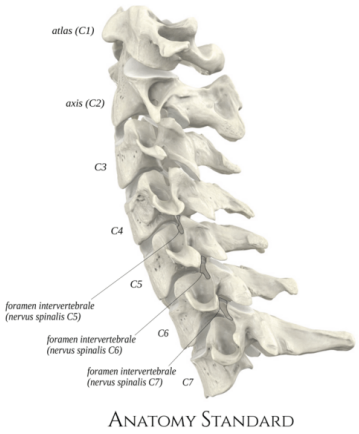

Figure 6.1.: Seven cervical vertebrae, going from C_1 down to C_7

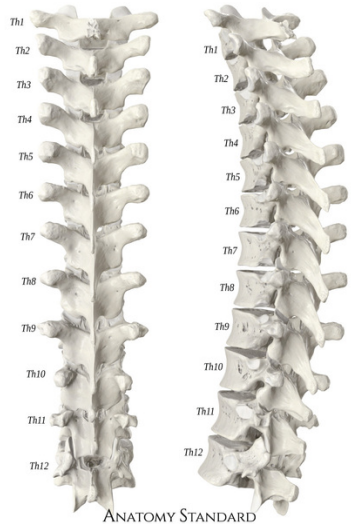

Figure 6.2.: Twelve thoracic vertebrae, going from T_1 down to T_{12}

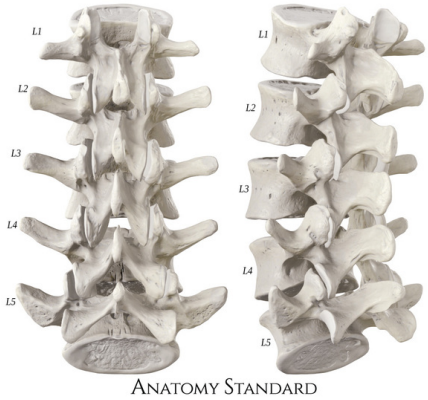

Figure 6.3.: Lumbar vertebrae, going from L_1 down to L_5



Figure 6.4.: Five fused sacral vertebrae, going from S_1 down to S_5, forming the sacral bone

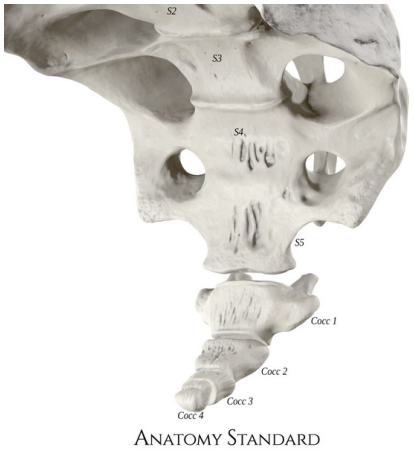

Figure 6.5.: Three to five fused coccygeal vertebrae, going from $Cocc_1$ down to $Cocc_3$, $Cocc_4$, or $Cocc_5$, forming the coccygeal bone

The combined region of the thoracic and lumbar vertebrae is also called the thoracolumbar region.

The intervertebral disc is a fibrocartilaginous joint which acts as a ligament to hold the vertebrae together and has the function of shock absorber for the spine, thanks to its gel-like center, the nucleus pulposus. There is one disc between each pair of vertebrae (Fig. 6.6).



Figure 6.6.: L_2 and L_3 separated by the intervertebral disc

6.1.2. Physiological spine curvature

The spine is made of four anterior-to-posterior curves. Two of them are kyphoses, the other being lordoses.

Kyphoses are curves that are convex posteriorly. They appear early in the fetal development and are thus called primary curves. The first kyphosis is the thoracic curve, which goes from T_2 to T_{12}. The second one is the pelvic curve, extending from the lumbosacral articulation to the coccyx.

Lordoses are curves that are convex anteriorly. They are called secondary (or compensatory) curves, as they only become apparent after the postnatal period. The first lordosis is the cervical curve, which covers the cervical region. The other

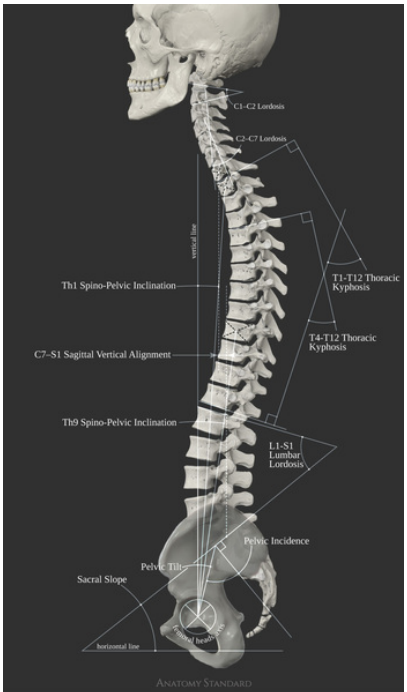

one is the lumbar curve, going from T_{12} to the lumbosacral articulation.

These curves are determined by a unique pelvic parameter: the Pelvic Incidence which is not influenced by the position of the subject (Legaye et al. 1998). There is an ideal lumbar lordosis in the standing position fitting a specific Pelvic Incidence (Roussouly et al. 2011), and in the same way there is an ideal thoracic kyphosis in the standing position (Clément et al. 2013). Lumbar lordosis and thoracic kyphosis change with the position of the subject. As an example, the lumbar lordosis and thoracic kyphosis both increase when going from the supine to the standing position (Wood et al. 1996). The spinal curves, with the help of the intervertebral discs and vertebral bodies, dissipate the load that would occur if the spine were straight.

6.1.3. Vertebral anatomy

The vertebra is a complex and irregular bone structure. It is made of the anterior vertebral body (vertebral body) and the posterior vertebral arch (posterior arch). Both parts are composed of a core of trabecular bone (also known as cancellous or spongious bone), surrounded by a compact shell of cortical bone. The trabecular bone is composed of trabeculae, oriented parallel to the line of greatest stress (Skedros et al. 1994). The space between the vertebral body and the posterior arch is defined as the vertebral foramen, which protects the spinal cord. The canal formed by the stacking of all the vertebral foramens is commonly called the spinal canal.

Vertebral body

The vertebral body is the anterior part of the vertebra. The vertebral body is the portion of the vertebra that supports body weight. It is cylindrical in shape, increasing in diameter from C_2 to L_3, probably due to the increasing weight supported by each successive vertebral body. The top and bottom parts of the vertebral body are called vertebral endplates, which are flat surfaces on which the intervertebral disc sits. The cortical bone of these endplates is thinnest in its center (we'll call this the vertebral endplate nucleus from here on), increasing in thickness as going towards the periphery (also called vertebral endplate ring) (Grosland et al. 2007).

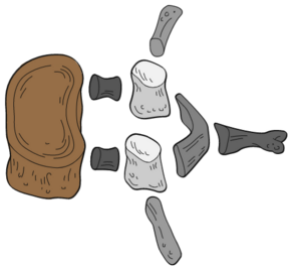

The posterior arch is the posterior part of the vertebra. It consists of two pedicles, two laminae, and seven processes. These seven processes, extending from the vertebra,

are:

- one spinous process,
- two transverse processes,
- four articular processes (two superior articular processes and two inferior articular processes).

Pedicles

The pedicles are the two symmetrical processes joining each side of the vertebral body to the posterior arch. They are short, thick and cylinder-shaped. From the pedicles, the laminae extend medially to the posterior part of the vertebra. They curve posteromedially to join in the spinous process, closing the posterior part of the vertebral foramen.

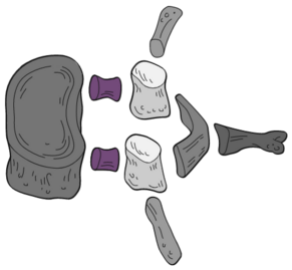

Spinous process

The spinous process extends posteriorly from the laminae, with its size, shape and direction varying greatly from one region of the spine to another. Moreover, it can deviate to the left or right of the vertebral column midline. These processes act as a series of levers for muscles of posture and movement. It is also one of the palpable part of the vertebra during a physical examination.

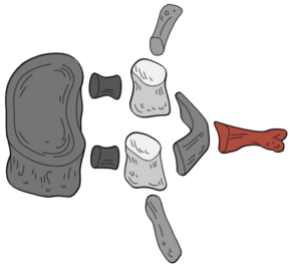

Transverse processes

The transverse processes are symmetrical. They project laterally from the junction of the pedicle and lamina, called the pediculolaminar junction. Like the spinous process, their overall direction varies from on region of the spine to another. They also serve as levers for muscles to maintain the posture, as well as generating rotation and lateral flexion of the spine.

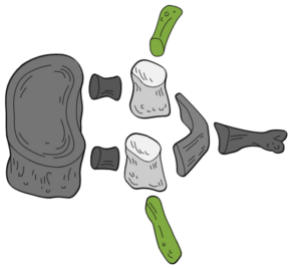

Articular processes

Like the transverse processes, the articular processes, also named zygapophyses are symmetrical, They extend from the pediculolaminar junction, with their articular surface named facets. The superior facets project superiorly and the inferior facets project inferiorly. Their overall direction depends on the region of the spine. The combined joint of the superior and inferior zygapophyses of two successive vertebra form the zygapophysal joint, also called Z joint.

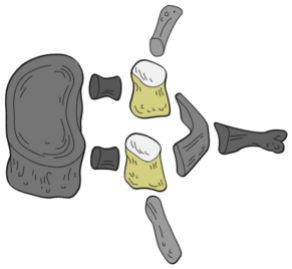

6.1.3.1. Intervertebral Differences

As indicated in the previous section, most parts of the vertebra have variable shapes depending on the region of the spine (summarized in Table 6.1) and more precisely of the vertebral level.

The vertebral body has different shapes depending on the region of the spine. Its transversal diameter tends to increase from C_2 to L_3, probably due to the increasing load on the vertebrae going down the spine.

The pedicles have a variation in their sizes and shapes. More compact and stronger bone is found in the most mobile regions (Pal et al. 1988).

The laminae increases in height from C_4 to T_{11}, then decreases from T_{12} to L_4 (Xu et al. 1999).

Vertebra structure	Region of the spine		
	Cervical	Thoracic	Lumbar
Vertebral body	Rectangular shaped, uncinate processes	Heart shaped, taller posterior than anterior, costal demi-facets	Kidney shaped, taller anterior than posterior
Pedicles	Small, superior and inferior vertebral notches	Large, no superior notch	Large, superior and inferior vertebral notches
Laminae	Short	Tall	Intermediate
Spinous process	Bifid	T_1-T_4: posterior direction, T_5-T_8: long and inferior direction, T_9-T_{12}: similar to lumbar	Spatule shaped
Transverse processes	Anterior and posterior tubercles, foramen of transverse process	Large, transverse costal facet	Large
Articular processes (superior facet direction)	Posterior, superior, medial, 45 degrees to the vertical plane	Posterior, superior, lateral, 30 degrees to the vertical plane	Posterior, medial, biplanar, within vertical plane

Table 6.1.: Summarized differences of the vertebra structures between region of the spine.

6.1.3.2. Human model vs. animal models

Various animal models, such as pig, calf, sheep, baboon, deer, goat and dog, have been used for in-vivo and in-vitro spinal research (Sheng et al. 2010). In-vitro models are cadaveric specimens, used to study the basic functions of the spine. In-vivo models are used to mimic living phenomena. In this case, human specimens are more suitable, but also come with drawbacks. It is becoming more and more difficult to obtain human specimens, especially young ones. Moreover, the large number of variables, like age, race, gender or pathology, greatly affects the variability of the geometry and the mechanical properties of the samples. These drawbacks create a need to find alternative animal models, which have more controllable and uniform geometric and mechanical properties. In order to simulate clinical situations, the ideal animal model should have similar anatomical geometry of the spine to humans.

Numerous studies have compared animal models to human models:

Baboon (Tominaga et al. 1995): They share similar geometry and anatomy of the cervical spine with humans , but vertebrae are about half of the size of human

vertebrae

Sheep (Kandziora et al. 2001): For the cervical spine, they demonstrate small inter-group standard deviations and good comparability with the human cervical spine

Pig (Bozkus et al. 2005, Dath et al. 2007): From T_6 to T_{10}, swine vertebrae are anatomically similar to their human counterpart; Considering lumbar vertebrae, they demonstrate small anatomical differences with humans

Calf (Cotterill et al. 1986): Calf vertebrae demonstrate differences in column length and curvature, and slight measurement differences

Deer (Kumar et al. 2000): Deer vertebrae have similar lower thoracic and upper lumbar vertebrae than human

Although some similarities have been found with animal models, every model shows some anatomical, geometric or size difference at some point. It means that every study must pick a specific model depending on the studied vertebral region and vertebral structure.

6.1.3.3. Morphological characterization of the vertebrae

Laporte et al. 2000 fully described vertebrae using an extensive set of parameters (Fig. 6.8, Table B.1). In total, 81 parameters were measured over 373 thoracic vertebrae from 50 adult spine.

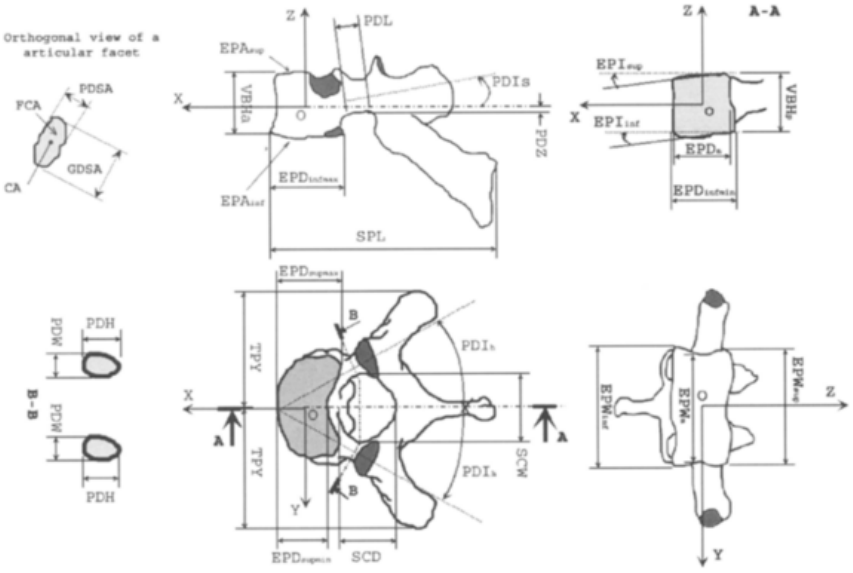

Figure 6.8.: Vertebra characterization (Laporte et al. 2000)

In order to capture the overall shape of the vertebra, anthropology has been using 2D and 3D landmarks.

K. A. Plomp et al. 2012 used 2D landmarks to analyze the effect of Schmorl's nodes over the shape of the vertebra, identifying 21 landmarks on the body and posterior elements of T_{10}, T_{11} and T_{12} (Fig. 6.9, Table 6.2).

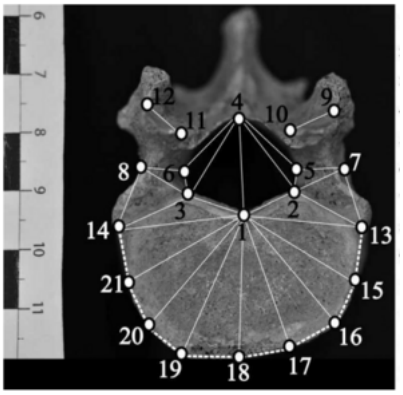

Figure 6.9.: 2D landmarks (K. A. Plomp et al. 2012)

Index	Description
1	Center of the posterior wall of the body
2	Intersection left pedicle/body
3	Intersection right pedicle/body
4	Posterior of neural foramen
5	Left of neural foramen
6	Right of neural foramen
7	External point of left pedicle
8	External point of right pedicle
9	Lateral-most point of left facet
10	Medial-most point of left facet
11	Lateral-most point of right facet
12	Medial-most point of right facet
13-21	Semi-landmarks for the superior margin of the body

Table 6.2.: 2D landmark description (K. A. Plomp et al. 2012)

K. Plomp et al. 2019 used 3D landmarks to study the differences of vertebra shapes between species. A total of 54 landmarks have been found relevant to capture the overall 3D shape of the vertebrae (Fig. 6.10).



Figure 6.10.: 3D landmarks (K. Plomp et al. 2019)

6.1.4. Vertebral cortical thickness

In skeletally mature human vertebrae, thickness of the cortical shell (Cortical Thickness (CTh)) is quite thin. According to Yeni et al. 2022, CTh in vertebrae ranges from (0.642 ± 0.146) mm to (0.701 ± 0.150) mm in the vertebral body. It is significantly thinner than in long bones like femur in which the CTh may be up to 12 mm (Niimi et al. 2015, Fig. 6.11).



Figure 6.11.: CTh of a femur assessed on a plain AP X-Ray (Niimi et al. 2015)

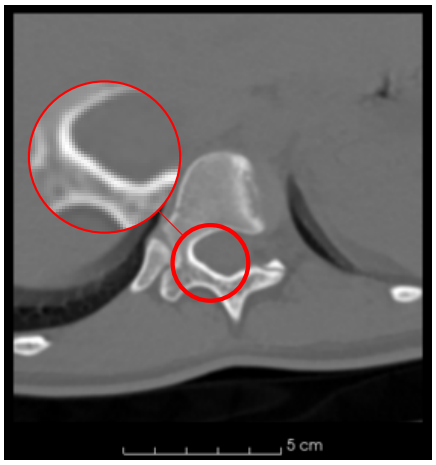

Figure 6.12.: CTh of a vertebra

The scale of CTh is significantly different between long bones (as femur) and vertebrae, as CTh is roughly 20 times thicker in femur than in vertebrae. This is why, in the literature, CTh in vertebrae is often assessed using micro CT more adapted to tiny structures assessment (Yeni et al. 2022). This is thoroughly explained in the chapter "Imaging modalities". But because of the incompatibility between an intact skeletally mature human body and the size-related specification of a micro CT, it is impossible to assess in vivo vertebral CTh using micro CT. This lead us to develop a method based on regular CT, usable in clinical practice, to assess and study the variability of CTh in vertebrae as CTh appears as a reliable avenue to get an automated patient-tailored 3D model of the spine.

6.2. Vertebral mechanical properties

The bone tissue is made of two types of tissues: the cortical bone (also known as compact or dense bone) and the trabecular bone (also known as cancellous or spongious bone). Cortical bone is in the form of a shell surrounding the trabecular compartment. As shown in Morgan; Unnikrisnan, et al. 2018, the main distinction between these tissues is porosity, which is the fraction of voids in the total volume. Cortical bone usually has a porosity ranging from 5% to 15%, while trabecular bone porosity ranges from 40% to 95%.

6.2.1. Microstructure of the bone tissue

6.2.1.1. Cortical bone

Cortical bone is a composite material composed of about 70% mineral (hydroxyapatite), 22% proteins (type *I* collagen) and 8% water by weight. In term of mechanical properties, these are determined by the overall quality and spatial arrangement of these constituents. The mineral constituents of the bone are mainly reponsible for the compression resistance, while having a poor ability to withstand tensile loads. The tensile strength comes from the collagen fibrils (arranged in lamellae). As the cortical bone is mostly loaded by bending moments (resulting in a high percentage of tensile strain), the structural quality of the bone depends highly on the quality and arrangement of the collagen fibrils. The stiffness of the cortical bone is mainly associated with its mineral content and bone density, while its toughness is associated with the quality of the collagen matrix (Zioupos et al. 1998).

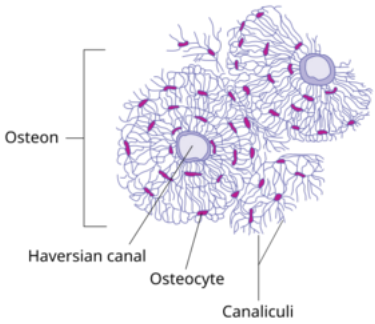

Figure 6.13.: Diagram of cortical bone structure (Wikipedia)

Structurally, cortical bone is organized into osteons (also called Haversian systems). These structures are cylinders of concentric layers of lamellae oriented parallel to the longitudinal axis of the bone, surrounding the Haversian canal which contains nerves and vessels supplying the osteocytes (bone cells).

The porosity of the cortical bone is due to the Haversian canals and resorption cavities embedded inside the tissue, with pore diameters ranging from a few up to several hundred micrometers.

6.2.1.2. Trabecular bone

Singh 1978 described and classified the human trabecular bone into seven types: I, IIa, IIb, IIc, IIIa, IIIb and IIIc.

Type I

This type of trabecular bone is made up exclusively of fine straight or curved rods, 0.08 mm to 0.14 mm in diameter and about 1 mm in length. These rods anastomose with each other to form a three-dimensional mesh, without any preferential orientation. It is typically found in the ends of long bones.

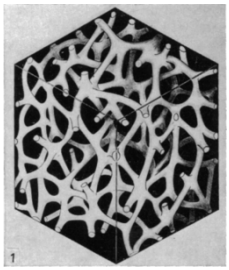

Figure 6.14.: Type I (Singh 1978)

Type II

This type is made up of both rods and plates.

Subtype IIa is often found in the mesh of Type I bone, with some of the rods being replaced by small plates of bone. These plates are 0.1 mm to 0.2 mm thick and about 1 mm long.

Subtype IIb is usually found in the calcaneum. It differs from IIa by having longer plates, up to several millimeters long, well oriented in preferred planes. The rods can also be much thicker and longer than IIa, up to 0.5 mm thick and several millimeters long.

Subtype IIc is closely related to some articular surfaces, often found at the lower end of the femur. It is composed mainly of plates parallel to each other. These plates are 0.16 mm to 0.3 mm thick. Their parallel structure can be retained up to a centimeter or more, before anastomosing with adjacent plates.

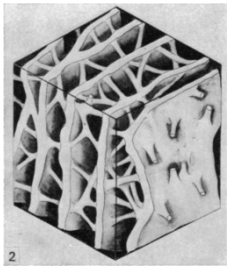

Figure 6.15.: Type IIc (Singh 1978)

Type III

This type of trabecular bone is made up entirely of plates of different sizes and shapes, forming a mesh.

Subtype IIIa is similar to IIa, with only plates 0.1 mm to 0.2 mm thick and about 1 mm long. It usually shows a preferential orientation.

Subtype IIIb is made up exclusively of plates in parallel formation. These plates are 0.12 mm to 0.24 mm thick. This type is present in the whole skeleton, and the architecture of lower vertebrae is mainly of this type.

Subtype IIIc is encountered under articular surfaces (e.g. the head of the femur). It

is also found in the upper cervical vertebrae and in the patella. It is made up of thick plates (0.2 mm to 0.4 mm).

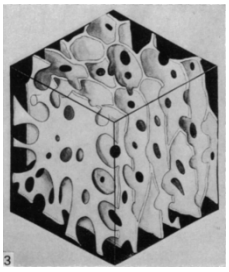

Figure 6.16.: Type IIIb, Singh 1978

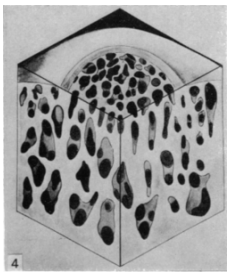

Figure 6.17.: Type IIIc, Singh 1978

6.2.1.3. Characterization of the bone microstructure

Characterization of the bone microstructure is performed using mostly microCT scan with a resolution which could varies from 20 µm to 80 µm. Several parameters to characterized such microstructure have been defined and could now be computed directly from dedicated software such as BoneJ (Domander et al. 2021):

- Trabecular bone anisotropy: which enable to described if there is an orientation of the bone trabeculae. This is based on computation of mean intercept length (MIL) in a specific direction (you could define n direction). For a specific point, all MIL vectors are plot and an ellipsoid is fits and the degree of anisotropy is computed from the radii of the ellipsoid.
- Area and volume fraction (BV/TV) the volume of mineralised bone BV per unit of volume TV. It could also be computed in 2D as BA/TA (area of bone per unit of the sample).
- Connectivity which described is the trabeculae is connected to a trabeculae network. The Euler characteristic/number or Euler-Poincaré characteristic which described the structure of a space (objects-handles/hole through + cavities/-holes enclosed). Selection of the volume of interest induces error depending of the volume selection.
- An ellipsoid factor which measure the rod/plate geometry (Doube 2015).
- the inter-trabecular angles depicting a nodes/vertices and edge/branches model of the trabecular bone. Valence (minimum and maximum), trabecular length and skeleton could be computed together with inter-trabecular angles (depending on the number of branch per node) as well as a percentage of type of edge to be modeled. (Reznikov et al. 2016)
- the thickness of the trabeculae (Tb.Th) and trabecular separation (Tb.Sp) based on a thickness map (R. Dougherty et al. 2007, Hildebrand et al. 1997).

6.2.2. Mechanical characterization of the bone tissue

Mechanical characterization of the vertebral bone tissue has been motivated by the assessment of pedicle screw insertion through bone quality assessment. The pedicle screws insertion quality and stability have been assessed by pullout tests. Additionally, bone tissue have also been tested, for long bones as well as for vertebral bone tissues, with different types of tests. These tests have been thoroughly described in Bailey et al. 2018 (Table 6.3). This section aims at providing the description of such tests and results for further discussion of the influence of trajectory and material properties in the context of perforation.

Length scale	Specimen type	Tests	Measurements
Whole bone	Long bone, vertebra	Bending, tension, compression, torsion	Extrinsic mechanical properties (e.g. structural stiffness, max load, ...)
Tissue	Cortical beam, cancellous cores	Tension, compression, torsion, bending fatigue	Intrinsic mechanical properties (e.g. Young's modulus, yield, fatigue, ...)
Micro	Cortical bone cubes (up to 5 mm), bone slices)	Microscratch, microindentation	Material level properties (e.g. hardness, modulus, ...)
Nano	Bone specimen (2 mm to 3 mm thick), bone slices	Nanoindentation, in-situ testing	Material level properties (e.g. hardness, modulus, fibril strain, ...)

Table 6.3.: Summary of mechanical characterization techniques (Bailey et al. 2018)

6.2.2.1. Mechanical testing of the bone tissue

Tensile tests

Tensile tests consist in a application of a tensile load and measurement of the force and distortion of the sample during the load. In long bone, dog bone shapes could be created and a tensile load is applied with a specific strain rate (dynamic or quasi-static) after preparation of the specimen to have an homogeneous thickness (and cross-section area). Preparations of the sample differ depending of the study (diamond wire saw, polishing, rinsing and soaking of the sample) as well as mounting of the specimen within the grips or fixtures. Extensonmeter or target tracking could be used to measure displacement. The test system as well as the load cell to be used will depend on the strain rate to be applied (as well as maximum force to be reach).

Compression tests

Standardization of bone testing has been intended thanks to a literature review article (S. Zhao et al. 2018). In the resulting 177 articles included in the qualitative synthesis, the authors were able to recommend sample preparation (wet or dry specimen have influence on stiffness measurement, freezing with marrow intact), to note and indicate

orientation and anatomical location of the sample, to use cylindrical geometry respecting aspect ratio to avoid buckling (between 1 to 2), minimum 5 mm diameter and 10 mm height (using irrigated, low speed, low force cutting device to avoid thermal and mechanical damage), to avoid non parallelism and misalignment between plates using pivoted on a ball bearing with polish and/or lubricated surface to avoid friction, to control the temperature and environment, to performed a cyclic preconditioning (0.3 to 0.5%) to minimize irreversible damage of the sample for testing with strain rate < 0.1 s^{-1}, to use strain gauge, extensiometer, or tracking if possible, to test with a strain rate between 0.005 s^{-1} and 0.08 s^{-1} for physiological strain rate. The authors also advice testing the protocol on known material for identification of measurement error and reproducibility.

Specificity of vertebral bone tissue characterization

Based on the previous section, the possibility to extract standardize specimen in vertebrae make is difficult to accurately characterize both cortical and trabecular bone tissue. However, compression test of vertebrae samples have been reported using inverse analysis for identification of bone tissue properties (El Masri et al. 2012). In this study, microCT scan is used for segmentation of the sample geometry. 22 vertebrae were tested. Reported Young's modulus ranged from 88 MPa to 791 MPa.

6.2.2.2. Pullout tests: Test methods to measure pedicle screw fixation strength

When a pedicle screw is pulled out from a vertebra, a fracture usually appears on the bone between the crests of the screw thread. Therefore, the quantity and quality of the bone between the threads is an important factor to measure the screw fixation strength. Several factors are believed to influence the pullout strength: 1. a larger outer diameter of the screw, 2. a smaller inner diameter of the screw, 3. a shorted pitch, and 4. a stronger bone. On the contrary, tapping has been proven to significantly reduce the pullout strength (Chapman et al. 1996).

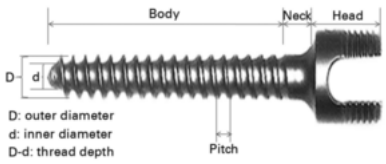

Figure 6.18.: Pedicular screw (Cho et al. 2010)

From a morphological point of view, Hirano et al. 1997 showed that about 60% of the screw pullout strength and 80% of the longitudinal stiffness depend on the pedicle, compared to the vertebral body. Moreover, Misenhimer et al. 1989 found that, because the pedicle is the first to deform, the screw does not gain purchase in the cortical bone inside the pedicle. This shows that a pedicle screw with a larger diameter than the endosteal diameter of the pedicle would probably damage the pedicle.

In order to measure the pedicle screw fixation strength, pullout strength tests have been designed. These tests have been described in the norm ASTM F543-07 (e.g. Fig. 6.19). A axial tensile load at a constant rate is applied on the screw and pullout

strength, pullout stiffness (elastic part slope of the strain and stress curve), pullout yield (maximum load before plastic part) and pullout energy to failure (area under the curve) are measured.

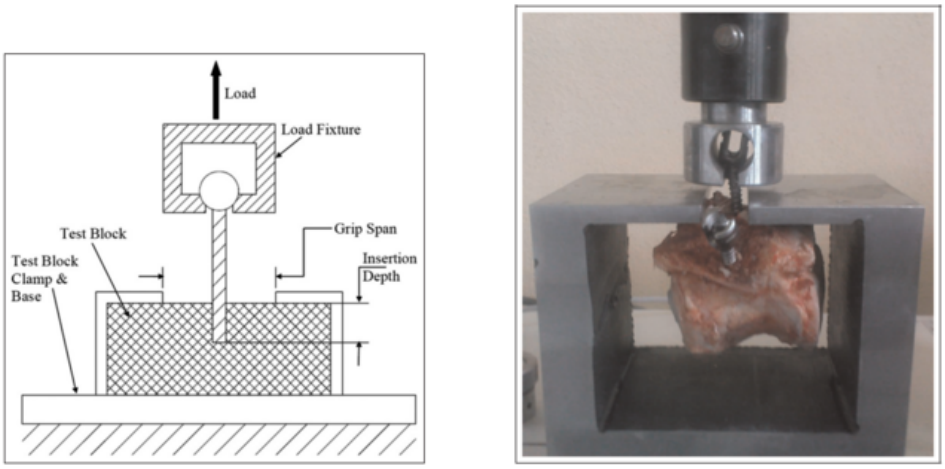

(a) Schematic view of the pullout test setup

(b) Pullout test on the calf vertebra

Figure 6.19.: Example of a pullout test (Demir et al. 2012)

6.2.2.3. Indentation tests: towards perforation characterization

Indentation testing (Fig. 6.20) is a widely used technique to assess the mechanical properties of materials, including bone. It provides information on two key properties: stiffness and hardness. Stiffness refers to a material's resistance to bending or deformation under an applied load. Hardness, on the other hand, reflects its ability to resist localized surface indentation.

The test involves preparing a thin slice of bone tissue (either cortical or trabecular) and subjecting it to a controlled static force using a specialized tip. The resulting indentation left by the tip is then analyzed visually. This technique allows us to measure two important mechanical properties: hardness and elastic modulus. Hardness is calculated as the applied force divided by the contact area between the indenter and the bone (Eq. 6.2). The elastic modulus, which represents the material's stiffness, is determined from the slope of the initial, linear portion of the force-displacement curve obtained during the indentation test (Eq. 6.1, Fig. 6.20d).

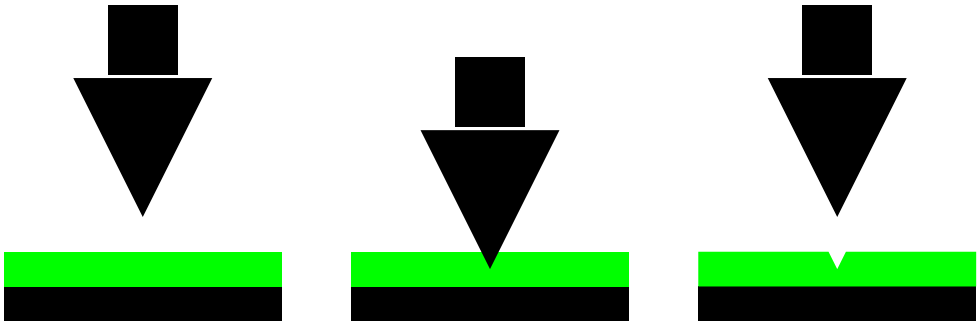

(a) Before indentation (b) During indentation (c) After indentation

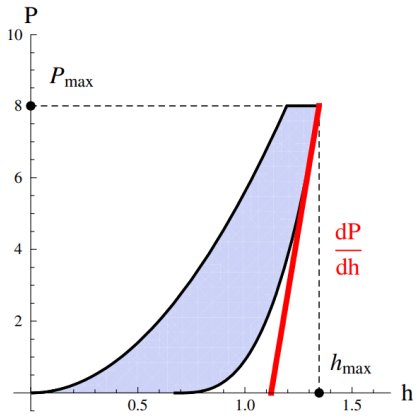

(d) Indentation curve (Zysset 2009)

Figure 6.20.: Indentation

Definition 1: Hardness H, Young's modulus E (indentation tests)

$$S = \frac{dP}{dh} = \frac{2}{\sqrt{\pi}} E_r \sqrt{A} \tag{6.1}$$

$$H = \frac{P_{max}}{A} \tag{6.2}$$

S: Stiffness (slope of the load (P) - displacement (h) curve, Fig. 6.20d)
A: Projected area of the tip-sample contact area
E_r: Reduced modulus with:

$$\frac{1}{E_r} = \frac{1-\nu_s^2}{E_s} + \frac{1-\nu_i^2}{E_i} \underset{E_i \gg E_s}{\approx} \frac{1-\nu_s^2}{E_s} \tag{6.3}$$

E_s, E_i: Young's modulus of the sample and indenter
ν_s, ν_i: Poisson's ratio of the sample and indenter

Indentation at different scales

The indentation technique can be applied at different scales to assess bone mechanics at various levels:

Microindentation This technique focuses on the microstructure of bone, such as osteons and trabeculae. It measures mechanical properties at a length scale ranging from 5 µm to 200 µm.

Nanoindentation This technique allows for characterization of bone mechanics at the sub-micrometer level. It can measure indentation depths as small as 100 nm and has a spatial resolution of 1 µm within the bone tissue.

Application to pedicle screw implantation

In Mehmanparast et al. 2014 research, indentation tests using a custom probe in the pedicle have been reported. These tests confirmed significant relationships between indentation, torque, pullout force and stiffness. It also indicates that screw pullout force and stiffness can be estimated from measurement during screw insertion, like indentation force and insertion torque).

6.3. Spinal diseases and their morphological consequences

6.3.1. Etiology of the spinal diseases

Spine diseases can be be separated into 5 categories:

Degeneration of the spine (Gallucci et al. 2007) Degenerative disease of the spine includes a wide spectrum of degenerative abnormalities. This degeneration is either age-related or pathological, and is considered the consequence of overuse injury. The lower cervical spine (C_6, C_7) is often affected, due to the inversion of the lordosis *through ageing*. The lumbosacral region (L_4, L_5, S_1) is the most frequent localization of spine degeneration, because it endures the highest static and dynamic loads (Resnick 1985). Thoracic degeneration is rare, as this region of the spine is less mobile and less involved in dynamic loading.

Trauma (Looby et al. 2011) Spinal trauma is a high-morbidity and-death related event. Spinal fractures represent 3 to 6% of all skeletal injuries:

1. Cervical fractures: the most common cervical fractures involve the upper and lower ends of the cervical spine (C_1: approx. 10%, C_2: approx. 33%, C_6 and C_7: approx. 50%).
2. Thoracolumbar fractures: Most thoracolumbar fractures involve the lower thoracic spine, with 60 to 70% of all thoracolumbar fractures occurring between T_{12} and L_2.

Tumor (Van Goethem et al. 2004) Spinal tumors are uncommon lesions and affect only a minority of the population. There are three types of spinal tumors:

1. Extradural tumors:
   - 60% of the spinal tumors.
   - The most common extradural tumor is metastasis. According to Maccauro (Ref), a metastasis is the spread of cancer from one part of the body to another. A spinal metastasis may cause pain, instability and neurological injuries. The diffusion through the venous system is the principal process of spinal metastasis, but the dissemination is possible also through arterial and lymphatic system or by contiguity.
   - **Morphological consequences:** bone destruction, sclerosis and/or remodelling.
2. Extramedullary intradural tumors:
   - 30% of the spinal tumors.
   - Meningiomas and nerve sheath tumors make up approximately 90% of all extramedullary intradural tumors, with nerve sheath tumors the most common (30% of all cases).
3. Intramedullary tumors:
   - Most uncommon lesion, 10% of the spinal tumors.
   - Ependymoma, which begins in the ependymal cells of the brain and spinal cord, makes up for about 95% of all intramedullary tumors.
   - Mainly affects the spinal cord.

Infection (Tyrrell et al. 1999) Infectious spondylitis represent 2 to 7% of all cases of bone infection (osteomyelitis). It can affect any component of the vertebra : the vertebral body, the intervertebral disc or the posterior elements. These infections can be split in two categories:

1. Pyogenic infection:
   - Caused by pyogenic organisms.
   - The most common site of infection is the lumbar spine.
   - **Morphological consequences:** sclerosis, new bone formation, kyphosis deformity, intervertebral disc height loss, loss of definition of bone endplate
2. Granulomatous (non-pyogenic) infection:
   - The most common infection site is the thoracic spine.
   - **Morphological consequences:** osteoporosis, osteolysis, intervertebral disc height loss, erosion of the anterior part of the vertebral body, development of calcified soft tissue masses

Deformity (Schlenk et al. 2003) Spinal deformities can be congenital like Congenital Scoliosis due to focal vertebral abnormality like hemi-vertebra or acquired during growth like Adolescent Idiopathic Scoliosis. Spinal deformities can be decomposed by rotations and/or translation in the three fundamental planes: sagittal, coronal and axial (also known as transverse plane).

1. Rotational deformation: kyphosis (flexion rotation in the sagittal plane), lordosis (extension rotation i, the sagittal plane) and scoliosis (lateral bending rotation in the frontal plane, frontal rotation, and transversal plane rotation), or a combination of these.
2. It is important to highlight that spinal deformities may be worsening over time, especially during the adolescence growth spurt.
3. Translational deformation: caused by shearing, compression, or distraction of the spinal segments.

All theses condition may require a specific treatment, sometimes a surgical treatment. In addition to these diseases, patients, mainly elder people, can come with co-morbidities, such as diabetes or malnutrition. These co-morbidities increase the risk of postoperative complications.

Kobayashi et al. 2022 demonstrated a net increase in spine surgeries during the last 15 years. This increase may be explained by the aging of the population.

6.3.2. Diagnosis of spinal diseases

6.3.2.1. clinical diagnosis

As highlighted by Rothman et al. 2018, caring for patients with spine disorders can be extremely challenging for clinicians because of the complexities of spinal anatomy and pathophysiology as well as the multifactorial nature of pain if any. To address the needs of patients with spine disorders and to select appropriate patients for whom specific care may be beneficial, clinicians need to identify the true nature of a patient problem. Frequently, the patient problem may extend well beyond any anatomic derangement that can be identified on imaging studies and involve numerous psychosocial factors in the patient life.

Through the history and physical examination, clinicians are able to identify not only the physical manifestations of a spine disorder but also the root causes of a patient distress, suffering, and disability, all of which ultimately need to be addressed if a successful outcome is to be achieved.

A thorough history and physical examination of a patient with a spine disorder has several aims. From a strictly medical perspective, the examiner must be aware of the full medical context of the patient complaints and how the complaints may relate to the overall health of the patient. It is imperative to ascertain the presence of an emergent medical problem promptly and to identify patients who need more urgent (or emergent) assessment and care.

Clinicians must also identify any secondary medical issues that may directly affect the

care of spine-related problems or may be associated with broader health concerns. In a more focused sense, the history and physical examination should allow an examiner to identify relevant spine problems that have led to the issue for which the patient is seeking care (e.g., the source of pain or neurological loss, anatomic derangement). he history and physical examination also allow the practitioner to understand the level of function and impairment that is associated with the patient presentation. The only way to identify the issues behind the presentation of many patients is by asking the right questions.
After obtaining a complete history, a focused examination can be performed to establish a baseline functional and neurologic assessment, identify pertinent positive and negative findings that can help narrow the differential diagnosis, and define further issues that may need to be addressed through additional testing. Neurologic and orthopaedic examinations of varying degree and complexity are also necessary.

6.3.2.2. Imaging modalities

After a careful history collection and a thorough physical examination, it is often necessary to rely on imaging modalities in order to establish a diagnosis. (Rothman et al. 2018). One can classify imaging modalities in 5 schematic clusters:

Biplanar conventional Radiographs - EOS

Routine conventional plain films are universally available and inexpensive, but are limited by an inability to directly visualize neural structures and nerve root or cord compression (Rothman et al. 2018).



Biplanar radiographs may expose the patient to a significant amount of radiations (conventional radiographs) or to a reduced amount of radiations (EOS) (Wade et al. 2013): EOS is a biplane X-ray imaging system manufactured by EOS imaging (formerly Biospace Med, Paris). It uses slotscanning technology, based on the Nobel prize-winning work of physicist Georges Charpak on multiwire proportional chambers, to produce a high-quality image with less radiation than standard imaging techniques. In the work of Wade et al. (Wade et al. 2013), the radiation dose has been shown to be significantly lower with EOS than conventional X-ray: the mean entrance surface dose with EOS for the spine Postero-Anterior view was 0.23 mGy compared with 1.2 mGy with conventional film. The mean entrance surface dose with EOS for the spine lateral view was 0.37 mGy compared with 2.3 mGy with conventional X ray. EOS has been developed for orthopaedic imaging, with the benefit that it can take postero-anterior (PA) and lateral images simultaneously, allowing the manual reconstruction (by manual contouring on both AP view and Lateral view) of a 3D model imaging of the spine (Wade et al. 2013).

CT-scan



CT scan stands for Computed Tomography scanner. It was mathematically theorized by Johannes Radon in 1917 and by Allan MacLeod Cormack in the early 70's, and then eventually released for a clinical use by Godfrey Hounsfield in the 70's. A CT scan is made from X-ray measurements took from different angles and processed through a tomography reconstruction in order to produce sectional images. The output of these measurements is a linear attenuation coefficient of the X-ray beam. This linear attenuation coefficient represents how much of the beam photons were absorbed along their path through the medium (e.g. human body).

Current multirow detector technology now available allows for extremely rapid thin-slice acquisitions over long body segments. The acquisition of isotropic voxels allows for multiplanar reformation of the CT data with no loss in spatial resolution. Changes in the windowing and leveling of the images can change the focus onto either dosshouse structures or sot tissues (Rothman et al. 2018).

Besides classic CT scan devices, there are microCT devices, in which the pixel sizes of the cross-sections are in the μm range. A patient full spine cannot be scanned in a microCT device because of the human body size. MicroCTs are devoted to limb extremities studies or bone sample studies (Folkestad; Hald, et al. 2012, Folkestad; Groth, et al. 2020, Mys et al. 2021).

The main disadvantages of CT scan is radiation exposure. Nevertheless, Abul-Kasim; Gunnarsson, et al. 2008 showed that using proper setting on regular CT machines, the lowest radiation dose which had no impact on image quality with regard to the information required for surgical planning of patients with scoliosis (whole spine CT scan) was 20 times lower than that of routinely used protocol for CT examination of the spine in children (0.38 mSv vs 7.76 mSv). He defined this peculiar setting as Ultra Low Dose CT scan (ULDCT scan). One can observe that this amount of radiation exposure compares favorably with conventional X-Rays, and is quite similar to the radiation exposure of a combined full-spine AP and Lateral EOS view.

Magnetic Resonance Imaging (MRI)

When a nucleus contains either unpaired protons, neutrons, or both, it has angular momentum. This property provides the basis for magnetic resonance imaging (MRI). Because of its abundance in the human body, hydrogen is used for clinical MRI. Within the MR magnet, the atoms are aligned with the magnetic field. The MR signal is generated by subjecting the atoms to radiofrequency (RF) pulsations, and the pulse sequences selected will determine the appearance of the image. The repetition time

(TR) is the time between the RF pulses, and the echo time (TE) is the time between the RF pulse and the recording of the signal. T1-weighted images (short TR/short TE) provide the best anatomic detail, but T2-weighted images (long TR/long TE) are often needed to demonstrate pathology (Seeger 1989).

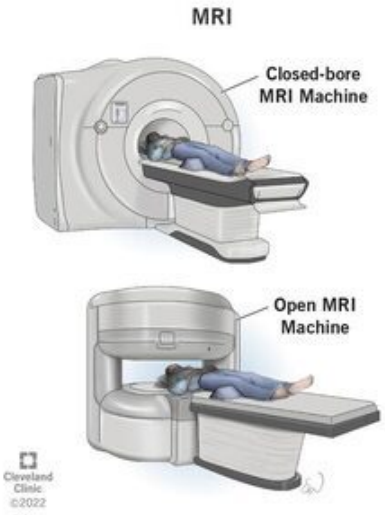

MRI can readily evaluate the extradural, intradural extramedullary, and intramedullary spaces and is also the only modality that can directly image bone marrow. Since the beginning of its clinical use in the early 1980s, MRI technology has progressed with improved quality and decreased examination times. It is a non-ionizing and non-invasive imaging modality. (Rothman et al. 2018). To date, Bone MRI is still not fully available in clinical practice as it requires a complex and AI-based image post processing, but it is probably the future of 3D bone imaging (van der Kolk et al. 2022).

Bone Scan

Bone scan also known as bone scintigraphy uses a radionucleotide (Technetium 99m (99mTc)) that is intravenously injected and sticks (metabolic uptake) to the bony structures. Bone scan measures metabolic uptake of 99mTc. It is commonly used for detecting inflammatory changes of the spine (Rothman et al. 2018).

DXA

Dual-energy X-ray absorptiometry (DXA) is a means of measuring bone mineral density (BMD) using spectral imaging. Two X-ray beams, with different energy levels, are aimed at the patient's bones. When soft tissue absorption is subtracted out, the bone mineral density (BMD) can be determined from the absorption of each beam by bone. Dual-energy X-ray absorptiometry is the most widely used and most thoroughly studied bone density measurement technology. Soft tissue and bone have different attenuation coefficients to X-rays. A single X-ray beam passing through the body will

be attenuated by both soft tissue and bone, and it is not possible to determine, from a single beam, how much attenuation was attributable to the bone. However, the attenuation coefficients vary with the energy of the X-rays, and, crucially, the ratio of the attenuation coefficients also varies. DXA uses two energies of X-ray. The difference in total absorption between the two can be used, by suitable weighting, to subtract out the absorption by soft tissue, leaving just the absorption by bone, which is related to bone density (Pietrobelli et al. 1996).

Intra-operative imaging (C-Arm, Cone Beam Computed Tomography)



C-Arm (also defined as fluoroscopy) is an imaging technique that uses X-rays to obtain real-time moving images of the interior of an object. In its primary application of medical imaging, a fluoroscope allows a surgeon to see the internal structure and function of a patient. This is useful for both diagnosis and therapy and occurs in general radiology, interventional radiology, and image-guided surgery. In its simplest form, a fluoroscope consists of an X-ray source and a fluorescent screen, between which a patient is placed. However, since the 1950s most fluoroscopes have included X-ray image intensifiers and cameras as well, to improve the image's visibility and make it available on a remote display screen. For many decades, fluoroscopy tended to produce live pictures that were not recorded, but since the 1960s, as technology improved, recording and playback became the norm. Fluoroscopy is similar to radiography and X-ray computed tomography (X-ray CT) in that it generates images using X-rays. The original difference was that radiography fixed still images on film, whereas fluoroscopy provided live moving pictures that were not stored. However, today radiography, CT, and fluoroscopy are all digital imaging modes with image analysis software and data storage and retrieval (Anderson 2017).

Cone Beam Computed Tomography

Also known as CBCT, Cone Beam Computed Tomography is a medical imaging technique consisting of X-ray computed tomography where the X-rays are divergent, forming a cone.Over the years, CBCT has become increasingly important in treatment planning and diagnosis in orthopedics, and interventional radiology (IR) (Tonetti et al. 2020).

6.3.2.3. Radiation risks in medical imaging

Even though medical imaging allowed for a lot of medical advancements (like more effective surgical treatments, shorter hospital stays or elimination of the need of exploratory surgery), a lot of its modalities also brought risks of ionizing radiation exposure (Table 6.4).

Type of procedure	No. of procedures (in millions)	Per-capita dose (mSv)
Diagnostic radiographic and fluoroscopic studies	293	0.33
Interventional procedures	17	0.43
CT scans	67	1.47
Nuclear medecine studies	18	0.77

Table 6.4.: Estimated dose in the United States (Mettler et al. 2009)

As their uses of these modalities increase with time (Table 6.5), it has become clear that the ionizing radiation exposure would become a more visible and known risk that needs to be addressed. One way to address this issue is by reducing the intrinsic power of the modality (e.g. ultra low dose CT scans, Mostafapour et al. 2024). Another way would be to simply reduce the overall number of procedure.

Type of procedure	1950	1964	1970	1980-1982	2006
Radiographic and fluoroscopic studies	25	109	136	177	293
CT scans				2 - 3.5	67
Interventional procedures					17
Nuclear medecine studies				7	18

Table 6.5.: Estimated number of procedures in the United States (Mettler et al. 2009), numbers are in millions

6.3.3. Morphological consequences of spinal diseases

Spinal diseases may have massive consequences on the vertebral and spinal anatomy.

6.3.3.1. Degeneration of the spine

According to Gallucci et al. 2007, there are multiple spine degenerations:

Vertebral osteochondrosis

Morphological consequences

Vertebral end plate and bone marrow alteration are observed, strictly associated with inter-vertebral disc degeneration. It is more frequently found in the lumbosacral region.

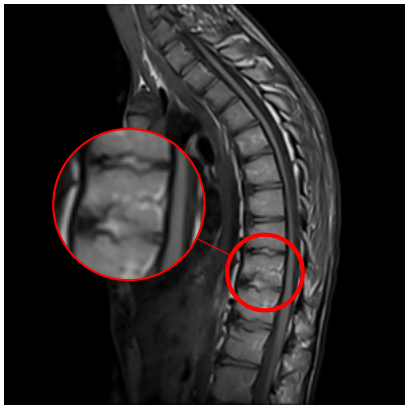

Figure 6.21.: MRI visualization of vertebral end plate and bone marrow alteration

Osteoarthritis

Morphological consequences

Joint space narrowing, subchondral sclerosis, cysts, osteophytosis (abnormal bone production), ligament thickening, intra-articular vacuum and joint fluid are observed. It happens frequently in facet joints (in the posterior arch). It often leads to vertebral instability.

Spondylolysis and spondylolisthesis

The most common kind of lumbar spondylolysis is isthmic: it is defined as a defect of the pars interarticularis of the vertebra. It is an acquired change over time. The most common sites of spondylolysis are L_5 (81%) and L_4 (14%). It often leads to spondylolisthesis (when the vertebral body slips on the vertebra below it), grading from I to V (Fig. A.1). An forward slip is called *anterolisthesis* (often simply called spondylolisthesis), while a posterior slip is called *retrolisthesis*.

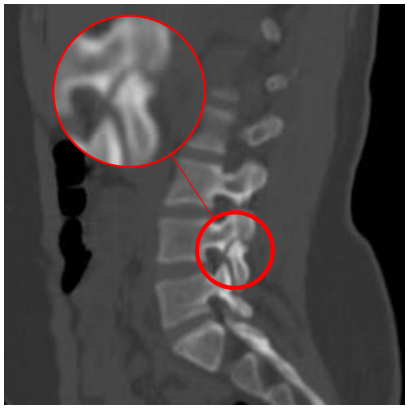

Figure 6.22.: CT visualisation of a L_4 spondylolysis

Degenerative stenosis

It is most frequently observed in the lumbar region. It is due to inter vertebral disc changes, joint space narrowing, cysts, osteophytosis (also known as bone spurs that are outgrowths of bone tissue that form around damaged joints) and ligament thickening all around the spinal canal.

Morphological consequences

Narrowing of the spinal canal diameter.

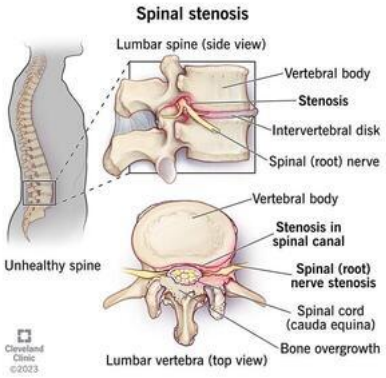

Figure 6.23.: Schematic visualization of degenerative stenosis in the lumbar spine

6.3.3.2. Trauma

Vertebral trauma may change vertebral and spinal morphology in many ways. It has been thoroughly described in Vaccaro; Oner, et al. 2013 (Fig. A.2). Basically, trauma can be divided in fractures (structural bone changes) and ligament tears. The grading of the trauma has been described as a simple decision tree (Fig. A.3).

6.3.3.3. Tumor

According to Maccauro et al. 2011, once cancer cells have invaded the bone, they produce growth factors that stimulate osteoblastic or osteolytic activity resulting in bone remodeling with release of other growth factors that lead to a vicious cycle of bone destruction and growth of local tumor (Fig. 6.24).

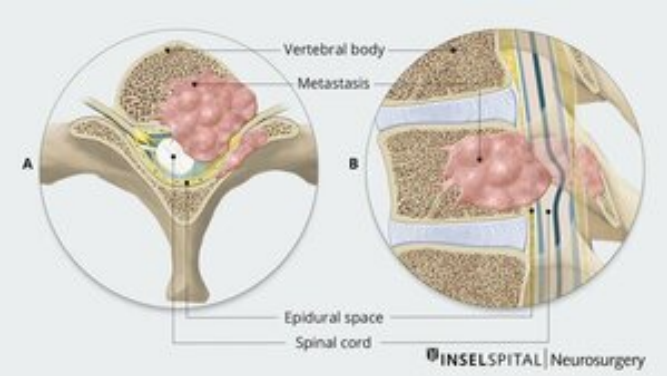

Figure 6.24.: Vertebral metastasis

6.3.3.4. Infection

According to Tyrrell et al. 1999, vertebral infection (vertebral osteomyelitis, Fig. 6.25) can affect any component of the vertebra: the vertebral body, the intervertebral disc or the posterior elements. Sclerosis, new bone formation, kyphosis deformity, intervertebral disc height loss, loss of definition of bone endplate can be observed in vertebral infection.

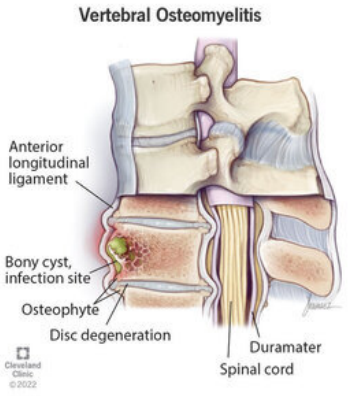

Figure 6.25.: vertebral osteomyelitis

6.3.3.5. Spinal deformities

Regardless of the cause of spine deformity (AIS, congenital scoliosis, degenerative scoliosis), one can observed combinations of rotations and/or translation in the three fundamental planes: sagittal, coronal and axial (also known as transverse plane). Moreover, the shape of vertebrae itself can be changed in scoliosis: they can be asymmetrical in a wedge shape. The *Cobb angle* is the most widely used measurement to quantify the magnitude of the spinal deformities. In order to measure this angle, one must first decide which vertebrae are the end vertebrae of the deformity (i.e. the vertebrae whose endplates are the most tilted toward each other). From these vertebrae endplates are drawn lines, with which the Cobb angle is defined (Fig. 6.26).

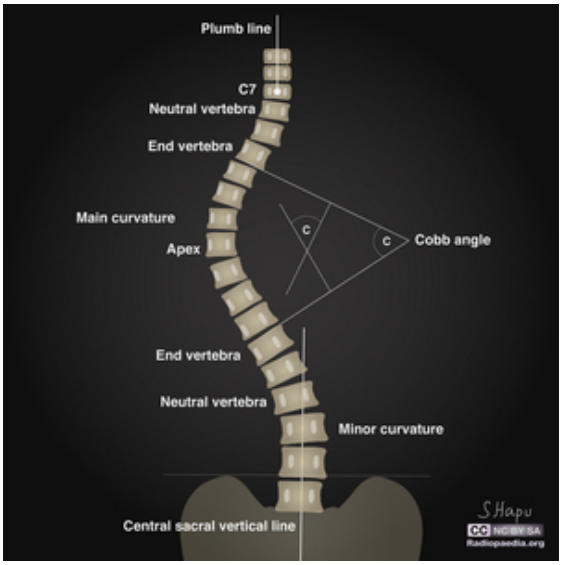

Figure 6.26.: Cobb angle

Scoliosis A scoliosis is any lateral spinal curvature with a Cobb angle greater than 10° (Fig. 6.27a). If the convexity of the curve is directed towards the left, the scoliosis is referred as *levoscoliosis*, while the opposite one is referred as *dextroscoliosis*.

Kyphosis An increased kyphosis can be seen in diseases like the *Scheuermann disease* (Fig. 6.27b). An example of a decreased kyphosis condition is the *straight back syndrome*. In both cases, the deformity is traditionally measured using the Cobb angle.

Lordosis An abnormal inward curvature of the spine is called *hyperlordosis*. Similar to the *straight back syndrome*, a decreased lumbar lordosis is called *flat back syndrome*.

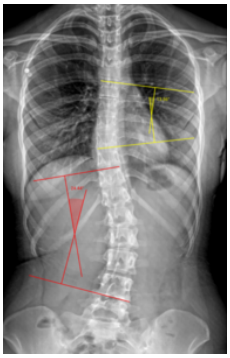

(a) Scoliosis, X-ray view

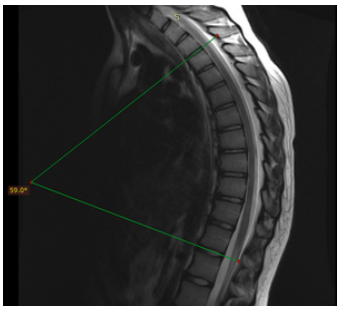

(b) Scheuermann disease, X-ray view

Figure 6.27.: Spine deformity examples

6.4. Spine surgery: pedicle screw implantation

6.4.1. Context



Pedicle screws are commonly used in spine surgery. This type of hardware setting can be conducted on patients with degenerative disease, trauma, tumor, infection or spine deformity (Smorgick et al. 2005). Pedicle screw fixation is used in spine surgery to stabilize the spine until a solid fusion occurs after bone autografting. It has been initially used in trauma since the 1960s and then progressively extended over time to other indications. This surgical procedure is usually credited to *Raymond Roy-Camille* who first introduced it in Roy-Camille; Berteaux, et al. 1977 as a way to achieve a strong and stable fixation of the lumbar segment for unstable spine fractures, using the pedicles as a strong attachment point (Fig. 6.28). Its practice has since been extended to other indications like trauma, vertebral tumors, vertebral malunions, bone defect reconstruction or low-back pain disorders (Roy-Camille; Saillant, et al. 1986b). In the last decades, studies report large growth of these surgeries of 169% in Australia (1997-2006, I. A. Harris et al. 2009), 63% in the United Kingdom (2005-2015, Sivasubramaniam et al. 2015), and 113% in the United States (1996-2001, Deyo et al. 2005). However, reported failure rates still range high, from 0 to 50% for cervical osteosynthesis (Riley et al. 1969; Phillips et al. 1997; G. J. J. Martin et al. 1999; Hilibrand et al. 1998; Emery et al. 1994; Bohlman et al. 1993; J. C. Wang et al. 2001), 18% for thoracic osteosynthesis (Y. J. Kim; Bridwell, et al. 2005), and 9 to 36% for lumbar osteosynthesis (B. I. Martin et al. 2007; Greiner-Perth et al. 2004; R. W. Hu et al. 1997; Malter et al. 1998; Elias et al. 2000; Brantigan 1994)..

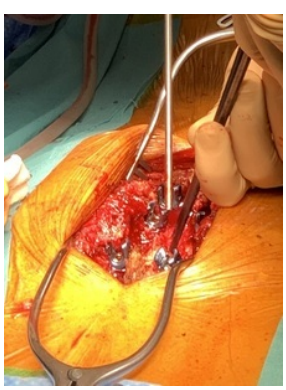

(a) Picture of a screw implantation surgery



(b) Frontal view of a posterior spinal fusion

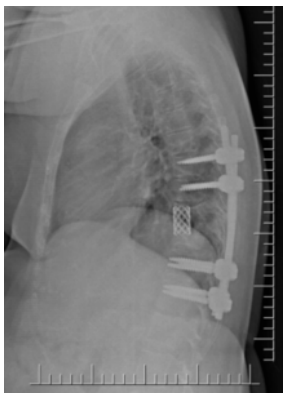

(c) Lateral view of a posterior spinal fusion

Figure 6.28.: Pedicle screw implantation

As the vertebra anatomy heavily changes depending on the vertebral level, several alternative implementations of this procedure has been developed over the years (Abumi et al. 1994, Magerl 1984, Fennell et al. 2014), with variations in the pedicle screw entry point localization and the pedicle screw trajectory. Screw implantation can be thoracic, lumbar or sacral (Jost et al. 2017). The objective of this surgery is to introduce screws in the pedicle without violation of the pedicle wall. Pedicle screws are often inserted using conventional techniques that are based on anatomical landmarks of the vertebrae or assisted with any intra-operative imaging systems like C-Arm (C-Arm guided technique) to help in the localization of the entry point to evaluate the position of the screw (Kosmopoulos et al. 2007).

6.4.2. Freehand pedicle screw insertion techniques

One of the most widely used and effective pedicle screw insertion method is known as the free-hand technique. This technique relies on the tactile feedback of the surgeon, and the use of anatomical markers to determine the correct screw entry point, without use of any intraoperative fluoroscopy, radiography or image-guided techniques. As such, the operative time and cost, as well as the radiation exposure is drastically reduced. However, this technique depends entirely on the surgeon ability and experience, thus needing a rather long learning curve in order to get satisfying results.

The free-hand technique can be broken down into multiple steps. The posterior part of the vertebra is first exposed to the tips of the transverse processes bilaterally (Fig. 6.29).

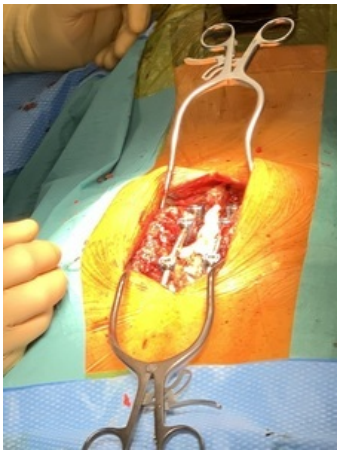

Figure 6.29.: Exposed vertebra during surgery.

A rongeur (Fig. 6.30a), or an acorn-tipped bur, is then used to remove the dorsal cortex at the screw entry point position (Fig. 6.31a), revealing a pedicle "blush" suggesting entrance into the cancelous bone. A large hole is punched in the blush and a blunt, flexible narrow probe ($\approx 2\,mm$, Fig. 6.30b) is then inserted down the pedicle (Fig. 6.31b). After the trajectory hole has been made, it is palpated with a pedicle feeler to assess for a breach. If no breach has been detected, the trajectory hole is then tapped and the screw is placed (Fig. 6.31c). In the case of a breach, the trajectory hole must be revised.



(a) An example of rongeur



(b) An example of pedicle probe

Figure 6.30.: Pedicle screw surgery instruments

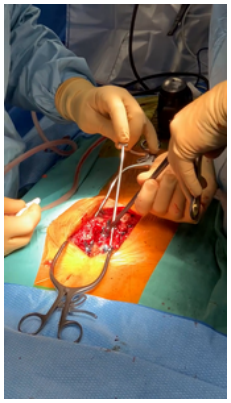

(a) Dorsal cortex removal.



(b) Cannulation.

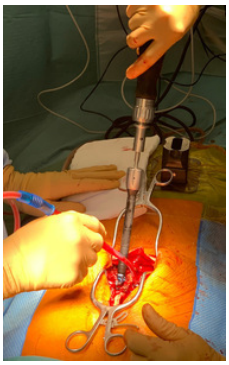

(c) Pedicle screw insertion.

Figure 6.31.: Pedicle screw freehand insertion

Due to the anatomical and size differences between vertebrae, the position of the screw entry point is different depending on the vertebra level. These different entry point positioning algorithms have been an ongoing subject of research for the last decades, building onto each other and leading to a wide range of surgeon practices. Moreover, these techniques are described as an *Ideal Pedicle Entry Point (IPEP)* and, as such, are subject to surgery, anatomical and pathology variances.

6.4.3. Freehand methods: thoracic vertebrae

In most cases, the entry point is localized around the junction of the transverse process and the lamina (Fig. 6.32).

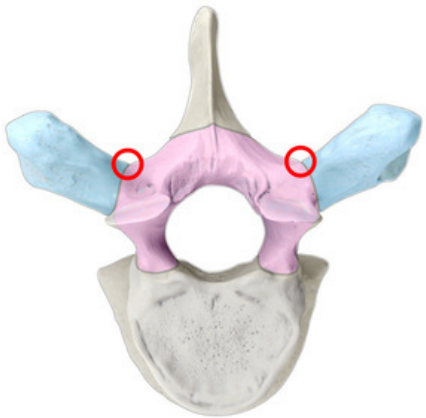

Figure 6.32.: Entry point general area for thoracic vertebrae (blue: transverse processes, pink: vertebral arch).

There are four main methods described in the literature:

Y. J. Kim; Lenke, et al. 2004

Three sub-levels are defined: proximal thoracic $T_{proximal}$ (T_1, T_2), mid thoracic T_{mid} (T_7 - T_9) and lower thoracic T_{low} (T_{11}, T_{12}). This technique uses the transverse process and lamina to process the entry point location (Fig. 6.33). In particular, at T_{low}, the entry point is placed at the junction of the bisected transverse process and lamina at, or just medial, to the lateral aspect of the pars. From there to T_{mid}, the entry point becomes more medial and cephalad, until it reaches its most medial point, where the entry point is placed at the junction of the proximal edge of the transverse process and lamina, where it meets the lamina and superior facet (Fig. 6.33b). Continuing from this point to $T_{proximal}$, the entry point trends toward a more lateral and caudad position, going back to a similar positioning as the T_{low} entry points (Fig. 6.33a). In the article, 3204 screws have been studied over 394 patients, covering most of the spine pathologies where screw implantation can be indicated.

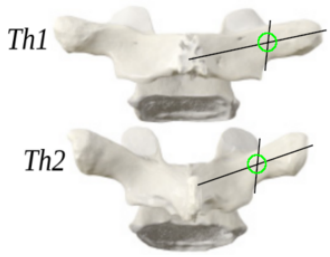

(a) Proximal thoracic $T_{proximal}$.

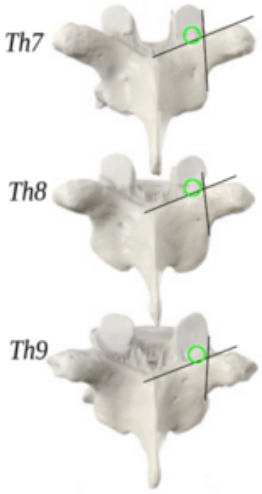

(b) Mid thoracic T_{mid}.

Figure 6.33.: Y. J. Kim; Lenke, et al. 2004

H. N. Modi et al. 2010

The entry point was placed at the junction of lateral and medial thirds of the facet joint. This study has been done on 482 screws over 26 scoliotic patients.

Parker et al. 2011

This technique brings up a more "geometric" approach. A triangle is formed from the ledge of the superior articular facet, the transverse process and the pars interarticularis, forming a *bony confluence*. The entry point is placed around the center of this triangle. This study is most exhaustive, to this day, studying 3443 screws over 964 patients and covering most of the spine pathologies where screw implantation can be indicated.

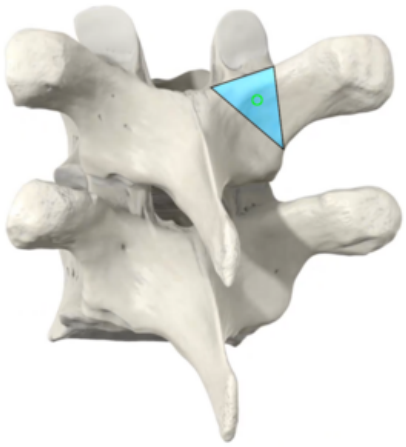

Figure 6.34.: Parker et al. 2011

Fennell et al. 2014

This technique uses a uniform entry point, 3 mm caudal to the junction of the transverse process and the lateral margin of the superior articular process. 219 screws over 219 patients have been studied.

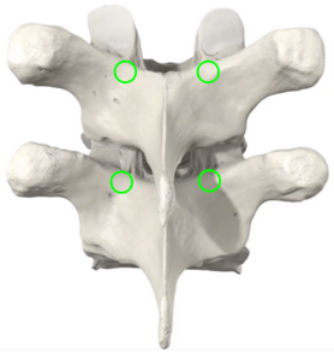

Figure 6.35.: Fennell et al. 2014

6.4.4. Freehand methods: lumbar vertebrae

In the case of lumbar vertebrae, three main methods are mainly cited as the base of the modern freehand methods.

Magerl 1984

The entry point is found at the intersection of two lines: the vertical line touching the lateral border of the superior articular process, and the horizontal line bisecting the base of the transverse process (Fig. 6.36).

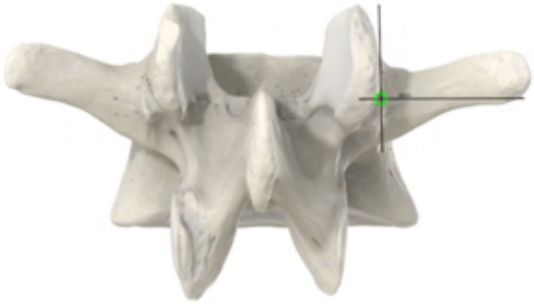

Figure 6.36.: Magerl 1984

Roy-Camille; Saillant, et al. 1986a

Similar to Magerl 1984, the entry point is found at the intersection of two lines: the vertical line given by the joint, and the horizontal line passing through the middle of the insertion of the transverse process (Fig. 6.37).

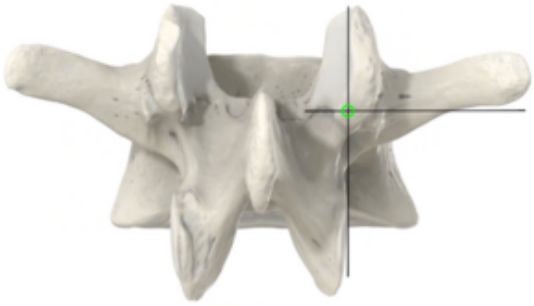

Figure 6.37.: Roy-Camille; Saillant, et al. 1986b

Weinstein et al. 1988

The goal of this technique, compared to Roy-Camille; Saillant, et al. 1986a, aims to reduce the interference with the uninstrumented and unfused segments. The entry point is at the lateral and inferior corner of the superior articular facet (the so-called "nape of the neck" of the superior articular facet, as called by the author) (Fig. 6.38).

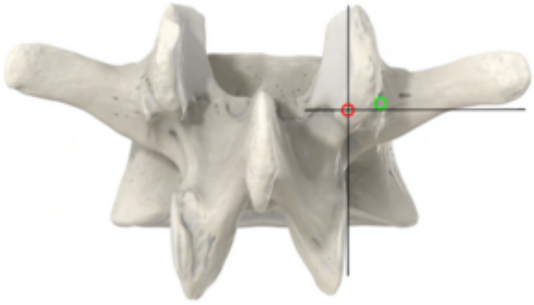

Figure 6.38.: Weinstein et al. 1988, in green, compared to Roy-Camille; Saillant, et al. 1986a, in red

7. Industrial context

In this chapter, we will introduce a short history of the Computer Assisted Spine surgery and the surgical navigation. We will also review some of the questions associated to the navigation. We will end describing the PYTHEAS NAVIGATION solution.

7.1. Computer Assisted Spine surgery

7.1.1. Historical context

Gaston Contremoulins used the principles of modern surgery in association with biplanar preoperative X-ray guidance for the first time in the late 19th century, allowing the successful removal of intracranial bullets in 2 patients. This surgical premiere, greatly acknowledged in the popular French newspaper "L'illustration" in 1897, received little scientific or governmental interest at the time, as it emanated from a young self-taught scientist without official medical education.

This surgical innovation was only made possible financially by popular crowdfunding and, despite widespread military use during World War I, with 37780 patients having benefited from this technique for intra- or extra-cranial foreign bodies, it never attracted academic or neurosurgical consideration. *Horsley* and *Clarke* popularized this technique for human brain surgery during the second part of the 20th century (Bourdillon et al. 2018).

Since the 1970s, anatomy and clinical practices have greatly influenced the field of clinical medical research, resulting in the development of many new surgical methods. The simulation of surgical procedures has since been used for clinical training, teaching, and operation design. Traditional clinical teaching is completely based on the two-dimensional plane, which can be intuitive. However, a three-dimensional dynamic display has been used recently, allowing visualization of the vascular tissue, nerve tissue, and anatomical structures. Digital technology uses dynamic three-dimensional images to supplement traditional two-dimensional medical images. For example, a computed tomography (CT) image is a three-dimensional reconstruction in rows, which can accurately show the complex structure of biological tissue.

The concept of digital orthopedics is based on digital medicine, digital technology, digital medical equipment, computer network platforms, and medical professional software provided the basis for a digital, three-dimensional orthopedic anatomical

atlas. The rapid developments of computer technology, image processing technology, and medical physics have improved medical diagnosis and treatment in all fields of medicine. Surgeons use digital orthopedics along with modern diagnostic imaging, surgical techniques, and advanced materials to ensure a patient safety and accurately perform minimally invasive surgery. The computer navigation system is a new advancement in the field of digital medicine, allowing for speed, accuracy, and flexibility in minimally invasive and highly unified surgery. This technology has been gradually introduced to spinal surgery from its initial applications in neurosurgical, orthopedic, and ear-nose-throat procedures. Thus, a new field of computer-aided navigation surgery was created. The successful use of computer-assisted navigation in orthopedics also fully embodies the advanced nature of digital bone science, and its applications will only become more extensive.

7.1.2. The early stage of navigation technology

Surgical navigation technology was originally applied in some experiment research for small animals by Horsley and Clarke in 1907. With aid of some mechanical devices and anatomic landmarks, this technology was used to determine the surgical object inside the body. Due to poor precision, it was inappropriate for the human operation.

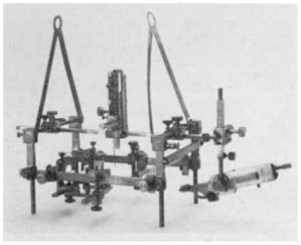

Figure 7.1.: Horsley-Clarke stereotaxic apparatus

With the discovery of X-ray images and rapid applications in medical field, X-ray fluoroscopy could provide doctors a lot of useful information, such as bone structures of the patient and locations of the surgical instruments within body, and the information was displayed and observed on the screen in real time. Mosher 1913 accurately inserted a probe into the frontal sinus with the help of X-ray photographic techniques in 1913. Spiegel et al. 1947 adopted “pneumoencephalography” to spatially position soft-tissue markers in 1947, and this new navigation technology was first applied to the human soft tissue. Since then, Leksell 1951, Riechert 1975, and Talairach et al. 1988 also respectively developed their own positioning systems based on the projection imaging techniques.

During the 1950s and 1960s, navigation technology was extensively used for thalamotomy. However, the navigation systems in the period were still based on graphic images. Because of slow development of the imaging and the X-ray radiography technology, early framework navigation technologies had some inherent drawbacks, not only highly inaccurate but also quite traumatic in the aspect of positioning. In addition, the small visual field, a certain degree of geometric distortions of X-ray images, and long-term accumulations of radioactive radiation to damage surgeon also affected significantly the clinical application of this technology. Therefore, framework navigation surgery developed quite slowly for a long time.

7.1.3. The later stage of Navigation Technology

In the early 1970s, computer technology had rapidly developed and then applied in the medical field. Computed tomography (CT) scans could clearly show the anatomical structure of the human body, which raised the image guided surgery (IGS). With the application of magnetic resonance imaging (MRI), it could further provide clearer view of anatomical structure. However, these scans from early CT and MRI could only provide two-dimensional (2D) image information, and it was frequently necessary to reconstruct three-dimensional (3D) images of anatomical structure in the mind of the surgeons based upon these 2D data in order to make operation plans.

With the rapid development of computer, radio and signal processing technologies, and other related disciplines, image-guided surgical techniques improved significantly, formed a truly interactive surgical planning and navigation tools, and contributed to the emergence of a new computer navigation system based on frameless stereotactic technique with more flexible use, more convenient manipulation, more accurate guidance, and more extensive application, thus provided interactive 3D images with which a certain operation could be carried out more accurately. The emergence and development of CT technology has promoted improvements of navigation system, especially in the field of 3D spatial orientation.

Between 1985 and 1987, Watanabe et al. 1987 and Hadley et al. 1985 successfully developed the first CT interactive neurosurgery navigation system simultaneously, with the former using a mechanical arm to track objects, while the latter using an ultrasonic locating method. In the 1990s, a positioning system with mechanical joint arms amenable to be controlled was invented. Although remote control of mechanical joint arms was not be disturbed by line of sight, clumsy bulk of the mechanical arms obviously added inconvenience to the operation. On the other hand, a stereo-specific infrared camera system based on the principles of ternary and binocular machine vision had increased position accuracy, but positioning was easy to be interfered for problem of line of sight, that is, an unobstructed view between the optical camera and the tracked objects at all times.

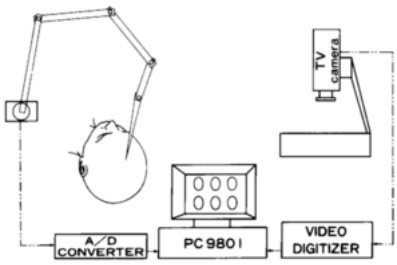

Figure 7.2.: Watanabe et al. 1987

Ultrasonic image can clearly and real timely display soft tissue and vascular constructs. Because the ultrasonic imaging equipment is relatively cheap and easy to carry, minimally invasive surgery under ultrasound guide is a more common surgery manner for some soft-tissue tumors. After local anesthesia, puncture needles through the skin can be accurately inserted into the tumor tissue with the guide of real-time ultrasound imaging, and further treatment will be subsequently carried out. It is a

typical application for liver tumor thermal ablation, including microwave ablation therapy and radio-frequency ablation therapy. In addition, ultrasound images can also help surgeons find some breast lumps which cannot be recognized through clinically physical examination during the operation of breast tumor. In the field of neurosurgery, ultrasonic image can be used to position lesions in real time, monitor focal extent, and determine the scope of the resection, which has obvious advantages to improve operation effect. However, compared with X-ray fluoroscopy images or CT scans, ultrasonic images of bone tissue are inferior; therefore, its applications in the field of joint surgery and orthopedic trauma are distinctly curtailed.



Figure 7.3.: Example of electromagnetic navigation (Rodt et al. 2007)

Among different types of medical imaging, MRI can display optimally soft-tissue structure. However, the MRI images themselves have a certain degree of geometric distortion and gray level distortion. Geometric distortion of MRI images is mainly attributed to the heterogeneity of the magnetic field of the equipment, which will increase the guidance errors of operation. With the further progress of technology, a new type of MRI device has significantly decreased geometric distortion and increased image accuracy, which makes it possible to become a navigation equipment. Currently, the intra-operative MRI image-guided surgery does not get extensive application, mainly because this technology has special requirements to MRI equipment and magnetic field environment. Compared with ordinary MRI images, low magnetic field environment reduces MRI quality and resolution. Currently, the *PoleStar* system (https://europe.medtronic.com) is a typically intraoperative MRI-guided equipment and works in a low magnetic field environment. In this system, magnetic field-generating equipment is placed in the bottom of operation bed and, if needed, ascended to the appropriate position. However, the *Magnetom Espree* system (https://www.siemens-healthineers.com) works in a high magnetic field environment. The design of this intraoperative imaging guidance system is similar to that of conventional MRI devices.

Since the 1990s, different navigation concepts and techniques have been developed, realized, and evaluated throughout the world. Some of them have proven to be successful, while others appeared to be dead ends and have consequently been abandoned. There is now a wide variety of different navigation concepts and philosophies implemented by system manufacturers in the form of navigation products as well as those being developed by research groups as prototypes or experimental devices. Recently, FRActure Computer-Aided Surgery (FRACAS) navigation system (Joskowicz et al. 1998, Fig. 7.4) has been developed to guide interlocking screws into the distal holes of intramedullary nail. This system improves the accuracy of screw fixation, and

positioning error is less than 0.5 mm.

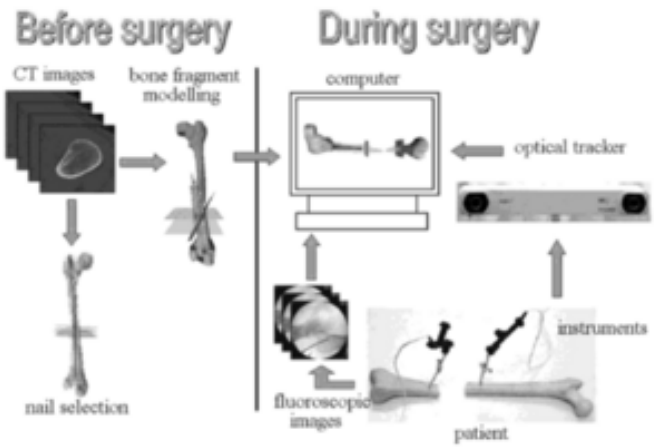

Figure 7.4.: FRACAS system concept (Joskowicz et al. 1998)

With the development of a new generations of medical imaging, image analysis, robotics, motion analysis, virtual reality, computational modeling, etc., Computer-Aided Surgery (CAS) is more and more frequently used in operating rooms all over the world. CAS can, on the one hand, help physicians make accurate diagnosis for the disease and, on the other hand, guide surgeons to perform quick and accurate operation procedures. We can highlight a few examples of these technologies:

Medtronic StealthStation S8

The StealthStation S8 surgical navigation system, developed by Medtronic, is a sophisticated technology designed to enhance precision and accuracy during a variety of surgical procedures, particularly in neurosurgery and spine surgery. At its core, it functions by providing surgeons with real-time, three-dimensional visualization of the patient's anatomy and the precise location of surgical instruments. This is achieved through the integration of preoperative or intraoperative imaging, such as CT or MRI scans, with advanced tracking technology.

Key features of the StealthStation S8 include its ability to track surgical instruments using both optical and electromagnetic systems, allowing for flexibility in various surgical settings. The system's software enables surgeons to plan their approach, simulate procedures, and navigate complex anatomical structures with greater confidence. Furthermore, the S8's user interface is designed for intuitive interaction, with touchscreen monitors and advanced visualization tools that simplify the interpretation of complex imaging data. This technology is intended to assist in procedures like tumor resection, deep brain stimulation lead placement, and complex spine fusions, with the goal of improving patient outcomes by minimizing surgical risks and enhancing accuracy.

In essence, the StealthStation S8 acts as a surgical GPS, guiding surgeons through intricate procedures with enhanced visual feedback. By combining advanced imaging

and tracking technologies, it aims to provide surgeons with the information they need to perform procedures with greater precision and minimize potential complications.

Brainlab Spine Navigation

The Brainlab Spine Navigation system is a comprehensive surgical navigation platform that transforms complex spinal procedures into more precise and predictable interventions. It operates on the principle of image-guided surgery, where patient-specific anatomical data derived from CT or MRI scans are integrated with real-time instrument tracking. This integration provides surgeons with a dynamic, three-dimensional visualization of the surgical field, enabling them to navigate intricate spinal structures with enhanced accuracy.

The system's core functionality revolves around its advanced optical tracking technology. This technology utilizes infrared cameras to monitor the position of surgical instruments equipped with reflective markers. By continuously tracking these markers, the system can precisely correlate the instrument's location with the patient's anatomical data, displayed on a high-resolution monitor. This real-time feedback allows surgeons to visualize the exact trajectory of their instruments, minimizing the risk of misplacement and potential complications.

Beyond basic navigation, the Brainlab system offers sophisticated preoperative planning tools. Surgeons can use these tools to simulate surgical approaches, plan screw trajectories, and visualize the potential impact of their interventions. This preplanning capability enhances surgical confidence and allows for more efficient and effective procedures. Furthermore, the system's intuitive user interface simplifies the interpretation of complex imaging data, ensuring that surgeons can quickly and easily access the information they need during the procedure.

Mazor Robotics (now Medtronic)

The Mazor Robotics system, now integrated into Medtronic's portfolio, represents a paradigm shift in spinal surgery by introducing robotic assistance to enhance precision and consistency. This system combines the power of preoperative planning with the accuracy of robotic execution, aiming to optimize pedicle screw placement and improve patient outcomes.

The process begins with a detailed preoperative CT scan, which is used to create a three-dimensional model of the patient's spine. Surgeons then use specialized software to plan the optimal screw trajectories and implant positions. This plan is then transferred to the robotic system, which precisely positions a robotic arm to guide the surgical instruments.

The robotic arm's movements are precisely controlled, ensuring that the instruments are positioned according to the preoperative plan. This eliminates the variability associated with manual screw placement and reduces the risk of errors. The system also provides real-time feedback and monitoring, allowing surgeons to make adjustments as needed.

One of the key advantages of robotic assistance is its ability to facilitate minimally invasive procedures. By reducing the size of incisions and minimizing tissue trauma, the Mazor system can potentially reduce patient recovery time and improve overall outcomes. Furthermore, the system's ability to precisely execute preoperative plans can lead to more consistent and predictable surgical results.

PediGuard (SpineGuard)

The PediGuard system is a handheld surgical device that brings an added layer of safety to pedicle screw placement by providing real-time feedback on potential pedicle wall breaches. It utilizes Dynamic Surgical Guidance (DSG) technology, which measures electrical conductivity to detect changes in tissue impedance, indicating potential violations of the pedicle wall.

The device's core functionality is based on the principle that different tissues exhibit different electrical conductivity properties. By measuring the conductivity of the tissue surrounding the surgical instrument, the PediGuard® system can detect changes that may indicate a breach of the pedicle wall.

The system provides both auditory and visual feedback to the surgeon, alerting them to potential breaches. This real-time feedback allows surgeons to adjust their instrument trajectory and avoid potential complications. The device is designed to be seamlessly integrated with standard surgical instruments, making it easy to incorporate into existing surgical workflows.

One of the key advantages of PediGuard® is its ability to provide immediate feedback, allowing surgeons to make informed decisions during the procedure. This real-time safety information can help to reduce the risk of neurological complications and improve patient outcomes. Furthermore, the device's simplicity and ease of use make it a valuable tool for surgeons of all experience levels.

7.1.4. Advantages and limitations of CAS

7.1.4.1. Advantages

Accurate positioning of the implants is mandatory for an operation success in spine surgery. Even so, it may be hard to avoid some screw misplacement even for some experienced physicians in performing this operation. A subtle screw misplacement opens the possibility to harm important anatomical structures.

In order to avoid screw misplacement during a surgery and increase the overall success rate, a spine surgery navigation system can be adopted to help the surgeon knowing clearly the current operating status and the specific position of the implants. In the application of pedicle screw, a navigation system can guarantee the accuracy of screws placement so as to avoid complications related to the operation.

Comparing results between conventional and computer-assisted pedicle screw

placement in the thoracic, lumbar, and sacral spine, Amiot et al. 2000 showed less neurological deficits and better alignment with image guided surgery. CAS systems also benefit the education and training of physicians. The educational potential of operating virtually by the use of 3D CT-based preoperative planning software, may be beneficial for younger and less experienced surgeons. CAS technology may also facilitate better performance and serve as a learning experience for the expert by providing real-time feedback (Amiot et al. 2000).

An important addition of CAS is the overall reduction of intraoperative radiation exposure. Indeed, Gebhard et al. 2006 showed a dramatic decrease of radiation exposure when comparing conventional surgery technique like fluoroscopy to CAS systems like C-arm (Table 7.1).

	Conventional technique (fluoroscopy)	CT-based	C-Arm based	Iso-C^{3D} C-arm base
Maximum (mGy)	3320	822	1083	391
Minimum (mGy)	490	114	333	43
Median (mGy)	1091	432	664	152

Table 7.1.: Radiation dosage at the radiation source (Gebhard et al. 2006)

7.1.4.2. Limitations

Especially during the early years, CAS planning was mainly composed of manual operations, usually trading preoperative time for the surgeon's team for surgery performance. Even in the more recent years and the advent of machine learning and automation, the preoperative planning still requires the surgeon validation and, possibly, manual improvements.

Bai et al. 2010 showed that, while reducing surgery time and decreasing the overall screw perforation rate over long-term uses, the use of CAS implied a long learning curve for the surgeon, where the operative time were actually increased (over the first six months of use). They attributed this learning curve to the unfamiliarity with the system, like the interference with the physical part of the system itself, or the need of intraoperative imaging.

Even though CAS reduces the overall radiation exposure, it is important to note that these techniques still imply a non-zero intraoperative radiation exposure, for both the surgery team and the patient (who has already been exposed to radiations during the preoperative imaging). While the overall exposure seems to be within safe values, any amount of exposure increases the risk of cancer (about 4.1% per sievert, Valentin et al. 2007). With that in mind, it is important to aim to reduce the accumulation of radiation dose (Duke et al. 2022) by, for example, applying the As Low As Reasonably

Achievable (ALARA) principle.

7.2. PYTHEAS NAVIGATION *Your Guided Trajectory*: a new Medical Device based on *Inertial Measurement Units* (IMU)

To overcome some of the CAS shortcomings, PYTHEAS NAVIGATION has developed a new guidance system for pedicle screw insertion based on Inertial Measurement Unit (IMU).

7.2.1. Brief history of PYTHEAS NAVIGATION

PYTHEAS NAVIGATION has been founded by *Dr. Yann Glard* and *Marc Forman* in 2015, with the original concept of the product PYTHEAS NAVIGATION *Your Guided Trajectory* being imagined two years earlier by Dr. Glard. It has since endured clinical trials and passed the CE marking at the end of 2023, allowing its commercialization and deployment into multiple hospital.

7.2.2. General considerations about Image guided trajectory guidance in spine surgery

7.2.2.1. Regulatory requirements for a Medical Device

Medical device development and commercialization is subjected to regulatory validation and follow-up. Regulatory requirements can differ depending on geographic areas and countries but are all based on a fundamental principle: ensure patient safety by demonstrating of a positive ratio between benefit for patient and existing related risks, as absence of risk does not exist.

Global development of such devices shall follow specific and defined design, development, verification, and validation activities, based on regulations requirements, and dedicated international norms. This is also the case of the medical software. Dedicated standards, especially international norms, guide manufacturers in the software design, development, verification, and validation activities to ensure the above principle is confirmed: a safe and performant software.

In this specific regulated context, a complete development of a medical device including software is a long process, with continuous device certification (for market introduction) as CE mark for devices implemented in Europe, and FDA clearance for devices implemented in the United States, for example.

7.2.2.2. Notes on Artificial Intelligence

Artificial Intelligence (AI) in medical practice is existing in three technical forms: software, hardware, and mixed forms using three main scientific-statistical approaches

- flowchart method, database method, and decision-making method. The main issues of AI implementation in healthcare are connected with the nature of technology in itself, complexities of legal support in terms of safety and efficiency, privacy, ethical and liability concerns (Pashkov et al. 2020). Undoubtedly, this is a promising area with a lot of gaps and grey zones to fill in. Furthermore, the main challenge is not on technology itself, which is rapidly growing, evolving, and uncovering new areas of its use, but rather on the legal framework that is clearly lacking appropriate regulations and some political, ethical, and financial transformations (Meszaros et al. 2022).

Despite its promising future, the application of AI and automated decision-making in healthcare services and medical research faces several legal and ethical hurdles. The *European Union* (EU) is tackling these issues with the existing legal framework and drafting new regulations, such as the proposed AI Act. The EU *General Data Protection Regulation* (GDPR) partly regulates AI systems, with rules on processing personal data and protecting data subjects against solely automated decision-making (Giansanti 2022). Many studies are devoted to the challenges of AI integration in the health domain. One of the most important challenges is that of regulations (Naik et al. 2022).

The legal and ethical issues that confront society due to Artificial Intelligence include privacy and surveillance, bias or discrimination, and potentially the philosophical challenge is the role of human judgment. Concerns about newer digital technologies becoming a new source of inaccuracy have arisen as a result of its use. Mistakes in the procedure or protocol in the field of healthcare can have devastating consequences for the patient who is the victim of the error. Because patients come into contact with physicians at moments in their lives when they are most vulnerable, it is crucial to remember this.

As currently, there are no well-defined regulations in place to address the legal and ethical issues that may arise due to the use of artificial intelligence in healthcare settings, the implementation of AI in healthcare products is a major issue. Algorithmic methods based on morphometric assessment and biomechanics are an alternative way to AI in the field of medical images post-processing automation. Algorithmic methods are more reliable than AI based methods and the regulation in place allows to use it.

7.2.3. General principles of the PYTHEAS NAVIGATION *Your Guided Trajectory* Medical Device

PYTHEAS NAVIGATION *Your Guided Trajectory* medical device provides intraoperative navigated angular guidance to a surgeon to aid in the pedicular hole drilling and screw insertion, relative to anatomical structures and preoperatively defines reference axes. This system is intended to assist the surgeon during manual perforation of the pedicle and pedicular screw insertion by providing navigated angular guidance when performing these actions, during posterior surgical approaches for sacral, lumbar and thoracic levels for skeletally mature patients.

The main goal of the device is to reduce the likelihood of incorrectly placed pedicle

screws, using angular guidance navigation, to assist the surgeon during the perforation and the pedicle screw placement, while minimizing the X-ray exposure for the patient and the surgeon (a single preoperative CT scan is needed) and having a low impact as possible on the surgical workflow. The system can be summarized as a two-step process: a preoperative surgery planning tool based on the patient CT scan (Section 7.2.3) and the intraoperative surgery navigation system.

Preoperative planning tool

In order to navigate the pedicle screw insertion procedure, a planning step is necessary (Section 7.2.3). The overall goal of this step is to fully describe the screw entry point position and trajectory on a 3D model of the patient spine generated from a preoperative CT scan. In addition to these operative requirements, the IMU-based angular guidance can be improved by being calibrated relative to the instrumented vertebra, to accommodate the inter-vertebra rotation variances that may occur between the preoperative CT scan and the real-life, peroperative patient spine positioning. In the PYTHEAS NAVIGATION *Your Guided Trajectory* case, this calibration process requires the positioning of two points on the vertebra.

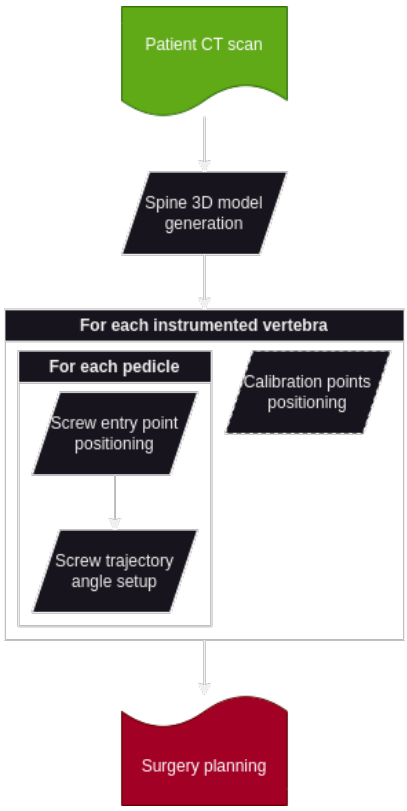

Figure 7.5.: PYTHEAS NAVIGATION *Your Guided Trajectory* planning

Surgery navigation system

PYTHEAS NAVIGATION *Your Guided Trajectory* navigation system provides an IMU-based angular guidance to the surgeon tools (Fig. 7.6a, Fig. 7.6b). The surgeon tools (e.g. probes and screwdrivers) are specifically instrumented with the IMU, with the measured angle being displayed and compared to the expected, planned angles on an in-operating room screen (tablet). The surgeon can then visualize the vertebra they

are currently working on, with their entry point shown on the spine 3D model, as well as the navigation angles. The surgeon can also increase the device accuracy by using the calibration they planned, using a custom-made instrumented tool (Fig. 7.6c).

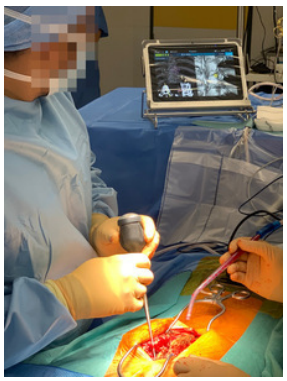

(a) Instrumented probe

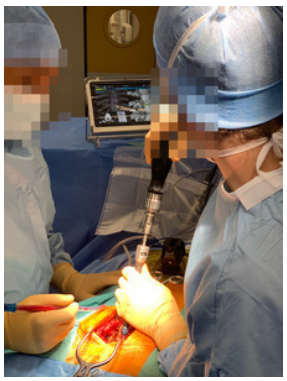

(b) Instrumented screwdriver



(c) Vertebra-relative calibration

Figure 7.6.: PYTHEAS NAVIGATION *Your Guided Trajectory* navigation

7.2.3.1. Indications/contra-indications

PYTHEAS NAVIGATION *Your Guided Trajectory* must follow some indications and contra-indications. In general, the MD can be used on skeletally mature patients, during posterior spine fusion procedures needed in case of spine deformity, degenerative spine, trauma, tumor or revision surgery.

On the contrary, the system must not be used in the following cases:

- Incoherence between the system information and the haptic feedback of the surgeon
- Manual perforation where the surgeon cannot get a haptic feedback (e.g. low mechanical contrast between the cortical and trabecular bone density in the pedicle)
- Severe osteopenia or loss of bone quality
- Trauma with neurologic impairment
- Patient in any position other than prone
- Stainless steel or Titanium allergia
- Prion protein presence or risk, or know neurodegenerative diseases linked to prion

7.2.4. Hardware

7.2.4.1. Background

In Inertial Measurement Units (IMU) technology, angle computation is the output of a fusion algorithm based on a combination of 3 types of measurements:

- Gyroscope, providing inertial rotation speeds along the 3 axes
- Accelerometer, providing linear accelerations along the 3 axes
- Magnetometer, providing magnetic field measurements along the 3 axes

The fusion principle is to integrate the rotation speeds to get 3 absolute angles. As with any time integration of biased and noisy raw measurements, the output drift in time. A process based on observations is required to compensate for the drift and to stabilize the angles.

7.2.4.2. PYTHEAS NAVIGATION *Your Guided Trajectory* IMU sensor

The IMU sensor used in the PYTHEAS NAVIGATION *Your Guided Trajectory* is the Movella (formerly Xsens) DOT (Fig. 7.7a). This sensor embed a fusion algorithm (Fig. 7.7b) based on the classical Kalman filtering (Kalman 1960) for angular calculation.



(a) Movella DOT sensor

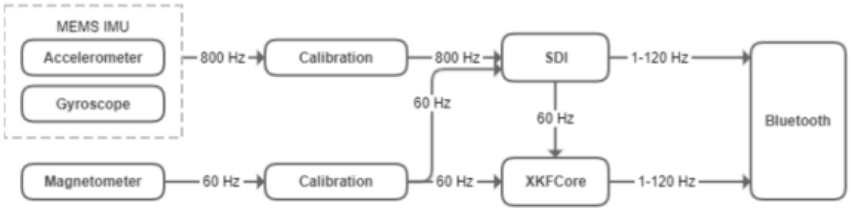

(b) Data processing algorithm
SDI: Strap-Down Integration (sampling and integrating sensor to determine the orientation of the sensor)
XKFCore: Xsens Kalman Filter core algorithm

Figure 7.7.: Movella DOT

Absolute angular rotations are calculated based on time integration of the 3 degrees of freedom (DOF) gyroscope at 800 Hz. To understand the integration bias compensation principle and limitations, it is convenient to use the Euler rotations about the earth frame. This is a widely used approach in all industries using inertial measurement technology. Roll and pitch are providing inclination rotations compared to vertical axis. Yaw, also called *Heading*, is the rotation about the vertical axis.

The integration biases are compensated by three means:

Vertical Reference Unit (VRU)

The first type of correction is based on gravity field. Gravity field is constant and not affected by the condition of use. The principle of correction is to use the inclination angles measured by the 3 DOF accelerometer to correct the estimation of gyroscope speed integration. This is provided by the gravity field that is sensed by accelerometers. This measurement is accurate when sensor is not in constant acceleration itself (beyond gravitational acceleration). This provides efficient stabilization and computes two biaises (out of 3) : roll and pitch. The compensation dynamics is fast (< 1 sec). VRU algorithm is not able to efficiently stabilize Yaw angle. In static condition (sensor at rest), yaw will slowly drift, due to 2 phenomena: time integration drift, and earth rotation. For pure static conditions, VRU integrates a feature that prevent yaw drift due to time integration when motion is detected as very low (integration is on hold). This feature helps to contain yaw drift in standard use condition.

Active Heading Stabilization (AHS)

The second type of correction is based on magnetic field. Magnetic field is caused by the earth natural magnetic field. The principle of correction is to use the magnetic field sensing as estimation of orientation of heading angle. This can be understood as a magnetic compass. The compensation is acting on the heading only (1 over 3 DOF). The limitation of this algorithm is the fact that the magnetic field may change locally depending on the magnetic disturbance interfered by magnetic source (magnet) or magnetic material (non magnetic transparent material).

Xsens Kalman Filter (XKF)

The final compensation is a balance between these two corrections through the XKF. This filter is configurable. The selected setting for our application is "nominal mode". In this mode, the compensation based on AHS is low, with a slow response time (30 s). When motion is slow, the VRU is mainly active. When motion is high, VRU and AHS are active. If the magnetic perturbation is lasting longer than the filter time response (30 s), the AHS is affected and thus generate heading drift.

7.2.5. Software

7.2.5.1. Imaging input: DICOM format

The *Digital Imaging and Communication in Medicine* (DICOM) is a standard for the communication and management of medical imaging information and related data. This standard is referred as *ISO 12052:2017* and *CEN 12052*. To facilitate the interoperability of the medical imaging equipment, the standard specifies:

1. A set of protocols for network communication,
2. A set of media storage services for media communication,
3. A file format and a medical directory structure to access the images, as well as the related information stored in said media.

DICOM is used worldwide, across a wide range of imaging modalities, such as radiography, ultrasonography, CT, MRI and radiation therapy. A DICOM data object groups information into data sets. These information are embedded within the file as to never being separated from the image itself. The filename extension of a DICOM file is *.dcm*. DICOM files can also be grouped as a collection of files (file-set). These file-sets must contain a root "DICOMDIR" file that describes the collection. These data sets consists of various attributes such as the patient information (e.g. name, age, ...), the modality specifications (e.g. voltage, product name, ...) and the pixel data. The pixel data can be compressed using a variety of standards like, for example, JPEG or run-length encoding (RLE). The whole data set can also be compressed using LZW (zip). It is important to note that the standard does not require an anonymized data source, as a lot of technical and patient data can be stored and retrieved inside a DICOM file. In this case, the DICOM file do not comply with data protection laws, especially the *General Data Protection Regulation* (GDPR), and must be processed to erase, or encode these information so that the patient identity can not be traced back.

7.2.5.2. Preoperative planning

The planning data input is a CT scan acquired in the supine position, provided by any medical imaging department. This data is then used to generate a 3D model of the patient spine using a segmentation algorithm. On this 3D model, the surgeon is able to place the entry points of the pedicle screws, their orientation and the calibration points, if necessary. The screw trajectories are then computed and expressed in a local (vertebra-specific) or global (relative to the trunk of the patient) reference frame.

7.2.5.3. Intraoperative angular guidance

Once the patient is under general anesthesia, in the prone position, PYTHEAS NAVIGATION *Your Guided Trajectory* provides the surgeon an intraoperative angular

guidance. Using a simple set of rotations, the current tool trajectory can be transformed from the sensor reference frame to the local or global reference frame. It allows a visual comparison with the planned trajectory (Fig. 7.8).

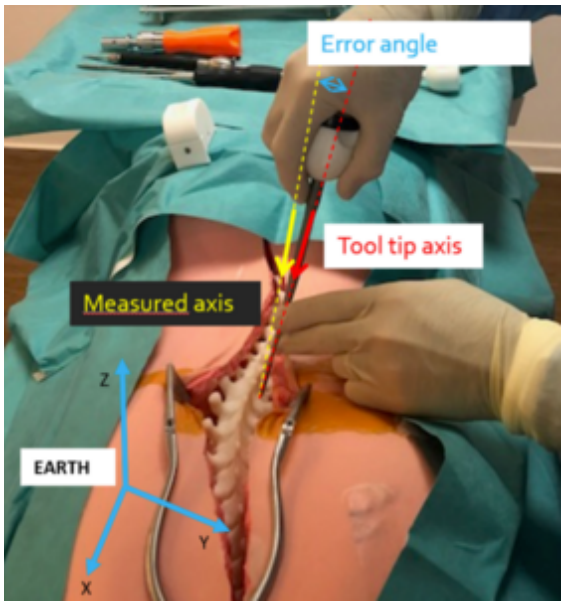

Figure 7.8.: Angular guidance

7.2.6. Registration and calibration issues

To overcome tricky and time-consuming registration/calibration procedures, hypothesizing that the change of vertebral orientation between the supine position and the prone position was small enough (Brink; Colo, et al. 2017) to fit angular precision requirement, PYTHEAS NAVIGATION has developed the concept of global calibration.

7.2.7. Challenges

In the case of the CT scan of the spine, multiple challenges can arise.

First, the CT modality is fairly complex. Indeed, a CT scanner must be calibrated, and this calibration can introduce a variance in the pixel value. Moreover, the settings of the CT scanner itself (e.g. power, voltage), as well as the acquisition (e.g. resolution, slice thickness) can be tweaked , which can also impact the pixel value. Also, the acquisition is obviously highly dependent on the patient where, for example, the measured value can vary depending on the age and condition of said patient. To summarize the issue, the values in the image are patient-dependent and scanner-dependent.

Another challenge is the dependency on the acquisition resolution. This resolution, i.e. the dimension of the pixel, directly impacts the level of detail the acquisition allows you to observe. As an example, a sub-millimeter structure cannot be observed if the resolution is greater than 1 mm. As a preoperative CT scan might have been acquired

for diverse reasons, not related to a surgery planning, the acquisition resolution might not be high enough for an accurate segmentation.

Finally, as a CT scan of the spine is a full torso scan, other anatomic elements conflicts with the spine. The soft tissues (e.g. organs, veins, fluids, ...) are also acquired during this procedure and can affect the segmentation. Also, different bone structures are usually present with potentially different measured values, like the ribs, the limbs and even, in some cases, the skull. Even inside the spine, the vertebra bone density differs from level to level.

All these challenges make it difficult to apply a simple segmentation method like thresholding as a universal solution, and a more robust solution must be found.

7.2.8. Prototype version: manual thresholding

During the early phases of development of PYTHEAS NAVIGATION *Your Guided Trajectory* prototype, the segmentation were achieved using a manual thresholding defined as followed:

Definition 2: Manual thresholding

$$S_t(x) = \begin{cases} 0 & \text{if } x < t \\ x & \text{otherwise} \end{cases}$$ where t is the threshold, x the input and S_t the output

In practice, the surgeon was able to manually choose a threshold that gave him the best representation of the spine (Figs. 7.9 and 7.10).

This method, although easy to understand and quite fast for the surgeon, has some flaws, as previously mentioned. The main and major flaw is the fact that it uses a single threshold for the whole spine. Indeed, choosing a threshold HU that works for T_4 and T_5 might not be satisfying for L_5, due to the differences in bone density along the spine. Another flaw is the fact that it is a manual step, making it time-consuming in some cases and, most likely, not repeatable.



(a) Example of a prototype segmentation

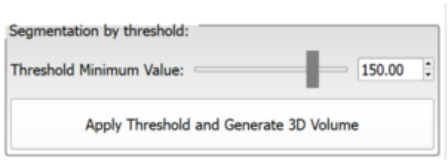

(b) Parameter control of the segmentation

Figure 7.9.: Prototype GUI

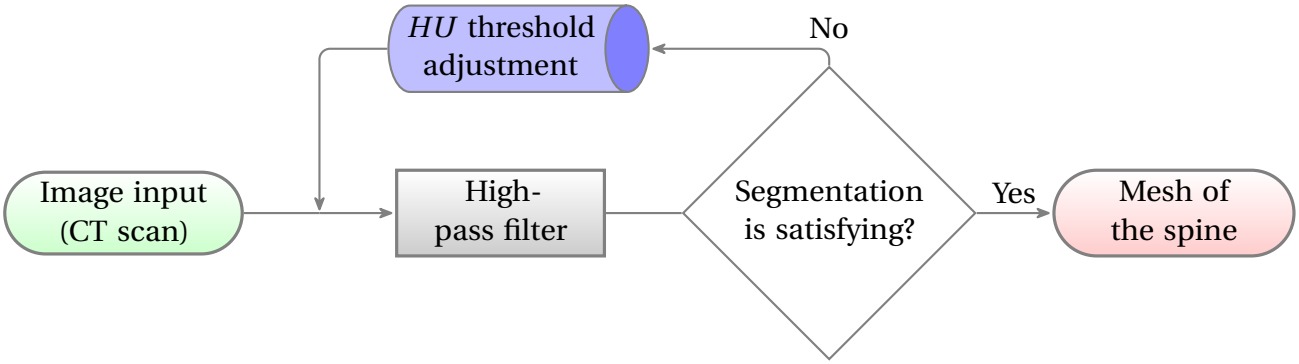

Figure 7.10.: Prototype segmentation

With this simple workflow, the surgeon have to accommodate both the screw placement and the visualization needs. It is fairly easy to give an example where this method fails: a single vertebra may be less dense (e.g. affected with osteoporosis) than the rest of the spine. In this case, this vertebra segmentation can be degraded (i.e. lacking anatomical details, missing parts of the bone), or simply not showing. This leads to the possible inability to instrument this vertebra.

8. State of the art

8.1. Image segmentation

Image segmentation is one of the most popular research field in computer vision. The development of image segmentation techniques relates to many fields, e.g., smart medical imaging, image search engine, autonomous vehicles, industrial inspection or augmented reality.

The main idea of these techniques is to divide an image into regions with different features, in order to extract Regions of Interest (ROIs).

Since the 1970's, image segmentation has received continuous attention from computer vision researchers (Brice et al. 1970, Pavlidis 1972, Rosenfeld 1979). By default, an image segmentation technique may not be automated and can simply be the result of an "expert" (i.e. a person with the knowledge to differentiate the region of interest from the rest of the image) selecting regions of the image.

Being a thoroughly explored area of computer vision, numerous kinds of image segmentation techniques have emerged (Fig. 8.1).

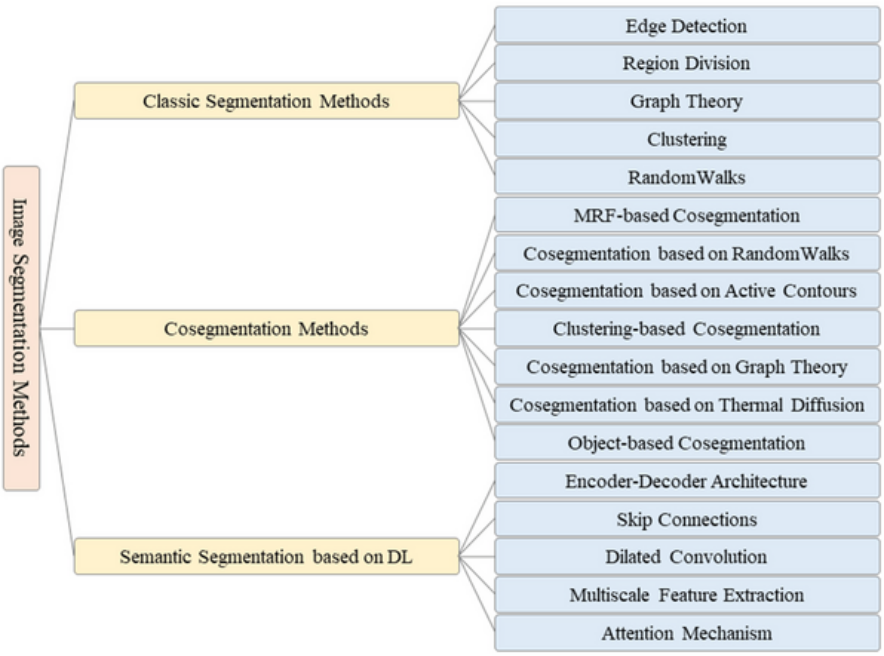

Figure 8.1.: Image segmentation methods (Yu et al. 2023)

8.1.1. Classic segmentation methods

Most classic segmentation algorithms have been developed considering the pixel values similarities in the same region and the discontinuities between different regions. Typically, segmentation is based on pixel value similarity, while edge detection is based on pixel value discontinuities.

8.1.1.1. Edge detection

Edge detection techniques is one of the earliest segmentation methods, and tries to identify the boundary of the different regions of the image. Usually, these methods uses the derivatives of the image in order to identify such boundaries.

The most used edge detection operators are:

Sobel-Feldman operator (Sobel et al. 1973)

This derivative computes an approximation of the gradient of the image intensity function. It is based on the convolution of the source image with small filters ($3x3$) in the horizontal and vertical directions and is therefore very inexpensive computationally.

Definition 3: Sobel-Feldman operator

$$D_x = \begin{bmatrix} +1 & 0 & -1 \\ +2 & 0 & -2 \\ +1 & 0 & -1 \end{bmatrix} * I,\ D_y = \begin{bmatrix} +1 & +2 & +1 \\ 0 & 0 & 0 \\ -1 & -2 & -1 \end{bmatrix} * I,\ D = \sqrt{D_x^2 + D_y^2}$$

where

I : source image
D_x : horizontal derivative
D_y : vertical derivative
D : gradient magnitude
$*$: convolution operator



(a) Example source image (b) Gradient magnitude (c) Horizontal derivative (d) Vertical derivative

Figure 8.2.: Sobel-Feldman operator example

Discrete Laplace operator

This operator is the analog of the continuous Laplace operator. As derivative filters are often sensitive to high-frequency noise, this operator is often preceded by a smoothing filter (typically a Gaussian filter), that can be combined with the Laplace filter into a single filter.

Definition 4: Discrete Laplace operator

$$D^2_{xy} = \begin{bmatrix} 0 & 1 & 0 \\ 1 & -4 & 1 \\ 0 & 1 & 0 \end{bmatrix} * I$$

where

I : source image
D^2_{xy} : derivative
$*$: convolution operator

Canny edge detector (Canny 1986)

This method uses a multi-stage algorithm to detect the edges in images.

Algorithm 1: Canny edge detector

Data:
$I \leftarrow$ Source image
$k \leftarrow$ Gaussian filter size (usually 5)
$\sigma \leftarrow$ Gaussian filter variance

1 *Apply Gaussian filter H to I in order to remove the noise*;
2
3 $I_{smooth} \leftarrow H * I$
$H_{ij} = \frac{1}{2\pi\sigma^2} \exp\left(-\frac{(i-(k+1))^2+(j-(k+1))^2}{2\sigma^2}\right), \{i,j\} \in [1, 2k+1]^2$
4 *Find the intensity gradient G of I_{smooth}, using an edge detection operator (e.g. Sobel-Feldman)*;
5 *Apply gradient magnitude thresholding or lower bound cut-off suppression to get rid of spurious response to edge detection*;
6 *Filter out edge pixels with a weak gradient value and preserve edge pixels with high gradient value (double threshold)*;
7 *Track edge by hysteresis: Finalize the detection of edges by suppressing all the other edges that are weak and not connected to strong edges*;

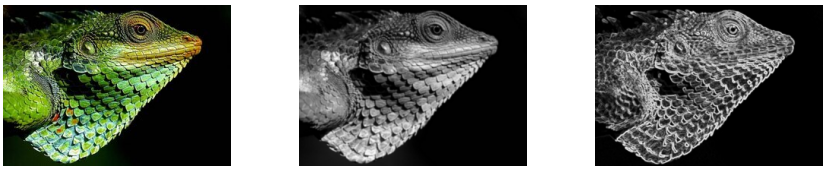

(a) Example source image (b) Smoothed image (c) Intensity gradient

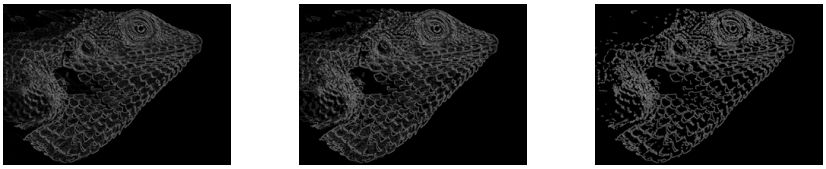

(d) Gradient magnitude thresholding (e) Double threshold (f) Hysteresis

Figure 8.3.: Canny edge detector example

8.1.1.2. Region division

Region-based segmentation divides the image into regions sharing the same logical predicate. It can be summarized as followed:

Definition 5: Region division

Every point in a region R_i must be connected to another point:

$$\forall i \in [1,n], R_i \text{ is a connected region} \tag{8.1}$$

Every pixel of the image must be in a region:

$$\bigcup_{i=1}^{n} R_i = R \tag{8.2}$$

The regions must be disjoint:

$$\forall i,j \in [1,n]^2, i \neq j, R_i \bigcap R_j = \emptyset \tag{8.3}$$

Every pixel in a region must satisfy the predicate P:

$$\forall i \in [1,n], P(R_i) = \text{TRUE} \tag{8.4}$$

Adjacent regions must be different in the sense of the predicate P:

$$P(R_i \bigcup R_j) = \text{FALSE}, \text{ for any adjacent } R_i \text{ and } R_j \tag{8.5}$$

A typical region division algorithm is *Thresholding*. This is probably one of the easiest method of segmentation, where a threshold is used to divide the image into two regions of pixels, where their values are either lower or greater than the threshold. As there are only two regions, the resulting segmentation is called a binary map, while the process is often called binarization. Automated algorithms exists to find the threshold of an image, like the popular *Otsu's method* (Otsu 1979). This method is determined by minimizing the intra-class intensity variance or, equivalently, by maximizing the inter-class variance. It is equivalent to a globally optimal *k-means* performed on the intensity histogram.

Region growing is another method of dividing an image. It uses multiple seeds as initiation points and combine the pixels with similar features in the seed neighborhood in the regions where the seed is located, according to a predefined growth rule until no more pixels can be merged. *Region merging* is a similar iterative method, where the similarity is measured by judging whether the difference between the average pixel value in the region obtained in the previous step and the pixel value of its adjacent pixels is less than a given threshold.

A *watershed* is a image transformation that mimics a geological watershed (i.e. drainage divide). In this context, the source image is treated like a topographic map in which the value of the pixel represent its "height", and the transformation finds the lines that runs along the tops of ridges (Fig. 8.4). The base version of this algorithm is prone to false segmentation when the source image become more complex. In order to solve this issue, a Gaussian Mixture Model (GMM) can be established. This method is especially effective for segmenting medical images.

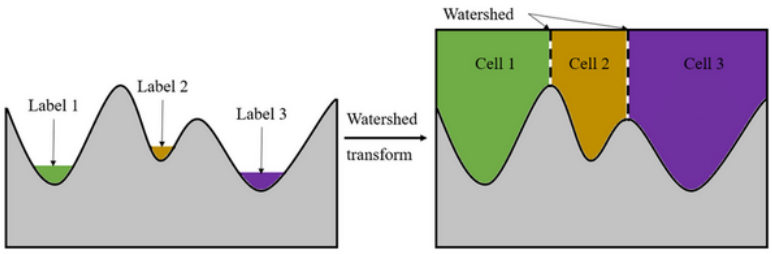

Figure 8.4.: Segmentation process of the watershed algorithm (Zheng et al. 2021)

8.1.1.3. Graph theory

An image segmentation based on graph theory treats the image as a graph, where pixels or regions are treated as vertices of the graph, and represents the similarity between vertices as weights of edges.

Graph-based region merging uses metrics to obtain an optimal global grouping. For example, Felzenszwalb et al. 2004 used the Minimum Spanning Tree (MST) to merge pixels when the image is represented as a graph. Based on Markov Random Field (MRF), some algorithms introduce Probabilistic Graphical Models (PGMs) to represent the randomness of the features of the image in a region. Indeed, in real-life images, regions are often homogeneous: neighboring pixels usually share similar

properties (e.g. pixel value, texture, ...). A MRF is a probabilistic model which captures this kind of contextual constrains.

8.1.1.4. Clustering methods

Clustering is the task of grouping a set of object in a way that such objects in the same group (called a *cluster*) are more similar to each other than to those in other groups.

Probably the most popular clustering method, *K-means clustering* is a thresholding segmentation algorithm based on the *Lloyd's algorithm* (Lloyd 1982). This is an iterative process that computes cluster centers, aiming to partition a dataset into K clusters. The naive version of the algorithm operates as follows:

Algorithm 2: Naive K-means algorithm

Data:
$M^{(1)} \leftarrow m_1^{(1)}, \cdots, m_k^{(1)}$ (initial set of means)
$X \leftarrow \{x_p, p = |X|\}$ (input data)
ϵ (convergence criteria)

while $M^{(t+1)} - M^{(t)} > \epsilon$ **do**
  Assignment step: assign each x to the cluster with the nearest mean (using the Euclidean distance);
  $C_i^{(t)} \leftarrow \{x_p : \|x_p - m_i^{(t)}\|^2 \leq \|x_p - m_j^{(t)}\|^2, \forall\, j \in [1,k]\}$
  Update step: means are updated using the cluster data;
  $m_i^{(t+1)} = \frac{1}{|C_i^{(t)}|} \sum_{x_j \in C_i^{(t)}} x_j$
end

There are several methods to process the first set of means, like manual or random assignment, or *K-means++* (Arthur et al. 2007). This algorithm is not guaranteed to converge.

Mean-shift clustering (Comaniciu et al. 2002) is an algorithm based on density function estimation. It models the image into a probability density function space. Through an iterative process, the centroids of the cluster kernel of radius r are shifted toward the maximum increase of the density. Convergence is achieved when no shift direction can accommodate more points inside the kernel.

8.1.1.5. Random walks

A *Random walk* algorithm based on graph theory that determines the segmentation of an image from a set of markers labeling several phases. An anisotropic diffusion equation is solved with tracers initiated at the markers' position. The local diffusivity coefficient is greater if neighboring pixels have similar values, so that diffusion is

difficult across high gradients. The label of each unknown pixel is attributed to the label of the known marker that has the highest probability to be reached first during this diffusion process (Grady 2006). This idea has been extended to 3D mesh images by Lai et al. 2008 and J. Zhang et al. 2010.

8.1.2. Co-segmentation methods

Collaborative segmentation (co-segmentation for short) is a special case of image segmentation, where multiple images are used to segment semantically similar objects. This method has been introduced in 2006 by Rother et al. 2006. These methods aim to minimize the segmentation energy function $E = E_s + E_g$ where E_s is the energy function of the seed image segmentation (difference between the foreground and the background of the image) and E_g is the energy function of the co-segmentation (similarity between foregrounds in the set of image).

With that knowledge, there are two ways of minimizing E. The first one is the improvement of the classic segmentation to minimize E_s. The second one is the optimization of the unsupervised learning method to learn good representations in image sets to minimize E_g.

In order to achieve such segmentation, classic segmentation method must be used to extract the features of the foreground of multiple images as prior knowledge, known as *seed images*, and then use this prior knowledge to process a set of images containing the same, or similar, objects. The co-segmentation problem has been solved using various classic segmentation methods (Table B.10).

8.1.3. Segmentation based on Machine Learning (ML)

Thanks to the advances of the image acquisition methods over the years, the complexity of the image have drastically increased, making more information available to process. However, this increase in image complexity raised new challenges in the segmentation field, as the classic methods lose efficiency and feature extraction methods cannot follow the computational complexity. The greater amount of information pushes forward methods based on generalizing said information: Artificial Intelligence (AI). The goal of these methods is the creation of a model (i.e. a mathematical formula) used to make predictions or classifications on new data. This model is trained using a training dataset. This training is accomplished using a learning algorithm.

8.1.3.1. AI: Machine Learning (ML) vs. Deep Learning (DL)

ML is a subset of the AI field of study (Fig. 8.5) which uses statistical algorithms to learn and generalize from input data, allowing the processing of a task without explicit instructions. DL is itself a subset of ML, using a complex structure of algorithm modeled after the human brain (e.g. neural network).

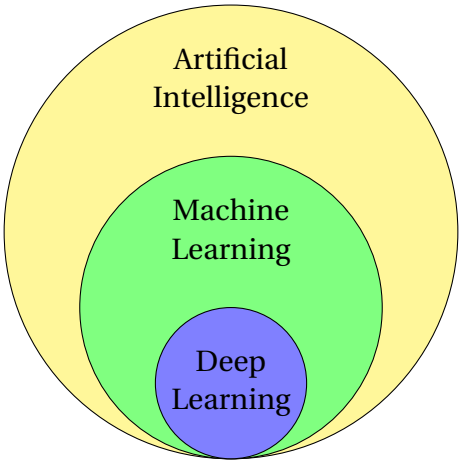

Figure 8.5.: Machine Learning (ML) vs. Deep Learning (DL)

8.1.3.2. Machine learning algorithms

Machine learning are usually divided into three categories: supervised, unsupervised or reinforcement.

Supervised learning

In supervised learning algorithms, the training data set consist of both the input data and the corresponding output. Each training sample is represented by a vector, often called feature vector, while the full training data is represented by a matrix. By iteratively optimizing an objective function, the algorithm learns a function that can be used to predict an output from a new input sample. A supervised learning algorithm can be described as followed:

Definition 6: Supervised learning algorithm

Given a set of N training samples $\{(X_0, y_0), \ldots, (X_N, y_N)\}$

$$X_i : \text{feature vector of the } i^{th} \text{ sample}$$
$$y_i : \text{label of the } i^{th} \text{ sample}$$

The learning algorithm seeks a function $g : X \rightarrow Y$, where

$$X : \text{input space}$$
$$Y : \text{output space}$$

When $f : X \times Y \rightarrow \mathbb{R}$ is a objective function,

$$g(x) = \arg\max_{y}(f(x, y))$$

Supervised learning falls into two types of problems:

- Classification: Assign test data into categories. Common methods are linear classifiers, Support Vector Machines (SVMs) (Cortes et al. 1995), decision trees, K-nearest neighbor algorithm (Fix et al. 1989) or random forest (Lindner et al. 2013),
- Regression: Used to understand the relationship between dependent and independent variables. Popular methods are linear regression, logistical regression and polynomial regression.

Unsupervised learning

Unsupervised learning algorithms work similarly to supervised learning algorithm with the difference that they learn exclusively from unlabeled data. Instead of responding to feedback, these algorithms tries to to analyze and cluster unlabeled data sets, and discover hidden patterns or data grouping without the need for human labeling.

These models are mainly used for clustering, association and dimensionality reduction:

- Clustering: Group unlabeled data based on their similarities or differences. Common methods are K-means clustering (Clustering methods), Ward's method (Ward 1963) or Gaussian Mixture Model (GMM).
- Association: Rule-based method for finding relationships between variables. The most common algorithms are the Apriori algorithms (Agrawal et al. 1994).

While more data usually yields more accurate results, it can also negatively impact the overall performance of the machine learning algorithm. For example, an *overfitted* model is a model that contains more parameters that can be justified by the data. In this case, the model corresponds too closely to a particular set of data and may fail to predict additional data. In order to reduce the number of features in a given data set while preserving the integrity of said data set, a dimensionality reduction can be used. As such, these methods are commonly used as a preprocessing step to other machine learning algorithms. Principal Component Analysis (PCA) (Pearson 1901) and Singular Value Decomposition (SVD) are the most commonly used methods.

Reinforcement learning

Reinforcement learning aims to optimize sequential decisions (decision taken recurrently across time). It is typically how we, humans, learn. It needs a *state space* (information useful to take a decision), an *action space* (decisions that can be taken) and a *reward signal* (feedback about performance). Monte Carlo methods (Metropolis et al. 1949) are a popular example of reinforcement learning.

8.1.3.3. Neural networks and deep learning

A neural network is a specific case of machine learning aiming to make decisions in a similar manner to the human brain, mimicking the way neurons work together to come to a conclusion. It consists of layers of nodes (i.e. artificial neurons), the first one being the input layer, the last one being the output layer, and separated by one or more hidden layers. The nodes connects to others with a weight and a threshold. When the output of a node is higher than the associated threshold, the node is activated and the data is sent to the next layer. They are the heart of the deep learning methods.

In short, a neuron can be described as a rule that transform an input vector $X = (x_1, \ldots, x_n)$ into an output signal h:

Definition 7: Neuron signal

$$h = \sigma(b + \sum_{i=1}^{n} w_i x_i)$$

b : neuron bias,
w_i : neuron connection weight,
σ : activation function

The activation function σ is usually a sigmoid (e.g. logistic function) or a Rectified Linear Unit (ReLU) function (Eq. 8.6, Eq. 8.7, Fig. 8.6).

Definition 8: Activation function σ

Sigmoid function (also known as logistic function)

$$\sigma(x) = \frac{1}{1 + \exp^{-x}} \tag{8.6}$$

Rectified Linear Unit (ReLU) function

$$\sigma(x) = \max(0, x) \tag{8.7}$$

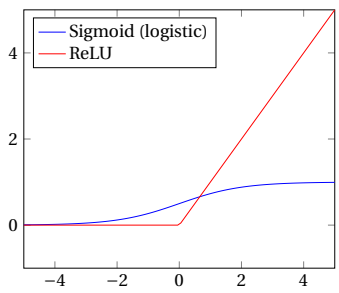

Figure 8.6.: Examples of activation functions: Sigmoid and ReLU

While the model is trained, its accuracy is evaluated using a cost (or loss) function J, commonly referred as the Mean Square Error (MSE):

Definition 9: Mean Square Error

$$J = \frac{1}{n}\sum_{i=1}^{n} \|y_i - \hat{y}_i\|^2 = \frac{1}{n}\sum_{i=1}^{n}\sum_{j=1}^{m}(y_{i,j} - \hat{y}_{i,j})^2$$

$\hat{y}_i = [\hat{y}_{i,1}, \ldots, \hat{y}_{i,m}]$ is the ground-truth for the ith training sample,
$y_i = [y_{i,1}, \ldots, y_{i,m}]$ is the network output

The goal of the training is to minimize the cost function by adjusting the weights and biases of the model until we reach a point of convergence or a local minimum. This process is usually achieved through backpropagation (e.g. gradient descent, Fig. 8.7).

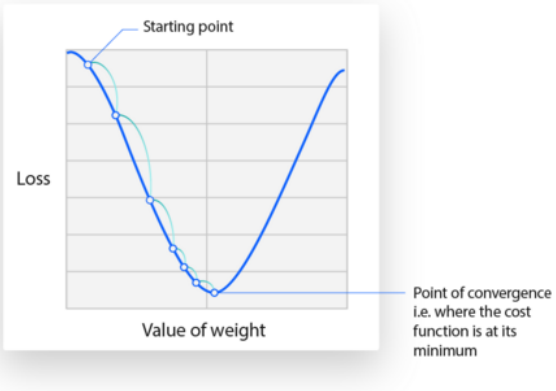

Figure 8.7.: Evolution of the cost function during backpropagation

Neural networks can be divided into two categories: *feedforward* and *backpropagation*. It is important to note that the backpropagation training algorithm previously described is not to be confused with the backpropagation neural network. Most of the deep neural network are feedforward, meaning they flow from input to output only.

Neural networks can be classified into different types, with the most common being:

Multi-Layer Perceptron (MLP)

Multi-Layer Perceptrons (MLPs) are feedforward neural networks. They are comprised of an input layer, an output layer, and one or more hidden layers. Even if they are called "perceptron", their nodes are actually sigmoid neurons, and not perceptrons. They are commonly used for computer vision and natural language processing, and are the foundation of other neural networks.

Convolutional Neural Network (CNN) (Krizhevsky et al. 2017)

Convolutional Neural Networks (CNNs) are similar to MLP, but are optimized for processing image, speech or audio signal. They have three types of layers: convolutional, pooling and fully-connected. The first layer is always a convolutional layer, while the fully-connected layer is the final one. With each layer, the CNN increases in complexity, identifying greater and more complex features. Most of the computation happens in the convolutional layer(s), which abstract the input to a feature map by convolving it with a filter (feature detector). Pooling layers are used to apply pooling, which is a form of non-linear downsampling. The fully-connected layer is usually seen as a regular, non-convolutional, neural network.

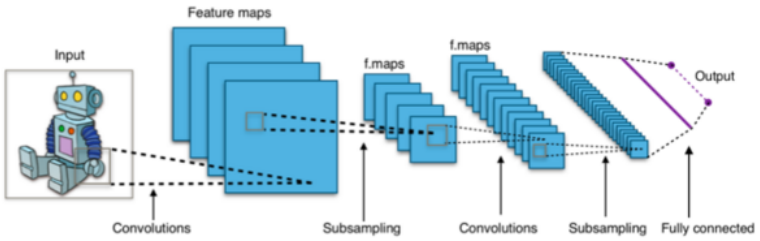

Figure 8.8.: Example of CNN architecture

Recurrent Neural Network (RNN)

Recurrent Neural Networks (RNNs) use sequential or time series data. They are commonly used for ordinal or temporal problems, like language translation, natural language processing or speech recognition. They leverage backpropagation through time, which is slightly different from traditional backpropagation, as it specifically uses sequential data.

In the recent history, deep learning and neural networks have been used interchangeably in conversations, which is not exactly correct. Indeed, deep learning is actually a subset of the neural network world, where the depth of layers in the neural network is the key factor of differentiation. When a neural network consists of more than three layers (including the input and output layers, meaning more than one hidden layer), it can be considered a deep learning algorithm. Otherwise, it is just a basic neural network.

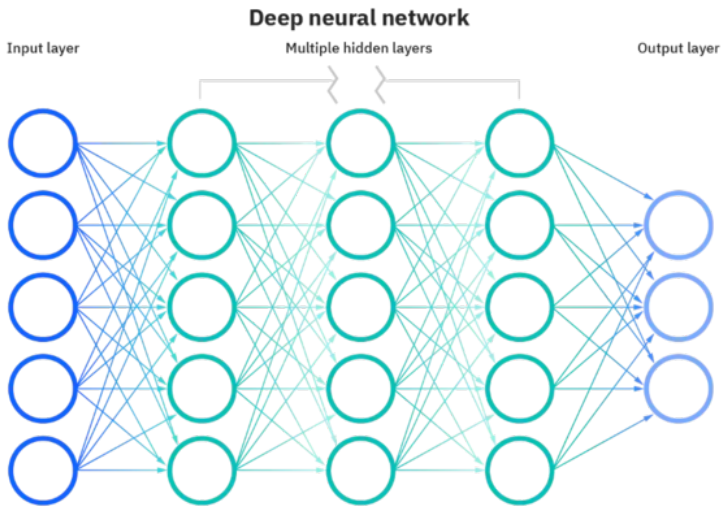

Figure 8.9.: Typical deep neural network

8.2. Image segmentation in medical imaging

Image segmentation has been a long-lasting topic in the medical field. Indeed, medical images play a vital role in assisting health care providers to give patients diagnostics and treatments. Without this kind of technique, the interpretation of medical images relies heavily on the time-consuming and, usually, subjective visual interpretation of a human being. Image segmentation is one of the many steps into overcoming these limitations.

In particular, medical images exposes unique challenges:

Image quality Medical images suffers from issues like noise, insufficient resolution and inhomogeneity. These issues make it difficult to accurately segment these images.

Inconsistencies Medical images can be acquired using different machines, with different settings and calibrations, operated by humans with different experiences. These parameters can generate inconsistencies between acquisitions, or even a variation of image quality that can be difficult to quantify and work around.

8.2.1. Segmentation evaluation metrics

Designing or choosing an appropriate measure of the effectiveness of image segmentation is no easy task, as the chosen metric must provide relevant information to the task.

The accuracy of a segmentation technique refers to which segmentation results agree to the ground-truth segmentation. Most of the time, a surrogate ground-truth

segmentation is usually obtained from either a manual segmentation (done by an expert of the task), a different imaging modality or a segmentation algorithm known to produce repeatable accurate results.

Definition 10: Segmentation

Let a volume $X = \{x_1, \dots, x_n\}, |X| = w \times h \times d$
where w, h and d are the dimensions of the volume (width, height and depth)
Let the ground-truth partition

$$S_g = \{S_g^1, S_g^2\} \tag{8.8}$$

With the assignment function

$$\forall x \in X, \begin{cases} f_g^i(x) = 0, \text{if } x \notin S_g^i, \\ f_g^i(x) = 1, \text{if } x \in S_g^i \end{cases} \tag{8.9}$$

Similarly, if the generated segmentation

$$S_t = \{S_t^1, S_t^2\} \tag{8.10}$$

With the assignment function

$$\forall x \in X, \begin{cases} f_t^i(x) = 0, \text{if } x \notin S_t^i, \\ f_t^i(x) = 1, \text{if } x \in S_t^i \end{cases} \tag{8.11}$$

In the next sections, the ground-truth point set will be noted T, while the segmentation point set generated from the image I will be noted G. Also, the four cardinalities derived from the the confusion matrix between G and T are noted TP for true positives, FP for false positives, TN for true negatives and FN for false negatives (Table 8.1).

Definition 11: Cardinalities

Let the sum of agreement

$$\forall \{i, j\} \in S_g \times S_t, m_{i,j} = \sum_{k=1}^{|X|} f_g^i(x_k) f_t^j(x_k)$$

$$\Rightarrow \begin{cases} TP = m_{1,1} = G \bigcap T, \\ FP = m_{1,2} = G - TP, \\ FN = m_{2,1} = (I - G) \bigcap (I - T), \\ TN = m_{2,2} = (I - G) - TN \end{cases}$$

		Generated segmentation G	
		Positive	Negative
Ground truth T	Positive	True positive TP	False negative FN
	Negative	False positive FP	True negative TN

Table 8.1.: Confusion matrix of G and T

Distance-based metrics

When the delineation of a boundary is the objective of the segmentation, a distance-based metric is important. It measures the distance between the the generated boundary B and the ground-truth boundary T. The most commonly used metrics for evaluating the distance between two point set A and B is the Hausdorff distance H (Eq. 8.13, Maurer et al. 2003, Cárdenes et al. 2009, Gouttard et al. 2008), defined by:

Definition 12: Hausdorff distance

$$h(A,B) = \max_{a \in A} \min_{b \in B} \|a-b\| \quad \text{(Directed Hausdorff distance)} \tag{8.12}$$

$$H(A,B) = \max(h(A,B), h(B,A)) \quad \text{(Hausdorff distance)} \tag{8.13}$$

where $\|\bullet\|$: norm operator, e.g. Euclidean distance

The averaged H over all points, known as the Average Hausdorff distance $\bar{H}$ (Eq. 8.15, Khotanlou et al. 2009) is known to stable and less sensitive to outliers than the classic H:

Definition 13: Average Hausdorff distance

$$d(A,B) = \frac{1}{N} \sum_{a \in A} \min_{b \in B} \|a-b\| \quad \text{(Directed Average Hausdorff distance)} \tag{8.14}$$

$$\bar{H}(A,B) = \max(d(A,B), d(B,A)) \quad \text{(Average Hausdorff distance)} \tag{8.15}$$

Because the calculation of $\bar{H}$ has a complexity $\mathcal{O}(|A||B|)$ (i.e. all possible point pairs), optimized algorithms such as J. Zhao et al. 2014 have to be used. Moreover, other norms can be applied instead of the classic Euclidean distance, like the Mahalanobis Distance d_{mh} (Eq. 8.16), which takes into account the correlation of all points in the point set.

Definition 14: Mahalanobis distance

$$d_{mh}(a,b) = \sqrt{(a-b)^T S^{-1} (a-b)} \tag{8.16}$$

where S^{-1} is the inverse of the covariance matrix of the point set

Overlap-based metrics

Overlap-based metrics measure the overlap between the ground-truth segmentation and the generated segmentation. The most common measurements are the Dice coefficient $DICE$ (Eq. 8.17, Dice 1945), also called the overlap index and the Jaccard index JAC (Eq. 8.18, Jaccard 1912).

Definition 15: Commonly used overlap-based metrics

$$DICE = \frac{2TP}{2TP + FP + FN} \quad \text{(Dice coefficient)} \tag{8.17}$$

$$JAC = \frac{TP}{TP + FP + FN} = \frac{DICE}{2 - DICE} \quad \text{(Jaccard index)} \tag{8.18}$$

$$TPR = \frac{TP}{TP + FN} \quad \text{(Recall/Sensitivity)} \tag{8.19}$$

$$FNR = 1 - TPR \quad \text{(False Negative Rate)} \tag{8.20}$$

$$TNR = \frac{TN}{TN + FP} \quad \text{(Specificity)} \tag{8.21}$$

$$FPR = 1 - TNR \quad \text{(Fallout)} \tag{8.22}$$

$$PPV = \frac{TP}{TP + FP} \quad \text{(Precision)} \tag{8.23}$$

8.2.2. Segmentation of the spine in CT scans

Vertebra segmentation is a challenging topic, as the anatomy and architecture of the vertebrae widely changes depending on the population, pathology or even the position of the vertebra within the spine.

8.2.2.1. Early work: classic techniques

Early techniques usually uses types of unsupervised segmentation techniques (Table 8.2). Kang et al. 2003 has developed an algorithm based on region-growing, using the local CT value histogram to to label the soft and bone tissues, allowing separation of the trabecular and cortical bones. Methods using initial labeling have also been explored by H. Li et al. 2005, with a version of the watershed algorithm, and Aslan et al. 2010, with a graph-cut approach. Such methods unfortunately lack automation, as a manual labeling is required to start the algorithm process.

To handle the complex topology of the vertebrae, level set methods have been a widely used base framework for the segmentation, in combination with other techniques. A level set of a function $f : (x_1, \ldots, x_n) \mapsto \mathbb{R}$ is a set where this function takes on a given constant value c so that $L_c(f) = \{(x_1, \ldots, _n) | f(x_1, \ldots, x_n) = c\}$. In the special case where $n = 3$, the level set is called an *isosurface*. Huang et al. 2013 proposed a level set method based on edge and region, namely Edge- and Region-Based Level Set

(*ERBLS*), allowing the segmentation of images with intensity inhomogeneity or discontinuous boundaries. It uses the *Otsu threshold* in order to remove the dependency on a manual initialization (while allowing manual re-initialization for fine-tuning). Y. Li et al. 2015 proposed another automatically initialized level set method, using an hybrid morphological filter (comprised in a succession of morphological erosions and dilations) and a GMM to generate a precise object boundary.

Yao et al. 2006 devised a fully automated method to segment the spine, isolate the spinal canal and separate the vertebrae. The segmentation was achieved using a simple high-pass filter ($HU \geq 200$), followed by a connected component analysis to find the largest blob as the spine segmentation. The spinal canal was found using a watershed algorithm, while the vertebrae were separated using the intensity profile projected onto the spinal canal line.

Reference	Methods	Evaluation
Kang et al. 2003	Region-growing, value histogram	Root mean square coefficient of variation (CV_{RMS}) Intraoperator: $CV_{RMS} = 0.29 \pm 0.17$ Interoperator: $CV_{RMS} = 0.27 \pm 0.15$ Average surface distance: $d =$ 18.36 mm
H. Li et al. 2005	Watershed	Not reported
Aslan et al. 2010	Graph-cut	$DICE = 0.94$
Huang et al. 2013	Edge- and region-based level set, Otsu threshold	$DICE = 0.94 \pm 0.02$ $H = 10.06 \pm 1.71$ mm
Y. Li et al. 2015	Level set, morphological filters, GMM	$DICE = 0.92 \pm 0.33$
Yao et al. 2006	High-pass filter, watershed	Not reported

Table 8.2.: Summary of classic segmentation techniques

8.2.2.2. Geometric/anatomical model- and atlas-based segmentation techniques

Recent works have been focused on models incorporating the anatomical knowledge about the vertebrae (Table 8.3). These models are trained to estimate the mean shape and variation of a typical vertebra from a training set of segmented vertebrae. The models were then fit to the image data using either forces derived from the image or via deformable registration. The result is determined from the initial estimation, which

can be done manually or automatically. Mastmeyer et al. 2006 developed an algorithm to segment the vertebral bodies, in order to measure the Bone Mineral Density (BMD) of these vertebrae. In this algorithm, the user is asked to coarsely position geometric shapes around the vertebra body on the three anatomical planes. These shapes are then iteratively inflated or deflated to match the vertebral body. Klinder et al. 2009 proposed a framework to fully automate vertebra detection, identification and segmentation. In this paper, the spinal canal is built from small tube-shaped segments. A generalized Hough transform (Ballard 1981), trained to recognize vertebrae from C_1 to L_5, is then applied to detect the vertebrae. These detected vertebrae are then compare to models to identify them. Finally, the model is adapted to the vertebra using a shape-constrained deformable models approach. Ma et al. 2010 based their work on an edge detector trained on mesh features from a set of vertebrae. This base model is then deformed to match the vertebra boundary. Ibragimov et al. 2014 proposed a landmark-based shape representation approach, where landmarks are considered as sources and destinations, and landmark connections as roads. These connections are represented as a *complete graph*. This segmentation consists of detecting a specific set of landmark in an image and deducing the outline of the object from the position of these landmarks, which is achieved using a landmark-based atlasing of the object. The landmark detection itself is achieved using game theory.

Reference	Methods	Evaluation
Mastmeyer et al. 2006	Basic shape deformation	$L_1 : DICE = 0.991$ $L_2 : DICE = 0.994$ $L_3 : DICE = 0.995$
Klinder et al. 2009	Spinal canal detection, generalized Hough transform, shape registration	Average surface distance: $d = 1.12 \pm 1.04\,\text{mm}$
Ma et al. 2010	Supervised edge detection, mesh deformation	Average surface distance: $d = 0.95 \pm 0.91\,\text{mm}$
Ibragimov et al. 2014	Landmark-base shape representation, game theory (strategy dominance)	$DICE = 0.939$

Table 8.3.: Summary of geometric/anatomical model- and atlas-based segmentation techniques

8.2.2.3. Deep learning segmentation techniques

This last decade, deep learning has been a rapidly growing topic of research in medical image segmentation. Compared to "traditional" segmentation methods, deep learning can present advantages in segmentation accuracy and speed, especially using modern hardware and algorithm implementations. However, the advent of these

new technologies came with a major obstacle: the availability of large data sample sizes. Indeed, when most deep learning application can have more than a million of samples (e.g. Russakovsky et al. 2015), it can be hard to get more than a thousand medical images to build a model without suffering from overfitting. To overcome this challenge, various strategies have been proposed:

- Use image patches (2D or 3D): Instead of using the full images, part of the images are used to reduce the input dimensionality.
- Data augmentation: Using affine transforms, samples are artificially generated from real data.
- Use models from other domains as a base: Using a model trained using non-medical images, the output layer can be trained on specific task-related medical images.
- Use non-medical images to train the model: The model can be "initialized" with non-medical images, then fine-tuned using specific task-related medical images.

In particular, because the structural characteristic of images is so important in medical application, convolutional neural networks have gained more and more interest (Shen et al. 2017). Moreover, CNNs do not require manual extraction of image features or excessive preprocessing. Nowadays, deep learning segmentation for medical images can be separated into three main methods: *Fully Convolutional Network (FCN)* (Long et al. 2015), *U-net* (Ronneberger et al. 2015) and *Generative Adversarial Network (GAN)* (Goodfellow et al. 2014).

Example of deep learning segmentation: U-net

U-net is a fully convolutional network architecture specialized in fast and precise image segmentation.

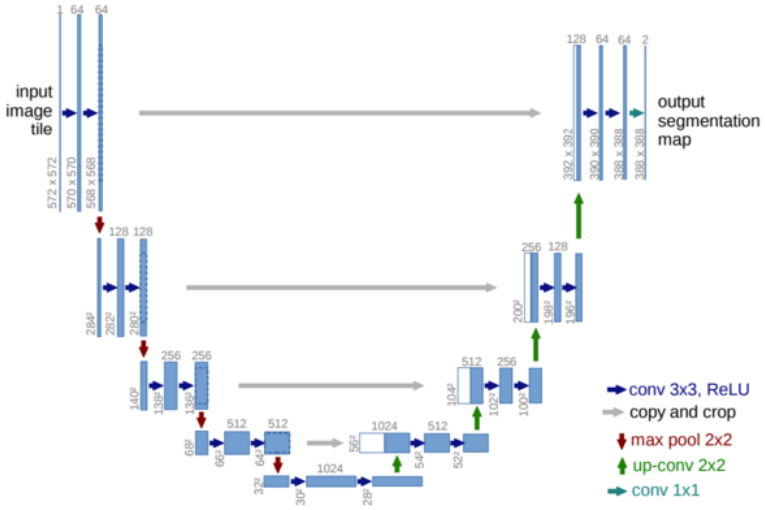

Figure 8.10.: U-net architecture (Ronneberger et al. 2015)

This network , commonly represented as a "U" (Fig. 8.10), consists of a contracting (downsampling) path (left part of the "U") and an expansive (upsampling) path (right part of the "U"), for a total of 23 convolutional layers.

The contracting path is composed of repeated application of 3x3 unpadded convolutions, followed bu a ReLU and a 2x2 max pooling operation for downsampling. At each downsampling step, the number of feature channels is doubled.

Each step in the expansive path is composed of an upsampling of the feature map, followed by a 2x2 convolution (halving the number of feature channels), a concatenation with the corresponding map from the contracting path, and two 3x3 convolutions followed by a ReLU.

The final layer is a 1x1 convolution to map each feature vector to a desired number of classes.

Examples of uses of advanced deep learning segmentation for medical uses

Lessmann et al. 2019 developed a U-net inspired architecture to iteratively detect, segment and identify vertebrae (Fig. 8.11). The algorithm starts by searching, using a sliding 3D window, part of a vertebra bone. The window is then shifted until the vertebra is fully encapsulated into the window. When the vertebra is fully segmented, it memorizes it (to ignore it in the next sweep of the window) and start looking for the next vertebra.

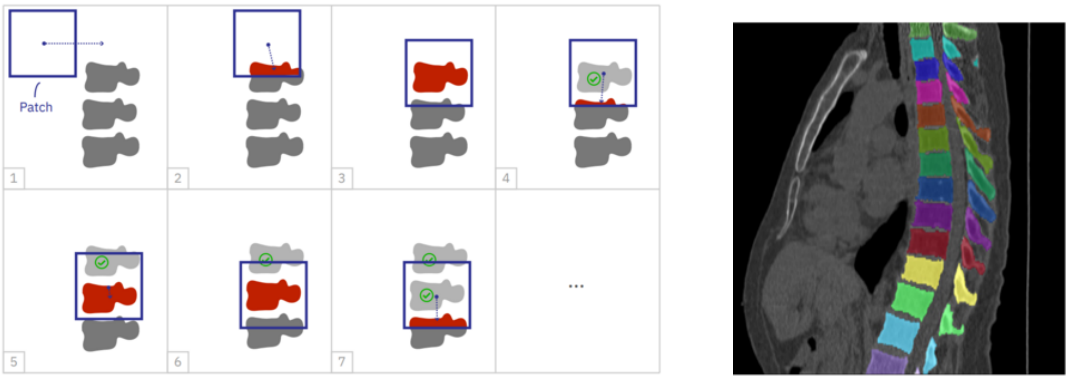

(a) Segmentation process

(b) Example of CT segmentation

Figure 8.11.: Segmentation (Lessmann et al. 2019)

Altini et al. 2021 (Fig. 8.12) used a V-Net architecture to achieve the same goal. However, they first preprocessed the image, by clamping the data between $[-150\,\text{HU}, 1000\,\text{HU}]$ to be closer to the bone values, cropped the image to closely fit the spine and resampled to an isotropic resolution of 1 mm. The training set has been augmented with every epoch of the training, by adding random noise.

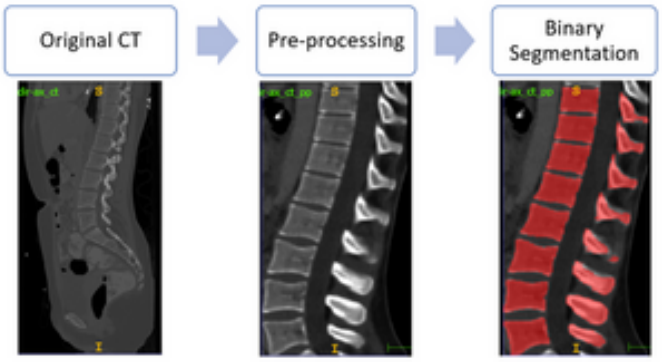

Figure 8.12.: Segmentation process (Altini et al. 2021)

Reference	Methods	Evaluation
Lessmann et al. 2019	U-Net inspired, iterative process	$DICE = 0.95 \pm 0.02$ Average surface distance: $d = 0.2 \pm 0.1\,\text{mm}$
Altini et al. 2021	V-Net inspired	$DICE = 0.89 \pm 0.03$ Average surface distance: $d = 1.43 \pm 0.63\,\text{mm}$

Table 8.4.: Summary of deep learning segmentation techniques

9. Objectives

Accurate pre-operative planning is paramount for successful spinal osteosynthesis procedures. In this domain, advancements in automated spine segmentation using advanced imaging techniques offer exciting possibilities. Automated segmentation can meticulously analyze CT scans, creating a detailed and highly accurate picture of the spinal anatomy. This includes crucial structures like the vertebrae and the cortical shell.

By providing a more precise understanding of the spine's anatomy pre-operatively, automated segmentation offers several advantages. First, it can improve the overall accuracy of surgical planning. Second, it can help address challenges arising from posture changes that occur between the CT scan and actual surgery. These posture changes can lead to variations in vertebral orientation, potentially impacting the planned placement of pedicle screws. Automated segmentation helps mitigate this issue by providing a more foundational understanding of the underlying anatomy.

However, limitations still exist. Cannulation, a critical step where surgeons guide a drill through the pedicle, relies heavily on surgeon feel. This inherent reliance can restrict screw placement options and potentially compromise patient safety.

My work explores the potential of automated spine segmentation for improved surgical planning in spinal fusion procedures. We discuss how this technology can provide a more accurate picture of the spine's anatomy, even before accounting for posture changes. We then explore the challenges of posture changes and the limitations of cannulation in this context. Finally, we highlight the potential benefits of automated segmentation for overcoming these limitations and achieving improved surgical outcomes.

9.1. Automated segmentation of the spine

Segmentation of the spine for pedicle implantation planning

Research on pedicle screw implantation practices highlights the critical role of spine segmentation in planning automation for three main reasons. First, accurate representation of the posterior vertebral arch, including its shape and geometry, is crucial for pinpointing the ideal screw entry point. Second, precise knowledge of the pedicle internal anatomy, particularly the cortical shell, is essential for safe screw trajectory

planning. Any breach of this critical structure can lead to severe patient complications. Finally, segmentation needs to deliver a highly accurate and consistent representation of the cortical shell, down to the sub-millimeter level.

Studies suggest limitation in CT scan accuracy for measuring cortical thickness (Silva et al. 1994; Prevrhal; Fox, et al. 2003; Liebschner et al. 2003). While Prevrhal; Fox, et al. 2003 demonstrated acceptable CT-based measurement with less than 10% error, accuracy may significantly decrease for shells thinner than 1.2 mm.

Clinical CT scanners have limited resolution, and the vertebral shell itself can be very thin, with reports of thickness below 0.5 mm in the lumbar spine (Edwards et al. 2001; Sandor et al. 1992; Vesterby et al. 1991). This suggests that CT scans likely overestimate cortical thickness in vertebral bodies (Silva et al. 1994; Prevrhal; Engelke, et al. 1999; Liebschner et al. 2003). Therefore, the core research question arises: how can we develop a spine segmentation process that accurately and reliably captures the sub-millimeter cortical shell thickness, despite the inherent limitations of clinical CT scan resolution?

Given the critical role of cortical thickness measurement, designing a segmentation process that can handle these limitations is essential. Specifically, this research aims to investigate and develop a segmentation methodology that mitigates the overestimation of cortical thickness in CT scans, ensuring the precise delineation of the vertebral shell for safe and effective pedicle screw implantation planning.

Cortical thickness and density

Pedicle screw loosening and pullout are significant complications in posterior spinal osteosynthesis, especially for patients with osteoporosis (Galbusera et al. 2015; Ohtori et al. 2013; Wu et al. 2012). This is because screw stability is heavily influenced by BMD (Halvorson et al. 1994; S. S. Hu 1997; Okuyama et al. 2001). In lumbar spine, areas with higher BMD offer stronger fixation compared to lower density areas. This can be assessed using automated CTh and CBD techniques, as presented in our research.

Identifying vertebrae at high risk of pullout pre-operatively would be valuable for adapting surgical strategies and minimizing this complication. Similar to Odeh et al. 2021, knowledge of potential BMD variations between vertebrae could guide surgical treatment and fixation choices. This applies to automated CTh and CBD assessment as well.

The optimal implant density (hooks, sublaminar bands or pedicle screws) for spine deformity correction remains a debate. In Adolescent Idiopathic Scoliosis (AIS), some studies suggest adding more fixation points distributes stress more effectively, allowing for greater curve correction (D. H. Clements et al. 2009; Sanders et al. 2011). However, other studies demonstrate that lower-density instrumentation with fewer screws can be equally effective and safe (Bharucha et al. 2013; M. Li et al. 2009; Hwang et al. 2011; Min et al. 2013; J. Li et al. 2016).

9.2. Understanding of the differences between pre-operative CT scan and surgery context

Surgical planning often relies on images, like CT scans, acquired before surgery under conditions quite different from the actual operating room. These pre-operative scans typically capture the patient in a supine (face-up) position, while surgery often involves a prone (face-down) position (Fig. 11.1). This significant change in posture can lead to variations in vertebral orientation, impacting the planned placement and trajectory of pedicle screw.

For navigated pedicle screw implantation techniques, such as those used with the *Your Guided Trajectory*, accurately accounting for these posture-induced changes is crucial. The device calibration relies heavily on the precise global orientation of each vertebra to function accurately.

To address this challenge, a robust model needs to be developed that captures the individual rotation changes experiences by each vertebra between the pre-operative imaging position and the surgical setting. This model can then be used to adjust surgical plans and guide implant placement during navigation. The central research question is: how can we create a predictive model that accurately quantifies and compensates for the individual vertebral rotation changes induced by postural shifts between pre-operative imaging and intra-operative settings, thereby enhancing the accuracy of navigated pedicle screw implantation?

The limitations of pre-operative imaging extend beyond posture changes. Factors like muscle relaxation under anesthesia and intra-operative manipulation of tissues can also affect vertebral positioning. A comprehensive model may need to incorporate these additional factors for improved accuracy. Specifically, this research aims to investigate and develop a model that not only addresses posture-induced changes but also explores the feasibility of incorporating other intra-operative variables to further refine the accuracy of vertebral position prediction.

A robust model that considers posture and anatomical variations offers several advantages. First, it can significantly improve screw placement accuracy for surgeons and potentially guide automated surgical planning by accounting for posture-induced changes in vertebral positions. This translates to enhanced surgical efficiency, as the need for extensive intra-operative adjustments due to unexpected vertebral shifts is minimized. Finally, the model underlying principles could potentially be adapted to other surgical procedures that rely on pre-operative imaging and intra-operative navigation.

9.3. Improvement of pedicle screw implantation: the cannulation process

Cannulation, the process of guiding a drill or probe through the pedicle during screw implantation, is a critical but inherently limited step. It relies heavily on the surgeon tactile feedback, making it susceptible to human error and inconsistencies.

Deviations from the intended trajectory during cannulation can have severe consequences for the patient. A breached cortical wall can damage critical neurovascular structures (nerves and blood vessels) in the spinal canal, leading to paralysis, bleeding, or other serious complications.

The limitations of cannulation directly translate into limitations for screw placement. Surgeon may be hesitant to explore certain screw angulations or trajectories due to the inherent difficulty and risk of cannulating at those angles. This can restrict the available options for achieving optimal screw purchase (anchorage) within the vertebra.

Cannulation limitations can hinder achieving optimal spinal stability in two key ways. Firstly, concerns about cortical breach can lead surgeons to opt for shorter screws, even though longer ones might provide superior fixation. Secondly, the difficulty of placing cannulae in multiple pedicles within a confined area may restrict the total number of screws inserted, potentially compromising the overall spinal stability. The central research question is: how can we mitigate the inherent limitations of tactile-feedback-dependent cannulation to improve the accuracy, safety, and consistency of pedicle screw placement, ultimately enhancing spinal stability?

Understanding the limitations of cannulation in pedicle screw implantation goes beyond simply avoiding risks. This knowledge empowers surgeons to make crucial decisions. By accurately assessing these limitations, surgeons can:

Improved safety Informed choices about screw trajectory and angulation can minimize the risk of neurovascular complications and the need for revision surgery.

Enhanced screw placement Acknowledging the limitations allows exploration of alternative techniques or technologies like automated planning. This opens up a wider range of safe and effective screw placement options, ultimately leading to improved screw purchase and overall spinal stability.

Refine patient selection Understanding limitations can inform patient selection. For patients with complex anatomy or osteoporosis, alternative fixation techniques that are less reliant on surgeon feel can be considered.

Guide technological advancements A clear understanding of cannulation challenges can guide the development of new technologies. This includes advance-

ments in image-guided navigation systems that can provide real-time trajectory guidance, like PYTHEAS NAVIGATION *Your Guided Trajectory*.

By acknowledging and addressing the limitation of cannulation, surgeons can improve the safety, efficiency, and overall outcomes of pedicle screw implantation procedures.

In summary, this research aims to address critical limitations in current pedicle screw implantation practices by focusing on three key areas: enhancing the accuracy of spine segmentation for precise cortical shell representation, developing a robust model to compensate for posture-induced vertebral rotation changes, and mitigating the inherent limitations of tactile-feedback-dependent cannulation. By addressing the challenges of sub-millimeter cortical thickness measurement in CT scans, accurately predicting vertebral shifts between pre-operative and intra-operative settings, and exploring advanced navigation technologies to overcome cannulation limitations, this work seeks to improve the safety, accuracy, and consistency of pedicle screw implantation. Ultimately, the goal is to develop and evaluate methodologies and technologies that empower surgeons to achieve optimal screw placement, minimize patient complications, and enhance overall spinal stability. Through these advancements, this research aims to contribute significantly to the field of spine surgery, paving the way for more precise and reliable automated surgical planning and navigation.

10. Automated segmentation of the spine

The first step in the automated planning is the segmentation of the spine. The reason is two-fold:

1. provide the surgeon a spine reconstruction to validate the planning, and to use during the surgery, and 2. generate a model of the spine, used in the next steps of the planning.

10.1. Region-growing based segmentation

For the first release of the PYTHEAS NAVIGATION *Your Guided Trajectory*, a more robust and less input-dependent segmentation method was needed, compared than the threshold-based segmentation used in the MD prototype. As this version didn't need a fully automated planning, a simple segmentation solution has been chosen and implemented.

10.1.1. Method

One of the most simple and popular segmentation method is the region growing method (Early work: classic techniques). However, in our case, it can present some flaws that need to be addressed. The main flaw is the fact that vertebrae are separated by non-bony structures (intervertebral discs), that can prevent the algorithm to jump from one vertebra to the other. Moreover, communication with surgeons made it clear that the ribs need to be present in order for the surgeons to have an easy way of locate themselves within the spine.

The base assumption for this method is the fact that, without the presence of any instrumentation, the bone is the object with the highest Hounsfield Unit value ($> 200\,\text{HU}$) in the human body. In the CT scan, the 99th percentile of the Hounsfield Units h_{99} is found. With this in mind, the whole CT scan volume is now split into a grid ($30 \times 30 \times 30$) where each cell can contain a seed for the region-growing algorithm. This seed is found as the voxel with the Hounsfield Unit closest to h_{99}, but not too far away from it ($|h - h_{99}| < 25\,\text{HU}$). It is to be noted that a region may not have a guaranteed seed. The seeds are then fed to a standard region-growing segmentation implementation, the flood fill algorithm, generating a binary mask.

The overall algorithm implementation is described in Line 9.

Algorithm 3: Region-growing algorithm implementation

Data:
$I \leftarrow$ Source image
$S \leftarrow$ Empty seed (voxel coordinates) list
Result: M: Segmentation mask

Find the 99th *percentile of* I *(Fig. 10.1)*
  $h_{99} \leftarrow 99^{th}$ percentile of I
Split I *into a* $30 \times 30 \times 30$ *grid* $G = \{C_{i,j,k}, \{i,j,k\} \in [0,30[^3\}$;
foreach $C \in G$ **do**
  $S_{candidate} = \{x,y,z\} \mid h_{x,y,z} = \min(|C(x,y,z) - h_{99}|)$;
  if $|h_{S_{candidate}} - h_{99}| < 25\,\text{HU}$ **then**
    $S \leftarrow S + S_{candidate}$
  end
end

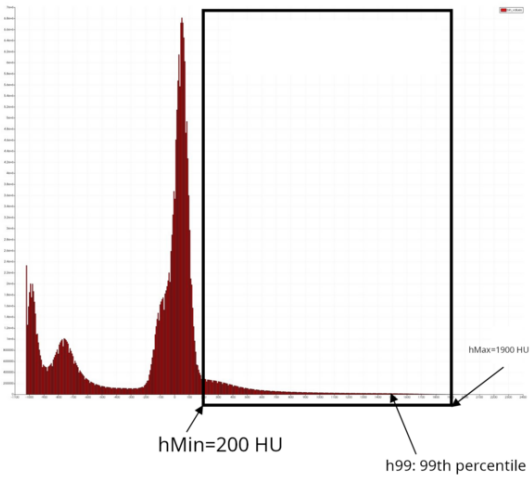

Figure 10.1.: Example of CT scan histogram

10.1.2. Clinical trials and validation

Preceding the release of the PYTHEAS NAVIGATION *Your Guided Trajectory*, the MD had to go through clinical trials in order to get the local regulatory approvals (CE for European Union, FDA for the USA).

Regulatory approval	Number of Surgeons	Number of specimens	Number of pedicles
CE	3	13 in-vivo patients	83
FDA	17	5 cadavers	147

Table 10.1.: PYTHEAS NAVIGATION *Your Guided Trajectory* clinical trials

As for the day of writing (23rd May 2025), the CE marking has been approved. It is important to not that this does not and cannot serve as validation material, but this acknowledges that the segmentation used in the software is usable during a surgery.

As for validation, the protocol uses a selection of CT scans extracted from the VerSe2020 dataset (MICCAI 2020 challenge, Löffler et al. 2020, Liebl et al. 2021, Sekuboyina et al. 2021). The selection of the scan has been done based on having a decent spatial resolution, and an ROI have been used to include only the lumbar vertebrae (in order to not have the ribs in the field of view). The resultant dataset includes 14 CT scans. The DICE coefficient has been calculated for each of these scans in order to compare the mask output by the proposed algorithm and the mask available in the dataset. As a result, the DICE coefficient $d = 71.62 \pm 4.26$ falls close to the 75.2 ± 28.5 displayed in Sekuboyina et al. 2021.

10.1.3. Discussion

This method addresses one of the points needed in the automated planning: a fully automated segmentation. It requires no input from the surgeon and outputs a mask in matters of seconds. However, this method segments every type of bone, including "unwanted" part of the human skeleton, like the skull or the hips. Moreover, this method is fairly sensitive to background noise, which can create "leaks" of the region-growing algorithm towards non-bony areas.

10.2. Gaussian Mixture Model-based segmentation (Tomi et al. 2024)

10.2.1. Introduction

Automated cortical bone segmentation has been described for tibial bone (C. Li et al. 2015) and for femoral bone (Serrurier et al. 2014), but to date, this technique has not been generalized to vertebrae. The description of the cortical bone structure and shape has been reported in different human body segments for a wide range of applications from fracture risk estimation to surgery planning. From micro-CT imaging, cortical thickness computation has been described. Such computation is based on the positioning of an integrable sphere within two surfaces (Hildebrand et al. 1997, G. Dougherty et al. 1999). However, the micro-CT technique applicable to ex-vivo samples required adaptation in in-vivo population. For such application, this requires spine segmentation as fe pre-processing of the imaging data. While

artificial intelligence has shown its capacity for such application (Constant et al. 2023), traditional techniques has also been largely reported with satisfactory results when compared to manual segmentation. Specificity of cortical bone segmentation is the capacity to detect both inner layer between trabeculae and cortical bone and outer layer of the cortical bone. In vertebrae, report of vertebral thickness change according with vertebrae location has been previously reported also depending of age and osteoporosis (Ritzel et al. 1997, Panjabi et al. 2001, Fazzalari et al. 2006, Wagnac et al. 2011).

Furthermore, incorporating cortical thickness and density parameters into the analysis offers a valuable avenue for enhancing the precision of pedicle localization and screw entry point identification. By leveraging the inherent topological features of the vertebral bone, alongside the subtle variations in its density distribution, we can create a more robust and accurate automated planning system.

Specifically, the cortical thickness data provides critical information about the structural integrity and boundaries of the pedicle. Regions of thinner cortex may indicate areas of increased fragility or potential risk during screw insertion. Conversely, areas of higher cortical density suggest stronger bone, potentially offering better screw purchase. By integrating this information with the overall vertebral topology – the geometric arrangement of the bone's surface – we can refine the localization of pedicles and accurately pinpoint optimal entry points.

Furthermore, the relative changes in bone density across the vertebra, as revealed by CT or potentially quantitative MRI, can provide additional clues about the internal architecture and structural support. Areas of higher density may indicate load-bearing regions or regions of increased bone remodeling. By analyzing these density gradients, we can further refine our understanding of the vertebral structure and improve the accuracy of pedicle localization and screw placement planning.

In essence, by combining topological data with cortical thickness and density parameters, we are creating a multi-faceted approach to pedicle localization. This holistic approach, which considers both the shape and material properties of the bone, holds the potential to significantly improve the safety and efficacy of pedicle screw implantation procedures.

In this paper, our aim was to describe an automated method to achieve cortical bone segmentation in vertebrae based on CT-scan, to assess Cortical Thickness (CTh), normalized CTh, and Cortical Bone Density (CBD), to validate these assessments, and to describe the distribution and the variability of normalized CTh and CBD among several vertebral anatomical zones. A hypothesis states that the vertebral bone density can be interpreted as the mixture of two Gaussian density distributions, one for the trabecular bone and another for the cortical bone.

10.2.2. Materials and methods

Samples

The dataset used in this study was made of 42 isolated thoracic and lumbar vertebrae: there were 21 human in-vivo vertebrae, 7 swine vertebrae, and 14 human cadaveric vertebrae (Table 10.2). Considering cadaveric vertebrae: cadavers were provided by the local Medical School. Fourteen vertebrae from three male donors (84.3 ± 8.7 years old) were included.

Considering swine vertebrae: 7 vertebrae from a single 4-month-old Landrace swine of approximately 60 kg were extracted post-mortem just after sacrifice. The whole procedure was compliant with the European Convention on the protection of vertebrates used for experimental or other scientific purposes. The government agreement number was C-013-15-022; Ethical committee CEEA 14. Extraction was made at the research center. The 21 in-vivo human vertebrae were obtained from 3 adults free of any bone or spinal disease who underwent a CT scan examination for another purpose. For each subject, a signed informed consent was obtained before performing the CT-scan. Data were anonymized according to the European General Data Protection Regulation. Ethical approval was waived by the local Ethics Committee in view of the retrospective nature of the study and all the procedures being performed were part of the routine care.

Subject	Model	Age	Gender	Vertebrae		
				High thoracic	Low thoracic	Lumbar
M23	In-vivo (human)	23 y.o.	Male	3	3	1
M34	In-vivo (human)	34 y.o.	Male	3	3	1
F34	In-vivo (human)	43 y.o.	Female	3	3	1
SW	Swine (landrace)	4 m.o.		3	3	1
SC	Cadaver (human)	82 y.o.	Male	3	3	1
SF	Cadaver (human)	77 y.o.	Male	3	3	1

Table 10.2.: Sample description: number of subjects, sub-groups (i.e. cadaveric vertebrae, swine vertebrae, and human in-vivo vertebrae), age and gender, and vertebral levels (i.e. high thoracic, low thoracic, and lumbar).

The CT scan used was a 128-MDCT GE Healthcare Optima CT660 with a mean spatial resolution of 0.7 mm on plane (ranging from 0.21 mm to 0.98 mm), a mean slice thickness of 1 mm (ranging from 0.65 mm to 1.25 mm), a mean generator power of 51,117 kW (ranging from 18,000 kW to 60,000 kW), a mean exposure time of 1080 ms (ranging from 700 ms to 1460 ms), a mean X-ray tube current of 156 mA (ranging from 99 mA to 249 mA), and a mean kilovoltage peak (kVp) of 123 kV (ranging from 120 kV to 140 kV).

Cortical bone segmentation

The loading of DICOM files and the processing of density data were done using ITK library (McCormick et al. 2014). For the in-vivo human, cadaver and the swine CT scans, each vertebra included was manually cropped within the CT scan volume using 3D Slicer software. A high-pass filter was used to remove any non-bone tissue with a cut-off value of 300 HU (Lim Fat et al. 2012). The whole segmentation algorithm chart is presented in Fig. 10.2.

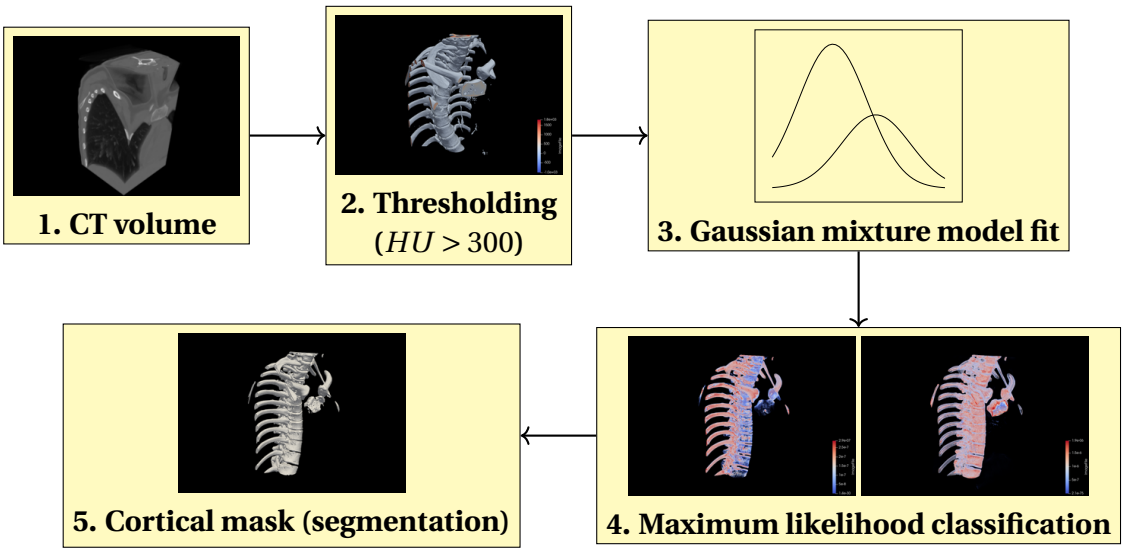

Figure 10.2.: Cortical segmentation algorithm chart: steps toward 3D cortical mask. CT: Computed Tomography, HU: Houndsfield Unit.

Gaussian Mixture Model (GMM)

In our study, the bone density distribution was considered as a mixture of two Gaussian distributions, one for each bone type (cortical and trabecular).

Definition 16: Bone density GMM

Let a Gaussian mixture model, with $N_g = 2$ distributions:

$$\mathcal{N}_t \text{ (mean = } \mu_t \text{, variance = } \sigma_t) \qquad \textit{Trabecular density distribution} \tag{10.1}$$
$$\mathcal{N}_c \text{ (mean = } \mu_c \text{, variance = } \sigma_c) \qquad \textit{Cortical density distribution} \tag{10.2}$$

And the corresponding density functions:

$$f_t \text{ (mean = } \mu_t \text{, variance = } \sigma_t) \qquad \textit{Trabecular density function} \tag{10.3}$$
$$f_c \text{ (mean = } \mu_c \text{, variance = } \sigma_c) \qquad \textit{Cortical density function} \tag{10.4}$$

Let π_t and π_c be the probability distributions defining how the data were shared among the two Gaussian distributions. The input data vector x has a density defined as:

$$p_\theta(x) = \pi_t f_t(x) + \pi_c f_c(x) \tag{10.5}$$

where $\theta = (\pi, \mu, \sigma)$ corresponds to:

- the *mixing distribution* $\pi : (\pi_t, \pi_c)$
- the distribution means $\mu : (\mu_t, \mu_c)$
- the distribution variances $\sigma : (\sigma_t, \sigma_c)$

To estimate the parameter θ based on n data samples, the maximum likelihood needs to be found.

Definition 17: Maximum likelihood estimator

For a sample $x = (x_0, ..., x_{n-1})$,

$$p_\theta(x) = \prod_{i=0}^{n-1} p_\theta(x_i) \qquad \text{Likelihood} \tag{10.6}$$
$$\ell(\theta) = \log p_\theta(x) = \sum_{i=0}^{n-1} \log p_\theta(x_i) \qquad \text{Log-likelihood} \tag{10.7}$$
$$\theta^\star = \arg\max_\theta \ell(\theta) \qquad \text{Likelihood estimator} \tag{10.8}$$

Expectation-maximization

The expectation-maximization algorithm (Dempster et al. 1977) is an iterative process to find a local maximum of likelihood, which can be applied to any mixture model, including our Gaussian mixture model. In order to find this maximum, the algorithm assumes that the problem can be solved given the variables $z = (z_0, ..., z_{n-1})$ which have been used as hidden variables to generate the samples x.

Given initial parameters θ_0 (obtained with either statically defined values, e.g. literature values, or values generated via the k-means algorithm), the algorithm alternates between two phases:

Phase of expectation Computes the probability of each value z

Phase of maximization Uses the values z to compute a new estimate of the parameter θ

This process is iterated until convergence: $\theta_k - \theta_{k-1} < \epsilon$. The output of this process, for each class (cortical and trabecular), was a mapping of log-likelihood values (for each voxel of the original volume) and the associated Gaussian distribution parameters (mean and variance). The expectation-maximization algorithm was implemented using the Armadillo library (Sanderson et al. 2016).

Segmentation

Once the log-likelihood mapping was processed, an iso-surface could be processed using the 95th percentile of the log-likelihood. This iso-surface represented points with a similar value, in our case, a high probability of being labeled as "cortical bone". Such an iso-surface could be obtained using a flying edges algorithm (Schroeder et al. 2006). This iso-surface was defined as our final segmentation and represented as the 3D triangular mesh $\mathscr{M}_{cortical}$. A mesh is a collection of N_v vertices $(v_0, ..., v_{N_v-1})$, N_e edges $(e_0, ..., e_{N_e-1})$ and N_f faces $(f_0, ..., f_{N_f-1})$ that describes the shape of a 3D object. In the case of a triangular mesh, faces are triangles. To guarantee the uniformity of the mesh and avoid aliasing effects, a smoothing filter was applied to $\mathscr{M}_{cortical}$ (Gabriel et al. 1996), making the faces better shaped and the vertices more evenly distributed. The iso-surface computation was achieved using the VTK library (Schroeder et al. 2006).

Cortical Thickness (CTh) and Cortical Bone Density (CBD) assessment

For each vertex of the triangular mesh, the Cortical Thickness (CTh) was processed using Möller et al. 1997 algorithm to compute the distance between the vertex point and the point on the opposite face of the mesh (ie. on the opposite side of the cortical shell, following the opposite direction normal to the surface). If the algorithm succeeds (which may not happen for each vertex, as in the case of extreme spiked surface vertices), the CTh value was inserted into the vertex data. When this rejection condition was met, a NaN (Not a Number) value was inserted into the vertex data. The algorithm implementation is described in Line 4. CTh assessment is presented in Fig. 10.3.

Algorithm 4: Cortical thickness

Input: 3D cortical mesh $\mathcal{M}_{cortical}$
Input: Vertebral body length L_{body}
$N_v \leftarrow$ number of vertices;
for $0 \leq i < N_v$ **do**
  v_i vertex at index i;
  $\vec{N}_i$ normal at the vertex v_i, pointing outward;
  $\vec{N_{inward}} \leftarrow -\vec{N}_i$;
  $I \leftarrow$ intersection point between the line $(v_i, \vec{N_{inward}})$ and any mesh face (Möller et al. 1997);
  if *I exists* **then**
    $t_i = \overline{v_i I}$;
    $t_i^\star = t_i / L_{body}$;
    add $t_i^\star$ in vertex v_i data;
  else
    Invalid cortical thickness;
  end
end

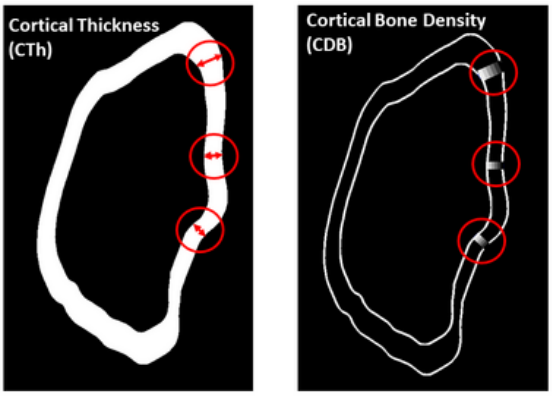

Figure 10.3.: Cortical bone segmentation - Cortical Thickness and Cortical Bone Density

To consider the global size variation between the vertebrae of our sample, the CTh t_n was normalized using measurement (vertebral body length) taken for each vertebral specimen, these measurements were done according to the protocol described in Laporte et al. 2000. In our case, the vertebral body length (Fig. 10.4) was used as the normalization value. Such normalized CTh was denominated t_n^*. The processing of the mesh data was done using OpenMesh library (Botsch et al. 1999).

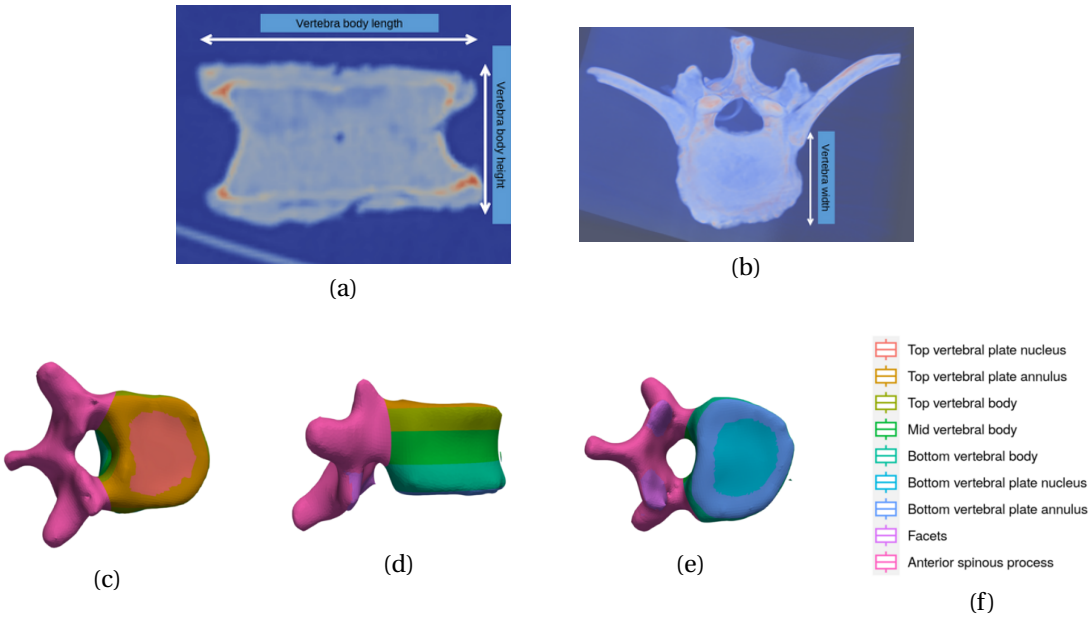

Figure 10.4.: Morphological features of the sample (a-b) and vertebral functional areas (c-f).

The Cortical Bone Density (CBD) was defined as the average density across the cortical shell at each vertex of the triangular mesh. It was processed inside a 0.5 mm radius cylinder going from the vertex towards the intersection with the mesh at the opposite side of the cortical shell. For this purpose, the previously processed Cortical Thickness (CTh) was used and thus, shared the same rejection condition. The algorithm implementation is described in Line 5. CBD assessment is presented in Fig. 10.3.

Algorithm 5: Regional cortical density

Input: 3D cortical mesh $\mathcal{M}_{cortical}$
Input: Density volume D, same reference frame as $\mathcal{M}_{cortical}$
$N_v \leftarrow$ number of vertices;
for $0 \leq i < N_v$ **do**
  if $t_i^\star \neq \varnothing$ **then**
    v_i vertex at index i;
    $\vec{N}_i$ normal at the vertex v_i, pointing outward;
    $\vec{N_{inward}} \leftarrow -\vec{N}_i$;
    $C \leftarrow$ cylinder with base center v_i and radius $0.5mm$, normal $\vec{N_{inward}}$, height $t_i^\star$;
    $C_{cortical} \leftarrow C \bigcap \mathcal{M}_{cortical}$;
    $d_i \leftarrow mean_{C_{cortical}}(D)$;
    add d_i in vertex v_i data;
  else
    Invalid regional density;
  end
end

Validation

Validation of the bone segmentation and CTh was two-fold:

A numerical validation based on custom-made synthetic spheres and cubes was achieved. One 1 cm side cube with a simulated CTh of 1 mm was created, and one 1 cm diameter sphere with a simulated CTh of 1 mm was created. The HU chosen to fill in the cube and the sphere mimicking trabecular bone was 175 HU and were based on measurements of in-vivo individuals. The HU chosen to fill in the simulated cortex was 750 HU and aimed to mimic cortical bone as reported between 500 HU and 1000 HU, also chosen based on in-vivo individual measurements (Nguyen et al. 2021).

The simulated cortical bone was segmented using our previously described algorithm, CTh of the cube and mean CTh of the sphere were computed. This test was used as a unit test for the implementation of the algorithm. As such, the test needed to measure the expected thickness with a 0.05 mm precision for the algorithm to be used on real samples. 3D printed spheres and cubes: 2 spheres of 10 mm diameter with different CTh (0.6 mm and 0.8 mm thickness) were printed using an Ultimaker 3D printer with Tough PLA white RAL 9003 and Infilled supports using PVA with a zigzag pattern. Similarly, 2 cubes of 10 mm side were also created with similar different CTh (0.6 mm and 0.8 mm thickness). Both sets of physical shapes (sphere and cube) were scanned using the identical CT scan with scan parameters as follows: mean spatial resolution of 0.2 mm on the plane, mean slice thickness of 0.5 mm. The shapes were segmented using our algorithm previously described and mean CTh of each physical shape was computed. Relative differences between CTh values from the algorithm

(averaged on the entire shape) and expected thickness of the shape were expressed as percentage of the expected thickness.

Post-processing and statistical analysis

Every vertebra mesh was parted into nine functional areas as described in the paper of Wagnac et al. 2011: as shown in Fig. 10.3. This is based on Fazzalari et al. 2006 in which cortical thickness is investigated within nine sections of vertebrae. This was done using Paraview software (Ahrens et al. 2005).

For each parameter (CTh and CBD), the following statistics and histogram were processed: minimum, maximum, mean, 5th and 95th percentiles. Vertebrae were compared to each other basing on normalized CTh and on CBD. To test the multivariate normality, the Shapiro-Wilk test was used. The MANOVA test was used to assess the data differences between more than two groups, while the Wilcoxon test was used when only two groups were compared. Statistical significance was parted into three levels, using the test p-value ($p < 0.05$: *, $p < 0.01$: **, $p < 0.001$: ***). Statistics were processed using Boost library. Statistical analysis was implemented using Python, with the help of the SciPy (Virtanen et al. 2020) and scikit-posthocs packages.

Boxplot representations were drawn using Python Matplotlib (Hunter 2007) package. The top and bottom bar represent the 25th and 75th percentile (Q_1 and Q_3), while the middle bar is the median (Q_2).

10.2.3. Results

Demographic and morphological characterization of the sample

The demographic description of the sample is shown in Table 10.2. The morphological characteristics of the samples are shown in Table 10.3.

Model	Age	Gender	Vertebral level	Vertebrae (N)	Vertebral body plate area (mm^2)	Vertebral body length (mm)	Vertebral body width (mm)	Vertebral body height (mm)
In-vivo	23	M	High thoracic	3	515.8 ± 38.5	30.5 ± 1.2	21.9 ± 1.4	21.2 ± 0.6
			Low thoracic	3	1022.4 ± 165.7	37.9 ± 4.4	33 ± 1.8	26.1 ± 1.9
			Lumbar	1	1266	43.4	35	30.7
	34	M	High thoracic	3	352.9 ± 234.4	29.7 ± 0.8	20.7 ± 1.2	20.3 ± 0.2
			Low thoracic	3	468.2 ± 299.6	30.1 ± 1	23.4 ± 5.5	21 ± 1.4
			Lumbar	1	1121.2	42.4	31.8	29.2
	43	F	High thoracic	3	401.6 ± 4.6	25.5 ± 1.2	20 ± 0.9	19.6 ± 0.7
			Low thoracic	3	849.5 ± 154.4	34.5 ± 3.1	30.1 ± 2.8	22.2 ± 2.1
			Lumbar	1	1254.2	44.9	35.1	26.3
Cadaver	82	M	High thoracic	3	433.6 ± 175.5	27.8 ± 5.5	23.6 ± 4.7	21.5 ± 0.6
			Low thoracic	3	1027.1 ± 94.8	41.8 ± 4.9	35.5 ± 6.1	25.9 ± 1.3
			Lumbar	1	919.1	43.1	37.5	29.6
	77	M	High thoracic	3	485.9 ± 84.5	27.3 ± 2.7	25.2 ± 2.2	21.5 ± 2.6
			Low thoracic	3	941.6 ± 88.7	47.4 ± 15.3	31.1 ± 2.8	24 ± 2.4
			Lumbar	1	1075	44.8	31.1	27.4
Swine			High thoracic	3	409.2 ± 83.5	29.2 ± 12.9	24.6 ± 6.5	23.3 ± 0.4
			Low thoracic	3	426.9 ± 67.5	33.3 ± 5.5	24.7 ± 5.1	24.4 ± 4.6
			Lumbar	1	482.2 ± 173.8	29.9 ± 4.4	24 ± 1.7	29.2 ± 1.5

Table 10.3.: Morphological characteristics of the sample: mean values ± standard deviation of vertebral end-plate area (mm^2), vertebral body length (mm), vertebra body width (mm), and vertebra body height (mm) by sub-group (i.e. cadaveric vertebrae, swine vertebrae, and human in-vivo vertebrae), and by vertebral levels (i.e. high thoracic, low thoracic, and lumbar).

Validation of the bone segmentation

Using the same dataset and method as the first method (Clinical trials and validation), we found a DICE coefficient of 74.12±5.22. This coefficient is close to the first proposed method (Method).

Validation of the CTh assessment

On numerical validation on sphere and cube, the unit tests passed on the final implementation of the algorithm, which was used to assess the samples. On calibrated 3D printed phantoms validation, absolute CTh values were found of 0.72 ± 0.18 mm for the 0.8 mm cube and 0.59 ± 0.14 mm for the 0.6 mm cube, 0.70 ± 0.22 mm for the 0.8 mm sphere and 0.62±0.26 for the 0.6 mm sphere. The relative differences were 9.4% and 1.6% on cube, and 12.9% and 3.7% on sphere. Our cortical bone segmentation algorithm and computed CTh assessment method were considered reliable.

Local variations of normalized CTh and CBD

Mean values of normalized CTh and CBD by vertebral functional area, by sub-group, and by vertebral levels are shown in Table B.7. Values are expressed as mean ± standard deviation.

Normalized CTh comparison between vertebral body functional area in the human in-vivo group is shown in Table 10.4. The Dunn post-hoc test was used for comparison.

Adjusted p-value (Bonferroni)	Bottom vertebral body	Bottom vertebral endplate nucleus	Bottom vertebral endplate ring	Mid vertebral body	Top vertebral body	Top vertebral endplate nucleus
Bottom vertebral endplate nucleus	0.0052 (**)					
Bottom vertebral endplate ring	1.0	0.0003 (***)				
Mid vertebral body	0.7349	0.9954	0.1289			
Top vertebral body	1.0	0.0212 (*)	1.0	1.0		
Top vertebral endplate nucleus	0.035	1.0	0.003 (**)	1.0	0.1163	
Top vertebral endplate ring	1.0	0.6352	0.2267	1.0	1.0	1.0

Table 10.4.: Normalized CTh comparison between vertebral body functional area in the human In-vivo group. The Bonferroni post-hoc test was used for comparison.
Kruskal-Wallis $\chi^2 = 28.4874$, $p < 1 \cdot 10^{-3}$

CBD comparison between vertebral body functional area in the human in-vivo group is shown in Table 10.5. The Dunn post-hoc test was used for comparison.

Adjusted p-value (Bonferroni)	Bottom vertebral body	Bottom vertebral endplate nucleus	Bottom vertebral endplate ring	Mid vertebral body	Top vertebral body	Top vertebral endplate nucleus
Bottom vertebral endplate nucleus	0.3262					
Bottom vertebral endplate ring	1.0	0.1163				
Mid vertebral body	1.0	1.0	0.8147			
Top vertebral body	1.0	1.0	1.0	1.0		
Top vertebral endplate nucleus	0.0071 (**)	1.0	0.0016 (**)	0.4571	0.0407 (*)	
Top vertebral endplate ring	1.0	0.0168 (**)	1.0	0.1813	1.0	0.0001 (***)

Table 10.5.: CBD comparison between vertebral body functional area in the human In-vivo group. The Bonferroni post-hoc test was used for comparison.
Kruskal-Wallis $\chi^2 = 28.5367$, $p < 1 \cdot 10^{-3}$

Normalized CTh comparison between vertebral functional area in the human in-vivo sub-group is shown in Table 10.6. The Kruskall-Wallis test was used to assess this comparison: $H = 98.006$, $p < 0.001$ (***).

Vertebra area	In-vivo model	
	F	p-value
Top vertebral endplate nucleus	1.1392	0.3421
Top vertebral endplate ring	4.5038	0.02595 (*)
Top vertebral body	12.554	0.0003858 (***)
Mid vertebral body	9.944	0.001233 (**)
Bottom vertebral body	14.194	0.0001995 (***)
Bottom vertebral endplate nucleus	3.7453	0.04365 (*)
Bottom vertebral endplate ring	4.1898	0.03206 (*)
Inferior articular processes	1.077	0.3616
Posterior arch (without inferior articular processes)	3.6859	0.04553 (*)

Table 10.6.: Normalized CTh comparison between vertebral functional area in the human In-vivo sub-group.
Multivariate normality test (Shapiro-Wilk): $W = 0.74657$, $p = 3.845 \cdot 10^{-7}$
MANOVA test:
$F = 5.1173$, $p = 0.0002203$ (***)

Normalized CTh comparison in each vertebral functional area between the human-In vivo sub-group and the cadaveric sub-group, and CBD comparison in each vertebral

functional area between the human in-vivo sub-group and the cadaveric sub-group are shown in Table B.8. The Wilcoxon test was used. In the human in-vivo sub-group, the posterior arch (including inferior articular processes) area was found to have notable lower normalized CTh (Fig. 10.5d, Fig. 10.5e, Fig. 10.5f, Table B.7), and higher CBD (Fig. 10.6d, Fig. 10.6e, Fig. 10.6f, Table B.7) compared to the vertebral body functional areas. Variations were also observed within the posterior arch area excluding the inferior articular processes area (Fig. 10.5a, Fig. 10.5b, Fig. 10.5c, Fig. 10.6a, Fig. 10.6b, Fig. 10.6c).

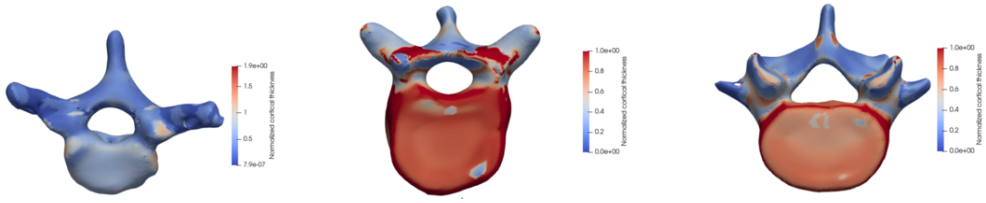

(a) High thoracic vertebra colormap

(b) Low thoracic vertebra colormap

(c) Lumbar vertebra colormap

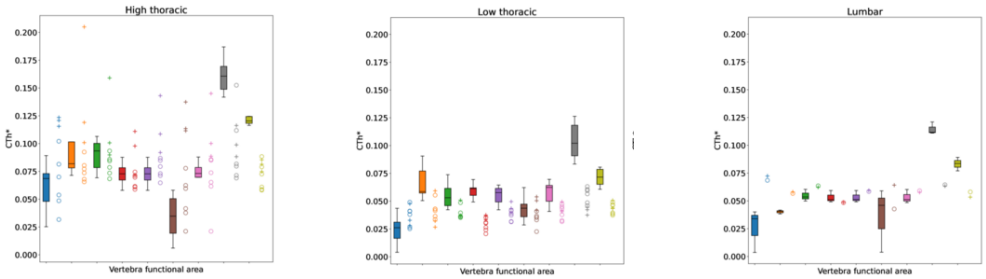

(d) High thoracic vertebra boxplot

(e) Low thoracic vertebra boxplot

(f) Lumbar vertebra boxplot

Figure 10.5.: Normalized Cortical Thickness (human in-vivo sub-group). Boxplot colors as per Figure 10.4.

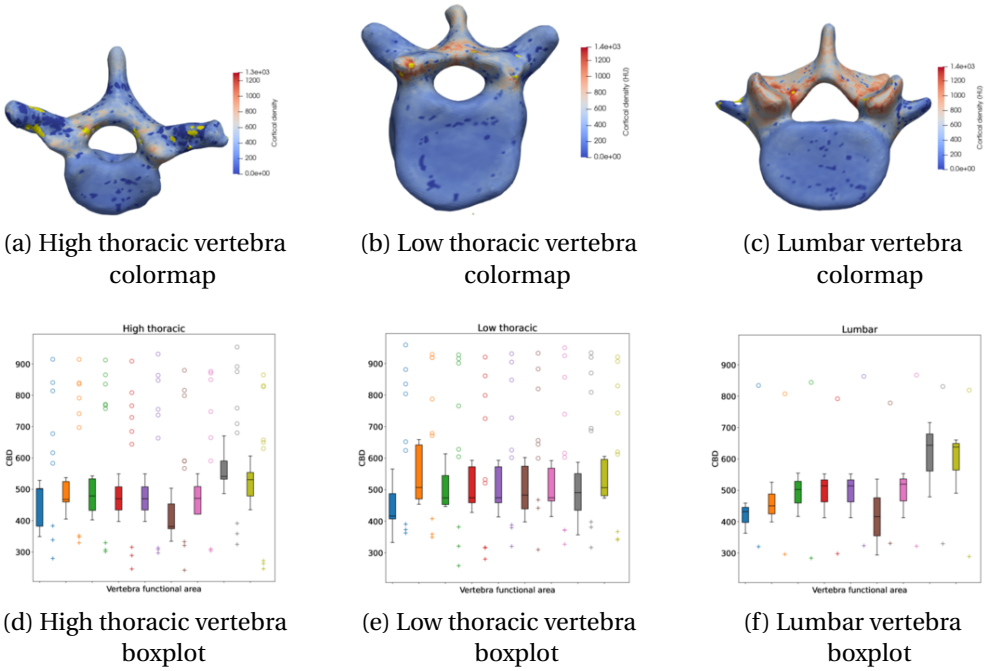

(a) High thoracic vertebra colormap

(b) Low thoracic vertebra colormap

(c) Lumbar vertebra colormap

(d) High thoracic vertebra boxplot

(e) Low thoracic vertebra boxplot

(f) Lumbar vertebra boxplot

Figure 10.6.: Cortical Bone Density (human in-vivo sub-group). Boxplot colors as per Figure 10.4.

In the human in-vivo sub-group, when compared to the inferior articular processes and posterior arch area, normalized CTh (Wilcoxon rank sum test: $W = -7.107, p < 0.001$ *** and $W = -5.286, p < 0.001$ ***) and CBD (Wilcoxon rank sum test: $W = -2.320, p < 0.02$ * and $W = -3.327, p < 0.001$ ***) vertebral body area were found significantly different. In the human in-vivo sub-group, CBD showed almost no difference between the functional areas inside the vertebra body (Kruskal-Wallis $H = 8.626, p < 1e-3$, Table 10.5).

Normalized CTh and CBD comparison between sub-groups

While being significantly different ($p < 0.001$ ***), normalized CTh showed few significant differences when comparing the human in-vivo subgroup and the cadaver sub-group, with only the mid vertebral body (p = 0.029 *), inferior articular processes ($p < 0.001$ ***) and posterior arch ($p < 0.001$ ***) being different. No significant differences were demonstrated between the human in-vivo subgroup and the swine sub-group.

On the contrary, CBD showed significant differences across every functional area when the human in-vivo sub-group is compared to the two other sub-groups ($p < 0.001$ ***).

10.2.4. Discussion

Image segmentation

One of the most challenging aspects of Software as a Medical Device (SaMD) is that it must meet regulatory compliance (Giansanti 2022) otherwise it can't be used in clinical practice. Thus, there is a need to search for methods not only based on AI to get high quality, fast and automated enhanced vertebral segmentation.

Generally speaking, enhanced medical images segmentation is one of the bases of automated medical imaging post-processing. Automated medical images post-processing saves time (Illies et al. 2016, Hardy et al. 2020). Conversely, non-automated images post-processing is deemed tedious (Wade et al. 2013).

In spine surgery, some powerful tools of diagnostic decision-making, prognosis prediction, and treatment planning were described (T. Illés; Tunyogi-Csapó, et al. 2011, T. Illés; Somoskeöy 2013, T. S. Illés et al. 2018). These tools have spread wider if they had been based on automated bone images post-processing (based on enhanced bone segmentation) instead of non-automated bone images post-processing.

Vertebral normalized Cortical Thickness and Cortical Bone Density assessment

Our result showed that normalized CTh and CBD were significantly different between the vertebral body and the posterior arch in the human in-vivo sub-group of our sample.

Literature is limited about CTh and CBD assessment in vertebrae (Silva et al. 1994, Ritzel et al. 1997, Prevrhal; Engelke, et al. 1999, Prevrhal; Fox, et al. 2003, Fazzalari et al. 2006, Odeh et al. 2021). Most of these papers were based on cadaveric studies using micro-CT or histomorphometrical measurements which are not directly usable by physicians in a clinical practice for any enhanced vertebral segmentation purpose.

Only the paper of Odeh et al. 2021 described a variability in CTh and Bone Mineral Density (BMD) assessed using CT scan images within different anatomical regions of cadaveric lumbar vertebrae (i.e; superior articular processes, inferior articular processes, lamina, pedicles, spinous process, transverse processes, and vertebral body). The limitations of this paper are that it only studied lumbar vertebrae and that it was a cadaveric study. Their results were partly consistent with ours: in their study CTh and CBD were higher in some of the posterior arch elements (i.e. inferior articular processes and lamina) than in the vertebral body. Considering pedicles, superior articular processes, spinous process, and transverse processes, CTh and CBD were found to be intermediate between inferior articular processes and lamina on one hand, and vertebral body on the other hand.

Validation of CTh assessment based on CT scan images

CTh assessment based on CT scan images is deemed inaccurate (Silva et al. 1994, Prevrhal; Engelke, et al. 1999, Prevrhal; Fox, et al. 2003, Liebschner et al. 2003, Odeh

et al. 2021). CT scan seems to overestimate vertebral body CTh (Silva et al. 1994, Prevrhal; Fox, et al. 2003, Liebschner et al. 2003). But these papers were based on simple thresholding and manual contouring in a single slice to measure CTh. Our results were found to be accurate (Validation of the CTh assessment). Our results are automated and based on CT scan images. They could be extrapolated to clinical use.

Usefulness of cadaveric model and swine model in the study of normalized CTh and CBD

Our results showed that cadaveric vertebrae and swine vertebrae were not good models for normalized CTh and CBD study as normalized CTh and CBD were significantly different between the human in-vivo and cadaveric or swine samples. This may come from the conservation processes of dead tissue.

Limitations

The main limitation is the low number of subjects included in the study. Another limitation is the relatively low resolution (about 1 mm) of the scans which decreases the precision of the normalized CTh assessment. In most CT scans, the resolution (distance between two voxels, in the three directions X, Y, Z) usually is about the same magnitude order of the typical cortical thickness (about 1 mm to 2 mm). Moreover, the Z axis slices are usually overlapping, meaning that the density value along this axis is impacted.

10.2.5. Conclusion

it has been shown that normalized CTh and CBD values were influenced by the vertebral level as well as by the sample sub-group (human in-vivo vs swine vs human cadaveric). Moreover, the vertebral functional areas had a strong impact on normalized CTh and CBD.

Thus, this method could be used to explore cortical bone geometry and quality in an automated and non-invasive way, opening possibilities for clinical applications.

11. Assessment of the difference between supine and prone position (Giorgi et al. 2023)

11.1. Introduction

To overcome tricky and time-consuming registration/calibration procedures, hypothesizing that the change of vertebral orientation between the supine position and the prone position was small enough (Brink; Colo, et al. 2017) to fit angular precision requirement, PYTHEAS NAVIGATION has developed the concept of global calibration. Nevertheless, some information were lacking in the literature to establish a scientific rationale for the global calibration procedure, and one was the the assessment of change of vertebral orientation, between the supine position and the prone position. As the PYTHEAS NAVIGATION medical device objective is to be minimally invasive for the patient ant the surgeon, it was important to develop a model for these changes that does not require an additional device or process during the surgery (as with concurrent product, like the Mazor system from Medtronic).

To our knowledge, there is no assessment in the literature of the changes in the vertebral orientation between what is shown on preoperative CT (made in the supine position) and what is seen when the patient lies prone on the operation table during the surgery. Our aim was to assess the change of vertebral orientation, defined as 3D vertebral rotation expressed in the sagittal plane, in the transversal plane and in the frontal plane, at each level from T_1 to S_1 between the supine position (like in in a CT scan) and the prone position lying on bolsters like in an operating room (Fig. 11.1).

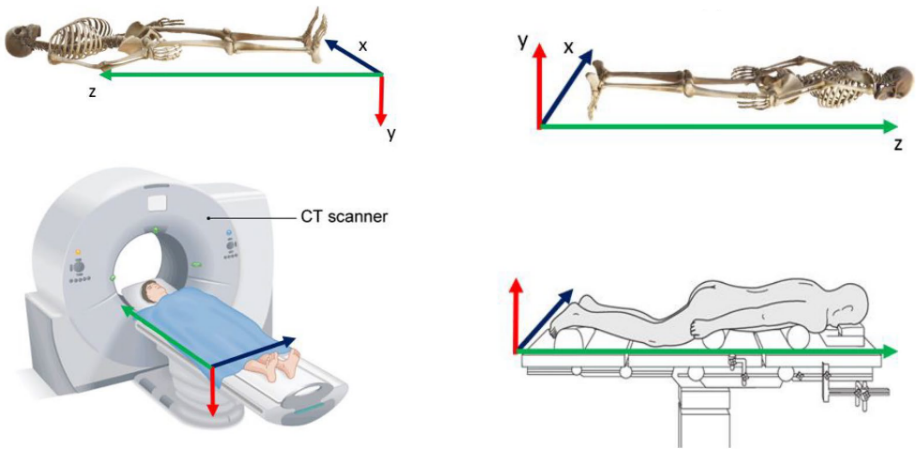

(a) Vertebral orientation in the supine position like in in a CT scan.

(b) Vertebral orientation in the prone position lying on bolsters.

Figure 11.1.: Difference of vertebral orientation between the preoperative CT scan and the operating room

I had the opportunity to contribute to both the computational and methodological dimensions of this research. On the computational side, I assisted in developing and refining the workflow for analyzing our experimental data. This involved tasks like designing data processing pipelines, working with specialized software, and scripting to automate complex analyses. My aim was to help ensure that we could extract accurate and reliable data, enabling the team to draw sound conclusions. Furthermore, I collaborated with the team in shaping the overall research methods. Through discussions, we defined the analytical strategy, selected appropriate statistical techniques, and decided on effective ways to visualize and interpret our findings. My contributions, both in the computational workflow and methodological design, aimed to support the scientific rigor and validity of the study.

11.2. Material and methods

11.2.1. Dataset

In view of the retrospective nature of the study and all the procedures being performed were part of the routine care. Paired preoperative CT scans and intraoperative Cone Beam Computed Tomography (CBCT) scans were selected from an anonymized database, acquired between 2016 and 2021.

The criteria for patient inclusion were:

- Spinal pathology undergoing a posterior fusion procedure
- Skeletally mature (DiMeglio et al. 2011, Dimeglio et al. 2012, Dimeglio et al. 2013) at time of surgery

- Preoperative CT scan (for intraoperative navigation purpose) available, with patient in supine position
- Intraoperative CBCT scan available, with patient in the prone position according to the AO recommendations with bolster support under the sternum, iliac crest, and the lower legs, with hips and knees in slight flexion, after induction of general anesthesia (Fig. 11.2)
- Non-instrumented vertebral levels visible on the intraoperative CBCT scan
- CBCT scan done before reduction/rod insertion available



Figure 11.2.: Patient in the prone position according to the AO recommendations with bolster support under the sternum, iliac crest, and the lower legs, with hips and knees in slight flexion.

The criterium for exclusion was an incomplete dataset.

In this study, patients were not exposed to any additional radiation, as in the standard procedure in our institution, a preoperative CT scan and an intraoperative CBCT scan are routinely performed. For each patient, preoperative CT scan and intraoperative CBCT scan radiation exposure, expressed in mSv, were extracted from the database. For each patient, informed consent was obtained from the patient, or from a parent or a legal guardian for participants younger than 18 years old. After the patient was discharged from the hospital, their parent or legal guardian for participants younger than 18 years was informed that his total radiation exposure during the preoperative workup, during the surgery, and during the postoperative period was available on request, as required in every patient by the local health authority.

11.2.2. Data processing

The processing of the data was done as followed: a single trained observer (Yann Glard, MD.) used the semi-automatic image processing technique and software 3D slicer (Fedorov et al. 2012), with a custom-made Python script add-on (Fig. A.4).

For each patient, paired preoperative CT scan and intraoperative CBCT scan were processed with 3D slicer to acquire complete spinal reconstructions in a consistent 3D coordinate system. The anatomical coordinate system is a continuous 3D space in

which an image has been sampled. The consistent 3D coordinate system used in this study was the commonly used LPS frame (Anatomical reference frame).

Step 1: Segmentation and entry point/pedicular direction identification

Thresholding as a method of segmentation was applied to get 3D surface of posterior aspect of the spine. The criterion used to set the segmentation threshold was to get a surface deemed representative of bone surface in real-life surgery. This criterion was only visual. For each pedicle, at each vertebral level included, on both preoperative 3D reconstruction and intraoperative 3D reconstructions, the entry point was selected on the 3D surface and the pedicular direction was set as shown in Fig. 11.3.

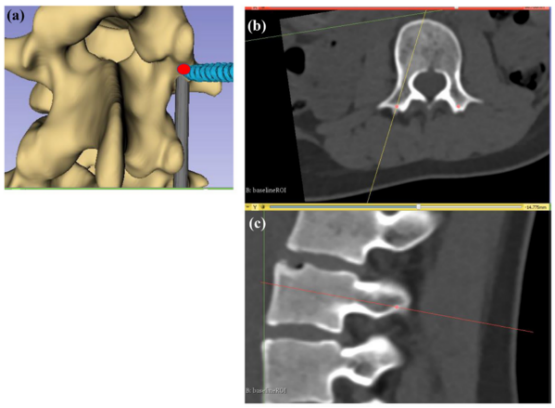

Figure 11.3.: Segmentation and entry point/pedicular direction identification
(a) 3D reconstruction of the spine
(b) The entry point was selected on the 3D surface
(c) The pedicular direction was set.

As for segmentation, criteria were only visual, and special care was taken to select the same entry points and pedicular directions between preoperative and intraoperative images. The outcome of this step was a set of points (entry points) and orientation vectors (pedicular directions), that were further used to assess vertebral rotations for method 1, and to find sagittal and transversal slices for method 2.

Step 2: Sagittal, transversal and frontal angle variation processing

This step aimed at automatically compute the first set of sagittal, transversal, and frontal rotations of each vertebral level of the same patient, using 3D slicer. This first method was based on purely geometrical processing, based on entry points and pedicular directions. The feature of automated geometrical processing of 3D slicer software was used to compute rotations, as follows:

- Sagittal angle: The sagittal angle of the pedicle was defined as the projection onto the sagittal plane of the pedicular direction. The sagittal angle of each pedicle

was computed (left and right) by the software, for the same level in supine and prone cases. The variation of sagittal angle of the vertebra between supine and prone was defined as the variation between left and right average value of the sagittal angle of the two pedicles. It was named **Method 1 — Sagittal angle result** and expressed in deg. As a convention, a positive value meant a change toward flexion.

- Transversal angle: The same method was applied: The transversal angle of the pedicle was defined as the projection onto the transversal plane of the pedicular direction. The transversal angle of each pedicle was computed (left and right) by the software, for the same level in supine and prone cases. The variation of transversal angle of the vertebra between supine and prone was defined as the variation between left and right average value of the transversal angle of the two pedicles. It was named **Method 1 — Transveral angle result** and expressed in deg.

- Frontal angle: The variation of the frontal angle of the vertebra was defined as the variation of the frontal angle of the orientation of the segment between the two entry points projected onto the frontal plane. It was named **Method 1 — Frontal angle result** and expressed in deg.

The limitation of this method is that its accuracy relies on the ability of the operator to precisely define repeatable entry points and pedicular directions. It was then intended to improve the results quality by adding a visual control that checks if the angular matching is acceptable, and by the same time adjusts more accurately the rotation angles. Method 2 is derived from the process detailed in step 3..

Step 3: Sagittal and transversal section extraction

The goal was to give the operator a superposition of slices of the same vertebral level, from supine and prone images, with some level of transparency, so the operator could adjust manually relative position and rotation to get a matching of the cortical shell of the vertebra (Fig. A.5). The resolution of the angular increment for matching paired vertebrae was at 0.5°.

The output of this analysis was the rotation angle. The operator could also decide to discard the level if the matching was unsuccessful. The reasons for discarding the level can be poor image quality, or bad slice selection. This method was not applied for frontal angle. A set of tools coded in Python has been developed specifically for this processing.

Step 4: Sagittal and transversal angle variation processing

The matching of paired vertebrae was done with the python script. The visual registration process provided the rotation of the vertebra in the sagittal plane (defined as **Method 2 — Sagittal angle** result) and in the transversal plane (defined as **Method 2 — Transversal angle** result) expressed in deg.

11.3. Results

The output parameters were: **Method 1 — Sagittal angle result, Method 1 — Transversal angle result, Method 1 — Frontal angle result, Method 2 — Sagittal angle result, Method 2 — Transversal angle result, Radiation exposure.**

Thirty-six patients were selected and included for a total number of 148 vertebral levels (Fig. 11.4). There were 30 females and 6 males. The mean age was 15 years and 9 months (ranging from 11 years and 11 months to 27 years and 4 months; standard deviation 3.13). There were 31 adolescent idiopathic scoliosis, 2 early onset scoliosis at the age of skeletal maturity, 2 Scheuermann's kyphosis, and 1 neuromuscular scoliosis in cerebral palsy. Preoperative CT scans were done in various institutions (hospitals or external radiology centers). Intraoperative CBCT scans were obtain using GE Discovery Hybrid IGS 730 OR.

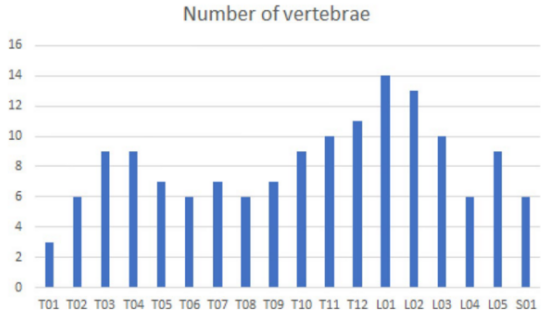

Figure 11.4.: Distribution of vertebral levels analyzed.

Method 1

148 levels were evaluated. Except for T_1 (with three samples), at least six vertebrae were analyzed per level from T_2 to S_1. Results are shown in Table B.2, Table B.3, Table B.4 and Fig. A.6.

Method 2

For the sagittal rotation, 144 levels were evaluated. Except for T_1 (with three samples), at least six vertebrae were analyzed per level from T_2 to S_1. Compared to the 148 levels of method 1, four levels were discarded at matching, because of poor quality images.

For the transversal rotation, 140 levels were evaluated. Except for T_1 (with three samples), at least five vertebrae were analyzed per level from T_2 to S_1. Compared to the 148 levels of method 1, 8 levels were discarded at matching, because of poor quality images.

Results are shown in Table B.5, Table B.6 and Fig. A.7.

Comparison between methods

Figure 11.5 provides a comparison between method 1 and method 2 distributions of standard deviations per level.

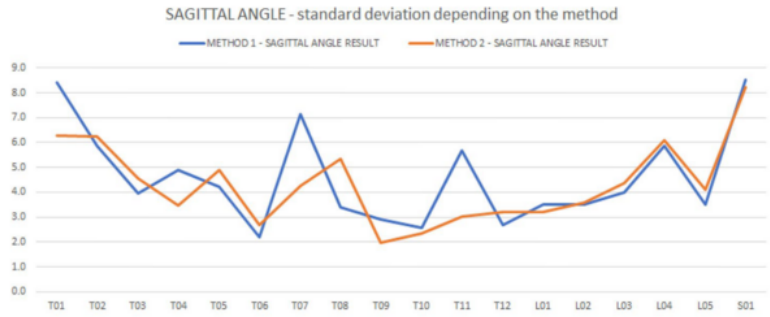

(a) Sagittal angle comparisons

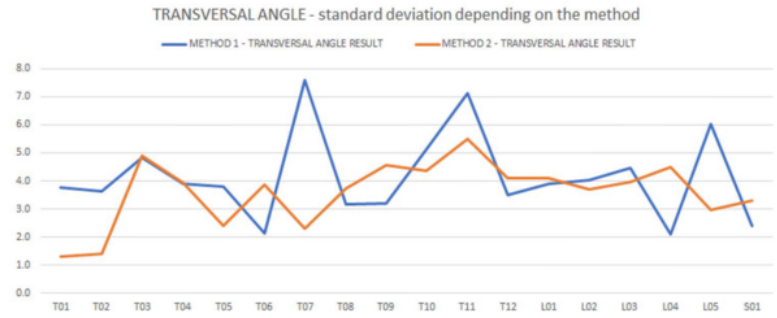

(b) Transversal angle comparisons

Figure 11.5.: Comparison between the two methods.

Changes of vertebral orientation in the sagittal plane, the transversal plane, and the frontal plane, at each level from T_1 to S_1 between the supine position (like in a CT scan) and the prone position lying on bolsters like in an OR were significant. In the sagittal plane, our results tend to indicate that the magnitude of the changes strongly depends on the vertebral level. It was less clear in the transversal and in the frontal plane.

Radiation exposure

The mean total preoperative CT scan and intra-operative CBCT scan radiation exposure was 20 mSv. The mean preoperative CT scan radiation exposure was 7 mSv. Between 2016 and 2018, we used conventional preoperative full-spine CT scan for planning and navigation purpose. Between 2018 and 2021, we used preoperative Ultra Low-Dose CT (ULDCT) scans for planning and navigation purpose. The mean radiation exposure generated by preoperative ULDCT scans was 2.8 mSv. The mean intra-operative CBCT scan radiation exposure was 13 mSv.

11.4. Discussion and conclusions

First, it must be said that radiation exposure in spine surgery, especially in spine deformity management, is a major issue: patients who were diagnosed and monitored for scoliosis have increased risk of breast cancer, endometrial cancer, thyroid cancers, leukemia, and heritable defect, clearly related to radiation exposure from diagnostic radiographs (Ronckers et al. 2010, Bone et al. 2000, Simony et al. 2016). To control and reduce the radiation exposure, the standard of care of perioperative workup of adolescent idiopathic scoliosis is well defined in the literature. Preoperatively, it is recommended to get a full-spine upright coronal X-ray, a full-spine upright sagittal X-ray, a full-spine left supine bending, and a full-spine right supine bending (Lenke; Betz; Bridwell, et al. 1998, Lenke; Betz; Haher, et al. 2001, Lenke; Betz; Harms, et al. 2001, Lenke; Betz; D. Clements, et al. 2002). Intraoperatively, it is still controversial whether a fluoroscopy or a 3D imaging, with or without navigation, is recommended (Duke et al. 2022, Y. J. Kim; Lenke, et al. 2004, Suk 2011). It has been shown that 3D imaging reduces complications and reoperations in Saarinen et al. 2022. Intraoperative 3D imaging is commonly achieved using CBCT. CBCT systems are fluoroscopy units with scintillation counters. They can reconstruct 3D images in the DICOM format. This technology was first used in dentistry in Arai et al. 1999. After oral surgery, radiation therapy, then interventional radiology and cardiology, and finally, orthopedic surgery have adopted this technology. The advantages of CBCT over CT are the possibility of producing true-size 3D images more quickly, generating 2D projections, consuming less energy, being less costly, allowing simple manipulations without specialized operators, allowing concurrent use of an image intensifier in the operating suite (Tonetti et al. 2020).

A meta-analysis showed that there was no statistically significant increase in radiation between usage of intraoperative CTCB versus freehand technique (Baldwin et al. 2022). In the study of Duke et al. 2022, the perioperative workup of a patient surgically treated for AIS generated a radiation exposure of 39 mSv. In his study, intraoperative fluoroscopy and immediate postoperative conventional CT scan accounted for 23 mSv. Postoperatively, it is recommended to get a full-spine upright coronal X-ray and a full-spine upright sagittal X-ray. In our protocol, the mean radiation exposure during the perioperative period was 20 mSv: 7 mSv preoperatively for planning and navigation purpose, and 13 mSv preoperatively for hardware position checking. Between 2016 and 2018, we used conventional preoperative full-spine CT scan for planning and navigation purpose. Between 2018 and 2021, we used ULDCT scans for planning and navigation purpose. In our study, the mean radiation exposure generated by ULDCT scans was 2.8 mSv. During the whole study, intraoperative CBCT was used to identify any screw malpositions. It is within the limits of the standard of care of perioperative workup of adolescent idiopathic scoliosis: it is below the upper limit of safety, 50 mSv per year, as proposed by both the Nuclear Regulatory Commission, reported by Presciutti et al. 2014 and the Occupational Safety and Health Administration (OSHA) (Law et al. 2016). While this is within safe limits, clinical decisions that diminish the amount of radiation exposure according to the As Low As Reasonably Achievable (ALARA)

principle should continue to be made to enhance patient safety. The use of ULDCT scans instead of classical CT scans is crucial. With ULDCT, a full-spine examination generates a radiation exposure between 0.4 mSv and 3 mSv (Abul-Kasim; Overgaard, et al. 2009, Abul-Kasim 2010, Kalra et al. 2013), comparing favorably with a classical CT scan that generates a radiation exposure of 12 mSv to 14 mSv. This has been exposed to our local IRB, and this protocol became the standard of care in our institution since 2016. This study falls within the scope of the French Reference Methodology MR-004 (Commission Nationale de l'Informatique et des Libertés 2018) and was approved by the institutional and ethical review board of the Saint Joseph Hospital of Marseille (December 8th 2020).

Virtual templating in spine surgery for Pedicle Screw (PS) insertion is a concept combining preoperative planning and freehand surgery. It has been described in 2011 by Abe et al. 2011 and in 2016 by X. Zhao et al. 2016. Virtual templating is a simple and cost-effective technique; it is popular because it only requires a picture archiving and communication system (PACS) to be achieved. In the PACS, the surgeon reconstructs a 3D model of the spine. The surgeon preoperatively selects for each pedicle (in each vertebra) the optimal entry point and direction of PS and the correct size of PS. As highlighted by Xin Zhao et al. X. Zhao et al. 2016, one of the limitations of this method is that the pedicle direction is shown on preoperative CT (made in the supine position) while patients lie prone on the operation table during the surgery: the actual position of the spine during surgery is not the same as that of the virtual spine on the preoperative CT. This leads to the difficulty in accurately following along the pedicle direction. Brink; Colo, et al. 2017 disclosed the same issue in their 2017 paper. In the PYTHEAS NAVIGATION Global calibration mode, this issue is also critical. Some authors have described the changes in spine position depending on if the patient lies prone (like during surgery) or supine (like during a CT scan): Yasuda et al. 2018 evaluated the radiographic data of 85 adult spinal deformity patients who underwent posterior corrective fusion surgery from the thoracic spine to L_5, S_1, or the ilium. Lumbar Lordosis (LL) was evaluated in the supine position preoperatively and in the prone position on the surgical frame. Changes in LL were assessed. The difference between supine LL and prone LL was within 5°. Changes in the transversal plane and in the frontal plane were not assessed. The series was made of adult patients with spine deformity, with a lumbar segment potentially stiffer and less mobile than younger patients (Kapandji 1969). Brink; Colo, et al. 2017 compared the coronal, axial, and sagittal morphology of the scoliotic spine in three different body positions (upright, prone, and supine) and between three different imaging modalities (X-ray, CT, and MRI) in 62 adolescent idiopathic scoliosis (AIS) patients. X-rays were made in the upright position, CT scans were made in the prone position, and MRI scans were made in the supine position. In all three positions, Thoracic Kyphosis (TK), Lumbar Lordosis (LL), and transversal vertebral rotation at the apical level were determined. The thoracic and lumbar apical vertebral rotation showed a good correlation among three positions (less than 3.6 deg). The TK and LL correlated well among three different positions (less than 5.1 deg). Even if it was described precisely in this paper, in another paper based on the same database (Brink; Homans, et al. 2020), the authors mentioned

that because of the limited space in the CT scan, the intraoperative pads or pillows were not used. Transversal rotation in non-apical levels was not assessed. Our aim was to assess the change of vertebral orientation at each level between the supine position and the intraoperative prone position lying on bolsters in the sagittal plane, in the transverse plane, and in the frontal plane and, in a population of surgically treated patients. As our results showed, the changes were significant.

Sagittal analysis

The results showed a behavior in the evolution of rotation depending on the level. Between T_1 and T_{10}, the rotation was between $-14°$ and $-8°$, in a rather small evolution. Between T_{10} and L_5, the sagittal rotation increased from $-10°$ up to $10°$ in a clear behavior. The relatively low standard deviation indicated that this behavior was repeatable among the cases. This also indicated that L_1 and L_2 were neutral levels: their sagittal attitude during prone or supine posture was equivalent.

Transversal analysis

Between T01 and T08, the average rotation was negative down to $-4°$. Between T_9 and S_1, the average rotation was close to $0°$. This indicated that the laterality was not uniform in the studied population. The overall rotation in transverse plane was considered low, and mainly driven by interindividual variations (standard deviation driven).

Frontal analysis

Results were available from method 1 only. It tended to indicate that there was not much rotation variation in average. We think that these results could be valuable to perform a safe virtual templating: the information given by the virtual templating seems to be more accurate in the transversal plane than in the sagittal plane. Some additional work is needed to know how far a surgeon placing pedicular screws could rely on preoperative planning based on preoperative (supine) CT scan; pedicle biometry should be considered and tolerance in angular error should be considered. The work from Rampersaud et al. 2001 suggests that extremely high accuracy is necessary to place pedicle screws at certain levels of the spine without perforating the pedicle wall. Conversely, other papers suggest that a certain tolerance in angular angle is allowed without perforating the pedicle wall (Karaikovic et al. 2001, Vialle et al. 2014, Viau et al. 2002, Yingsakmongkol et al. 2007). Overall, human ability to estimate an angle should be considered. Baba et al. 2020 showed that the human ability to estimate an angle could be with an error up to 6°.

12. Assessment of the limits of the surgeon maneuver (Leblond; Yves Godio-Raboutet, et al. 2023)

12.1. Introduction

To ensure a surgery planning can guarantee the safety of the patient, it is primordial to assess the limits of the main phase of the surgery: the pedicle cannulation. This critical step, involving the precise insertion of a drill or probe into the pedicle of a vertebra, forms the foundation for secure pedicle screw placement. However, it is inherently a procedure reliant on surgeon experience and tactile feedback, making it susceptible to a range of potential errors. Understanding these limitations is not merely an academic exercise; it is a fundamental prerequisite for developing robust and reliable surgical planning tools.

The consequences of inaccurate cannulation are significant, ranging from minor complications to severe patient injuries. Breaches of the pedicle cortical wall can damage delicate neurovascular structures, leading to devastating outcomes such as paralysis or hemorrhage. Furthermore, the reliance on tactile feedback introduces variability, potentially hindering the exploration of optimal screw trajectories and limiting the achievement of maximum screw purchase. Therefore, a thorough examination of the cannulation process, its challenges, and its limitations is crucial for enhancing patient safety and optimizing surgical outcomes. This chapter delves into these aspects, aiming to provide a comprehensive understanding of the cannulation process and its implications for surgical planning and patient safety.

Two information were lacking in the literature to establish a scientific rationale for the PYTHEAS NAVIGATION pedicle cannulation assistance:

- The acceptable tolerance angle for a safe pedicle cannulation.
- The assessment of the entry point offset between the planed entry point and the actual entry point.

These two topics were also thoroughly explored by our team in Leblond; Godio Raboutet, et al. 2024 and in an abstract by Yves Godio-Raboutet presented in the 2022 Computer Methods in Biomechanics and Biomedical Engineering annual symposium.

My role in these articles involved supporting the research from its conceptualization through to its execution. I participated in the design of the experimental protocols, contributing to discussions with the team to define study objectives, choose appropriate methodologies, and set up robust parameters for data collection and analysis. My input helped to ensure the experimental design was both scientifically sound and ethically compliant.

Crucially, I also provided the computational expertise and infrastructure needed for the segmentation and measurement tasks. This meant developing and implementing algorithms and workflows for processing medical imaging data, particularly CT scans. By accurately segmenting vertebral structures and precisely measuring key parameters such as cortical thickness and vertebral dimensions, I aimed to provide the objective, quantifiable data that underpinned the research findings and enabled meaningful conclusions.

12.2. Assessment and validation of the incertitude of tolerance angle in synthetic bones

12.2.1. Introduction

Pedicle screw insertion is one of the most practiced procedure in spinal surgeries (Liu et al. 2021). Prior to any screw implantation, surgeon first performs a cannulation of the pedicle with a specific tool during which he self-adapts the cannulation tool motion using tactile feedback. The perception of the difference between trabecular bone and cortical bone influences the accuracy of pedicular cannulation and screw placement as it guides the surgeon along the pedicle to reach the intended axis. When the surgeon feels a resistance, sign of contact with the vertebral cortical shell, he changes the trajectory of the perforation tool and he lets the tool slip against the cortical shell to avoid any cortical wall perforation. This was thoroughly described in the literature (Gaines 2000, Y. J. Kim; Lenke, et al. 2004, Suk 2011 Vialle et al. 2014). Accurate placement of pedicle screw is a real issue as it is associated with 2 to 22.4% chances of perforation of the cortical shell (N. Li et al. 2015). To optimize this medical intervention based on the surgeon experience, a pre-surgery planning is recommended as it saves time and causes less critical cases resulting in heavy damages for the patient (Vaccaro; J. A. Harris, et al. 2020). Such planning tools aimed at providing computation of the angle for screw insertion are based on mathematical analysis without consideration of surgeon perception (Rampersaud et al. 2001. Screw insertion techniques have been widely described in the literature. The free-hand insertion technique (Folkestad; Groth, et al. 2020, Swaminathan et al. 2020) is based on anatomical landmarks identification to choose an entry point and determine the trajectory by feeling intraosseous differences between cortical bone and cancellous bone inside the pedicle(Y. J. Kim; Lenke, et al. 2004). The ideal location of the entry point on the posterior surface of the vertebral lamina has been the subject of different descriptions and is still controversial (Abe et al. 2011, Chung et al. 2008, H. Modi et al.

2009, Swaminathan et al. 2020). To ensure correct and safe pedicle cannulation, the trajectory definition down inside the pedicle is also crucial. It has been highlighted that both the entry point and the trajectory within the pedicle depend on the spinal level, patient-specificity of the pedicle morphology and spine orientation (Brown et al. 2010, H. Modi et al. 2009, Chung et al. 2008, Y. Zhang et al. 2014).

Bone quality strongly influences the mechanical behaviour of bone tissue during the pedicular cannulation procedure and the screw insertion procedure (Cook et al. 2004, Cornaz et al. 2022, Makaram et al. 2021, Swaminathan et al. 2020), and needs to be considered. During the cannulation procedure, the influence of bone quality mostly depends on surgeons perception as well as on the force required to be applied for trabecular bone cannulation on the cannulation tool. It is to relate to the bone microarchitecture and patients age and gender. Consideration of bone quality has been described extensively in a biomechanical perspective through pedicle screw pull-out studied and specific compression tests associated with in-vivo density measurements. Relationship between Young modulus and apparent bone density have been described as being correlated to modulus and compressive yield stress (Morgan; Unnikrisnan, et al. 2018) citing (Morgan; Bayraktar, et al. 2003, Morgan; Keaveny 2001).

The main objective of this study was to characterize the cannulation process and to determine a tolerance angle between the surgical tool and the cortical pedicle shell during the cannulation procedure (prior to any pedicle screw insertion) while considering different material densities. This work offered an experimental and reproducible cannulation protocol using a standard surgical cannulation tool to identify the maximal angle for which the perforation tool slips on the cortical shell without damaging it.

12.2.2. Material and methods

This work reported 1. the experimental simulation of the pedicle cannulation by the cannulation tool in a synthetic model of pedicle, 2. the characterization of the trabecular-cortical transition with perforation and sliding on cortical shell, and 3. the definition of the critical angle between cortical shell and cannulation tool for perforation

Two synthetic materials were assembled to design bi-components cylinders reproducing transition between trabecular and cortical bones (Fig. 12.1). Special care was given at the transition.



Figure 12.1.: Cylindrical samples: Cylinder without epoxy (left) and with epoxy (right).

Creaplast foam (Generic block, Solid foam, Creaplast, Verton, France) was chosen as the cortical bone surrogate. The trabecular bone was represented by three rigid polyurethane foams from Sawbone (Block, Solid foam PCF5, PCF10 and PCF20, Sawbones Europe AB, Malmö, Sweden) with different densities and one Creaplast foam. Foams characteristics provided by the manufacturers are given in Table 12.1.

Properties	Unit	PCF20	PCF10	PCF5	Creaplast
Young's modulus (tension)	MPa	284	86	32	
Young's modulus (compression)	MPa	210	58	16	
Shear modulus	MPa	49	19	7.1	
Tensile strength	MPa	5.6	2.1	1.0	
Compressive strength	MPa	8.4	2.2	0.6	3.8
Shear strength	MPa	4.3	1.6	0.59	
Density	$g\,cm^{-3}$	0.32	0.14	0.8	0.249
Hardness ISO 868-2003	Shore D				25
Flexural strength ISO 168-2010	MPa				5.4

Table 12.1.: Table of mechanical properties of the used synthetic materials given by the manufacturers materials guides

Cylinders were shaped to have a 17 mm diameter. Both material sections were stuck together using a thin layer of glue (Cyanoacrylate, Loctite). A design of experiment on synthetic materials samples was reported in Table 12.2. Cannulation angles of 10°, 15°, 20°, 25° and 30° were tested. In the table, the cannulation angle was called the β angle.

	PCF5			PCF10			PCF20			CC			All		
β (°)	N	Perf. (N)	Perf. (%)	N	Perf. (N)	Perf. (%)	N	Perf. (N)	Perf. (%)	N	Perf. (N)	Perf. (%)	N	Perf. (N)	Perf. (%)
10	5	0	0	5	0	0	3	0	0	4	3	75	13	0	0
15	4	1	25	3	0	0	4	0	0	2	2	100	11	1	9.1
20	4	3	75	3	3	100	4	1	25	1	1	100	11	7	63.6
25	2	2	100	2	2	100	2	2	100	1	1	100	6	6	100
30	3	1	33.3	1	1	100	2	2	100	1	1	100	6	4	66.7
All	18	7	38.9	14	6	42.8	15	5	33.3	9	8	88.9	47	18	38.3

Table 12.2.: Table of experiment on synthetic materials samples with cannulation angles (β) of 10°, 15°, 20°, 25° and 30°

12.2.2.1. System setting and perforation testing

The cannulation tool selected from the regular surgical toolkit had a slightly curved tip (Fig. 12.2).



Figure 12.2.: Cannulation tool with curved tip

All tests were performed on an MTS Acumen 3 A/T electrodynamic test system (MTS Systems corporation, Minnesota, USA) composed of an MTS Flextest 40 controller (frequency of 100 Hz) and servo actuator controlled using Test Suite Multipurpose Testing Software (MPE). Two load sensors were used: the MTS Acumen 3 axial/torsion (MTS System corporation, Eden Prairie, Minnesota, USA) and a triaxial load sensor (9317C – range ± 3000 N - Kistler, Winterthour, Swiss) installed at the top of the cannulation tool. The cannulation tool motion was then controlled in displacement and rotation. The cylinders were then positioned under the cannulation tool, guided by two fixation parts and enabling rotation between the test in order to precisely control the angle between the surgical cannulation tool and the transition between foam mimicking trabecular bone and foam mimicking cortical bone (Fig. 12.3). The initial position of the cannulation tool was set for the tool to be parallel to the line of transition between the two types of foams.

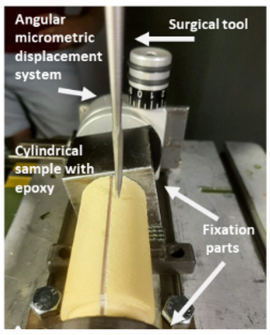

Figure 12.3.: Cylinder positioned under the cannulation tool, guided by two fixation parts enabling rotation between the tests in order to precisely control the angle between the surgical cannulation tool and the transition between foam mimicking trabecular bone and foam mimicking cortical bone.

To control the experiment during the tool positioning and the cannulation or perforation, two cameras were set (Miro camera, C110, Vision Research, Wayne, New Jersey, USA). Samples were positioned to the entry point thanks to a biaxial and circular positioning tables (21161-10-08, Norelem, Fontaine-les-Grès, France), enabling rotation of the samples according to the expected computed angles (Fig. 12.4).

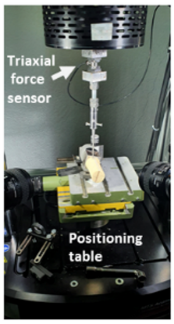

Figure 12.4.: Controlled rotation of the samples according to the expected computed angles.

The test procedure consisted in a simplified version of the surgical cannulation tool motion during cannulation of the pedicle before pedicle screw insertion. The movement of cannulation was decomposed into three rotations (100°, 100° and 60°) coupled with three translations (10 mm, 10 mm and 6 mm) insuring a constant boring speed of $10\,^{\circ}\,\mathrm{mm}^{-1}$. The device was pulled out reversing angle values (translation and rotation) with similar speed in order to prevent any material damage due to cannulation tool extraction.

12.2.2.2. Post-processing

Measurements of the cannulation tool displacement and angle, the torque and the X, Y and Z components of the force were recorded during the whole cannulation procedure

(Fig. 12.5).

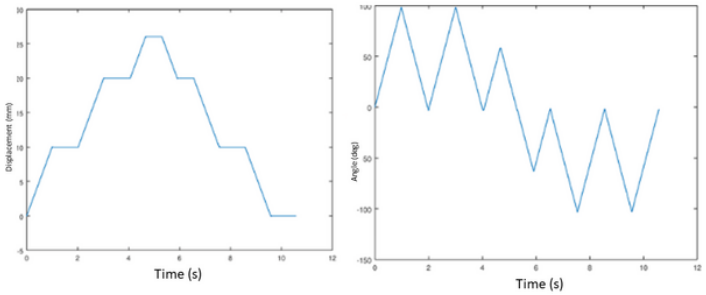

(a) Measurements of the cannulation tool displacement and angle during the whole cannulation procedure.

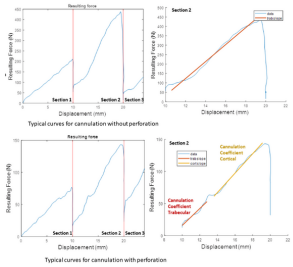

(b) Typical cannulation curves with and without perforation.

Figure 12.5.: Cannulation procedure measurements

A custom-made Matlab (MATLAB Release 2020b, The MathWorks, Inc., Natick, Massachusetts, United States) code was used to post-process the data. The raw signal was filtered by a low pass filter with a frequency determined using a Fast Fourier Transform. The resulting data were divided into three sections depicting the three parts of the cannulation process. On each of these sections, two cannulation coefficients (cc) were computed by the linear slope between two points manually chosen for each of the subsections of the signal. The choice was made depending of the cannulation tool position, either one defining the foam surrogate for trabecular bone (cc_{trab}) or one defining the foam surrogate for cortical bone (cc_{cort}).

In case of perforation or degradation of the line of transition between the two type of foams, the critical point was graphically found and cc_{trab} and cc_{cort} were computed in the corresponding sub-section. If the test was performed without perforation or degradation of the line of transition, both cc_{trab} and cc_{cort} were considered equals. In the other sections, only one cannulation coefficient was determined.

Perforation or degradation of the cortical shell were detected using force measurements and were verified with a CT scan performed after the tests (Fig. 12.6). The CT scan used was a on 128-MDCT (GE Healthcare 109 Optima CT660) with spatial resolution of 0.54 mm on plane and a slice thickness of 1.25 mm enabling clear visualization of the perforation if any.

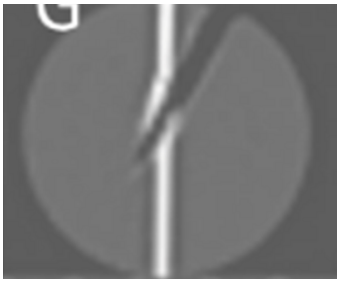

Figure 12.6.: Perforation or degradation of the cortical shell verified with a CT scan performed after the tests.

12.2.2.3. Statistical analysis

The R (R Core Team. 2020) was used for the whole statistical analysis performed on the results. Data were compared using a Wilcoxon Signed Rank Test. Exact p-values were computed and $p \leq 0.05$ indicated a statistically significant differences. Reproducibility of the cannulation on protocol was assessed using:

Intraclass Correlation Coefficient (ICC) computed for cannulation coefficient using 'irr' R library

Coefficient of variation (COV) on reproducibility data

The reproducibility data consisted in two dataset at cannulation at 10° in samples with epoxy (dataset 1) and samples without epoxy (dataset 2). Boxplot representations were provided in order to depict the results according to the cannulation protocol section, angles of the tools and types of foam. Principal Component Analysis (PCA) was performed in order to determine the best parameters to be considered for analysis of the perforation of the cortical shell. The Area Under Curve (AUC) and Receiver Operating Characteristic (ROC) analysis enabled a clear representation of perforation prediction based on the angle as well as a determination of an angular threshold by foam type.

12.2.3. Results

12.2.3.1. Reproducibility of the cannulation protocol

Reproducibility of the cannulation coefficient with epoxy (Sawbone samples) showed higher ICC considering all foam densities with 0.979 ($p < 0.001$) with a larger standard deviation in section 2, respectively, 0.982 ($p < 0.001$) and 0.416 ($p = 0.08$) for section 3 and large standard deviations between section 1 and 3 compared to section 2 results (Fig. 12.7).

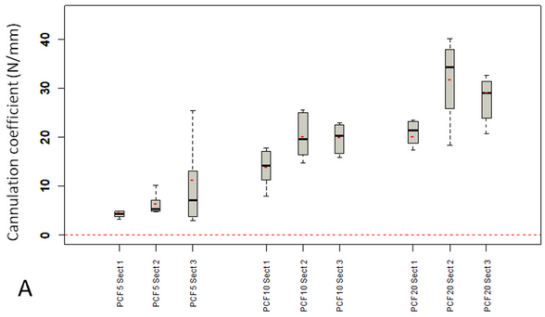

Figure 12.7.: Cannulation coefficient reproducibility of the measurement for 10° perforation angle for each type of samples with epoxy.

For sample without epoxy (Creaplast), less than 10% of difference was found between the tests, ensuring the reproducibility for the bi-components cylinders made with Creaplast-PCF20 and Creaplast-PCF10 foams. ICC results considering all foam densities for section 2 for samples without epoxy were 0.09 ($p < 0.001$), 0.923 for section 1 ($p = 0.00045$) and 0.957 for section 3 ($p < 0.001$). Perforations were not accurately reproduced in samples with Creaplast-PCF5 foams as the Sawbone foam was highly brittle (Fig. 12.8).

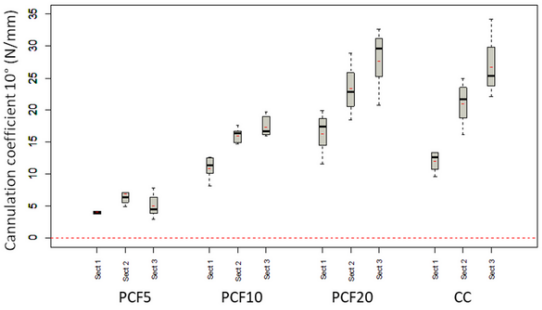

Figure 12.8.: Cannulation coefficient reproducibility of the measurement for 10° perforation angle for each type of samples with bi-foam model.

COV for section 2 in samples with epoxy were 39.9 (PCF5), 7.1 (PCF10) and 7.3% (PCF20) and COV in samples without epoxy were 36.10 (PCF5), 7.7 (PCF10) and 22.5% (PCF20).

12.2.3.2. Perforation test and influence of the perforation angle

Highest resultant forces were found for Sawbone PCF20 foam coupling with Creaplast foam and for Creaplast foams, i.e., 3495.7 ± 257.8 N for PCF 20 (angle 30°), 238.8 N for CC (angle 25°), 136.8 N for PCF 10 (angle 30°) and 67.5 ± 25.6 N for PCF 5 (angle of 20°) (Fig. A.8). When comparing maximum force values for the Z-axis and for XY-axis, values were higher for the Z-axis, from angle 20° and XY-axis force were found higher for CC than for PCF20. When focusing on PCF10 and PCF20 Sawbone result in term of young modulus, changes in cannulation coefficients were highlighted in section 2. An inversion in cannulation coefficient measurements appeared around 25°, i.e $30.1 \pm 10.8\,\mathrm{N\,mm^{-1}}$ for PCF 20, $8.5 \pm 4.7\,\mathrm{N\,mm^{-1}}$ for PCF 10. Figure A.8 also highlights that increasing the perforation angle leads to change in resultant forces and Z and XY forces during the perforation section.

Neither XY Force, Z force only nor torque measurements for PCF10 and PCF20 presented differences between perforated and non-perforated tests (Fig. 12.9).

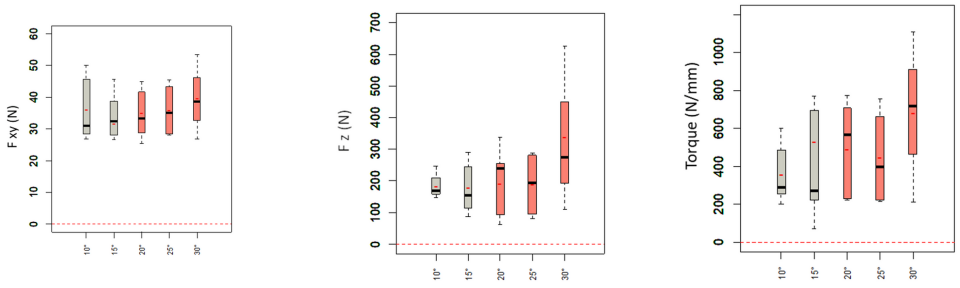

(a) Section 2 maximum XY Force.

(b) Section 2 maximum Z force.

(c) Torque.

Figure 12.9.: PCF10 and PCF20 measurements.

12.2.3.3. Measurement analysis for perforation detection

The PCA showed that Z force and resultant forces, XY forces, trabecular cannulation coefficient and cortical cannulation coefficient - in such order – were mostly present in the first dimension of the PCA (Fig. 12.10a).

The second dimension of the PCA was composed of X and Y force components resulting in the transition between the two materials when perforation occurs as shown in Fig. 12.10b.

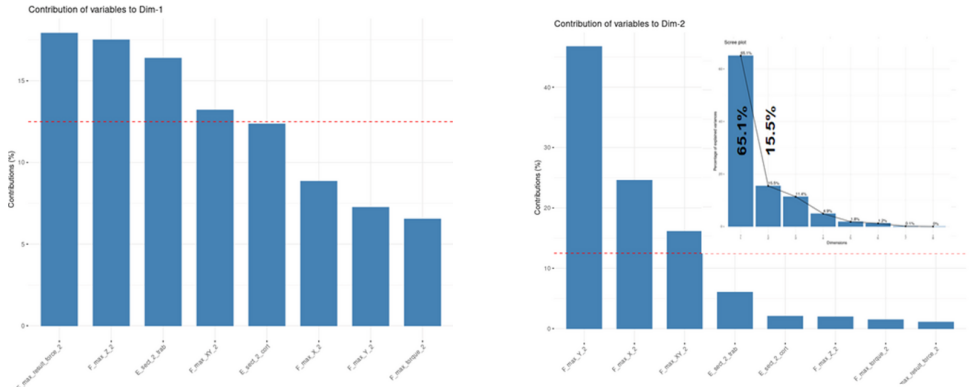

(a) First dimension of the PCA. (b) Second dimension of the PCA.

Figure 12.10.: Principal Component analysis of the perforation tests

PCA analysis allowed to define the parameters which contributed the most in the perforation description, namely Z forces, resulting forces or shear forces. In all, the statistical analysis showed a variance of 80% in all tests.

Determination of the angle threshold for prediction of perforation ROC curve analysis demonstrated the model was able to predict the perforation at 89.5% when considering all materials densities with an angular threshold of 17.5°. Prediction was found to be at 100% and 77.9% for Creaplast-PCF10 and Creaplast-PCF5 foam respectively with as threshold determine at 17.5° for both foam type. Prediction was found to be at 97% for Creaplast-PCF20 foam with an angulation threshold estimated at 22.5°.

12.2.4. Discussion

12.2.4.1. Reproducibility of the cannulation protocol

The increase in the cannulation coefficient observed between first, second and third section can be explained by the material density and by the depth of the tool in the material. During perforation, material transportation caused by the perforation from the sections above occurred. The reproducibility of the foam with epoxy presented higher cannulation coefficient for the second section which could be explained by contact with epoxy and justify the use of bi foam material rather than similar foam with epoxy.

12.2.4.2. Synthetic material for trabecular and cortical bone experimental simulation

When comparing bi-material samples, the influence of the differences between mechanical properties of Creaplast foam and Sawbone foam, especially their compressive strength, can be highlighted (as shown in the previos table about mechanical properties of the used synthetic materials given by the manufacturers' materials guide). As Sawbone (Sawbones Europe AB, Malmö, Sweden) provides foam blocks of different

densities aminated with 1 mm Short Fiber Epoxy Sheet representing the cortical shell, first tests were performed with cylinders made of this synthetic material. However, the epoxy sheet was tough, avoiding any possibility of perforation and making the tests unexploitable. As Sawbone PCF 10 foam is the surrogate of osteoporosis and osteopenic bone and PCF 20 foam is the surrogate of healthy bone (Amirouche et al. 2016, Nagaraja et al. 2016, Nowak 2019), these tests demonstrated that, in vivo, pedicle wall perforation is influenced by the patient bone quality. Most studies demonstrate that Sawbone foams are an accurate alternative material to human cadaver samples. Indeed, it was shown that, while testing orthopaedic implants, the foams correspond to human bone regarding rigidity and tension (Horak et al. 2020). Studies compared pedicle screw insertion strength and pull-out between cadaveric vertebrae and different densities of polyurethane foams. It was highlighted that results were significantly different depending on the foams densities. Therefore, the use and determination of foam bone vertebra model should be done considering the quality of bone in the location of testing (Nowak 2019). Indeed, it was assessed that the influence of density on pull-out strength is the strongest when working with surrogate materials of low densities. Insertion angle has a minor influence on pedicle screw pull-out strength when compared with bone density as it is most evident in osteoporotic bone, where changes in insertion angle have little to no effect on pull-out strength (Amirouche et al. 2016).

12.2.4.3. Determination of the angle threshold for prediction of perforation

Under the threshold angle, the cannulation tool slipped in the cavity and over the threshold, it perforated the material. The ROC curve analysis identified that the threshold angle depended on the foam type. This angle was the angle for which the surgeon could slip on the cortical shell without damages with a reproducible protocol. While the force applied by the surgeon during the cannulation process is an unknown in the description of this act, the influence of the trabecular bone type has been highlighted and a threshold angle (17.5°) and a variation of this angle as the bone goes denser (up to 22.5°) has been statistically described. Mathematical model describing pedicle screw orientation within the pedicle should consider the patient specificity in term of both pedicle morphology and bone quality (both trabeculae and cortical bone material properties).

12.2.4.4. Towards standardization of the cannulation protocol

While those experimental tests were neither pure material mechanical characterization neither material damage assessment, they rather accurately reproduced the action of boring prior to insert any pedicle screw. As underlined, it enabled the definition of threshold angles for each of the tested material which could be considered as surrogate of bone types as well as highlighted the slipping behaviour of the cannulation tool during pedicle cannulation. Bilayer synthetic material has also been reported as adequate in term of pull-out strength for pedicle screw insertion (Varghese et al.

2018), and in comparison with one layer only material. It is known that biological samples offer high variance in mechanical properties, caused by age, weight, gender and physical characteristics. However, comparability and reproducibility of the results achieved require a large number of tested specimens. Synthetic material has the potential to have constant material properties and be reproducible (Oroszlány et al. 2015). However, it is important to note that some studies on orthopaedic applications have shown that insertional torques or screw extraction forces in synthetic bone were in poor agreement compared to human samples and therefore suggested to develop home-made bi-synthetic vertebrae that could differentiate the cancellous bone and the cortical shell (Hollensteiner; Augat, et al. 2017 Tsuji et al. 2013) or to manufacture their own foams adding additives (Asriyanti et al. 2022 Hollensteiner; Botzenmayer, et al. 2018).

12.2.4.5. Limitations

Several limitations should be reported regarding this work. The main limitations relied on the possibility to accurately simulate the cannulation process such as in a surgical context. Indeed, both the simplification of the cannulation test protocol as well as the synthetic material used could be questioned. The material bone properties have been discussed previously, but the effects of the glue at the interface also need to be considered. The simplification of the cannulation protocol has been done in order to be able to reproduce the cannulation with a standardized motion of the cannulation tool (constant angular and translational velocities). A more realistic protocol could have considered acceleration which could be assumed in a realistic surgeon motion. Further studies of cannulation process during surgery should be performed in order to provide this protocol with accurate values of speed and acceleration of the cannulation tool. Additionally, simulation of the cortical shell by a plane could be discussed together with specificity of the surgical tool used in this study and a further parametrization of the pedicle and tool geometries should be taking into account the local topography as well as the range of pedicle morphology of the population in which pedicle screws could be inserted.

12.2.5. Conclusion

The reliability of our protocol has been assessed by characterizing the cannulation process prior to any pedicle screw insertion, resulting in a high ICC which depended of the synthetic material used. The angle of screw insertion (17.5°) under which the surgical tools was predicted to slip on the cortical shell so at which the trajectory becomes critical for the patient has be determined experimentally. The accurate reproduction of the cannulation prior to any pedicle screw insertion was innovative and might be used for the identification, development and validation of the future bone surrogate material as well as enhancing current pedicle screw normative testing. Further studies need to be conducted for a full description of the surgeon act as well as further description of the bone material properties model for test of pedicle screw

implantation and navigation systems.

12.3. Assessment and validation of the incertitude of tolerance angle in swine and cadavers

12.3.1. Introduction

Vertebrae are composed of cortical and trabecular bones with specific material properties. Vertebral bone can be considered as inhomogeneous and isotropic. The cortical bone is the hard and resistant thin outer shell around the vertebra.

According to the papers found in the literature, the cortical thickness ranges from 0.15 mm to 3.18 mm depending on the regions of the vertebrae (Odeh et al. 2021) and the vertebral level (Edwards et al. 2001 Kothe et al. 1996).

The trabecular bone is less dense, highly porous (between 75 and 95%) and composed of 100 to 300 µm thick trabeculae. The trabeculae distribution is inhomogeneous and isotropic and their organization and orientation are governed by the mechanical stresses exerted on the vertebral body. Young modulus reported by compression testing for vertebrae bone (cortico-cancellous bone specimens) were 374 ± 208 MPa with cortical thickness of 0.4 mm (El Masri et al. 2012). A previous study also reported 475 ± 931 MPa with cortical thickness of 0.35 mm (Liebschner et al. 2003). Relationship between Young modulus and apparent density have been described as correlating in Morgan; Unnikrisnan, et al. 2018. Considering such a description in the literature of bone mechanical characteristics and considering the instrumentation possibility during an operation, there is a need for a reliable cannulation protocol between material characterization and indentation force measurement for further assessment of pedicle screw placement and in perspective of future intra-operative instrumentation. To study the cannulation act performed by the surgeon before any pedicle screw insertion, an experimental protocol was reported using cadaver vertebrae and swine vertebrae. This protocol aimed to assess:

- the influence of the patient specificity of the pedicle morphology and cortical and trabecular bone properties
- the comparison between cadavers and swine vertebral model, 3) the full characterization of the cannulation procedure

12.3.2. Material and methods

Twenty vertebrae from three male donors (mean age 84.3 ± 8.7 yr) were selected in the range between T_2 and L_5. The cadavers were provided by the Faculty of Medicine of Marseille, France. Donors with pre-existing fractures, bony lesions or known bony diseases were excluded as the medical record was reviewed, and CT scans were performed prior to any vertebral extractions.

Fourteen vertebrae from a single 4-month-old Landrace swine weighting around 60 kg were extracted post-mortem, just after sacrifice in compliance with the European Convention on the protection of vertebrates used for experimental or other scientific purposes. Extraction took place at the C.E.R.C. (Centre d'Enseignement et de Recherche Chirurgical), Faculty of Medicine of Marseille, France, (government agreement number C-013-15-022; Ethical committee CEEA 14).

12.3.2.1. Ex-vitro samples preparation

Human cadavers were injected with diluted solution of zinc chloride (ZnCl2) for conservation. The swine vertebrae were directly frozen after extraction. All samples were maintained in a freezer at $-20\,^{\circ}$C. Even if preservation and storage methods are not supposed to affect bones mechanical properties (Baum et al. 2015, Hale et al. 2017), thawing and refreezing were avoided as much as possible. Separation of the vertebrae from the whole spine was performed after cautious removal of soft tissue. Separation of the vertebrae were performed as follow:

1. Vertebral disks incision
2. Costal facets incision
3. Release of the vertebral body using the costal facet of the adjacent vertebrae
4. Release of the section between the articular facets and the transverse processes

12.3.2.2. Surgical planning of the cannulation trajectories

For both cadavers and swine vertebrae, entry points were defined by a senior surgeon (YG). All vertebrae were imaged using CT scan after entry points were defined and bored (2 mm depth hole) for planning of the cannulation trajectory. The CT scan used was a on 128-MDCT (GE Healthcare 109 Optima CT660) with spatial resolution of 0.54 mm on plane and a slice thickness of 1.25 mm. The surgical planning consisted in identification of a vertebral reference system based on the selection of articular facets, superior and inferior endplates of the vertebral body, and two landmarks in the spinal canal as described in Danesi et al. 2014 .Sections of the pedicle were computed based on the landmark locations and oriented along the normal to frontal plane or mean between this normal with the higher point of fitted facet plane. Barycenter of the minimal section of the pedicle was then used to determine the ideal cannulation trajectory.

12.3.2.3. Design for experiment

Design of experiment for assessing trabecular-cortical transition with and without perforation was performed on ex-vivo material (Table 12.3). It included a tolerance angle addition α to the ideal trajectory ranging from 5° to 30° in the sagittal plane in either outward (toward the the ribs) or chord (toward the vertebral canal) direction.

Pseudo randomization of the tests was done to vary tolerance angle and direction of cannulation as follow. For each vertebra, one pedicle cannulation was performed according to the ideal trajectory while the other was planned with the tolerance angle addition.

Additionally, as the angle α did not characterized the cannulation angle in the cortical pedicle bone, the angle β between a fitted line to the pedicle cortical bone was additionally computed between the modified trajectory and the fitted line at the minimum location between the two system setting and perforation testing.

Vertebra	Pedicle	Subject C	Subject D	Subject F	Swine 28	Swine 29
T_2	R	25° **medullar**	0	0	-	15° costal
	L	0	30° **costal**	5° **medullar**	-	0
T_3	R	0	-	20° **medullar**	10° **costal**	0
	L	15° **costal**	-	0	0	5° **medullar**
T_4	R	20° **medullar**	-	0	5° **medullar**	25° **costal**
	L	0	-	30° **costal**	15° **costal**	0
T_9	R	0	0	10° medullar	0	0
	L	30° **costal**	25° **costal**	0	25° **costal**	20° **medullar**
T_{11}	R	0	15° medullar	0	0	30° **costal**
	L	10° **costal**	0	20° costal	20° **medullar**	0
T_{12}	R	25° **costal**	-	0	30° **medullar**	30° **medullar**
	L	0	-	5° **costal**	0	0
L_1	R	0	20° costal	0	30° **medullar**	10° costal
	L	5° **costal**	0	15° **medullar**	0	0
L_5	R	-	5° medullar	0	-	20° **medullar**
	L	-	0	25° **costal**	-	0
Vertebra (N)		7	5	8	6	8
Perforated (N)		8	2	9	9	8

Table 12.3.: Design of experiment of the perforated pedicles and angle of deviation (°) from the ideal trajectory (external angle) for each configuration. The samples are divided according their vertebral level: blue for high thoracic, green for low thoracic and orange for lumbar spinal segment. 0: no perforation; medullar and costal to indicate pedicle side; -: no tested sample; writings in bold illustrate perforated pedicles

The cannulation tool selected from the standard surgical toolkit had a slightly curved tip (Fig. 12.2, Fig. 12.11).

All tests were performed on an MTS Acumen 3 A/T electrodynamic test system (MTS Systems corporation, Minnesota, USA) composed of a MTS Flextest 40 controller and servo actuator controlled using Test Suite Multipurpose Testing Software (MPE). Two load sensors were used: on one hand the Acumen 3 kN load sensor placed above the specimen and on the other hand a Kistler 9317C triaxial load sensor (range ± 3000 N – Kistler group, Winterthur, Switzerland) installed at the top of the medical device. Two Miro C110 cameras (Vision Research Phantom, Wayne, New Jersey, USA) were set to control the experiment during its different phases. Samples were positioned to the entry point thanks to a biaxial and circular Norelem, 21161-10-08 positioning tables

(Norelem, Fontaine-les-Grès), enabling rotation of the samples according with the expected computed angles.

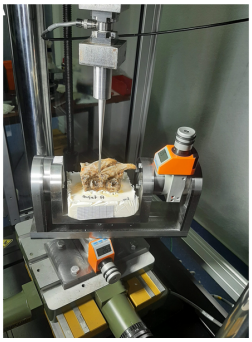

Figure 12.11.: Cannulation tool mounted on the MTS device.

The test procedure aimed at reproducing the surgeon action during pedicle screw insertion. This movement was composed of three rotations (100°, 100° and 60°) coupled with three translations (10 mm, 10 mm and 6 mm) insuring a constant perforation speed of 10 ° mm^{-1}. The device was pulled out by reversing angle values (translation and rotation) with similar speed in order to prevent any material damage due to device extraction. As morphology of the pedicle is circular, the tool was set to be above the entry point and parallel to the sagittal plane defined as a cutting plane dividing the spinous process into two equal sections as in the planning.

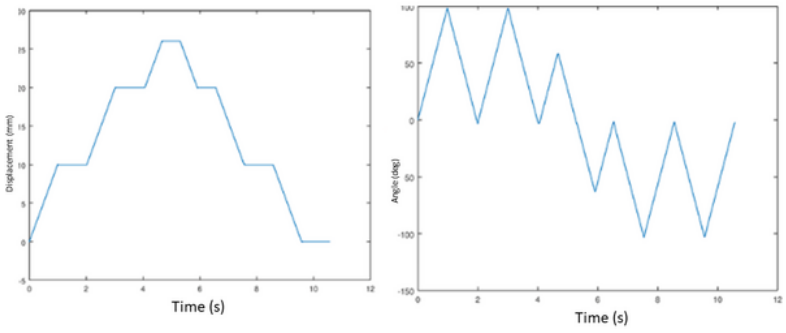

Figure 12.12.: Typical displacement and angle command signal

12.3.2.4. Bone density characterization

CT scans were performed before and after testing each vertebra. An electron density phantom (Model 062M, CIRS. Sun Nuclear, Norfolk. USA) was used for comparison with calibrated bone density (Solid Dense Bone 1000 mg cm^{-3} Calcium Hydroxyapatite (HA), physical density of 1.66 g cm^{-3}, 5.243 e23 electrons/cc, 1.57 RED relative to H2O); Solid Dense Bone (1500 mg cm^{-3} HA. physical density of 1.99 g cm^{-3}, 6.134 e23 electrons/cc, 1.837 RED relative to H2O); Solid Dense Bone (1750 mg cm^{-3} HA. physical density of 2.15 g cm^{-3}, 6.6 e23 electrons/cc, 1.976 RED relative to H2O). Cortical and trabeculae bones averaged density were derived from the peak histogram of

Hounsfield Units (HU) converted to physical density using a custom-made python script and Paraview 5.9.1 for visualisation (Ahrens et al. 2005). A K-mean filter was applied on a volume derived from CT-scan images of samples pre-test to differentiate cortical from trabeculae bone and classes corresponding to respectively trabeculae and cortical bone were identified. Mean, minimum and maximum (peak) values were then computed as a surrogate of the bone density range. Similar process was performed on phantom probe. Conversion between HU and physical density was identified by a linear regression from the three peaks histogram of the phantom probes. Additionally, CT scan images analysis of detected perforation or damage was performed directly on the post-test CT scans with gradation of the perforation (0 to 2 from no perforation to clear perforation).

12.3.2.5. Post-processing

The X, Y and Z components of the force measurements (respectively F_x, F_y, F_z) were triggered with the MTS data (displacement and torque measurement-F_z). A custom-made Matlab (MATLAB Release 2020b. The MathWorks. Inc. Natick. Massachusetts, United States) code was used to post-process the data. The frequency filtered by a low pass filter was determined using a Fast Fourier Transform in Matlab. The signal was divided into three sections representing the three translations performed during the MTS procedure. On each of these sections, two Elastic Moduli were computed by the linear slope between two points chosen manually for each of the subsection of the signal: one defined for the trabecular bone (E_{Trab}) and one defined for the cortical bone (E_{Cort}). In case of perforation or degradation of the cortical wall, occurring in section 2, the critical point was graphically found and E_{Trab2} and E_{Cort2} were computed in the corresponding sub-section (Fig. 12.13).

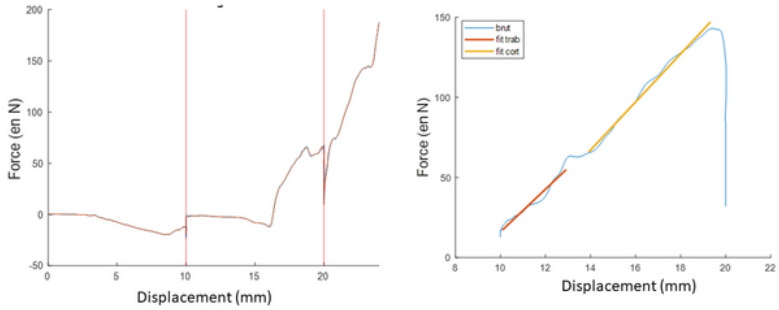

Figure 12.13.: Typical force-displacement signals for perforated pedicles

If the test was performed without perforation or degradation of the cortical wall in section 2, both E_{Trab2} and E_{Cort2} were considered as equals. In the other sections, only one Elastic Modulus was determined. Additionally, E_{Trab} to E_{Cort} ratio were computed for perforated samples.

12.3.3. Statistical analysis

Principal Component Analysis (PCA), Area Under Curve (AUC) and Receiver Operating Characteristic (ROC) analysis and boxplot representations were achieved using R (R Core Team 2021).

12.3.4. Results

12.3.4.1. Pedicle morphology – swine and cadaver

A total of 68 pedicles were tested: 21 perforated and 19 non-perforated human pedicles, 13 non-perforated and 15 perforated swine pedicles. The design of experiment resulted in 11 perforated pedicles on the 34 planned with an angle modification of ideal trajectory. The morphological characteristics of the tested pedicles are described in Table 12.4.

		High thorax		Low thorax		Lumbar	
		Mean	Std. Dev.	Mean	Std. Dev.	Mean	Std. Dev.
Pedicle Height (mm)	Human	4.58	1.92	5.71	1.2	5.5	1.3
	Swine	5.81	1.38	5.0	1.17	5.25	0.0
Medullar radius (mm)	Human	1.28	1.58	2.67	1.74	1.55	0.68
	Swine	1.78	1.89	2.13	1.48	2.8	2.2
Costal radius (mm)	Human	3.79	1.83	3.62	2.22	1.99	0.98
	Swine	3.72	1.82	4.31	1.19	5.38	1.28

Table 12.4.: Pedicle morphometric specifications

When comparing pedicle morphometry between swine and human model, the height of pedicles was greater in low thoracic in human and in high thoracic in human with larger costal radius than medullar one in all vertebral levels for both models. Differences between costal and medullar radius should be noted between swine and human in lumbar vertebrae ($p < 0.001$) for costal radius, non-significant for medullar radius).

12.3.4.2. Cadaveric pedicle wall perforation

When studying the tolerance angle in the trajectory, negative elastic moduli were measured as shown in previously shown in Table 12.3. As an example, a perforation test on a T_2 vertebra reported X and Y force components significantly higher than Z force component in section 1.

Computation of the resulting β angle between cannulation tool and cortical bone resulted in a β distribution ranging from 0.44° to 33.1°, depicted in Fig. 12.14.

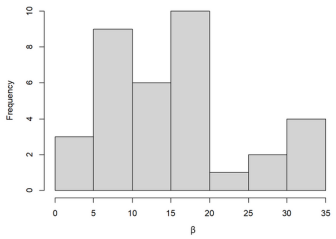

Figure 12.14.: Tested β number for β threshold identification and prediction by maximal forces and torque.

When comparing the elastic modulus for all vertebrae with pedicle perforation to non-perforated pedicle elastic modulus within the three sections, a slight increase was highlighted in non-perforated pedicles as shown in Fig. 12.15.

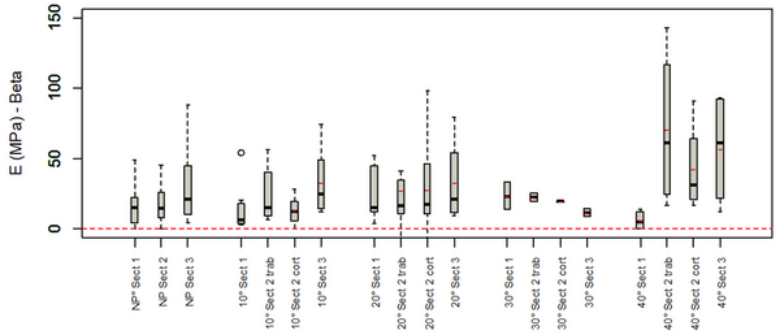

Figure 12.15.: Beta angle and vertebral level influence on elastic moduli. L: Lumbar; LT: Low Thorax; HT: High Thorax, SW: Swine model, HS: Human Subject

While under 20° β angle conditions presented similar results in term of elastic modulus, β angle ranging between 20° to 30° resulted in lower elastic modulus in all sections and β angle over 30° presented far higher elastic moduli from section 2 ($p = 0.018$) between non-perforated E_{Cort2} and perforated E_{Cort2}, non-significant otherwise). E ratio was found lower for $\beta > 10°$ and similar to non-perforated pedicle E ratio as shown in Fig. 12.16.

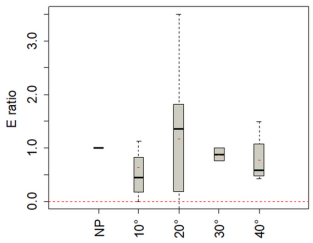

Figure 12.16.: β angle and E ratio

As expected, maximum Z force and torque were found higher from $\beta > 30°$, and Low thoracic vertebrae presented lower ratio when compared to high thoracic vertebrae as shown in Fig. 12.17.

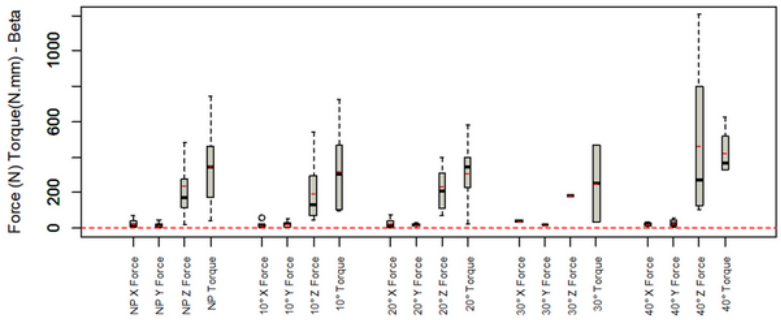

Figure 12.17.: β angle and vertebral level influence on forces and torque

Differences between swine and cadaver model were highlighted during tests. Elastic moduli were found significantly different, as p-value for comparison of trabecular elastic modulus was equal to 0.054 (non-significant) and for cortical elastic modulus was equal to 0.004. Lumbar vertebrae and swine E ratio were found higher than human subject E ratio (Fig. 12.18).

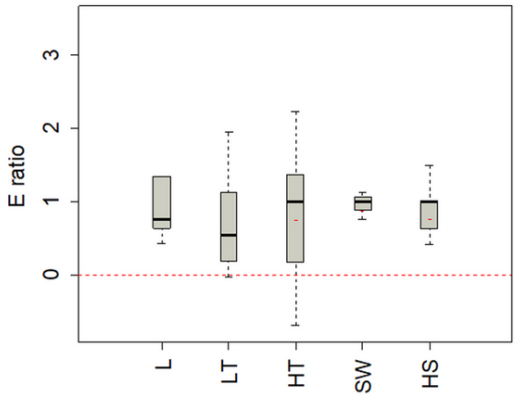

Figure 12.18.: E ratio. L: Lumbar; LT: Low Thorax; HT: High Thorax, SW: Swine model, HS: Human Subject

12.3.5. Vertebra by vertebra results with and without pedicle perforation

Vertebra by vertebra results with and without pedicle perforation were depicted in Fig. A.9.

Such results showed that there was similar elastic modulus between cortical and trabecular bone, while depending on location, there were some differences between swine and human model.

12.3.5.1. Perforation measurements threshold

In order to define a threshold for β angle perforation, a ROC analysis was performed and the threshold for 100% determination of perforation regarding β was 21.73° as show in Fig. 12.19.

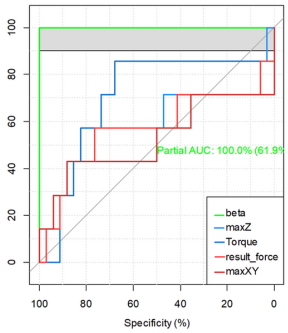

Figure 12.19.: ROC analysis for β threshold identification and prediction by maximal forces and torque.

When predicting perforation trough, the different measurements of the experiment, the torque presented a better AUC (AUC: 70.17%; accuracy: 70.7; threshold: 421.4 N mm) than force resultant (AUC: 57.14%; accuracy: 73.2; threshold: 325.6 N) or force components maximums (XY component: AUC: 57.98%; accuracy: 80.5 threshold: 74 N; Z components: AUC: 52.52%; accuracy: 73.2; threshold: 281.5 N).

12.3.5.2. Bone density influence on perforation measurements

Correlation between perforation test measurements and cortical and trabecular bone density were computed. Significant correlations were found for both density with maximum Y force ($p < 0.001$) and XY components force ($p < 0.007$). Cortical bone density correlated with trabecular elastic modulus of section 2 ($p = 0.02$) when perforated and section 1 and 2 for all vertebrae ($p = 0.008$ section 1 and $p = 0.004$ section 2). Finally, cortical bone density significantly correlates with trabecular elastic modulus ($p = 0.02$) and maximum Z force ($p = 0.02$).

12.3.6. Discussion

Reported results were mainly about 1. the identification of a β angle threshold over which the perforation of the cortical bone is likely to occur, 2. the study of the influence of vertebral level and swine and human model, and 3. the possibility to determine the more accurate acquisition parameter to detect perforation. Measurements of

negative elastic moduli can be due to the higher values found for the shear force, i.e. X and Y forces, during the perforation, and the perforation force itself i.e. Z force. These observations allowed the description of the perforation tool motion, knowing the moment the tool slips in the pedicle and when it perforates the pedicle wall. Combining the post-tests CT scan images and the results, we demonstrated that considering the complex morphology of the pedicle, the bone density, which shows variability within vertebrae and within individuals, and the inter-individual anatomical differences were crucial parameters for pedicle screw insertion.

The extraction of cadaveric vertebrae correlated with data found in the literature highlighting the fact that specific morphological characteristics are observed in each vertebral level. High thoracic vertebrae tests resulted in higher variability than lower vertebrae or lumbar vertebrae tests. Swine and cadaveric samples showed different results and this could be due to the differences between their bone densities and morphology. Furthermore, the age of the swine model as well as the absence of pathology, ensuring relative bone quality without ensuring sufficient bone maturity could be a factor of influence. CT scan images showed that the cortical shells were thicker in swine than in human cadavers while quantification of cortical thickness and impact on perforation was still to be fully studied and characterized. The fact that cadavers were injected for preservation, unlike the swine, could lead to a degradation of the bone architecture, i.e. the density of the trabeculae. These results highlighted that the tolerance angle was 21.7° in our experimental conditions. Additionally, the tests performed on synthetic materials were able to determine a finer threshold angle by considering the material density (see previous section of this chapter). The torque measurement has been shown to be the best predictor of perforation after the β measurements which could be explained because this measurement took into account not only the bone density which varied intra and inter individually, but also the required torque to be applied for perforation of the cortical bone as compared to the trabecular bone. The torsion motion of the surgical cannulation tools was then generating a torque which was a good predictor for perforation description. This is a way to go for the development of surgical assisting device.

All the results allowed us to conclude that the best trajectory for pedicle screw insertion depended on the vertebral level, the pedicle morphology and the spine orientation, which was in agreement with the literature (Y. Zhang et al. 2014). Some limitations can be found in this study such as the advanced age of the subjects and the fact that only male specimen were tested. Also, the preservation method could change the bone micro-architecture. Both limitations could explain the behavior of the trabecular bone and the thin cortical shell observed. Also, a higher number of specimens should be tested in order to make further conclusions. Finally, only one perforation tool shape was used during the tests when in real life, surgeons have access to tools of different shapes.

12.3.7. Conclusion

As a conclusion, in this study a reliable protocol characterizing the pedicle cannulation process was developed allowing the quantification of bony wall perforation by maximal strength and elastic modulus change at the trabecular and cortical bone interface. The influence of bone mineral density and patient-specific morphology has been highlighted as well as the comparison between swine and cadaver models for pedicle screw implantation study.

13. Perspectives

Several perspectives could be drawn from the researches done during this thesis. First, they could form the building blocks toward an automated planning of the pedicle implantation surgery. Then, they could lead to some advancements in the surgeon practices and the study of the biomechanics of the spine.

13.1. Planning automation

The current trend in spine and vertebrae segmentation points towards dominance by AI techniques. However, achieving robust and reliable segmentation requires further investigation into training data. Deep learning algorithms specifically need diverse datasets encompassing healthy subjects, various pathologies, a broad age range, and different image resolutions. This is crucial because real-world uses encounter significant variations in these parameters.

Even after vertebrae segmentation has been dealt with, achieving fully automated surgery planning requires addressing four key areas (Fig. 13.1):

Identifying the specific vertebral level This involves pinpointing the exact vertebra among the spinal column.

Locating the entry point for the pedicle screw

Determining the trajectory of the screw within the pedicle The path of the screw inside the vertebra needs to be carefully planned.

Positioning the three calibration point These points are crucial for PYTHEAS NAVIGATION *Your Guided Trajectory* for an accurate alignment during surgery

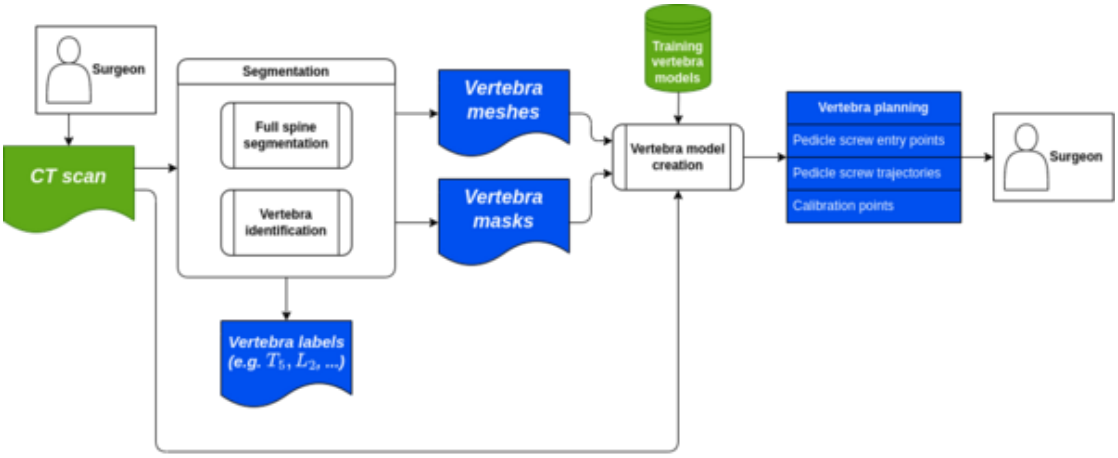

Figure 13.1.: Planning automation. Input data is colored green. Output data is colored blue.

Identification of the vertebra level

Vertebra level is critical for automated surgery planning. Research shows it directly influences the placement of the IPEP.

A straightforward approach might involve counting vertebrae based on the scan range provided by the surgeon. However, this relies on manual input and fails to consider variations in spinal anatomy. Some people have extra (supernumerary) or missing (subnumerary) vertebrae, making simple counting unreliable. Fortunately, automated algorithms can now accurately identify vertebrae withing a scan, eliminating the need for manual counting and improving the reliability of the entire automation process.

Ehm et al. 2009 applied a method called Generalized Hough Transform (GHT) to identify vertebrae in spine CT scans. Their algorithm achieved a success rate of 93.7% on a test set of 63 images from patients with various spinal conditions, including calcification between vertebrae, scoliosis, implanted pedicle screws, and collapsed vertebrae. However, they also found that the algorithm performance could be affected by the number of vertebrae visible in the image (Fig. 13.2a). Additionally, the accuracy varied depending on the specific vertebra being identified. It performed less well on vertebrae in the mid to lower thoracic spine (T_5 - T_{10}, Fig. 13.2b, Fig. 13.2c).

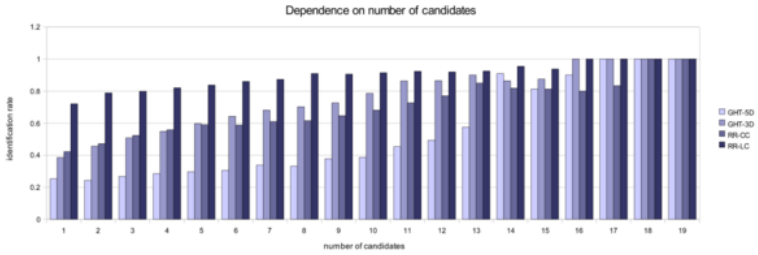

(a) Dependence on the number of visible vertebra.

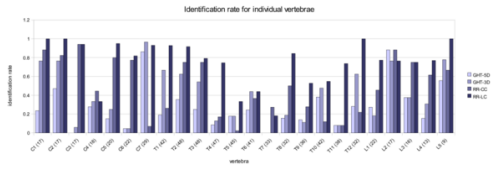

(b) Identification rate for individual vertebra

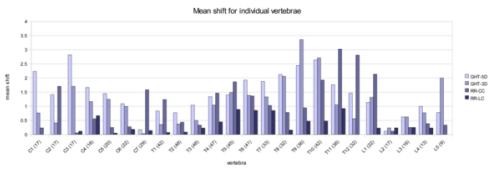

(c) Identification deviation for individual vertebra

Figure 13.2.: Ehm et al. 2009
GHT-5D: GHT extended to 5 degrees of freedom
GHT-3D: GHT reduced to 3 dimensions
RR-CC: With use of cross-correlation as similarity measure
RR-LC: With use of local correlation as similarity measure

Another approach leverages AI, as demonstrated in F. Wang et al. 2020. Their method utilizes a U-Net architecture,a type of AI model, to pinpoint the center of each vertebra in a scan. This is achieved by generating "activation maps" that highlight these vertebral centers. The model then refines these locations along the spinal centerline. This AI-based method achieved an impressive identification rate of 97.4% on a publicly available dataset of 302 CT scans with various spinal conditions and imaging qualities. This dataset is provided by SpineWeb (Dataset 3: Vertebrae Localization and Identification, 2nd MICCAI Workshop and Challenge, CSI 2014).

Positioning of the pedicular screw entry point and identification of the pedicular screw trajectory inside the pedicle

As discussed in Freehand pedicle screw insertion techniques, surgeons have various methods for placing pedicle screws. The ideal entry point depends heavily on the specific anatomy of each vertebra. Therefore, we believe that a detailed description of the vertebral geometry and topology could be used to implement these different placement techniques.

The algorithm developed in this research can be used to enrich the existing anatomical model of the vertebra with additional information, such as cortical thickness and density. This enriched model could then be used to guide automated selection of the optimal entry point for each screw.

One approach to identify entry points involves deforming a template of vertebrae

and their screw paths. Goerres et al. 2017 achieved an average angular error of $3.01 \pm 2.81^\circ$ for the trajectory and a deviation of 1.05 ± 0.74 mm at the pedicle center, based on CT or MRI scans.

An alternative method involves first identifying the pedicles within the vertebra, potentially by fitting them with paired tube shapes. The screw trajectory would then be chosen to follow a path that maximizes its distance from the inner bone layer (cortical shell) of the pedicle. The entry point would be the spot where this trajectory intersects the back surface of the vertebra.

Additionally, AI can be trained to directly identify either the screw entry points and trajectory, or the pedicle themselves.

Position of the three calibration points

Among the three calibration points, only the ones on top of the two articular processes needs to be identified. The third point location is predictable based on the other two points and the vertebra anatomy, so it can be omitted. Similar to identifying screw entry points (Positioning of the pedicular screw entry point and identification of the pedicular screw trajectory inside the pedicle), algorithms can be used to locate these calibration points. For instance, the method from Goerres et al. 2017 could be adapted to include these points, potentially even incorporating the third one for additional reference.

Radioprotection

A significant limitation of relying solely on CT scans for surgical planning lies in the substantial increase in patient exposure to ionizing radiation. To mitigate this risk, exploring alternative medical imaging modalities is essential. Magnetic Resonance Imaging (MRI) stands out as a prime candidate, offering the distinct advantage of eliminating radiation exposure altogether when used in place of pre-operative CT scans. Integrating MRI into automated surgical planning workflows presents two primary pathways.

Firstly, a conversion strategy can be employed, transforming MRI data into synthetic CT scans. This approach leverages the established workflow designed for CT-based planning, effectively bridging the gap between the two modalities. Notably, companies like MRIGuidance have pioneered this technique (Arbabi et al. 2023), utilizing sophisticated artificial intelligence algorithms to generate highly accurate synthetic CT images from MRI scans. This allows surgeons to maintain familiar planning protocols while minimizing radiation exposure.

Secondly, a direct segmentation approach can be developed, tailored specifically for MRI data. This path necessitates the creation of new segmentation algorithms and workflows optimized for the unique characteristics of MRI images. An example of this is the "Black Bone" MRI sequence (Eley et al. 2013), a specialized imaging technique that renders bone tissue as dark regions within the image. This enhanced contrast facilitates more straightforward and accurate bone segmentation compared

to conventional MRI sequences. By pursuing either of these avenues, the goal is to leverage the benefits of MRI while maintaining or improving the precision and safety of surgical planning.

13.2. Surgeon practices

A significant challenge in automating surgery planning for pedicle screw implantation is accommodating the diversity of surgical practices. Surgeons may favor specific approaches based on their training and experience, making it difficult to develop a one-size-fits-all automation solution.

This chapter describes a unique protocol designed to capture the nuances of these practices and integrate surgeon expertise into the automation process. By modeling surgeon decision-making and surgical techniques, we aim to create an adaptable automation tool that reflects individual preferences while allowing for adjustments during surgery.

The protocol employs a two-pronged approach to comprehensively understand surgeon practices:

Structured questionnaire A comprehensive questionnaire prompts surgeons to articulate their thought processes and decision-making steps throughout a typical pedicle screw implantation procedure. This helps capture the rationale behind their technique and identify underlying factors influencing their surgical approach. In addition to the thought process and decision-making steps, the questionnaire should include sections on the surgeon educational background (e.g. residency program, medical school) and experience (e.g. years of experience, number of pedicle screw implantation surgeries performed annually).

Simulated surgery with replica vertebra Surgeons participate in a simulated surgery using a replica vertebra. During this process, their instrument use, hand movements, and eye gaze are tracked. This data provides valuable insights into the practical execution of their surgical techniques within a realistic setting.

By including education path and experience in the questionnaire, you can potentially discover interesting correlations with surgical practices:

- Impact of training: Surgeons who received training at specific institutions or who completed fellowships might demonstrate preferences for certain techniques influenced by their educational background.
- Experience and refinement: Surgeons with more experience might exhibit greater efficiency or subtle variations in their technique compared to less experienced surgeons.

While the protocol focuses on establishing a foundation for understanding individual surgeon practices, analyzing the collected data may also reveal underlying commonalities across different surgical approaches. This information could be valuable for developing automation tools that are adaptable to a wider range of surgical preferences. Additionally, identifying these commonalities could have a significant impact on surgeon education.

By highlighting these commonalities in surgical decision-making and technique execution, future educational programs could emphasize these core principles. This emphasis could ensure a strong foundation for all surgeons, regardless of the specific techniques they are exposed to during training. Furthermore, understanding these commonalities could help identify areas where variations in practice might lead to suboptimal outcomes. This knowledge could be used to refine educational curriculums to promote best practices and potentially improve overall surgical outcomes.

13.3. Biomechanics

Healthy bones are essential for mobility, stability, and overall health. However, assessing bone quality and diagnosing bone diseases like osteoporosis often relies on techniques like dual-energy X-ray absorptiometry (DXA), which requires additional radiation exposure. This chapter explores the potential of using a single CT scan to estimate bone mineral density (BMD) and cortical thickness, offering a potentially more comprehensive and radiation-efficient approach to bone health assessment.

Bone mineral density (BMD) is a crucial factor in assessing bone quality and diagnosing conditions like osteoporosis or osteopenia. It's typically measured with a special imaging technique called DXA. DXA uses two low-dose X-ray beams with different energies compared to a regular X-ray. However, DXA adds some radiation exposure when combined with a standard X-ray. Therefore, it would be advantageous to estimate BMD using a single CT scan, when possible.

The technique described in GMM-based segmentation allows us to measure the density (Hounsfield Units) and thickness of the cortical bone directly from a CT scan. Research from Schreiber et al. 2011 suggests that Hounsfield Units can be used to estimate BMD, while S. Li et al. 2024 showed cortical thickness can predict osteoporosis. This means a single CT scan could potentially assess the overall bone quality of a vertebra.

In the context of pedicle screw implantation, Paxinos et al. 2010 found that osteopenic bone has significantly lower pullout strength for screws compared to healthy bone (1414.5 ± 554.8 N for the healthy bone vs. 473.2 ± 179.2 N for the osteopenic bone). Pullout strength tests, as discussed previously, assess the force required to remove an implant from bone. While these tests provide valuable information, they are not routinely used in clinical settings. However, even if the cortical density may improve

the pullout strength of the screw, there are no know evidence of it improving the curve correction of the spine (Larson et al. 2013)

The ability to estimate BMD and cortical thickness from CT scans offers an exciting possibility to predict pullout strength non-invasively. Since BMD and cortical thickness reflect bone density and microarchitecture, important factors influencing pullout strength, CT scans have the potential to become a powerful tool for pre-operative planning. Further research is needed to establish a direct correlation between CT scan measurements and pullout strength. However, if successful, this approach could eliminate the need for separate pullout strength tests and provide surgeons with crucial information to select optimal implant types and sizes, personalize treatment plans, and potentially improve surgical outcomes.

Similar to the challenge of predicting pullout strength, assessing the influence of bone quality around the pedicle on the cannulation process remains an active area of research. During cannulation, surgeons often rely on the integrity and strength of the cortical wall of the pedicle to guide screw placement. In this context, understanding whether the bone quality of the cortical bone, combined with the chosen trajectory, affects the success rate of cannulation becomes crucial.

Several potential consequences can arise when cannulation is performed in bone with compromised quality:

Increased risk of cortical breach During screw insertion, brittle or weak bone might be more susceptible to fractures along the cortical wall. These cortical breaches can jeopardize screw stability and potentially damage neurovascular structures surrounding the vertebral column.

Difficulty maintaining screw trajectory Poor quality bone might offer less resistance to drilling and tapping, making it harder for the surgeon to precisely maintain the intended screw trajectory. Deviations from the planned trajectory can lead to screw malplacement and potentially increase the risk of neurological complications.

While CT scans have emerged as a valuable tool for assessing bone mineral density (BMD) and cortical thickness, further research is needed to establish a direct correlation between these measurements and the success of cannulation. Such a correlation could potentially allow surgeons to pre-operatively identify patients at higher risk of cannulation difficulties due to poor bone quality. This information could guide treatment planning decisions, such as selecting alternative implant designs or considering bone augmentation procedures to improve bone integrity before surgery.

14. Conclusion

Pedicle screw placement is a cornerstone of spinal surgery, ensuring stability and minimizing complications. Yet, even minor inaccuracies can have serious consequences. These include nerve damage, leakage of cerebrospinal fluid (CSF), and extended recovery times, ultimately leading to increased healthcare costs. This thesis tackled these challenges by investigating novel methods to improve the accuracy of pre-operative planning, a crucial step towards achieving optimal screw placement. By focusing on pre-operative planning, this research aimed to enhance patient safety and ultimately improve surgical outcomes in spinal surgery.

This thesis investigated the potential of automated spine segmentation using advanced imaging techniques to improve the accuracy of pre-operative planning. Traditional pre-operative planning methods often rely on manual segmentation of CT scans, a time-consuming and subjective process. Automated segmentation algorithms, on the other hand, offer the potential for:

Enhanced planning accuracy and objectivity Automating segmentation removes the inherent subjectivity of manual methods, leading to more consistent and potentially more accurate results. This more reliable foundation can minimize errors during pre-operative planning and ultimately contribute to improved screw placement during surgery.

Streamlined planning workflows By automating segmentation, this research significantly reduces the time required for this critical step. This frees up valuable surgeon time for other crucial tasks, such as patient consultations, surgical planning itself, or even surgery time. Improved efficiency can lead to faster treatment pathways for patients.

This research explored two promising methods for automated spine segmentation:

Method 1: Efficiency and accuracy

This method leverages a region-growing algorithm, achieving results comparable to more advanced techniques while processing a complete spine in under a minute. This speed and accuracy make it a valuable asset in a busy clinical setting, promoting faster and more efficient pre-operative planning workflows. This method has been tried and tested by surgeons, during *Your Guided Trajectory* clinical trials (over 200 instrumented pedicles, NCT05565131) and on the field, after its release.

Method 2: Beyond segmentation: Valuable bone information

This method utilizes a Hounsfield Unit (HU) based statistical model to not only segment the spine but specifically segment the cortical bone, while extracting information about bone quality. This information, such as cortical thickness and density, can be crucial for surgeons in assessing screw selection and placement, potentially improving long-term surgical outcomes. By exploring these two distinct methods, this research demonstrates the potential for automated spine segmentation in pre-operative planning. It highlights the value of both improved accuracy and the ability to extract valuable bone information, ultimately contributing to a reduction in complications and improved surgical outcomes for patients undergoing spinal procedures with pedicle screws.

By exploring these two distinct methods, this research demonstrates the potential for automated spine segmentation in pre-operative planning. It highlights the value of both improved accuracy and the ability to extract valuable bone information, ultimately contributing to a reduction in complications and improved surgical outcomes for patients undergoing spinal procedures with pedicle screws. Furthermore, the improved segmentation accuracy achieved by these methods (comparable to AI-powered algorithms) has the potential to translate into a measurable reduction in screw placement errors.

While the second method offers valuable bone information grounded in a biological hypothesis, it comes at the cost of reduced processing speed compared to the first method. This method can be expanded upon, to improve both processing speed and accuracy.

This research extended beyond spine segmentation to explore characterizing surgeon maneuvers and patient positioning during surgery. These investigations, though seemingly secondary to the core objective, significantly contribute to automating surgical planning.

In the context of PYTHEAS NAVIGATION medical device (*Your Guided Trajectory*), patient positioning, particularly supine/prone deviations, is a crucial factor during the calibration phase. Patients are typically scanned supine (on their back), but surgery is performed prone (face down). This difference creates measurable variations in spinal alignment, which the calibration process must account for. While this study's findings contribute to the PYTHEAS NAVIGATION calibration algorithm, further research is needed to refine the model and enhance device navigational precision.

Understanding the limitations of surgeon motion during pedicle cannulation is essential for automating pedicle screw implantation surgery planning. This step is challenging because surgeons rely on tactile feedback, which is difficult to replicate with automation. These findings played a significant role in the regulatory groundwork for PYTHEAS NAVIGATION.

Appendices

A. Figures

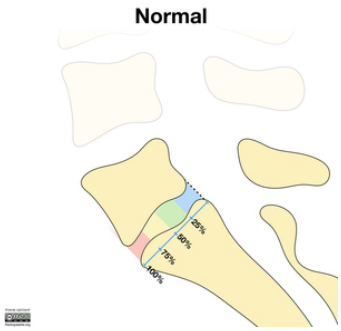

(a) No spondylolisthesis

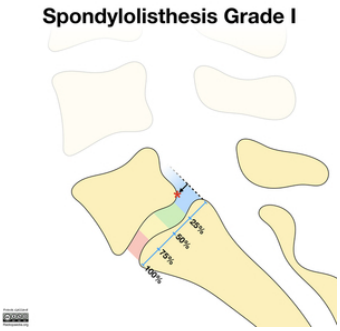

(b) Spondylolisthesis grade I

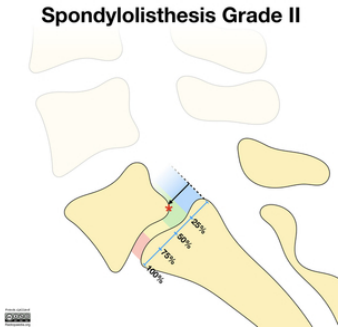

(c) Spondylolisthesis grade II

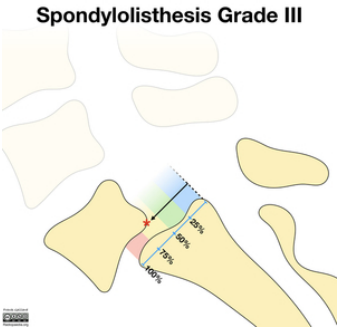

(d) Spondylolisthesis grade III

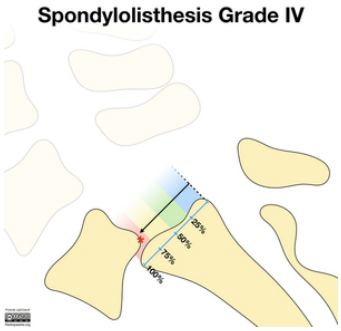

(e) Spondylolisthesis grade IV

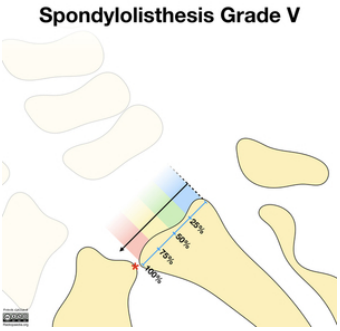

(f) Spondylolisthesis grade V

Figure A.1.: Spondylolisthesis grading

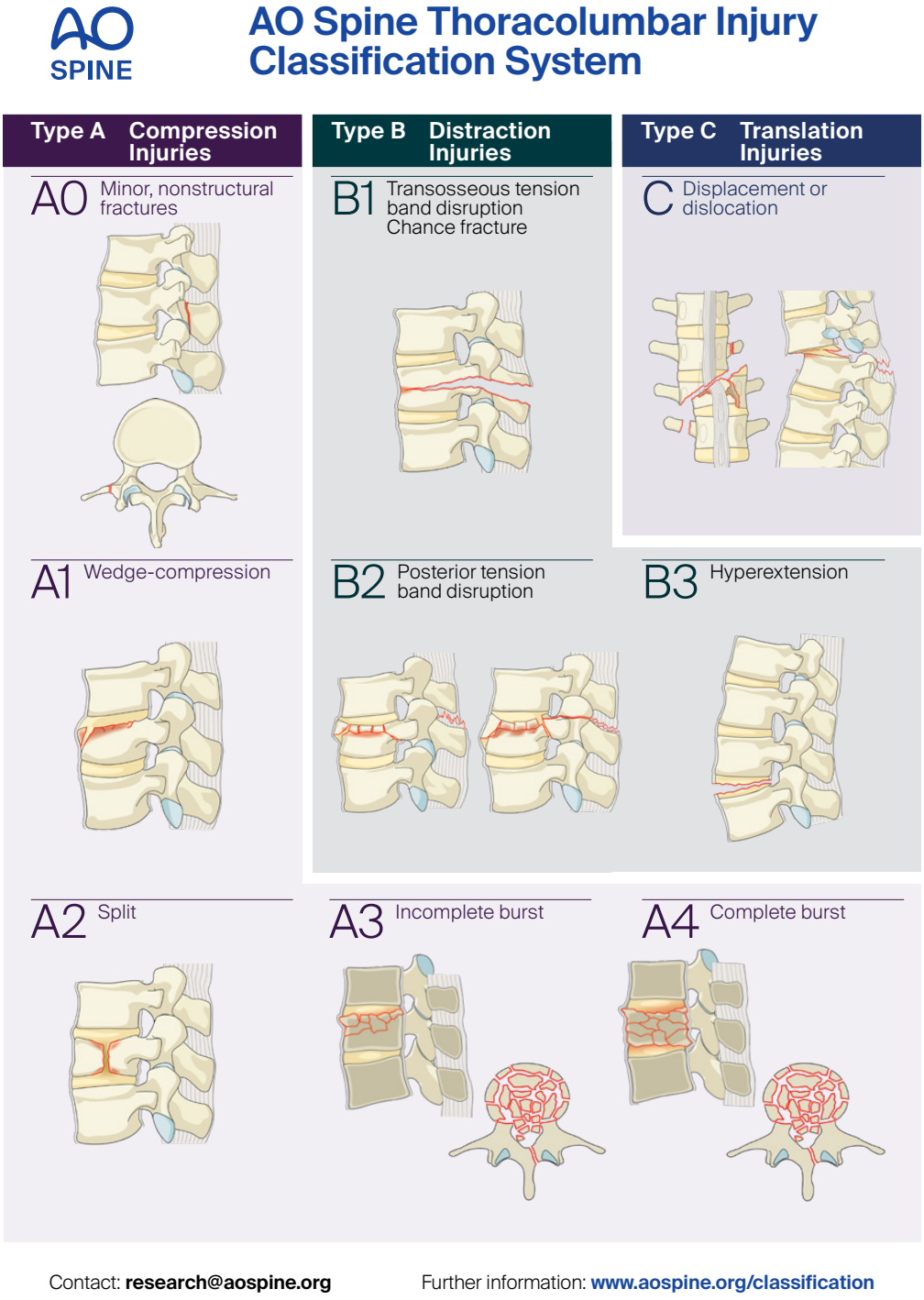

Figure A.2.: AO Spine System (2013) classifications

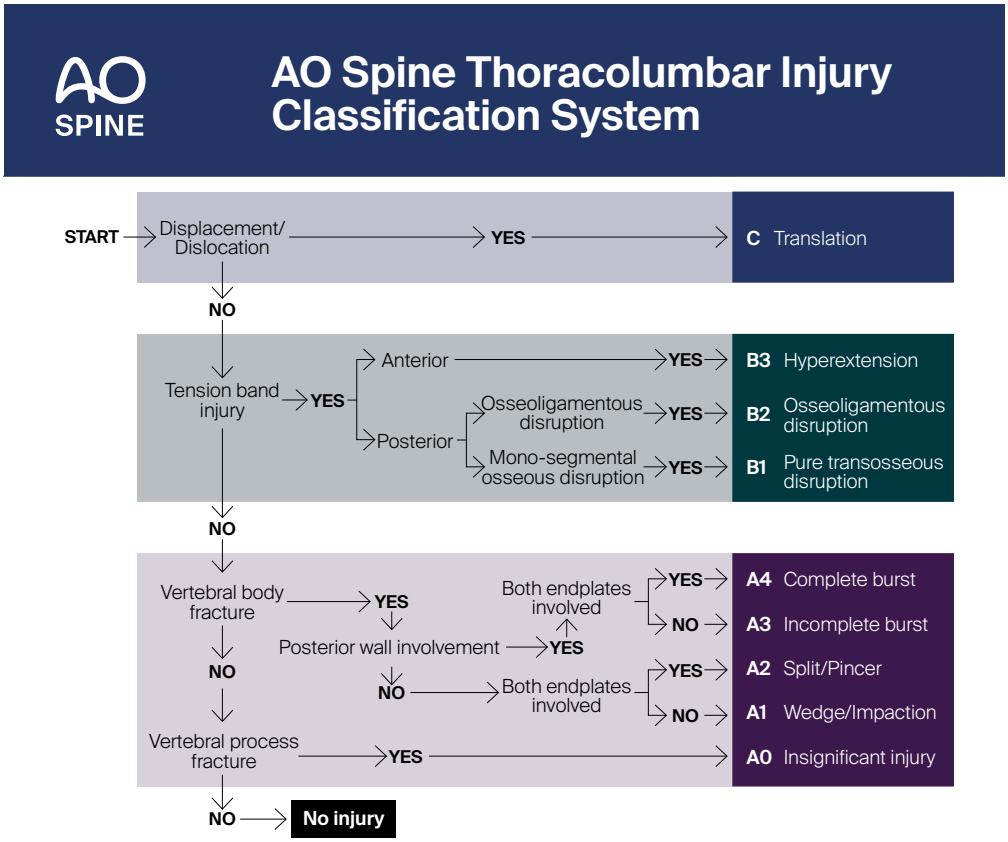

Neurology

Type	Neurological
N0	Neurology intact
N1	Transient neurologic deficit
N2	Radicular symptoms
N3	Incomplete spinal cord injury or any degree of cauda equina injury
N4	Complete spinal cord injury
NX	Cannot be examined
+	Continued spinal cord compression

Modifiers

Type	Description
M1	This modifier is used to designate fractures with an indeterminate injury to the tension band based on spinal imaging with or without MRI. This modifier is important for designating those injuries with stable injuries from a bony standpoint for which ligamentous insufficiency may help determine whether operative stabilization is a consideration.
M2	Is used to designate a patient-specific comorbidity, which might argue either for or against surgery for patients with relative surgical indications. Examples of an M2 modifier include ankylosing spondylitis or burns affecting the skin overlying the injured spine.

© 2020 AO Foundation, AO Spine
This work is licensed under the Creative Commons Attribution-NonCommercial-NoDerivatives 4.0 International License.
To view a copy of this license, visit http://creativecommons.org/licenses/by-nc-nd/4.0/

Figure A.3.: AO Spine System (2013) decision tree

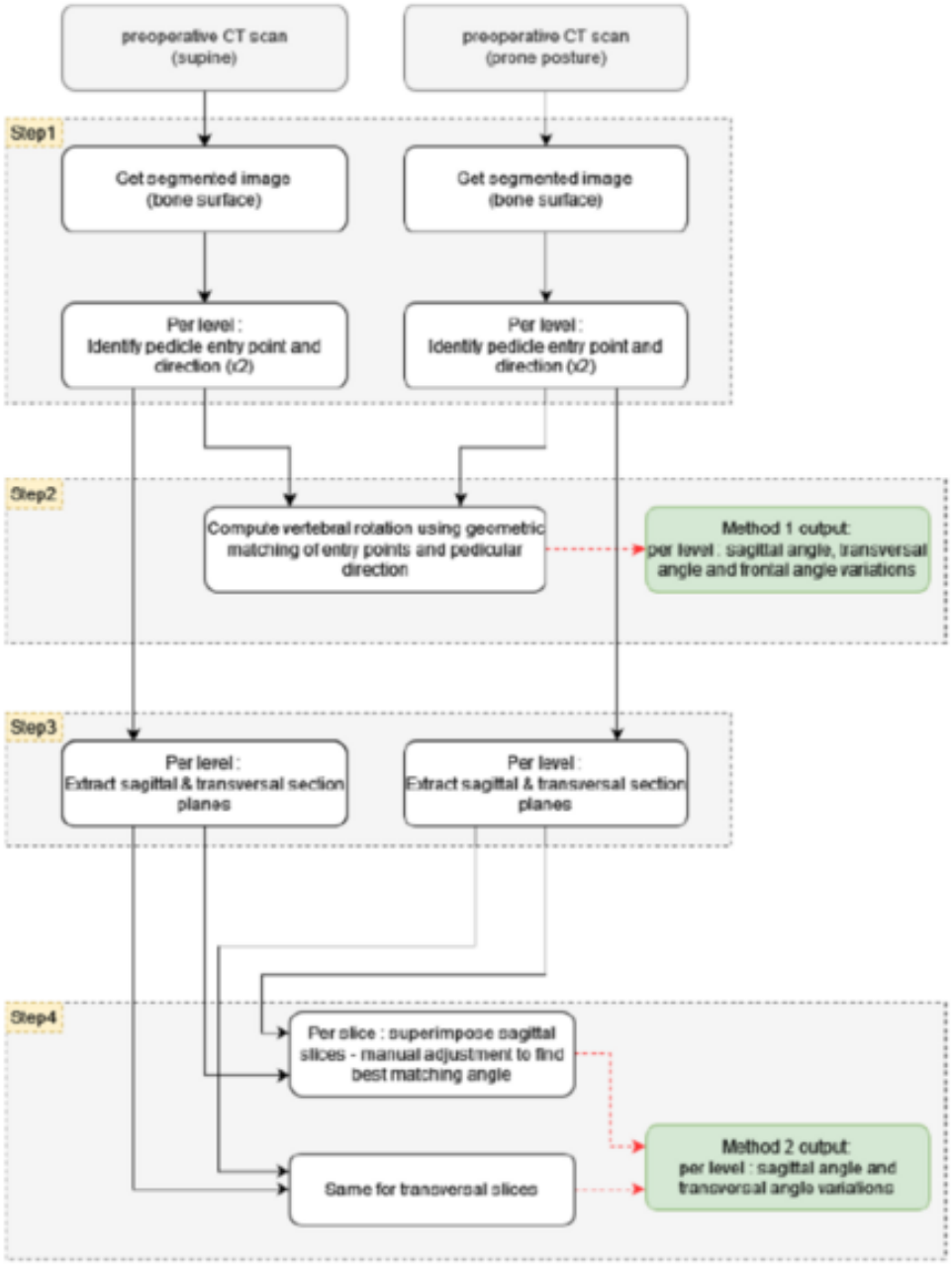

Figure A.4.: Processing method

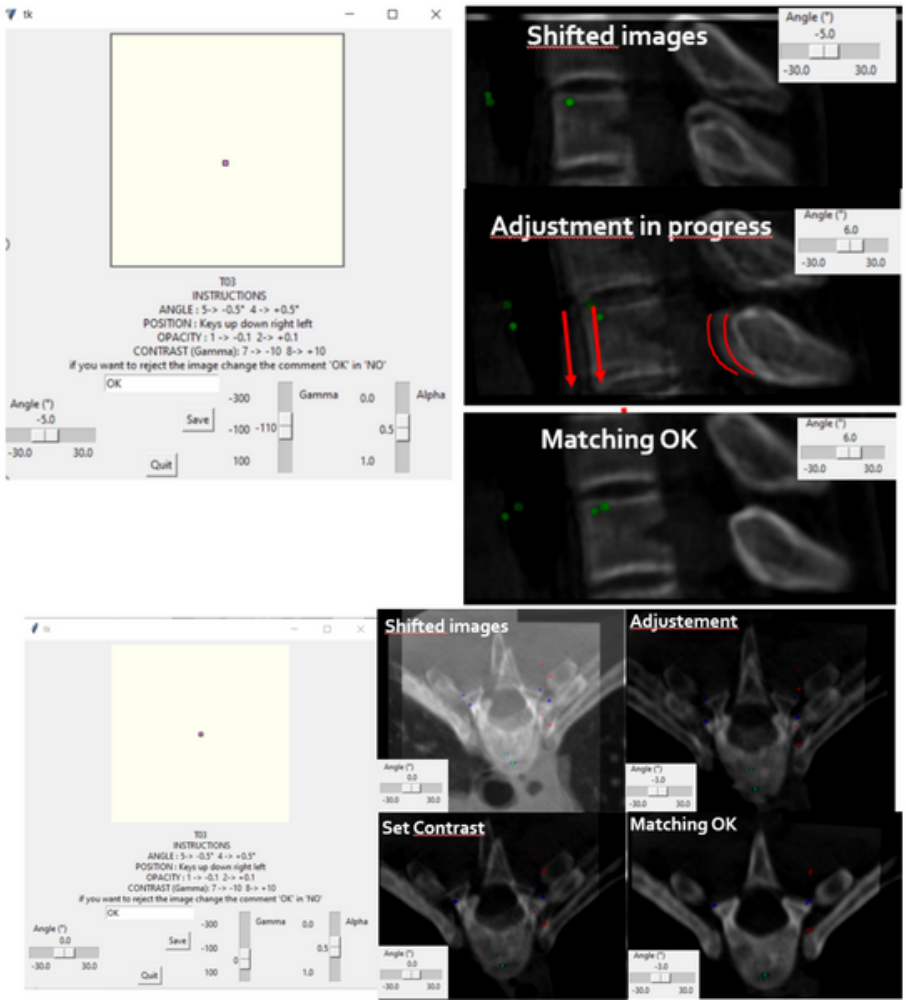

Figure A.5.: Superposition of slices of the same vertebral level, from supine and prone images, with some level of transparency, so the operator could adjust manually relative position and rotation to get a matching of the cortical shell of the vertebra.

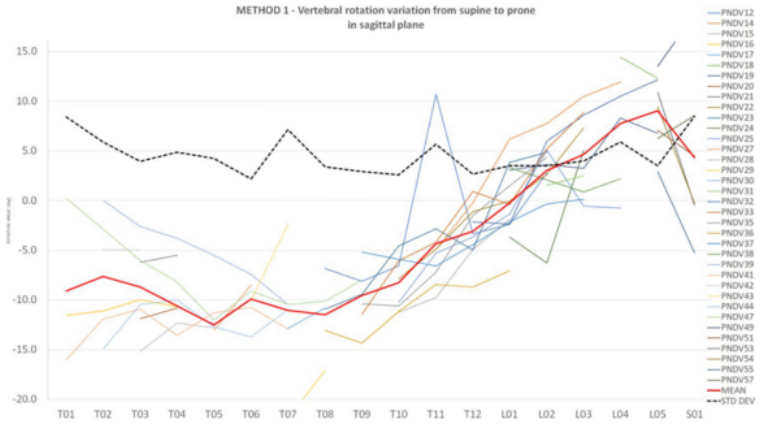

(a) Sagittal angle results

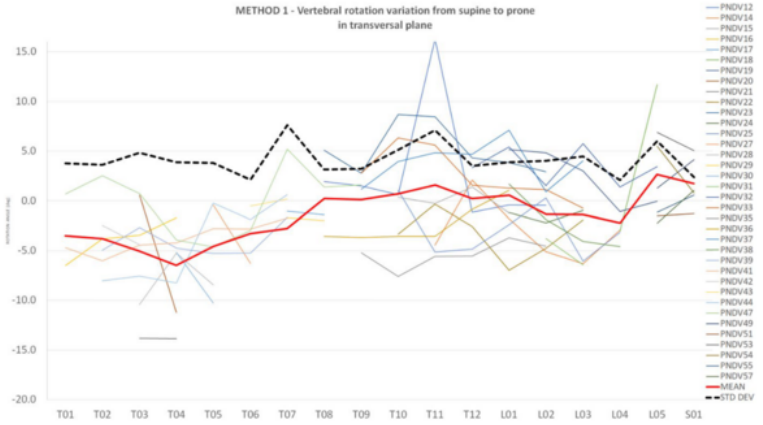

(b) Tranversal angle results

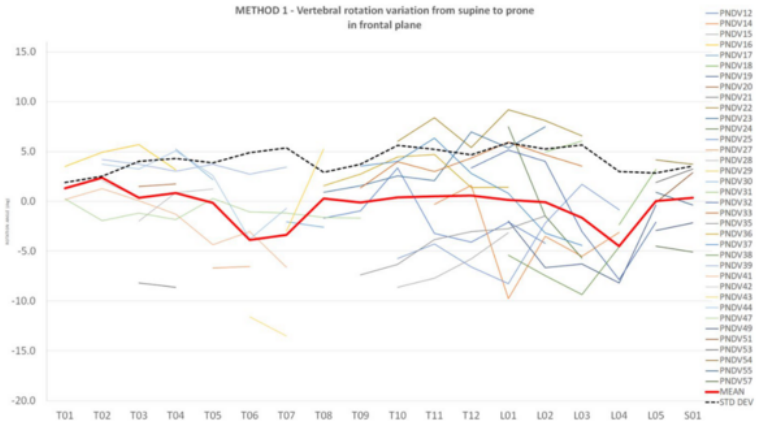

(c) Frontal angle results

Figure A.6.: Method 1 — Vertebral rotation variation from supine to prone.
The mean rotation is represented by a red line.
The standard deviation is represented by a dotted line.

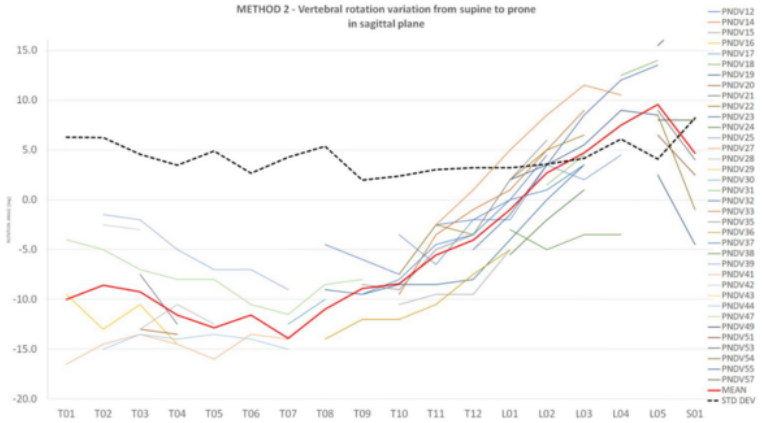

(a) Sagittal angle results

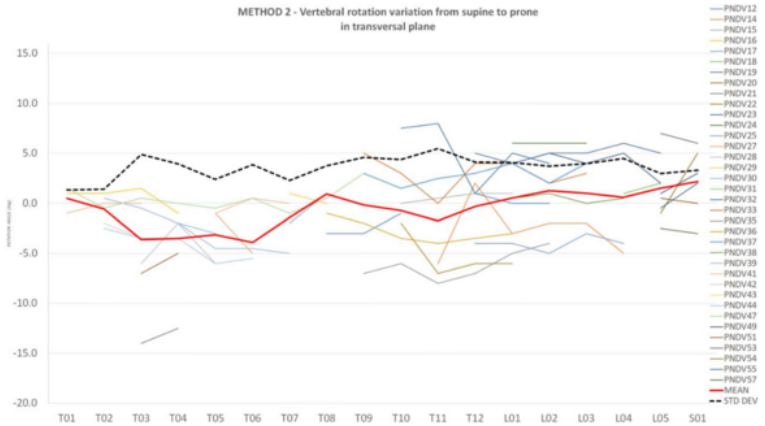

(b) Tranversal angle results

Figure A.7.: Method 2 — Vertebral rotation variation from supine to prone.
The mean rotation is represented by a red line.
The standard deviation is represented by a dotted line.

			Cannulation Coefficient Section 2 (N/mm)				F max Resultant (N)				F max Z (N)				F max XY (N)			
			PCF5	PCF10	PCF20	CC	PCF5	PCF10	PCF20	CC	PCF5	PCF10	PCF20	CC	PCF5	PCF10	PCF20	CC
10°	NP		7±2.5	16.1±1.2	23.4±5.3	21.1±3.7	60.8±19.2	189.2±9.3	266.9±35.7	253.4±39.1	35.8±13.6	160.5±9.3	222.4±33.9	176.1±26.5	25.5±6.5	29.2±1.9	47.2±2.6	77.3±13
15°	NP		3.9±2.1	10.7±4.3	17.1±12.1	26.1	55.2±5.8	142.4±35.2	261.2±81.9	247.3	47.7±5.8	112.9±35.4	228.6±66.2	185.6	9.5±2	29.6±2.9	33.1±16.6	61.9
	P	Trabecular	4			70.4	101.8			187.6	72.5			127.7	29.4			61.6
		Cortical	0.9			22.1												
20°	NP		6.7		26.4		67.4		282.4		61.5		239.2		11.6		43.2	
	P	Trabecular	6±5.6	8.2±8.2	29.6±13.6	28	67.5±25.6	110±25.2	320.9±45.4	200.8	56.9±19.3	82.5±23.9	281.7±49.9	148.3	13.3±9.2	27.6±1.9	39.5±5.8	52.5
		Cortical	9.4±9.2	10.3±3.2	26.7±10.6	21.4												
25°	NP																	
	P	Trabecular	5.4±0.9	8.5±4.7	30.1±10.8	40.7	54.4±7.5	124.1±19.2	324.6±5.9	238.8	41±20	95.6±19.7	281.3±9.1	164.8	16.6±7.8	28.5±0.4	43.3±3.2	74
		Cortical	7.6±2.3	12.8±2.7	24.8±3.4	34.8												
30°	NP		3.6±0.3				44.8±10.1				34.2±19.2				12.8±6.6			
	P	Trabecular	4.5	13.8	59.5±58.4	16.5	46.5	136.8	495.7±257.8	217.6	42.8	109.9	450.5±248.3	147.2	8.2	26.9	46.1±10.5	70.5
		Cortical	2.8	15.4	22.7±6.4	16.7												

Figure A.8.: Table showing the cannulation coefficient, the maximum resultant force, the maximum force in the z axis (load axis) and the maximum XY forces for different angles of perforation (10°, 15°, 20°, 25° and 30°) and for Sawbone PCF 5, 10 and 20 with Creaplast foam and Creaplast foam only (CC). Values are depicted as mean value ± standard deviation. NP: no perforation, P: perforation. Upper cannulation coefficient refers to trabeculae and lower one to cortical bone.

		No perforation				Perforation				
Vertebral location	Type	ETrab2=ECort2 (MPa/mm)	Max Strengh Fz Trab (kN)	Max Strengh shear Trab (kN)	Max Torque (kN.mm)	ETrab2 (MPa/mm)	ECort2 (MPa/mm)	Max Strengh Fz Cort (kN)	Max Strengh shear Cort (kN)	Max Strengh shear Cort (kN)
T2	H	12.16±7	136.52±73.18	24.12±16.93	235.18±169.7	-0.14±0.48	11.65±3.3	75.07±33.01	28.93±9.64	248.78±264.51
	S	8.68±6.68	95.14±86.89	23.54±5.63	249.48±104.47					
T3	H	41.22	296.41±232.42	76.73±56.79	408.51±51.4	19.51±12.55	7189.94±10159.59	935.97±291.18	38.62±27.18	329.31±133.23
	S	9.77	233.54	56.5	666.39	18.8±6.81	25.8±26.49	277.15±91.29	42.91±37.51	431.17±69.38
T4	H					29.43±23.27	39.31±18.81	220.94±156.85	77.23±35.18	280.58±185.96
	S	1.67±0.3	143.94±179.83	33.69±10.98	366.3±248.66	35.59±25.57	57.47±59.59	191.5±22.39	19.92±2.66	318.41±76.65
High Thoracic	H	19.42±15.61	200.48±154.44	45.16±42.19	304.51±155.15	19.56±20.53	1820.05±5072.54	197.88±175.46	52.55±33.79	280.81±183.44
	S	6.09±5.26	142.34±114.75	34.19±14.81	379.59±217.49	17.23±17.77	32.78±33.21	198.39±114.68	28.44±25.6	416.03±151.83
T9	H	30.68±32.47	352.67±410.79	33.2±38.57	368.85±263.17	22.79±30.27	29.35±19.82	239.41±262.54	59.42±42.94	376.17±65.39
	S	10.78±3.47	197.63±88.65	36.2±15.66	428.58±236.25	98.29	72.3	111.8	59.47	106.25
T11	H	19.93±25.38	266.32±154.35	45.41±41.31	391.72±163.38	35.81±39.91	26.55±53	539.38±383.89	61.85±18.09	570.35±86.54
	S	0±0	0±0	0±0	0±0	16.22±9.26	20.57±3.29	174.26±117.66	22.97±15.74	218.67±340.75
T12	H	30.45±21.53	310.88±197.52	44.32±41.04	229.81±118	31.71±37.46	21.51±14.83	367.44±354.12	65.28±78.49	323.44±319.21
	S	10.82	130.62	32.17	403.34	3.42±10.23	23.3±23.8	124.23±140.88	19.64±19.48	465.97±243.55
Low Thoracic	H	27.09±24.06	315.87±235.37	41.32±35.29	364.45±186.53	29.06±29.02	26.31±25.46	361.69±294.02	61.79±41.26	416.58±176.76
	S	10.79±2.83	180.87±79.76	35.19±12.95	422.27±193.31	21.68±32.63	28.06±22.09	147.69±111.47	26.28±19.93	297.35±296.06
L1	H	13.38±10.25	200.49±245.17	40.49±23.84	129.09±29.64	59.17±44.97	75.59±94.89	396.44±0.17	39.29±15.21	363.56±46.76
	S	23.68±6.85	212.23±83.55	40.23±13.18	452.46±58.74	19.04	25.36	192.89	50.87	469.67
L5	H	48.46±31.23	460.69±328.59	69.57±8	457.41±248.28	37.67	90.16	1208.66	68.89	628.89
	S	17.11	66.33	53.11	311.87	46.5	34.49	312.62	38.58	582.6
Lumbar	H	28.41±27.01	312±292.21	52.95±23.39	269.8±227.56	52.01±34.14	80.45±67.63	667.18±468.93	49.16±20.19	452.01±156.72
	S	22.04±6.49	175.75±99.88	43.45±12.54	417.31±85.09	32.77±19.42	29.92±6.45	252.76±84.66	44.72±8.69	526.13±79.86

Figure A.9.: Mean values of trabecular and cortical elastic moduli found for human and swine samples according the vertebral level. p-value for statistically significant difference between cadaver and animal models (*: $p < 0.05$). The samples are divided according their spinal location: blue for high thoracic. green for low thoracic and orange for lumbar. Types are H: Human. S: Swine.

B. Tables

Anatomical part	Description	Mnemonic	Unit
Global	Half lateral vertebra width	TPY	mm
	Transverse apophyse extremity position vs. mid-transverse plane	TPZ	mm
	Postero-anterior vertebra length	SPL	mm
Vertebral body	Height	VBH	mm
	End-plate depth	EPD	mm
	End-plate width	EPW	mm
	End-plate area	EPA	mm^2
	End-plate inclination to the mid-transverse plane	EPI	°
Spinal canal	Depth	SCD	mm
	Width	SCW	mm
Facet interarticularis	Inclination to the sagittal plane	SA	°
	Inclination to the transverse plane	TA	°
	Width	GDSA	mm
	Depth	PDSA	mm
	Area	FCA	mm^2
	Distance from the center to the frontal plane	CA X	mm
	Distance from the center to the sagittal plane	CA Y	mm
	Distance from the center to the mid-transverse plane	CA Z	mm
Pedicle	Inclination to the sagittal plane	PDIs	°
	Inclination to the mid-transverse plane	PDIh	°
	Length from the vertebral wall to the posterior arch	PDL	mm
	Width	PDW	mm
	Height	PDH	mm
	Distance from the lower base to the mid-transverse plane	PDZ	mm

Table B.1.: Vertebra parameter set (Laporte et al. 2000)

	PNDV12	PNDV14	PNDV15	PNDV16	PNDV17	PNDV18	PNDV19	PNDV20	PNDV21	PNDV22	PNDV23	PNDV24	PNDV25	PNDV27	PNDV28	PNDV29	PNDV30	PNDV31	PNDV32	PNDV33	PNDV35	PNDV36	PNDV37	PNDV38	PNDV39	PNDV41	PNDV42	PNDV43	PNDV44	PNDV47	PNDV49	PNDV51	PNDV53	PNDV54	PNDV55	PNDV57	Mean	Std. Dev.	N
T_1				-11.6																						-16.0				0.3							-9.1	8.4	3
T_2				-11.1																					0.0	-11.9	-4.9		-15.0	-2.9							-7.6	5.9	6
T_3				-10.0				-11.9	-6.2						-15.2										-2.6	-10.9	-5.0		-10.4	-6.0							-8.7	4.0	9
T_4				-10.7				-10.8	-5.5						-12.3		-20.6								-3.8	-13.6			-10.0	-8.2							-10.6	4.9	9
T_5														-13.1	-12.8		-20.0								-5.5	-11.3			-12.7	-12.1							-12.5	4.2	7
T_6														-8.5											-7.4	-10.8		-10.0	-13.7	-9.1							-9.9	2.2	6
T_7					-12.9											-22.0									-10.4	-12.9		-2.4	-11.0	-10.5							-11.0	7.2	7
T_8	-6.8				-10.8						-10.9					-17.1						-13.1								-10.1							-11.5	3.4	6
T_9	-8.1										-9.4									-11.5	-10.4	-14.4	-5.2						-8.0							-9.6	2.9	7
T_{10}	-6.6		-11.2							-7.9	-4.6		-10.2							-6.1	-10.6	-11.1	-5.9													-8.2	2.6	9
T_{11}	10.7	-4.9	-9.8							-4.9	-2.8		-5.3							-4.2	-7.2	-8.5	-6.6													-4.3	5.7	10
T_{12}	-3.3	-0.2	-4.9							-1.1	-5.0		-3.7						-2.1	0.9	-1.5	-8.7	-4.5													-3.1	2.7	11
L_1	-2.4	6.2	-1.9				3.1			-0.1	3.9	-3.7	-1.4						-2.3	-0.4	1.5	-7.0	-2.1	3.3												-0.2	3.5	14
L_2	2.8	7.8					3.6			2.6	4.9	-6.3	5.1					1.5	6.0	5.2	4.3		-0.3	2.1												3.0	3.5	13
L_3		10.5					3.2			7.3		5.1	-0.6					2.5	8.6	8.8			0.1	0.9												4.7	4.0	10
L_4		11.9				14.4	8.3						-0.7						10.5					2.2												7.8	5.9	6
L_5						12.3	6.8												12.2												13.5	7.1	10.9	9.4	2.9	6.3	9.0	3.5	9
S_1																															18.8	4.5	-0.5	-0.3	-5.3	8.6	4.3	8.5	6
Std. Dev.	6.7	6.5	4.3	0.7	1.5	1.5	2.4	0.8	0.5	5.4	6.0	5.9	4.7	3.2	1.5	3.5	0.4	0.7	6.3	6.9	6.3	2.9	2.7	1.0	3.7	1.9	0.1	5.4	2.0	3.9	3.7	1.8	8.0	6.9	5.8	1.6			148
Mean	-2.0	5.2	-7.0	-10.8	-11.8	13.4	5.0	-11.4	-5.9	-0.7	-3.4	-1.6	-2.4	-10.8	-13.4	-19.5	-20.3	2.0	5.5	-1.0	-4.0	-10.5	-3.5	2.1	-5.0	-12.5	-5.0	-6.2	-12.1	-7.4	16.1	5.8	5.2	4.6	-1.2	7.4			

Table B.2.: Method 1 - Sagittal angle

	PNDV12	PNDV14	PNDV15	PNDV16	PNDV17	PNDV18	PNDV19	PNDV20	PNDV21	PNDV22	PNDV23	PNDV24	PNDV25	PNDV27	PNDV28	PNDV29	PNDV30	PNDV31	PNDV32	PNDV33	PNDV35	PNDV36	PNDV37	PNDV38	PNDV39	PNDV41	PNDV42	PNDV43	PNDV44	PNDV47	PNDV49	PNDV51	PNDV53	PNDV54	PNDV55	PNDV57	Mean	Std. Dev.	N
T_1				-6.5																						-4.7				0.7							-3.5	3.8	3
T_2				-3.8																					-5.0	-6.0	-2.5		-8.0	2.5							-3.8	3.6	6
T_3				-3.5				0.6	-13.8						-10.4										-2.7	-4.4	-4.4		-7.6	0.7							-5.1	4.8	9
T_4				-1.7				-11.2	-13.9						-5.3		-5.2								-4.7	-4.2			-8.3	-3.9							-6.5	3.9	9
T_5														-0.4	-8.4		-10.3								-5.3	-2.8			-0.2	-4.6							-4.6	3.8	7
T_6														-6.3											-5.2	-2.8		-0.5	-1.9	-3.0							-3.3	2.1	6
T_7					-1.0											-1.7									-1.6	-1.7		0.2	0.6	5.2							-2.8	7.6	7
T_8	1.9				-1.4						5.1					-2.0						-3.6								1.4							0.2	3.2	6
T_9	1.5										2.8									2.8	-5.2	-3.7	1.2							1.6							0.1	3.2	7
T_{10}	0.6		0.4							-3.3	8.7		1.1							6.3	-7.6	-3.6	3.9														0.7	5.1	9
T_{11}	16.3	-4.4	-0.2							-0.3	8.5		-5.2							5.6	-5.6	-3.6	4.8														1.6	7.1	10
T_{12}	-1.2	2.1	1.4							-2.6	4.3		-4.9						3.3	1.6	-5.5	-0.9	4.7															0.2	3.5	11
L_1	-0.4	-1.8	-1.2				5.2			-7.0	3.8	-1.2	-2.4						5.4	1.3	-3.7	1.1	7.1	1.7														0.6	3.9	14
L_2	-0.4	-5.1					4.8			-4.8	2.9	-2.2	0.3					-3.8	1.5	1.1	-4.5		0.9	-1.9														-1.4	4.0	13
L_3		-6.3					3.0			-1.9		-0.9	-6.0					-6.4	5.7	-0.8			4.0	-4.1														-1.4	4.5	10
L_4		-2.9				-3.1	-1.1						-3.2						1.4					-4.6														-2.2	2.1	6
L_5						11.7	-0.1												3.4												1.3	-1.5	6.9	5.5	-1.1	-2.2	2.6	6.0	9
S_1																															4.1	-1.3	5.1	0.8	0.6	1.1	1.7	2.4	6
Std. Dev.	6.1	3.0	1.1	2.0	0.3	10.4	2.8	8.4	0.0	2.3	2.5	0.7	2.7	4.2	2.6	0.2	3.6	1.9	1.8	2.6	1.3	2.0	2.2	2.8	1.5	1.4	1.4	0.5	4.2	3.2	2.0	0.1	1.3	3.3	1.2	2.3			148
Mean	2.6	-3.1	0.1	-3.9	-1.2	4.3	2.4	-5.3	-13.8	-3.3	5.2	-1.4	-2.9	-3.3	-8.0	-1.8	-7.7	-5.1	3.5	2.6	-5.4	-2.4	3.8	-2.2	-4.1	-3.8	-3.4	-0.2	-4.2	0.1	2.7	-1.4	6.0	3.1	-0.3	-0.6			

Table B.3.: Method 1 - Transversal angle

	PNDV12	PNDV14	PNDV15	PNDV16	PNDV17	PNDV18	PNDV19	PNDV20	PNDV21	PNDV22	PNDV23	PNDV24	PNDV25	PNDV27	PNDV28	PNDV29	PNDV30	PNDV31	PNDV32	PNDV33	PNDV35	PNDV36	PNDV37	PNDV38	PNDV39	PNDV41	PNDV42	PNDV43	PNDV44	PNDV47	PNDV49	PNDV51	PNDV53	PNDV54	PNDV55	PNDV57	Mean	Std. Dev.	N
T_1				3.5																						0.2				0.2							1.3	1.9	3
T_2				4.9																					4.2	1.3	2.0		3.7	-1.9							2.4	2.5	6
T_3				5.7				1.5	-8.2						-2.0										3.7	0.1	0.4		3.3	-1.2							0.4	4.0	9
T_4				3.2				1.8	-8.6						0.9		5.3								3.0	-1.3			5.1	-1.8							0.8	4.3	9
T_5														-6.7	1.3		2.2								3.7	-4.4			2.6	0.3							-0.1	3.9	7
T_6														-6.5											2.7	-3.0		-11.6	-3.8	-1.1							-3.9	4.9	6
T_7					-2.0											-3.0									3.4	-6.6		-13.5	-0.7	-1.2							-3.4	5.4	7
T_8	-1.7				-2.6						0.9					5.2						1.6								-1.6							0.3	2.9	6
T_9	-0.9										1.6									1.4	-7.4	2.7	3.5							-1.7							-0.1	3.7	7
T_{10}	3.3		-8.6							6.0	2.6		-5.7							4.0	-6.3	4.5	4.0														0.4	5.6	9
T_{11}	-3.2	-0.3	-7.7							8.4	2.1		-4.3							3.0	-3.8	4.7	6.3														0.5	5.2	10
T_{12}	-4.1	1.6	-5.8							5.4	7.0		-6.6						3.4	4.3	-3.0	1.4	2.8															0.6	4.7	11
L_1	-2.1	-9.8	-3.1				-2.0			9.2	5.4	7.5	-8.3						5.2	5.9	-2.8	1.4	0.8	-5.4														0.1	5.9	14
L_2	-4.2	-3.5					-6.7			8.1	7.5	-1.5	-2.2					5.0	4.0	4.7	-1.5		-3.2	-7.5														-0.1	5.3	13
L_3		-5.5					-6.3			6.6		-5.7	1.7					6.1	-3.0	3.5			-4.4	-9.4														-1.6	5.6	10
L_4		-3.1				-2.3	-8.2						-0.8						-7.8					-4.5														-4.5	3.0	6
L_5						3.2	-0.4												-2.1												-2.9	-0.1	1.9	4.2	0.9	-4.5	0.0	2.9	9
S_1																															-2.1	2.9	3.2	3.7	-0.4	-5.1	0.4	3.5	6
Mean	-1.8	-3.4	-6.3	4.3	-2.3	0.4	-4.7	1.6	-8.4	7.3	3.8	0.1	-3.7	-6.6	0.1	1.1	3.7	5.5	-0.1	3.8	-4.1	2.7	1.4	-6.7	3.5	-2.0	1.2	-12.6	1.7	-1.1	-2.5	1.4	2.6	3.9	0.3	-4.8			148
Std. Dev.	2.6	4.0	2.4	1.2	0.4	3.9	3.3	0.2	0.3	1.5	2.7	6.7	3.5	0.1	1.8	5.8	2.2	0.8	5.1	1.4	2.3	1.5	3.9	2.2	0.5	2.8	1.2	1.4	3.3	0.8	0.6	2.1	1.0	0.3	0.9	0.4			

Table B.4.: Method 1 - Frontal angle

	PNDV12	PNDV14	PNDV15	PNDV16	PNDV17	PNDV18	PNDV19	PNDV20	PNDV21	PNDV22	PNDV23	PNDV24	PNDV25	PNDV27	PNDV28	PNDV29	PNDV30	PNDV31	PNDV32	PNDV33	PNDV35	PNDV36	PNDV37	PNDV38	PNDV39	PNDV41	PNDV42	PNDV43	PNDV44	PNDV47	PNDV49	PNDV51	PNDV53	PNDV54	PNDV55	PNDV57	Mean	Std. Dev.	N
T_1				-9.5																						-16.5				-4.0							-10.0	6.3	3
T_2				-13.0																					-1.5	-14.5	-2.5		-15.0	-5.0							-8.6	6.3	6
T_3				-10.5				-13.0	-7.5						-13.0										-2.0	-13.5	-3.0		-13.5	-7.0							-9.2	4.5	9
T_4				-14.5				-13.5	-12.5						-10.5										-5.0	-14.5			-14.0	-8.0							-11.6	3.5	8
T_5															-12.5		-20.0								-7.0	-16.0			-13.5	-8.0							-12.8	4.9	6
T_6														-13.5											-7.0	-13.5		-11.0	-14.0	-10.5							-11.6	2.7	6
T_7					-12.5											-21.5									-9.0	-14.0			-15.0	-11.5							-13.9	4.3	6
T_8	-4.5				-10.0						-9.0					-20.0						-14.0								-8.5							-11.0	5.4	6
T_9	-6.0										-9.5										-8.5	-12.0	-9.5							-8.0							-8.9	2.0	6
T_{10}	-7.5		-10.5							-7.5	-8.5		-3.5							-9.5	-9.0	-12.0	-8.0														-8.4	2.4	9
T_{11}	-2.5	-2.5	-9.5							-2.5	-8.5		-6.5							-3.5	-5.0	-10.5	-4.5														-5.6	3.0	10
T_{12}	-2.0	1.0	-9.5							-3.5	-8.0		-2.0						-5.0	-1.0	-3.5	-7.5	-3.5														-4.0	3.2	11
L_1	0.0	5.0	-5.0				2.0			2.0	-4.0	-5.5	-2.0						-1.5	1.0	2.0	-5.0	0.0	-3.0													-1.0	3.2	14
L_2	4.5	8.5					3.5			5.0	0.0	-2.0	3.5					1.5	3.5	5.0	6.0		1.0	-5.0													2.7	3.6	13
L_3		11.5					5.5			6.5		1.0	2.0					4.5	8.5	9.0			3.5	-3.5													4.9	4.4	10
L_4		10.5				12.5	9.0						4.5						12.0					-3.5													7.5	6.1	6
L_5						14.0	8.5												13.5												15.5	6.5	9.0	8.5	2.5	8.0	9.6	4.1	9
S_1																															19.0	2.5	4.0	-1.0	-4.5	8.0	4.7	8.2	6
Std. Dev.	4.0	5.6	2.5	2.3	1.8	1.1	3.1	0.4	3.5	5.4	3.5	3.3	4.0		1.3	1.1		2.1	7.5	6.5	5.9	3.3	4.8	0.9	3.0	1.2	0.4		0.7	2.4	2.5	2.8	3.5	6.7	4.9	0.0			144
Mean	-2.6	5.7	-8.6	-11.9	-11.3	13.3	5.7	-13.3	-10.0	0.0	-6.8	-2.2	-0.6	-13.5	-12.0	-20.8	-20.0	3.0	5.2	0.2	-3.0	-10.2	-3.0	-3.8	-5.3	-14.6	-2.8	-11.0	-14.2	-7.8	17.3	4.5	6.5	3.8	-1.0	8.0			

Table B.5.: Method 2 - Sagittal angle

	PNDV12	PNDV14	PNDV15	PNDV16	PNDV17	PNDV18	PNDV19	PNDV20	PNDV21	PNDV22	PNDV23	PNDV24	PNDV25	PNDV27	PNDV28	PNDV29	PNDV30	PNDV31	PNDV32	PNDV33	PNDV35	PNDV36	PNDV37	PNDV38	PNDV39	PNDV41	PNDV42	PNDV43	PNDV44	PNDV47	PNDV49	PNDV51	PNDV53	PNDV54	PNDV55	PNDV57	Mean	Std. Dev.	N
T_1				1.0																						-1.0				1.5							0.5	1.3	3
T_2				1.0																					0.5	0.0	-2.0		-2.5	-0.5							-0.6	1.4	6
T_3				1.5				-7.0	-14.0						-6.0										-0.5	0.0	-3.5		-3.5	0.5							-3.6	4.9	9
T_4				-1.0				-5.0	-12.5						-2.0		-2.0								-2.0				-3.5	0.0							-3.5	3.9	8
T_5														-1.0	-6.0		-3.0								-4.5	-1.0			-6.0	-0.5							-3.1	2.4	7
T_6														-5.0											-4.5	0.5		-9.5	-5.5	0.5							-3.9	3.9	6
T_7					-2.0											1.0									-5.0	0.0				-1.0							-1.4	2.3	5
T_8	-3.0				1.0						8.0					0.0						-1.0								0.5							0.9	3.7	6
T_9	-3.0																			5.0	-7.0	-2.0	3.0							3.0							-0.2	4.6	6
T_{10}	-1.0		0.0							-2.0	7.5		-6.0							3.0	-6.0	-3.5	1.5														-0.7	4.4	9
T_{11}		-6.0	0.5							-7.0	8.0									0.0	-8.0	-4.0	2.5														-1.8	5.5	8
T_{12}	1.0	2.0	1.0							-6.0	1.0		-4.0						5.0	4.0	-7.0	-3.5	3.0															-0.3	4.1	11
L_1	0.0	-3.0	1.0				4.0			-6.0	5.0	6.0	-4.0						4.0	4.0	-5.0	-3.0	4.0	0.5														0.5	4.1	14
L_2	0.0	-2.0					5.0				4.0	6.0	-5.0						5.0	2.0	-4.0		2.0	1.0														1.3	3.7	11
L_3		-2.0					4.0			-6.0		6.0	-3.0					-1.0	5.0	3.0			4.0	0.0														1.0	4.0	10
L_4		-5.0				1.0	5.0						-4.0						6.0					0.5														0.6	4.5	6
L_5						2.0	2.0												5.0												1.0	0.5	7.0	-1.0	-0.5	-2.5	1.5	3.0	9
S_1																															3.0	0.0	6.0	5.0	2.0	-3.0	2.2	3.3	6
Std. Dev.	1.7	2.8	0.5	1.1	2.1	0.7	1.2	1.4	1.1	1.9	2.8	0.0	1.0	2.8	2.3	0.7	0.7		0.6	1.6	1.5	1.1	0.9	0.4	2.3	0.6	1.1		1.5	1.2	1.4	0.4	0.7	4.2	1.8	0.4			140
Mean	-1.0	-2.7	0.6	0.6	-0.5	1.5	4.0	-6.0	-13.3	-5.4	5.6	6.0	-4.3	-3.0	-4.7	0.5	-2.5	-1.0	5.0	3.0	-6.2	-2.8	2.9	0.5	-2.7	-0.3	-2.8	-9.5	-4.2	0.4	2.0	0.3	6.5	2.0	0.8	-2.8			

Table B.6.: Method 2 - Transversal angle

Normalized cortical thickness											
Sub-group	Spinal Level	Vertebra (N)	Top vertebral endplate nucleus	Top vertebral endplate ring	Bottom vertebral endplate nucleus	Bottom vertebral plate ring	Top vertebral body	Mid vertebral body	Bottom vertebral body	Inferior articular processes	Posterior arch without inferior articular processes)
In-vivo	High thoracic	9	0.7 ± 0.06	0.68 ± 0.06	0.66 ± 0.07	0.82 ± 0.07	0.72 ± 0.05	0.71 ± 0.07	0.79 ± 0.09	0.39 ± 0.07	0.35 ± 0.02
	Low thoracic	9	0.45 ± 0.2	0.55 ± 0.13	0.52 ± 0.18	0.64 ± 0.1	0.48 ± 0.26	0.46 ± 0.16	0.61 ± 0.19	0.3 ± 0.07	0.28 ± 0.03
	Lumbar	3	0.5 ± 0.36	0.59 ± 0.34	0.43 ± 0.32	0.53 ± 0.35	0.59 ± 0.38	0.43 ± 0.26	0.42 ± 0.27	0.35 ± 0.05	0.25 ± 0.05
Cadaver	High thoracic	6	0.54 ± 0.2	0.56 ± 0.12	0.52 ± 0.15	0.48 ± 0.18	0.48 ± 0.14	0.5 ± 0.16	0.52 ± 0.17	0.19 ± 0.018	0.28 ± 0.09
	Low thoracic	6	0.37 ± 0.13	0.39 ± 0.11	0.35 ± 0.14	0.36 ± 0.13	0.33 ± 0.1	0.34 ± 0.12	0.33 ± 0.11	0.19 ± 0.09	0.2 ± 0.04
	Lumbar	2	0.49 ± 0.08	0.38 ± 0.1	0.45 ± 0.15	0.35 ± 0.22	0.36 ± 0.11	0.33 ± 0.03	0.37 ± 0.17	0.18 ± 0.06	0.19 ± 0.08
Swine	High thoracic	3	0.66 ± 0.06	0.63 ± 0.03	0.67 ± 0.09	0.57 ± 0.04	0.47 ± 0.13	0.44 ± 0.03	0.4 ± 0.03	0.25 ± 0.02	0.2 ± 0.01
	Low thoracic	3	0.64 ± 0.04	0.58 ± 0.06	0.58 ± 0.08	0.58 ± 0.07	0.42 ± 0.08	0.39 ± 0.02	0.37 ± 0.02	0.14 ± 0.05	0.13 ± 0.03
	Lumbar	1	0.56	0.44	0.76	0.71	0.35	0.39	0.44	0.19	0.18
Cortical density (HU)											
Sub-group	Spinal Level	Vertebra (N)	Top vertebral endplate nucleus	Top vertebral endplate ring	Bottom vertebral endplate nucleus	Bottom vertebral plate ring	Top vertebral body	Mid vertebral body	Bottom vertebral body	Inferior articular processes	Posterior arch without inferior articular processes)
In-vivo	High thoracic	9	195.5 ± 57.68	344.32 ± 86.04	206.06 ± 59.79	296.28 ± 63.06	289.54 ± 74.19	265.51 ± 78.19	288.67 ± 87.99	576.67 ± 71.33	312.3 ± 57.03
	Low thoracic	9	276.85 ± 20	326 ± 27.7	303.52 ± 25	326.15 ± 35.9	299.27 ± 39.44	285.44 ± 31.44	310.65 ± 46.89	642.82 ± 97	492.64 ± 50.47
	Lumbar	3	262.17 ± 19.42	305.84 ± 29.06	306.79 ± 47.82	329.1 ± 66.41	306.66 ± 17.75	310.17 ± 32.36	344.22 ± 64.22	664.63 ± 127.05	555.69 ± 94.32
Cadaver	High thoracic	6	513.77 ± 92.03	645.31 ± 95.61	544.77 ± 60.1	642.82 ± 113.77	584.91 ± 161.37	502.22 ± 133.82	571.12 ± 146.75	872.63 ± 258.61	672.24 ± 106.63
	Low thoracic	6	508.79 ± 60.21	628.66 ± 44.45	468.32 ± 59.72	642.61 ± 75.2	650.18 ± 66.69	533.44 ± 57.49	578.33 ± 93.61	770.98 ± 191.86	654.72 ± 91.50
	Lumbar	2	452.88 ± 65.99	604.08 ± 10.88	414.93 ± 15.32	602.43 ± 132.51	642.44 ± 20.91	510.07 ± 47.63	609.66 ± 45.93	745.4 ± 186.29	652.01 ± 107.27
Swine	High thoracic	3	371.44 ± 15.04	373.19 ± 14.65	433.59 ± 9.94	398.14 ± 15.78	352.57 ± 7.1	351.42 ± 10.72	369.94 ± 12.48	573.49 ± 19.23	466.79 ± 11.5
	Low thoracic	3	374.88 ± 27.49	363.18 ± 14.25	423.75 ± 7.34	383.62 ± 24.78	339.16 ± 13.2	336.38 ± 14.01	359.18 ± 15.64	416.76 ± 76.8	369.37 ± 21.17
	Lumbar	1	450.06	394.79	448.57	410.75	372.86	347.65	381.70	397.8	386.78

Table B.7.: Mean values of Normalized CTh and CBD by vertebral functional area, by sub-group (i.e. cadaveric vertebrae, swine vertebrae, and human in-vivo vertebrae), and by vertebral levels (i.e. high thoracic, low thoracic, and lumbar). Values are expressed as mean ± standard deviation.

Normalized Cortical Thickness				
Functional area	In-vivo - Cadaver		In-vivo - Swine	
	W	p-value	W	p-value
Top vertebral endplate nucleus	266	$1.476 \cdot 10^{-5}$ (***)	111	0.047,95 (*)
Top vertebral endplate ring	279	$5.888 \cdot 10^{-7}$ (***)	133	0.0007314 (***)
Top vertebral body	290	$1.035 \cdot 10^{-8}$ (***)	146	$3.378 \cdot 10^{-6}$ (***)
Mid vertebral body	281	$3.216 \cdot 10^{-7}$ (***)	146	$3.378 \cdot 10^{-6}$ (***)
Bottom vertebral body	285	$8.362 \cdot 10^{-8}$ (***)	147	$1.689 \cdot 10^{-6}$ (***)
Bottom vertebral endplate nucleus	270	$6.075 \cdot 10^{-6}$ (***)	90	0.4046
Bottom vertebral endplate ring	294	$8.621 \cdot 10^{-10}$ (***)	146	$3.378 \cdot 10^{-6}$ (***)
Inferior articular processes	286	$5.776 \cdot 10^{-8}$ (***)	147	$1.689 \cdot 10^{-6}$ (***)
Posterior arch (without inferior articular processes)	259	$5.944 \cdot 10^{-5}$ (***)	147	$1.689 \cdot 10^{-6}$ (***)
Cortical Bone Density				
Functional area	In-vivo - Cadaver		In-vivo - Swine	
	W	p-value	W	p-value
Top vertebral endplate nucleus	0	$8.621 \cdot 10^{-10}$ (***)	0	$1.689 \cdot 10^{-6}$ (***)
Top vertebral endplate ring	0	$8.621 \cdot 10^{-10}$ (***)	22	0.004726 (**)
Top vertebral body	1	$1.724 \cdot 10^{-9}$ (***)	17	0.001569 (**)
Mid vertebral body	2	$3.448 \cdot 10^{-9}$ (***)	10	0.000223 (***)
Bottom vertebral body	2	$3.448 \cdot 10^{-9}$ (***)	30	0.0199 (*)
Bottom vertebral endplate nucleus	0	$8.621 \cdot 10^{-10}$ (***)	0	$1.689 \cdot 10^{-6}$ (***)
Bottom vertebral endplate ring	0	$8.621 \cdot 10^{-10}$ (***)	6	$5.067 \cdot 10^{-5}$ (***)
Inferior articular processes	72	0.01074 (*)	124	0.005767 (**)
Posterior arch (without inferior articular processes)	10	$1.198 \cdot 10^{-7}$ (***)	66	0.7166

Table B.8.: Normalized CTh comparison in each vertebral functional area between the human-In vivo sub-group and the cadaveric sub-group, and CBD comparison in each vertebral functional area between the human-In vivo sub-group and the cadaveric sub-group. The Wilcoxon test was used.

Revision per diagnosis (%)	ICD-9-CM	ICD-9 description
Cervical fusion		
1. 46.4	996.49	Other mechanical complication of other internal orthopedic device, implant, and graft
2. 8.2	996.78	Other complications due to other internal orthopedic device, implant, and graft
3. 7.7	721.0	Cervical spondylosis without myelopathy
4. 6.8	722.0	Displacement of cervical intervertebral disc without myelopathy
5. 5.3	723.0	Cervicalgia
6. 4.1	722.4	Degeneration of cervical intervertebral disc
Thoracic fusion		
1. 46.7	996.49	Other mechanical complication of other internal orthopedic device, implant, and graft
2. 4.1	737.10	Kyphosis (acquired) (postural)
3. 3.9	996.78	Other complications due to other internal orthopedic device, implant, and graft
4. 3.2	737.30	Scoliosis [and kyphoscoliosis], idiopathic
5. 2.9	737.19	Other kyphosis (acquired)
6. 2.4	724.01	Spinal stenosis, thoracic region
Lumbar fusion		
1. 39.6	996.49	Other mechanical complication of other internal orthopedic device, implant, and graft
2. 10.4	996.78	Other complications due to other internal orthopedic device, implant, and graft
3. 9.6	724.02	Spinal stenosis, lumbar region, without neurogenic claudication
4. 8.1	722.52	Degeneration of lumbar or lumbosacral intervertebral disc
5. 5.9	722.83	Postlaminectomy syndrome, lumbar region
6. 5.2	721.3	Lumbosacral spondylosis without myelopathy

Table B.9.: Primary diagnoses for spinal fusion revisions (Rajaee et al. 2014)

Methods	Reference	Foreground feature
MRF	Rother et al. 2006	Pixel value histogram
	Mukherjee et al. 2009	Pixel value histogram
	Hochbaum et al. 2009	Pixel value and texture histograms
	Vicente et al. 2010	Pixel value histogram
	G. Kim; Xing, et al. 2011	Pixel value and SIFT features
	Chang et al. 2011	SIFT features
	Alexe et al. 2010	SIFT features
Random walks	Collins et al. 2012	Pixel value and texture histograms
	Fabijańska et al. 2015	Intensity and gray difference
	Dong et al. 2016	Label prior from user scribbles
Active contours	Fanman Meng et al. 2012	Pixel value histogram
	T. Zhang et al. 2012	Co-registered atlas and statistical features
	Z. Zhang et al. 2016	Saliency information
Clustering	Joulin et al. 2010	SIFT, Gabor filter and pixel value histogram
	Joulin et al. 2012	Pixel value and location information
	E. Kim et al. 2012	Pyramid of LAB color, HOG texture, SURF feature histogram
Graph theory	Fanman Meng et al. 2012	Pixel value histogram
	Meng et al. 2012	Pixel value and shape information
Thermal diffusion	G. Kim; Xing, et al. 2011	LAB color and texture information
	G. Kim; Xing 2012	Pixel value and texture histogram
Object	Alexe et al. 2010	Multi-scale saliency, color contrast, edge density, superpixel straddling
	Vicente et al. 2010	33 types of features

Table B.10.: Examples of co-segmentation methods

Bibliography

ABE, Y.; ITO, M.; ABUMI, K., et al., 2011. A Novel Cost-Effective Computer-Assisted Imaging Technology for Accurate Placement of Thoracic Pedicle Screws. *Journal of Neurosurgery. Spine*. Vol. 15, no. 5, pp. 479–485. ISSN 1547-5646. Available from DOI: 10.3171/2011.6.SPINE10721 (cit. on pp. 130, 133).

ABUL-KASIM, K.; GUNNARSSON, M.; MALY, P., et al., 2008. Radiation Dose Optimization in CT Planning of Corrective Scoliosis Surgery: A Phantom Study. *The Neuroradiology Journal* [online]. Vol. 21, no. 3, pp. 374–382 [visited on 2023-07-19]. ISSN 1971-4009, ISSN 2385-1996. Available from DOI: 10.1177/197140090802100313 (cit. on p. 44).

ABUL-KASIM, K., 2010. Low-Dose Spine CT: Optimisation and Clinical Implementation. *Radiation Protection Dosimetry*. Vol. 139, no. 1-3, pp. 169–172. ISSN 1742-3406. Available from DOI: 10.1093/rpd/ncp306 (cit. on p. 130).

ABUL-KASIM, K.; OVERGAARD, A.; MALY, P., et al., 2009. Low-Dose Helical Computed Tomography (CT) in the Perioperative Workup of Adolescent Idiopathic Scoliosis. *European Radiology* [online]. Vol. 19, no. 3, pp. 610–618 [visited on 2023-03-08]. ISSN 0938-7994, ISSN 1432-1084. Available from DOI: 10.1007/s00330-008-1178-4 (cit. on p. 130).

ABUMI, K.; ITOH, H.; TANEICHI, H., et al., 1994. Transpedicular Screw Fixation for Traumatic Lesions of the Middle and Lower Cervical Spine: Description of the Techniques and Preliminary Report. *Journal of Spinal Disorders*. Vol. 7, no. 1, pp. 19–28. ISSN 08950385. Available from DOI: 10.1097/00002517-199407010-00003 (cit. on p. 53).

AGRAWAL, R.; SRIKANT, R., 1994. Fast Algorithms for Mining Association Rules in Large Databases. In: *Proceedings of the 20th International Conference on Very Large Data Bases* [online]. San Francisco, CA, USA: Morgan Kaufmann Publishers Inc., pp. 487–499 [visited on 2024-03-28]. VLDB '94. ISBN 978-1-55860-153-6 (cit. on p. 86).

AHRENS, J.; GEVECI, B.; LAW, C., 2005. ParaView: An End-User Tool for Large-Data Visualization. In: *Visualization Handbook*. Elsevier, pp. 717–731. Available from DOI: 10.1016/B978-012387582-2/50038-1 (cit. on pp. 115, 149).

ALEXE, B.; DESELAERS, T.; FERRARI, V., 2010. What Is an Object? In: *2010 IEEE Computer Society Conference on Computer Vision and Pattern Recognition* [online], pp. 73–80 [visited on 2024-03-22]. ISSN 1063-6919. Available from DOI: 10.1109/CVPR.2010.5540226 (cit. on p. 184).

ALTINI, N.; DE GIOSA, G.; FRAGASSO, N., et al., 2021. Segmentation and Identification of Vertebrae in CT Scans Using CNN, k-Means Clustering and k-NN. *Informatics* [online]. Vol. 8, no. 2, p. 40 [visited on 2024-04-05]. ISSN 2227-9709. Available from DOI: 10.3390/informatics8020040 (cit. on p. 98).

AMIOT, L. P.; LANG, K.; PUTZIER, M., et al., 2000. Comparative Results between Conventional and Computer-Assisted Pedicle Screw Installation in the Thoracic, Lumbar, and Sacral Spine. *Spine*. Vol. 25, no. 5, pp. 606–614. ISSN 0362-2436. Available from DOI: 10.1097/00007632-200003010-00012 (cit. on p. 67).

AMIROUCHE, F.; SOLITRO, G. F.; MAGNAN, B. P., 2016. Stability and Spine Pedicle Screws Fixation Strength-A Comparative Study of Bone Density and Insertion Angle. *Spine Deformity*. Vol. 4, no. 4, pp. 261–267. ISSN 2212-1358. Available from DOI: 10.1016/j.jspd.2015.12.008 (cit. on p. 143).

ANDERSON, A. C., 2017. *The Radiology Technologist's Handbook to Surgical Procedures* [online]. Routledge [visited on 2023-08-21]. ISBN 978-0-203-73609-8. Available from DOI: 10.1201/9780203736098 (cit. on p. 46).

ARAI, Y.; TAMMISALO, E.; IWAI, K., et al., 1999. Development of a Compact Computed Tomographic Apparatus for Dental Use. *Dento Maxillo Facial Radiology*. Vol. 28, no. 4, pp. 245–248. ISSN 0250-832X. Available from DOI: 10.1038/sj/dmfr/4600448 (cit. on p. 129).

ARBABI, S.; FOPPEN, W.; GIELIS, W. P., et al., 2023. MRI-based Synthetic CT in the Detection of Knee Osteoarthritis: Comparison with CT. *Journal of Orthopaedic Research: Official Publication of the Orthopaedic Research Society*. Vol. 41, no. 11, pp. 2530–2539. ISSN 1554-527X. Available from DOI: 10.1002/jor.25557 (cit. on p. 159).

ARTHUR, D.; VASSILVITSKII, S., 2007. K-Means++: The Advantages of Careful Seeding. In: *Proc. of the Annu. ACM-SIAM Symp. on Discrete Algorithms*. Vol. 8, pp. 1027–1035. Available from DOI: 10.1145/1283383.1283494 (cit. on p. 83).

ASLAN, M. S.; ALI, A.; RARA, H., et al., 2010. An Automated Vertebra Identification and Segmentation in CT Images. In: *2010 IEEE International Conference on Image Processing* [online], pp. 233–236 [visited on 2024-04-04]. ISSN 2381-8549. Available from DOI: 10.1109/ICIP.2010.5651959 (cit. on pp. 93, 94).

ASRIYANTI, A.; SAPTAJI, K.; KHOIRIYAH, N., et al., 2022. Fabrication of Rigid Polyurethane Foam Lumbar Spine Model for Surgical Training Using Indirect Additive Manufacturing. *International Journal of Technology* [online]. Vol. 13, no. 8, p. 1612 [visited on 2023-09-13]. ISSN 2087-2100, ISSN 2086-9614. Available from DOI: 10.14716/ijtech.v13i8.6125 (cit. on p. 144).

BABA, S.; KAWAGUCHI, K.; ITAMOTO, K., et al., 2020. Use of an Inertial Measurement Unit Sensor in Pedicle Screw Placement Improves Trajectory Accuracy. *PloS One*. Vol. 15, no. 11, e0242512. ISSN 1932-6203. Available from DOI: 10.1371/journal.pone.0242512 (cit. on p. 131).

BAI, Y.-s.; ZHANG, Y.; CHEN, Z.-q., et al., 2010. Learning Curve of Computer-Assisted Navigation System in Spine Surgery. *Chinese Medical Journal* [online]. Vol. 123, no. 21, p. 2989 [visited on 2024-06-03]. ISSN 0366-6999. Available from DOI: 10.3760/cma.j.issn.0366-6999.2010.21.007 (cit. on p. 67).

BAILEY, S.; VASHISHTH, D., 2018. Mechanical Characterization of Bone: State of the Art in Experimental Approaches—What Types of Experiments Do People Do and How Does One Interpret the Results? *Current osteoporosis reports* [online]. Vol. 16, no. 4, pp. 423–433 [visited on 2024-05-29]. ISSN 1544-1873. Available from DOI: 10.1007/s11914-018-0454-8 (cit. on p. 36).

BALDWIN, K. D.; KADIYALA, M.; TALWAR, D., et al., 2022. Does Intraoperative CT Navigation Increase the Accuracy of Pedicle Screw Placement in Pediatric Spinal Deformity Surgery? A Systematic Review and Meta-Analysis. *Spine Deformity*. Vol. 10, no. 1, pp. 19–29. ISSN 2212-1358. Available from DOI: 10.1007/s43390-021-00385-5 (cit. on p. 129).

BALLARD, D. H., 1981. Generalizing the Hough Transform to Detect Arbitrary Shapes. *Pattern Recognition* [online]. Vol. 13, no. 2, pp. 111–122 [visited on 2024-04-04]. ISSN 0031-3203. Available from DOI: 10.1016/0031-3203(81)90009-1 (cit. on p. 95).

BAUM, T.; GRANDE GARCIA, E.; BURGKART, R., et al., 2015. Osteoporosis Imaging: Effects of Bone Preservation on MDCT-based Trabecular Bone Microstructure Parameters and Finite Element Models. *BMC Medical Imaging* [online]. Vol. 15, no. 1, p. 22 [visited on 2023-09-14]. ISSN 1471-2342. Available from DOI: 10.1186/s12880-015-0066-z (cit. on p. 146).

BHARUCHA, N. J.; LONNER, B. S.; AUERBACH, J. D., et al., 2013. Low-Density versus High-Density Thoracic Pedicle Screw Constructs in Adolescent Idiopathic Scoliosis: Do More Screws Lead to a Better Outcome? *The Spine Journal: Official Journal of the North American Spine Society*. Vol. 13, no. 4, pp. 375–381. ISSN 1878-1632. Available from DOI: 10.1016/j.spinee.2012.05.029 (cit. on p. 100).

BOHLMAN, H. H.; EMERY, S. E.; GOODFELLOW, D. B., et al., 1993. Robinson Anterior Cervical Discectomy and Arthrodesis for Cervical Radiculopathy. Long-term Follow-up of One Hundred and Twenty-Two Patients. *JBJS* [online]. Vol. 75, no. 9, p. 1298 [visited on 2024-06-10]. ISSN 0021-9355 (cit. on p. 52).

BONE, C. M.; HSIEH, G. H., 2000. The Risk of Carcinogenesis from Radiographs to Pediatric Orthopaedic Patients. *Journal of Pediatric Orthopedics*. Vol. 20, no. 2, pp. 251–254. ISSN 0271-6798 (cit. on p. 129).

BOTSCH, M.; STEINBERG, S.; BISCHOFF, S., et al., 1999. OpenMesh-a Generic and Efficient Polygon Mesh Data Structure. *Computational Geometry*. Vol. 13, no. 1, pp. 65–90. ISBN 0-89791-973-4. ISSN 09257721 (cit. on p. 112).

BOURDILLON, P.; APRA, C.; LÉVÊQUE, M., 2018. First Clinical Use of Stereotaxy in Humans: The Key Role of x-Ray Localization Discovered by Gaston Contremoulins. *Journal of Neurosurgery* [online]. Vol. 128, no. 3, pp. 932–937 [visited on 2024-02-21]. ISSN 0022-3085, ISSN 1933-0693. Available from DOI: 10.3171/2016.11.JNS161417 (cit. on p. 60).

BOZKUS, H.; CRAWFORD, N. R.; CHAMBERLAIN, R. H., et al., 2005. Comparative Anatomy of the Porcine and Human Thoracic Spines with Reference to Thoracoscopic Surgical Techniques. *Surgical Endoscopy* [online]. Vol. 19, no. 12, pp. 1652–1665 [visited on 2023-05-09]. ISSN 0930-2794, ISSN 1432-2218. Available from DOI: 10.1007/s00464-005-0159-9 (cit. on p. 30).

BRANTIGAN, J. W., 1994. Pseudarthrosis Rate After Allograft Posterior Lumbar Interbody Fusion With Pedicle Screw and Plate Fixation. *Spine* [online]. Vol. 19, no. 11, p. 1271 [visited on 2024-06-10]. ISSN 0362-2436 (cit. on p. 52).

BRICE, C. R.; FENNEMA, C. L., 1970. Scene Analysis Using Regions. *Artificial Intelligence* [online]. Vol. 1, no. 3-4, pp. 205–226 [visited on 2024-03-21]. ISSN 00043702. Available from DOI: 10.1016/0004-3702(70)90008-1 (cit. on p. 78).

BRINK, R. C.; COLO, D.; SCHLÖSSER, T. P. C., et al., 2017. Upright, Prone, and Supine Spinal Morphology and Alignment in Adolescent Idiopathic Scoliosis. *Scoliosis and Spinal Disorders*. Vol. 12, p. 6. ISSN 2397-1789. Available from DOI: 10.1186/s13013-017-0111-5 (cit. on pp. 75, 122, 130).

BRINK, R. C.; HOMANS, J. F.; DE REUVER, S., et al., 2020. A Computed Tomography-Based Spatial Reference for Pedicle Screw Placement in Adolescent Idiopathic Scoliosis. *Spine Deformity*. Vol. 8, no. 1, pp. 67–76. ISSN 2212-1358. Available from DOI: 10.1007/s43390-020-00032-5 (cit. on p. 130).

BROWN, B. S.; MCIFF, T. E.; GLATTES, R. C., et al., 2010. Effect of Starting Point Placement Technique on Thoracic Transverse Process Strength: An Ex Vivo Biomechanical Study (cit. on p. 134).

CANNY, J., 1986. A Computational Approach to Edge Detection. *IEEE Transactions on Pattern Analysis and Machine Intelligence* [online]. Vol. PAMI-8, no. 6, pp. 679–698 [visited on 2024-03-21]. ISSN 0162-8828. Available from DOI: 10.1109/TPAMI.1986.4767851 (cit. on p. 80).

CÁRDENES, R.; DE LUIS-GARCÍA, R.; BACH-CUADRA, M., 2009. A Multidimensional Segmentation Evaluation for Medical Image Data. *Computer Methods and Programs in Biomedicine* [online]. Vol. 96, no. 2, pp. 108–124 [visited on 2024-03-29]. ISSN 0169-2607. Available from DOI: 10.1016/j.cmpb.2009.04.009 (cit. on p. 92).

CHANG, K.-Y.; LIU, T.-L.; LAI, S.-H., 2011. From Co-Saliency to Co-Segmentation: An Efficient and Fully Unsupervised Energy Minimization Model. In: *CVPR 2011* [online], pp. 2129–2136 [visited on 2024-03-22]. ISSN 1063-6919. Available from DOI: 10.1109/CVPR.2011.5995415 (cit. on p. 184).

CHAPMAN, J. R.; HARRINGTON, R. M.; LEE, K. M., et al., 1996. Factors Affecting the Pullout Strength of Cancellous Bone Screws. *Journal of Biomechanical Engineering* [online]. Vol. 118, no. 3, pp. 391–398 [visited on 2024-05-30]. ISSN 0148-0731. Available from DOI: 10.1115/1.2796022 (cit. on p. 37).

CHO, W.; CHO, S. K.; WU, C., 2010. The Biomechanics of Pedicle Screw-Based Instrumentation. *The Journal of Bone & Joint Surgery British Volume* [online]. Vol. 92-B, no. 8, pp. 1061–1065 [visited on 2024-05-30]. ISSN 2049-4408. Available from DOI: 10.1302/0301-620X.92B8.24237 (cit. on p. 37).

CHUNG, K. J.; SUH, S. W.; DESAI, S., et al., 2008. Ideal Entry Point for the Thoracic Pedicle Screw during the Free Hand Technique. *International Orthopaedics*. Vol. 32, no. 5, pp. 657–662. ISSN 03412695. Available from DOI: 10.1007/s00264-007-0363-4 (cit. on pp. 133, 134).

CLÉMENT, J.-L.; GEOFFRAY, A.; YAGOUBI, F., et al., 2013. Relationship between Thoracic Hypokyphosis, Lumbar Lordosis and Sagittal Pelvic Parameters in Adolescent Idiopathic Scoliosis. *European Spine Journal* [online]. Vol. 22, no. 11, pp. 2414–2420 [visited on 2024-02-02]. ISSN 0940-6719, ISSN 1432-0932. Available from DOI: 10.1007/s00586-013-2852-z (cit. on p. 26).

CLEMENTS, D. H.; BETZ, R. R.; NEWTON, P. O., et al., 2009. Correlation of Scoliosis Curve Correction with the Number and Type of Fixation Anchors. *Spine*. Vol. 34, no. 20, pp. 2147–2150. ISSN 1528-1159. Available from DOI: 10.1097/BRS.0b013e3181adb35d (cit. on p. 100).

COLLINS, M. D.; XU, J.; GRADY, L., et al., 2012. Random Walks Based Multi-Image Segmentation: Quasiconvexity Results and GPU-based Solutions. In: *2012 IEEE Conference on Computer Vision and Pattern Recognition* [online], pp. 1656–1663 [visited on 2024-03-21]. ISSN 1063-6919. Available from DOI: 10.1109/CVPR.2012.6247859 (cit. on p. 184).

COMANICIU, D.; MEER, P., 2002. Mean Shift: A Robust Approach toward Feature Space Analysis. *IEEE Transactions on Pattern Analysis and Machine Intelligence* [online]. Vol. 24, no. 5, pp. 603–619 [visited on 2024-03-21]. ISSN 01628828. Available from DOI: 10.1109/34.1000236 (cit. on p. 83).

COMMISSION NATIONALE DE L'INFORMATIQUE ET DES LIBERTÉS, 2018. *Délibération n° 2018-155 du 3 mai 2018 portant homologation de la méthodologie de référence relative aux traitements de données à caractère personnel mis en œuvre dans le cadre des recherches n'impliquant pas la personne humaine, des études et évaluations dans le domaine de la santé (MR-004). [Deliberation No. 2018-155 of May 3, 2018 Approving the Reference Methodology Relating to the Processing of Personal Data Implemented in the Framework of Research not Involving Human Persons, Studies and Evaluations in the Health Field (MR-004)]*. Journal Officiel de République Française (cit. on p. 130).

CONSTANT, C.; AUBIN, C.-E.; KREMERS, H. M., et al., 2023. The Use of Deep Learning in Medical Imaging to Improve Spine Care: A Scoping Review of Current Literature and Clinical Applications. *North American Spine Society Journal (NASSJ)* [online]. Vol. 15, p. 100236 [visited on 2024-05-13]. ISSN 26665484. Available from DOI: 10.1016/j.xnsj.2023.100236 (cit. on p. 107).

COOK, S. D.; SALKELD, S. L.; STANLEY, T., et al., 2004. Biomechanical Study of Pedicle Screw Fixation in Severely Osteoporotic Bone. *The Spine Journal: Official Journal of the North American Spine Society*. Vol. 4, no. 4, pp. 402–408. ISSN 1529-9430. Available from DOI: 10.1016/j.spinee.2003.11.010 (cit. on p. 134).

CORNAZ, F.; FARSHAD, M.; WIDMER, J., 2022. Location of Pedicle Screw Hold in Relation to Bone Quality and Loads. *Frontiers in Bioengineering and Biotechnology*. Vol. 10, p. 953119. ISSN 2296-4185. Available from DOI: 10.3389/fbioe.2022.953119 (cit. on p. 134).

CORTES, C.; VAPNIK, V., 1995. Support-Vector Networks. *Machine Learning* [online]. Vol. 20, no. 3, pp. 273–297 [visited on 2024-03-28]. ISSN 1573-0565. Available from DOI: 10.1007/BF00994018 (cit. on p. 86).

COTTERILL, P. C.; KOSTUIK, J. P.; D'ANGELO, G., et al., 1986. An Anatomical Comparison of the Human and Bovine Thoracolumbar Spine. *Journal of Orthopaedic Research* [online]. Vol. 4, no. 3, pp. 298–303 [visited on 2023-05-09]. ISSN 0736-0266, ISSN 1554-527X. Available from DOI: 10.1002/jor.1100040306 (cit. on p. 30).

DANESI, V.; ZANI, L.; SCHEELE, A., et al., 2014. Reproducible Reference Frame for in Vitro Testing of the Human Vertebrae. *Journal of Biomechanics*. Vol. 47, no. 1, pp. 313–318. ISSN 1873-2380. Available from DOI: 10.1016/j.jbiomech.2013.10.005 (cit. on p. 146).

DATH, R.; EBINESAN, A.; PORTER, K., et al., 2007. Anatomical Measurements of Porcine Lumbar Vertebrae. *Clinical Biomechanics* [online]. Vol. 22, no. 5, pp. 607–613 [visited on 2023-05-09]. ISSN 02680033. Available from DOI: 10.1016/j.clinbiomech.2007.01.014 (cit. on p. 30).

DEMIR, T.; CAMUŞCU, N.; TÜREYEN, K., 2012. Design and Biomechanical Testing of Pedicle Screw for Osteoporotic Incidents. *Proceedings of the Institution of Mechanical Engineers, Part H: Journal of Engineering in Medicine* [online]. Vol. 226, no. 3, pp. 256–262 [visited on 2024-05-30]. ISSN 0954-4119. Available from DOI: 10.1177/0954411911434680 (cit. on p. 38).

DEMPSTER, A. P.; LAIRD, N. M.; RUBIN, D. B., 1977. Maximum Likelihood from Incomplete Data Via the EM Algorithm. *Journal of the Royal Statistical Society: Series B (Methodological)*. Vol. 39, no. 1, pp. 1–22. Available from DOI: 10.1111/j.2517-6161.1977.tb01600.x (cit. on p. 110).

DEYO, R. A.; GRAY, D. T.; KREUTER, W., et al., 2005. United States Trends in Lumbar Fusion Surgery for Degenerative Conditions. *Spine* [online]. Vol. 30, no. 12, p. 1441 [visited on 2024-06-10]. ISSN 0362-2436. Available from DOI: 10.1097/01.brs.0000166503.37969.8a (cit. on p. 52).

DICE, L. R., 1945. Measures of the Amount of Ecologic Association Between Species. *Ecology* [online]. Vol. 26, no. 3, pp. 297–302 [visited on 2024-03-29]. ISSN 0012-9658. Available from DOI: 10.2307/1932409 (cit. on p. 93).

DIMEGLIO, A.; CANAVESE, F., 2012. The Growing Spine: How Spinal Deformities Influence Normal Spine and Thoracic Cage Growth. *European Spine Journal* [online]. Vol. 21, no. 1, pp. 64–70 [visited on 2023-08-29]. ISSN 1432-0932. Available from DOI: 10.1007/s00586-011-1983-3 (cit. on p. 123).

DIMEGLIO, A.; CANAVESE, F., 2013. Progression or Not Progression? How to Deal with Adolescent Idiopathic Scoliosis during Puberty. *Journal of Children's Orthopaedics*. Vol. 7, no. 1, pp. 43–49. ISSN 1863-2521. Available from DOI: 10.1007/s11832-012-0463-6 (cit. on p. 123).

DIMEGLIO, A.; CANAVESE, F.; CHARLES, Y. P., 2011. Growth and Adolescent Idiopathic Scoliosis: When and How Much? *Journal of Pediatric Orthopedics*. Vol. 31, no. 1 Suppl, S28–36. ISSN 1539-2570. Available from DOI: 10.1097/BPO.0b013e318202c25d (cit. on p. 123).

DOMANDER, R.; FELDER, A. A.; DOUBE, M., 2021. BoneJ2 - Refactoring Established Research Software. *Wellcome Open Research* [online]. Vol. 6, p. 37 [visited on 2024-05-23]. ISSN 2398-502X. Available from DOI: 10.12688/wellcomeopenres.16619.2 (cit. on p. 35).

DONG, X.; SHEN, J.; SHAO, L., et al., 2016. Sub-Markov Random Walk for Image Segmentation. *IEEE Transactions on Image Processing* [online]. Vol. 25, no. 2, pp. 516–527 [visited on 2024-03-22]. ISSN 1941-0042. Available from DOI: 10.1109/TIP.2015.2505184 (cit. on p. 184).

DOUBE, M., 2015. The Ellipsoid Factor for Quantification of Rods, Plates, and Intermediate Forms in 3D Geometries. *Frontiers in Endocrinology*. Vol. 6, p. 15. ISSN 1664-2392. Available from DOI: 10.3389/fendo.2015.00015 (cit. on p. 35).

DOUGHERTY, G.; NEWMAN, D., 1999. Measurement of Thickness and Density of Thin Structures by Computed Tomography: A Simulation Study. *Medical Physics*. Vol. 26, no. 7, pp. 1341–1348. ISSN 0094-2405. Available from DOI: 10.1118/1.598629 (cit. on p. 106).

DOUGHERTY, R.; KUNZELMANN, K.-H., 2007. Computing Local Thickness of 3D Structures with ImageJ. *Microscopy and Microanalysis* [online]. Vol. 13, no. S02 [visited on 2024-02-23]. ISSN 1431-9276, ISSN 1435-8115. Available from DOI: 10.1017/S1431927607074430 (cit. on p. 35).

DUKE, A.; MARCHESE, R.; KOMATSU, D. E., et al., 2022. Radiation in Adolescent Idiopathic Scoliosis Management: Estimated Cumulative Pre-Operative, Intra-Operative, and Post-Operative Exposure. *Orthopedic Research and Reviews*. Vol. 14, pp. 487–493. ISSN 1179-1462. Available from DOI: 10.2147/ORR.S387369 (cit. on pp. 67, 129).

EDWARDS, W. T.; ZHENG, Y.; FERRARA, L. A., et al., 2001. Structural Features and Thickness of the Vertebral Cortex in the Thoracolumbar Spine. *Spine*. Vol. 26, no. 2, pp. 218–225. ISSN 0362-2436. Available from DOI: 10.1097/00007632-200101150-00019 (cit. on pp. 100, 145).

EHM, M.; KLINDER, T.; KNESER, R., et al., 2009. Automated Vertebra Identification in CT Images. In: PLUIM, J. P. W.; DAWANT, B. M. (eds.). *SPIE Medical Imaging* [online]. Lake Buena Vista, FL, 72590B [visited on 2024-05-06]. Available from DOI: 10.1117/12.811836 (cit. on pp. 157, 158).

EL MASRI, F.; DE SAPIN BROSSES, E.; RHISSASSI, K., et al., 2012. Apparent Young's Modulus of Vertebral Cortico-Cancellous Bone Specimens. *Computer Methods in Biomechanics and Biomedical Engineering*. Vol. 15, no. 1, pp. 23–28. ISSN 10255842. Available from DOI: 10.1080/10255842.2011.565751 (cit. on pp. 37, 145).

ELEY, K. A.; WATT-SMITH, S. R.; GOLDING, S. J., 2013. "Black Bone" MRI: A Potential Non-Ionizing Method for Three-Dimensional Cephalometric Analysis—a Preliminary Feasibility Study. *Dentomaxillofacial Radiology* [online]. Vol. 42, no. 10, p. 20130236 [visited on 2025-03-20]. ISSN 0250-832X. Available from DOI: 10.1259/dmfr.20130236 (cit. on p. 159).

ELIAS, W. J.; SIMMONS, N. E.; KAPTAIN, G. J., et al., 2000. Complications of Posterior Lumbar Interbody Fusion When Using a Titanium Threaded Cage Device. *Journal of Neurosurgery: Spine* [online]. Vol. 93, no. 1, pp. 45–52 [visited on 2024-06-10]. Available from DOI: 10.3171/spi.2000.93.1.0045 (cit. on p. 52).

EMERY, S. E.; BOLESTA, M. J.; BANKS, M. A., et al., 1994. Robinson Anterior Cervical Fusion: Comparison of the Standard and Modified Techniques. *Spine* [online]. Vol. 19, no. 6, p. 660 [visited on 2024-06-10]. ISSN 0362-2436 (cit. on p. 52).

FABIJAŃSKA, A.; GOCŁAWSKI, J., 2015. The Segmentation of 3D Images Using the Random Walking Technique on a Randomly Created Image Adjacency Graph. *IEEE Transactions on Image Processing* [online]. Vol. 24, no. 2, pp. 524–537 [visited on 2024-03-22]. ISSN 1941-0042. Available from DOI: 10.1109/TIP.2014.2383323 (cit. on p. 184).

FANMAN MENG; HONGLIANG LI; GUANGHUI LIU, et al., 2012. Object Co-Segmentation Based on Shortest Path Algorithm and Saliency Model. *IEEE Transactions on Multimedia* [online]. Vol. 14, no. 5, pp. 1429–1441 [visited on 2024-03-22]. ISSN 1520-9210, ISSN 1941-0077. Available from DOI: 10.1109/TMM.2012.2197741 (cit. on p. 184).

FAZZALARI, N. L.; PARKINSON, I. H.; FOGG, Q. A., et al., 2006. Antero–Postero Differences in Cortical Thickness and Cortical Porosity of T12 to L5 Vertebral Bodies. *Joint Bone Spine*. Vol. 73, no. 3, pp. 293–297. ISSN 1297319X. Available from DOI: 10.1016/j.jbspin.2005.03.023 (cit. on pp. 107, 115, 120).

FEDOROV, A.; BEICHEL, R.; KALPATHY-CRAMER, J., et al., 2012. 3D Slicer as an Image Computing Platform for the Quantitative Imaging Network. *Magnetic resonance imaging*. Vol. 30, no. 9, pp. 1323–41. ISSN 1873-5894. Available from DOI: 10.1016/j.mri.2012.05.001 (cit. on pp. 20, 124).

FELZENSZWALB, P. F.; HUTTENLOCHER, D. P., 2004. Efficient Graph-Based Image Segmentation. *International Journal of Computer Vision* [online]. Vol. 59, no. 2, pp. 167–181 [visited on 2024-03-21]. ISSN 0920-5691. Available from DOI: 10.1023/B:VISI.0000022288.19776.77 (cit. on p. 82).

FENNELL, V. S.; PALEJWALA, S.; SKOCH, J., et al., 2014. Freehand Thoracic Pedicle Screw Technique Using a Uniform Entry Point and Sagittal Trajectory for All Levels: Preliminary Clinical Experience - Clinical Article. *Journal of Neurosurgery: Spine*. Vol. 21, no. 5, pp. 778–784. ISSN 15475646. Available from DOI: 10.3171/2014.7.SPINE1489 (cit. on pp. 53, 57).

FIX, E.; HODGES, J. L., 1989. Discriminatory Analysis. Nonparametric Discrimination: Consistency Properties. *International Statistical Review / Revue Internationale de Statistique* [online]. Vol. 57, no. 3, pp. 238–247 [visited on 2024-03-28]. ISSN 0306-7734. Available from DOI: 10.2307/1403797 (cit. on p. 86).

FOLKESTAD, L.; GROTH, K. A.; SHANBHOGUE, V., et al., 2020. Bone Geometry, Density, and Microarchitecture in the Distal Radius and Tibia in Adults With Marfan Syndrome Assessed by HR-pQCT. *Journal of Bone and Mineral Research* [online]. Vol. 35, no. 12, pp. 2335–2344 [visited on 2023-08-19]. ISSN 1523-4681. Available from DOI: 10.1002/jbmr.4138 (cit. on pp. 44, 133).

FOLKESTAD, L.; HALD, J. D.; HANSEN, S., et al., 2012. Bone Geometry, Density, and Microarchitecture in the Distal Radius and Tibia in Adults with Osteogenesis Imperfecta Type I Assessed by High-resolution pQCT. *Journal of Bone and Mineral Research* [online]. Vol. 27, no. 6, pp. 1405–1412 [visited on 2024-05-29]. ISSN 0884-0431. Available from DOI: 10.1002/jbmr.1592 (cit. on p. 44).

GABRIEL, T.; ZHANG, T.; GOLUB, G., 1996. Optimal Surface Smoothing as Filter Design Fourier Analysis of Discrete Graph Signals. *Computer*. Vol. 1064, pp. 283–292 (cit. on p. 111).

GAINES, R. W., 2000. The Use of Pedicle-Screw Internal Fixation for the Operative Treatment of Spinal Disorders. *The Journal of Bone and Joint Surgery. American Volume*. Vol. 82, no. 10, pp. 1458–1476. ISSN 0021-9355. Available from DOI: 10.2106/00004623-200010000-00013 (cit. on p. 133).

GALBUSERA, F.; VOLKHEIMER, D.; REITMAIER, S., et al., 2015. Pedicle Screw Loosening: A Clinically Relevant Complication? *European Spine Journal: Official Publication of the European Spine Society, the European Spinal Deformity Society, and the European Section of the Cervical Spine Research Society*. Vol. 24, no. 5, pp. 1005–1016. ISSN 1432-0932. Available from DOI: 10.1007/s00586-015-3768-6 (cit. on p. 100).

GALLUCCI, M.; LIMBUCCI, N.; PAONESSA, A., et al., 2007. Degenerative Disease of the Spine. *Neuroimaging Clinics of North America* [online]. Vol. 17, no. 1, pp. 87–103 [visited on 2023-05-11]. ISSN 10525149. Available from DOI: 10.1016/j.nic.2007.01.002 (cit. on pp. 40, 47).

GEBHARD, F. T.; KRAUS, M. D.; SCHNEIDER, E., et al., 2006. Does Computer-Assisted Spine Surgery Reduce Intraoperative Radiation Doses? *Spine* [online]. Vol. 31, no. 17, p. 2024 [visited on 2024-06-03]. ISSN 0362-2436. Available from DOI: 10.1097/01.brs.0000229250.69369.ac (cit. on p. 67).

GIANSANTI, D., 2022. The Regulation of Artificial Intelligence in Digital Radiology in the Scientific Literature: A Narrative Review of Reviews. *Healthcare* [online]. Vol. 10, no. 10, p. 1824 [visited on 2023-12-20]. ISSN 2227-9032. Available from DOI: 10.3390/healthcare10101824 (cit. on pp. 69, 120).

GIORGI, H.; TOMI, F.; GLARD, Y., et al., 2023. Change of Vertebral Orientation, between the Supine Position and the Prone Position. *Spine Deformity*. ISSN 2212-1358. Available from DOI: 10.1007/s43390-023-00704-y (cit. on pp. 3, 122).

GOERRES, J.; UNERI, A.; DE SILVA, T., et al., 2017. Spinal Pedicle Screw Planning Using Deformable Atlas Registration. *Physics in Medicine and Biology* [online]. Vol. 62, no. 7, pp. 2871–2891 [visited on 2024-05-06]. ISSN 0031-9155, ISSN 1361-6560. Available from DOI: 10.1088/1361-6560/aa5f42 (cit. on p. 159).

GOODFELLOW, I.; POUGET-ABADIE, J.; MIRZA, M., et al., 2014. Generative Adversarial Nets. In: *Advances in Neural Information Processing Systems* [online]. Curran Associates, Inc. Vol. 27 [visited on 2024-04-05] (cit. on p. 96).

GOUTTARD, S.; STYNER, M.; PRASTAWA, M., et al., 2008. Assessment of Reliability of Multi-site Neuroimaging Via Traveling Phantom Study. In: METAXAS, D.; AXEL, L.; FICHTINGER, G., et al. (eds.). *Medical Image Computing and Computer-Assisted Intervention – MICCAI 2008*. Berlin, Heidelberg: Springer, pp. 263–270. ISBN 978-3-540-85990-1. Available from DOI: 10.1007/978-3-540-85990-1_32 (cit. on p. 92).

GRADY, L., 2006. Random Walks for Image Segmentation. *IEEE Transactions on Pattern Analysis and Machine Intelligence* [online]. Vol. 28, no. 11, pp. 1768–1783 [visited on 2024-03-21]. ISSN 0162-8828, ISSN 2160-9292. Available from DOI: 10.1109/TPAMI.2006.233 (cit. on p. 84).

GREINER-PERTH, R.; BOEHM, H.; ALLAM, Y., et al., 2004. Reoperation Rate After Instrumented Posterior Lumbar Interbody Fusion: A Report on 1680 Cases. *Spine* [online]. Vol. 29, no. 22, p. 2516 [visited on 2024-06-10]. ISSN 0362-2436. Available from DOI: 10.1097/01.brs.0000144833.63581.c1 (cit. on p. 52).

GROSLAND, N. M.; GOEL, V. K., 2007. Vertebral Endplate Morphology Follows Bone Remodeling Principles. *Spine*. Vol. 32, no. 23, E667–E673. ISSN 0362-2436. Available from DOI: 10.1097/BRS.0b013e318158cfaf (cit. on p. 26).

HADLEY, M. N.; SHETTER, A. G.; AMOS, M. R., 1985. Use of the Brown-Roberts-Wells Stereotactic Frame for Functional Neurosurgery. *Stereotactic and Functional Neurosurgery* [online]. Vol. 48, no. 1-6, pp. 61–68 [visited on 2024-02-21]. ISSN 1011-6125, ISSN 1423-0372. Available from DOI: 10.1159/000101098 (cit. on p. 62).

HALE, A. R.; ROSS, A. H., 2017. The Impact of Freezing on Bone Mineral Density: Implications for Forensic Research. *Journal of Forensic Sciences* [online]. Vol. 62, no. 2, pp. 399–404 [visited on 2023-09-14]. ISSN 1556-4029. Available from DOI: 10.1111/1556-4029.13273 (cit. on p. 146).

HALVORSON, T. L.; KELLEY, L. A.; THOMAS, K. A., et al., 1994. Effects of Bone Mineral Density on Pedicle Screw Fixation. *Spine*. Vol. 19, no. 21, pp. 2415–2420. ISSN 0362-2436. Available from DOI: 10.1097/00007632-199411000-00008 (cit. on p. 100).

HARDY, M.; HARVEY, H., 2020. Artificial Intelligence in Diagnostic Imaging: Impact on the Radiography Profession. *The British Journal of Radiology* [online]. Vol. 93, no. 1108, p. 20190840 [visited on 2023-12-20]. ISSN 0007-1285, ISSN 1748-880X. Available from DOI: 10.1259/bjr.20190840 (cit. on p. 120).

HARRIS, I. A.; DAO, A. T. T., 2009. Trends of Spinal Fusion Surgery in Australia: 1997 to 2006. *ANZ Journal of Surgery* [online]. Vol. 79, no. 11, pp. 783–788 [visited on 2024-06-10]. ISSN 1445-1433, ISSN 1445-2197. Available from DOI: 10.1111/j.1445-2197.2009.05095.x (cit. on p. 52).

HILDEBRAND, T.; RÜEGSEGGER, P., 1997. **A New Method for the Model-independent Assessment of Thickness in Three-dimensional Images**. *Journal of Microscopy* [online]. Vol. 185, no. 1, pp. 67–75 [visited on 2024-02-23]. ISSN 0022-2720, ISSN 1365-2818. Available from DOI: 10.1046/j.1365-2818.1997.1340694.x (cit. on pp. 35, 106).

HILIBRAND, A. S.; DINA, T. S., 1998. The Use Of Diagnostic Imaging To Assess Spinal Arthrodesis. *Orthopedic Clinics* [online]. Vol. 29, no. 4, pp. 591–601 [visited on 2024-06-10]. ISSN 0030-5898, ISSN 1558-1373. Available from DOI: 10.1016/S0030-5898(05)70033-X (cit. on p. 52).

HIRANO, T.; HASEGAWA, K.; TAKAHASHI, H. E., et al., 1997. Structural Characteristics of the Pedicle and Its Role in Screw Stability. *Spine* [online]. Vol. 22, no. 21, p. 2504 [visited on 2024-05-30]. ISSN 0362-2436 (cit. on p. 37).

HOCHBAUM, D. S.; SINGH, V., 2009. An Efficient Algorithm for Co-segmentation. In: *2009 IEEE 12th International Conference on Computer Vision* [online], pp. 269–276 [visited on 2024-03-22]. ISSN 2380-7504. Available from DOI: 10.1109/ICCV.2009.5459261 (cit. on p. 184).

HOLLENSTEINER, M.; AUGAT, P.; FURST, D., et al., 2017. Novel Synthetic Vertebrae Provide Realistic Haptics for Pedicle Screw Placement. *Annual International Conference of the IEEE Engineering in Medicine and Biology Society. IEEE Engineering in Medicine and Biology Society. Annual International Conference*. Vol. 2017, pp. 46–49. ISSN 2694-0604. Available from DOI: 10.1109/EMBC.2017.8036759 (cit. on p. 144).

HOLLENSTEINER, M.; BOTZENMAYER, M.; FÜRST, D., et al., 2018. Characterization of Polyurethane-Based Synthetic Vertebrae for Spinal Cement Augmentation Training. *Journal of Materials Science. Materials in Medicine*. Vol. 29, no. 10, p. 153. ISSN 1573-4838. Available from DOI: 10.1007/s10856-018-6161-2 (cit. on p. 144).

HORAK, Z.; DVORAK, K.; ZARYBNICKA, L., et al., 2020. Experimental Measurements of Mechanical Properties of PUR Foam Used for Testing Medical Devices and Instruments Depending on Temperature, Density and Strain Rate. *Materials (Basel, Switzerland)*. Vol. 13, no. 20, p. 4560. ISSN 1996-1944. Available from DOI: 10.3390/ma13204560 (cit. on p. 143).

HU, R. W.; JAGLAL, S.; AXCELL, T., et al., 1997. A Population-Based Study of Reoperations After Back Surgery. *Spine* [online]. Vol. 22, no. 19, p. 2265 [visited on 2024-06-10]. ISSN 0362-2436 (cit. on p. 52).

HU, S. S., 1997. Internal Fixation in the Osteoporotic Spine. *Spine*. Vol. 22, no. 24 Suppl, 43S–48S. ISSN 0362-2436. Available from DOI: 10.1097/00007632-199712151-00008 (cit. on p. 100).

HUANG, J.; JIAN, F.; WU, H., et al., 2013. An Improved Level Set Method for Vertebra CT Image Segmentation. *BioMedical Engineering Online*. Vol. 12, no. 1, pp. 1–16. ISSN 1475925X. Available from DOI: 10.1186/1475-925X-12-48 (cit. on pp. 93, 94).

HUNTER, J. D., 2007. Matplotlib: A 2D Graphics Environment. *Computing in Science & Engineering* [online]. Vol. 9, no. 3, pp. 90–95 [visited on 2023-12-20]. ISSN 1521-9615. Available from DOI: 10.1109/MCSE.2007.55 (cit. on p. 115).

HWANG, C. J.; LEE, C.-K.; CHANG, B.-S., et al., 2011. Minimum 5-Year Follow-up Results of Skipped Pedicle Screw Fixation for Flexible Idiopathic Scoliosis. *Journal of Neurosurgery. Spine*. Vol. 15, no. 2, pp. 146–150. ISSN 1547-5646. Available from DOI: 10.3171/2011.4.SPINE10321 (cit. on p. 100).

IBRAGIMOV, B.; LIKAR, B.; PERNUŠ, F., et al., 2014. Shape Representation for Efficient Landmark-Based Segmentation in 3-D. *IEEE Transactions on Medical Imaging* [online]. Vol. 33, no. 4, pp. 861–874 [visited on 2024-04-05]. ISSN 1558-254X. Available from DOI: 10.1109/TMI.2013.2296976 (cit. on p. 95).

ILLÉS, T.; SOMOSKEÖY, S., 2013. Comparison of Scoliosis Measurements Based on Three-Dimensional Vertebra Vectors and Conventional Two-Dimensional Measurements: Advantages in Evaluation of Prognosis and Surgical Results. *European Spine Journal* [online]. Vol. 22, no. 6, pp. 1255–1263 [visited on 2023-12-20]. ISSN 0940-6719, ISSN 1432-0932. Available from DOI: 10.1007/s00586-012-2651-y (cit. on p. 120).

ILLÉS, T.; TUNYOGI-CSAPÓ, M.; SOMOSKEÖY, S., 2011. Breakthrough in Three-Dimensional Scoliosis Diagnosis: Significance of Horizontal Plane View and Vertebra Vectors. *European Spine Journal* [online]. Vol. 20, no. 1, pp. 135–143 [visited on 2023-12-20]. ISSN 0940-6719, ISSN 1432-0932. Available from DOI: 10.1007/s00586-010-1566-8 (cit. on p. 120).

ILLÉS, T. S.; BURKUS, M.; SOMOSKEŐY, S., et al., 2018. Axial Plane Dissimilarities of Two Identical Lenke-type 6C Scoliosis Cases Visualized and Analyzed by Vertebral Vectors. *European Spine Journal* [online]. Vol. 27, no. 9, pp. 2120–2129 [visited on 2023-12-20]. ISSN 0940-6719, ISSN 1432-0932. Available from DOI: 10.1007/s00586-018-5577-1 (cit. on p. 120).

ILLIES, T.; SAERING, D.; KINOSHITA, M., et al., 2016. Feasibility of Quantification of Intracranial Aneurysm Pulsation with 4D CTA with Manual and Computer-Aided Post-Processing. *PLOS ONE* [online]. Vol. 11, no. 11, e0166810 [visited on 2023-12-20]. ISSN 1932-6203. Available from DOI: 10.1371/journal.pone.0166810 (cit. on p. 120).

JACCARD, P., 1912. The Distribution of the Flora in the Alpine Zone. *New Phytologist* [online]. Vol. 11, no. 2, pp. 37–50 [visited on 2024-03-29]. ISSN 1469-8137. Available from DOI: 10.1111/j.1469-8137.1912.tb05611.x (cit. on p. 93).

JOSKOWICZ, L.; MILGROM, C.; SIMKIN, A., et al., 1998. FRACAS: A System for Computer-Aided Image-Guided Long Bone Fracture Surgery. *Computer Aided Surgery* [online]. Vol. 3, no. 6, pp. 271–288 [visited on 2024-06-03]. ISSN 1097-0150. Available from DOI: 10.1002/(SICI)1097-0150(1998)3:6<271::AID-IGS1>3.0.CO;2-Y (cit. on pp. 63, 64).

JOST, G. F.; WALTI, J.; MARIANI, L., et al., 2017. Inertial Measurement Unit-Assisted Implantation of Thoracic, Lumbar, and Sacral Pedicle Screws Improves Precision of a Freehand Technique. *World Neurosurgery*. Vol. 103, pp. 11–18. ISSN 1878-8769. Available from DOI: 10.1016/j.wneu.2017.02.079 (cit. on p. 53).

JOULIN, A.; BACH, F.; PONCE, J., 2010. Discriminative Clustering for Image Co-Segmentation. In: *2010 IEEE Computer Society Conference on Computer Vision and Pattern Recognition* [online], pp. 1943–1950 [visited on 2024-03-22]. ISSN 1063-6919. Available from DOI: 10.1109/CVPR.2010.5539868 (cit. on p. 184).

JOULIN, A.; BACH, F.; PONCE, J., 2012. Multi-Class Cosegmentation. In: *2012 IEEE Conference on Computer Vision and Pattern Recognition* [online], pp. 542–549 [visited on 2024-03-22]. ISSN 1063-6919. Available from DOI: 10.1109/CVPR.2012.6247719 (cit. on p. 184).

KALMAN, R. E., 1960. A New Approach to Linear Filtering and Prediction Problems. *Journal of Basic Engineering* [online]. Vol. 82, no. 1, pp. 35–45 [visited on 2024-02-23]. ISSN 0021-9223. Available from DOI: 10.1115/1.3662552 (cit. on p. 72).

KALRA, M. K.; QUICK, P.; SINGH, S., et al., 2013. Whole Spine CT for Evaluation of Scoliosis in Children: Feasibility of Sub-milliSievert Scanning Protocol. *Acta Radiologica (Stockholm, Sweden: 1987)*. Vol. 54, no. 2, pp. 226–230. ISSN 1600-0455. Available from DOI: 10.1258/ar.2012.110625 (cit. on p. 130).

KANDZIORA, F.; PFLUGMACHER, R.; SCHOLZ, M., et al., 2001. Comparison Between Sheep and Human Cervical Spines: An Anatomic, Radiographic, Bone Mineral Density, and Biomechanical Study. *Spine* [online]. Vol. 26, no. 9, pp. 1028–1037 [visited on 2023-05-09]. ISSN 0362-2436. Available from DOI: 10.1097/00007632-200105010-00008 (cit. on p. 30).

KANG, Y.; ENGELKE, K.; KALENDER, W., 2003. A New Accurate and Precise 3-D Segmentation Method for Skeletal Structures in Volumetric CT Data. *IEEE Transactions on Medical Imaging* [online]. Vol. 22, no. 5, pp. 586–598 [visited on 2024-04-04]. ISSN 1558-254X. Available from DOI: 10.1109/TMI.2003.812265 (cit. on pp. 93, 94).

KAPANDJI, I. A., 1969. [Functional anatomy of the lumbosacral spine]. *Acta Orthopaedica Belgica*. Vol. 35, no. 3, pp. 543–566. ISSN 0001-6462 (cit. on p. 130).

KARAIKOVIC, E. E.; YINGSAKMONGKOL, W.; GAINES, R. W., 2001. Accuracy of Cervical Pedicle Screw Placement Using the Funnel Technique. *Spine*. Vol. 26, no. 22, pp. 2456–2462. ISSN 0362-2436. Available from DOI: 10.1097/00007632-200111150-00012 (cit. on p. 131).

KHOTANLOU, H.; COLLIOT, O.; ATIF, J., et al., 2009. 3D Brain Tumor Segmentation in MRI Using Fuzzy Classification, Symmetry Analysis and Spatially Constrained Deformable Models. *Fuzzy Sets and Systems* [online]. Vol. 160, no. 10, pp. 1457–1473 [visited on 2024-03-29]. ISSN 0165-0114. Available from DOI: 10.1016/j.fss.2008.11.016 (cit. on p. 92).

KIM, E.; LI, H.; HUANG, X., 2012. A Hierarchical Image Clustering Cosegmentation Framework. In: *2012 IEEE Conference on Computer Vision and Pattern Recognition* [online], pp. 686–693 [visited on 2024-03-22]. ISSN 1063-6919. Available from DOI: 10.1109/CVPR.2012.6247737 (cit. on p. 184).

KIM, G.; XING, E. P., 2012. On Multiple Foreground Cosegmentation. In: *2012 IEEE Conference on Computer Vision and Pattern Recognition* [online], pp. 837–844 [visited on 2024-03-28]. ISSN 1063-6919. Available from DOI: 10.1109/CVPR.2012.6247756 (cit. on p. 184).

KIM, G.; XING, E. P.; FEI-FEI, L., et al., 2011. Distributed Cosegmentation via Submodular Optimization on Anisotropic Diffusion. In: *2011 International Conference on Computer Vision* [online], pp. 169–176 [visited on 2024-03-22]. ISSN 2380-7504. Available from DOI: 10.1109/ICCV.2011.6126239 (cit. on p. 184).

KIM, Y. J.; BRIDWELL, K. H.; LENKE, L. G., et al., 2005. Pseudarthrosis in Primary Fusions for Adult Idiopathic Scoliosis: Incidence, Risk Factors, and Outcome Analysis. *Spine* [online]. Vol. 30, no. 4, p. 468 [visited on 2024-06-10]. ISSN 0362-2436. Available from DOI: 10.1097/01.brs.0000153392.74639.ea (cit. on p. 52).

KIM, Y. J.; LENKE, L. G.; BRIDWELL, K. H., et al., 2004. Free Hand Pedicle Screw Placement in the Thoracic Spine: Is It Safe. *Spine*. Vol. 29, no. 3, pp. 333–342. ISSN 03622436. Available from DOI: 10.1097/01.BRS.0000109983.12113.9B (cit. on pp. 56, 129, 133).

KLINDER, T.; OSTERMANN, J.; EHM, M., et al., 2009. Automated Model-Based Vertebra Detection, Identification, and Segmentation in CT Images. *Medical Image Analysis*. Vol. 13, no. 3, pp. 471–482. ISSN 13618415. Available from DOI: 10.1016/j.media.2009.02.004 (cit. on p. 95).

KOBAYASHI, K.; SATO, K.; KATO, F., et al., 2022. Trends in the Numbers of Spine Surgeries and Spine Surgeons over the Past 15 Years. *Nagoya J. Med. Sci.* Vol. 84, pp. 155–162. Available from DOI: 10.18999/nagjms.84.1.155 (cit. on p. 42).

KOSMOPOULOS, V.; SCHIZAS, C., 2007. Pedicle Screw Placement Accuracy. *Spine*. Vol. 32, no. 3, E111–E120. ISSN 0362-2436. Available from DOI: 10.1097/01.brs.0000254048.79024.8b (cit. on p. 53).

KOTHE, R.; O'HOLLERAN, J. D.; LIU, W., et al., 1996. Internal Architecture of the Thoracic Pedicle. An Anatomic Study. *Spine*. Vol. 21, no. 3, pp. 264–270. ISSN 0362-2436. Available from DOI: 10.1097/00007632-199602010-00002 (cit. on p. 145).

KRIZHEVSKY, A.; SUTSKEVER, I.; HINTON, G. E., 2017. ImageNet Classification with Deep Convolutional Neural Networks. *Communications of the ACM* [online]. Vol. 60, no. 6, pp. 84–90 [visited on 2024-03-29]. ISSN 0001-0782. Available from DOI: 10.1145/3065386 (cit. on p. 89).

KUMAR, N.; KUKRETI, S.; ISHAQUE, M., et al., 2000. Anatomy of Deer Spine and Its Comparison to the Human Spine. *The Anatomical Record* [online]. Vol. 260, no. 2, pp. 189–203 [visited on 2023-05-09]. ISSN 0003-276X, ISSN 1097-0185. Available from DOI: 10.1002/1097-0185(20001001)260:2<189::AID-AR80>3.0.CO;2-N (cit. on p. 30).

LAI, Y.-K.; HU, S.-M.; MARTIN, R. R., et al., 2008. Fast Mesh Segmentation Using Random Walks. In: *Proceedings of the 2008 ACM Symposium on Solid and Physical Modeling* [online]. Stony Brook New York: ACM, pp. 183–191 [visited on 2024-03-21]. ISBN 978-1-60558-106-4. Available from DOI: 10.1145/1364901.1364927 (cit. on p. 84).

LAPORTE, S.; MITTON, D.; ISMAEL, B., et al., 2000. Quantitative Morphometric Study of Thoracic Spine. A Preliminary Parameters Statistical Analysis. *European Journal of Orthopaedic Surgery and Traumatology*. Vol. 10, no. 2, pp. 85–91. ISSN 09484817. Available from DOI: 10.1007/bf02803102 (cit. on pp. 30, 112, 175).

LARSON, A. N.; AUBIN, C.-E.; POLLY, D. W., et al., 2013. Are More Screws Better? A Systematic Review of Anchor Density and Curve Correction in Adolescent Idiopathic Scoliosis. *Spine Deformity* [online]. Vol. 1, no. 4, pp. 237–247 [visited on 2025-03-20]. ISSN 2212-134X. Available from DOI: 10.1016/j.jspd.2013.05.009 (cit. on p. 162).

LAW, M.; MA, W.-K.; LAU, D., et al., 2016. Cumulative Radiation Exposure and Associated Cancer Risk Estimates for Scoliosis Patients: Impact of Repetitive Full Spine Radiography. *European Journal of Radiology*. Vol. 85, no. 3, pp. 625–628. ISSN 1872-7727. Available from DOI: 10.1016/j.ejrad.2015.12.032 (cit. on p. 129).

LEBLOND, L.; GODIO RABOUTET, Y.; GLARD, Y., et al., 2024. Assessment of the Tolerance Angle for Pedicle Screw Insertion. *Medical & Biological Engineering & Computing* [online]. Vol. 62, no. 4, pp. 1265–1275 [visited on 2025-03-20]. ISSN 1741-0444. Available from DOI: 10.1007/s11517-023-03002-x (cit. on p. 132).

LEBLOND, L.; YVES GODIO-RABOUTET; TOMI, F., et al., 2023. Sliding on Cortical Shell: Biomechanical Characterization of the Vertebral Cannulation for Pedicle Screw Insertion. *Clinical Biomechanics* [online]. Vol. 110, p. 106102 [visited on 2025-03-20]. ISSN 0268-0033. Available from DOI: 10.1016/j.clinbiomech.2023.106102 (cit. on pp. 3, 132).

LEGAYE, J.; DUVAL-BEAUPRE, G.; MARTY, C., et al., 1998. Pelvic Incidence: A Fundamental Pelvic Parameter for Three-Dimensional Regulation of Spinal Sagittal Curves. *European Spine Journal* [online]. Vol. 7, no. 2, pp. 99–103 [visited on 2024-02-02]. ISSN 0940-6719, ISSN 1432-0932. Available from DOI: 10.1007/s005860050038 (cit. on p. 26).

LEKSELL, L., 1951. The Stereotaxic Method and Radiosurgery of the Brain. *Acta Chirurgica Scandinavica*. Vol. 102, no. 4, pp. 316–319. ISSN 0001-5482 (cit. on p. 61).

LENKE, L. G.; BETZ, R. R.; BRIDWELL, K. H., et al., 1998. Intraobserver and Interobserver Reliability of the Classification of Thoracic Adolescent Idiopathic Scoliosis. *The Journal of Bone and Joint Surgery. American Volume*. Vol. 80, no. 8, pp. 1097–1106. ISSN 0021-9355. Available from DOI: 10.2106/00004623-199808000-00002 (cit. on p. 129).

LENKE, L. G.; BETZ, R. R.; HAHER, T. R., et al., 2001. Multisurgeon Assessment of Surgical Decision-Making in Adolescent Idiopathic Scoliosis: Curve Classification, Operative Approach, and Fusion Levels. *Spine*. Vol. 26, no. 21, pp. 2347–2353. ISSN 0362-2436. Available from DOI: 10.1097/00007632-200111010-00011 (cit. on p. 129).

LENKE, L. G.; BETZ, R. R.; HARMS, J., et al., 2001. Adolescent Idiopathic Scoliosis: A New Classification to Determine Extent of Spinal Arthrodesis. *The Journal of Bone and Joint Surgery. American Volume*. Vol. 83, no. 8, pp. 1169–1181. ISSN 0021-9355 (cit. on p. 129).

LENKE, L. G.; BETZ, R. R.; CLEMENTS, D., et al., 2002. Curve Prevalence of a New Classification of Operative Adolescent Idiopathic Scoliosis: Does Classification Correlate with Treatment? *Spine*. Vol. 27, no. 6, pp. 604–611. ISSN 1528-1159. Available from DOI: 10.1097/00007632-200203150-00008 (cit. on p. 129).

LESSMANN, N.; VAN GINNEKEN, B.; DE JONG, P. A., et al., 2019. Iterative Fully Convolutional Neural Networks for Automatic Vertebra Segmentation and Identification. *Medical Image Analysis* [online]. Vol. 53, pp. 142–155 [visited on 2024-04-05]. ISSN 1361-8415. Available from DOI: 10.1016/j.media.2019.02.005 (cit. on pp. 97, 98).

LI, C.; JIN, D.; CHEN, C., et al., 2015. Automated Cortical Bone Segmentation for Multirow-Detector CT Imaging with Validation and Application to Human Studies. *Medical Physics*. Vol. 42, no. 8, pp. 4553–4565. ISSN 00942405. Available from DOI: 10.1118/1.4923753 (cit. on p. 106).

LI, H.; WANG, Z., 2005. A Seepage Flow Model for Vertebra CT Image Segmentation. In: *2005 IEEE Engineering in Medicine and Biology 27th Annual Conference* [online], pp. 6364–6367 [visited on 2024-04-04]. ISSN 1558-4615. Available from DOI: 10.1109/IEMBS.2005.1615953 (cit. on pp. 93, 94).

LI, J.; CHEUNG, K. M. C.; SAMARTZIS, D., et al., 2016. Key-Vertebral Screws Strategy for Main Thoracic Curve Correction in Patients With Adolescent Idiopathic Scoliosis. *Clinical Spine Surgery*. Vol. 29, no. 8, E434–441. ISSN 2380-0194. Available from DOI: 10.1097/BSD.0000000000000129 (cit. on p. 100).

LI, M.; SHEN, Y.; FANG, X., et al., 2009. Coronal and Sagittal Plane Correction in Patients with Lenke 1 Adolescent Idiopathic Scoliosis: A Comparison of Consecutive versus Interval Pedicle Screw Placement. *Journal of Spinal Disorders & Techniques*. Vol. 22, no. 4, pp. 251–256. ISSN 1539-2465. Available from DOI: 10.1097/BSD.0b013e3181884940 (cit. on p. 100).

LI, N.; HE, D.; XING, Y., et al., 2015. The Effect of Lateral Wall Perforation on Screw Pull-out Strength: A Cadaveric Study. *Journal of Orthopaedic Surgery and Research*. Vol. 10, p. 6. ISSN 1749-799X. Available from DOI: 10.1186/s13018-015-0157-0 (cit. on p. 133).

LI, S.; YAO, Q.; LI, Y., et al., 2024. To Evaluate the Value of Vertebral Body Cortical Thickness in Predicting Osteoporosis by Opportunistic CT. *Academic Radiology* [online]. Vol. 31, no. 4, pp. 1491–1500 [visited on 2024-05-07]. ISSN 1076-6332. Available from DOI: 10.1016/j.acra.2023.08.041 (cit. on p. 161).

LI, Y.; LIANG, W.; TAN, J., et al., 2015. A Novel Automatically Initialized Level Set Approach Based on Region Correlation for Lumbar Vertebrae CT Image Segmentation. In: *2015 IEEE International Symposium on Medical Measurements and Applications (MeMeA) Proceedings* [online], pp. 291–296 [visited on 2024-04-04]. Available from DOI: 10.1109/MeMeA.2015.7145215 (cit. on p. 94).

LIEBL, H.; SCHINZ, D.; SEKUBOYINA, A., et al., 2021. A Computed Tomography Vertebral Segmentation Dataset with Anatomical Variations and Multi-Vendor Scanner Data. *Scientific Data* [online]. Vol. 8, no. 1, p. 284 [visited on 2024-05-13]. ISSN 2052-4463. Available from DOI: 10.1038/s41597-021-01060-0 (cit. on p. 106).

LIEBSCHNER, M. A. K.; KOPPERDAHL, D. L.; ROSENBERG, W. S., et al., 2003. Finite Element Modeling of the Human Thoracolumbar Spine: *Spine* [online]. Vol. 28, no. 6, pp. 559–565 [visited on 2023-12-20]. ISSN 0362-2436. Available from DOI: 10.1097/01.BRS.0000049923.27694.47 (cit. on pp. 100, 120, 121, 145).

LIM FAT, D.; KENNEDY, J.; GALVIN, R., et al., 2012. The Hounsfield Value for Cortical Bone Geometry in the Proximal Humerus—an in Vitro Study. *Skeletal Radiology* [online]. Vol. 41, no. 5, pp. 557–568 [visited on 2025-02-20]. ISSN 0364-2348, ISSN 1432-2161. Available from DOI: 10.1007/s00256-011-1255-7 (cit. on p. 109).

LINDNER, C.; THIAGARAJAH, S.; WILKINSON, J. M., et al., 2013. Fully Automatic Segmentation of the Proximal Femur Using Random Forest Regression Voting. *IEEE Transactions on Medical Imaging* [online]. Vol. 32, no. 8, pp. 1462–1472 [visited on 2024-03-28]. ISSN 1558-254X. Available from DOI: 10.1109/TMI.2013.2258030 (cit. on p. 86).

LIU, L.-d.; HONG, X.; LI, J.-B., et al., 2021. Delayed Presentation of Thoracic Aortic Pseudoaneurysm Following Pedicle Screw Implantation: A Case Report. *Orthopaedic Surgery*. Vol. 13, no. 1, pp. 338–341. ISSN 1757-7861. Available from DOI: 10.1111/os.12793 (cit. on p. 133).

LLOYD, S., 1982. Least Squares Quantization in PCM. *IEEE Transactions on Information Theory* [online]. Vol. 28, no. 2, pp. 129–137 [visited on 2024-03-21]. ISSN 0018-9448. Available from DOI: 10.1109/TIT.1982.1056489 (cit. on p. 83).

LÖFFLER, M. T.; SEKUBOYINA, A.; JACOB, A., et al., 2020. A Vertebral Segmentation Dataset with Fracture Grading. *Radiology: Artificial Intelligence* [online]. Vol. 2, no. 4, e190138 [visited on 2024-05-13]. ISSN 2638-6100. Available from DOI: 10.1148/ryai.2020190138 (cit. on p. 106).

LONG, J.; SHELHAMER, E.; DARRELL, T., 2015. Fully Convolutional Networks for Semantic Segmentation. In: *Proceedings of the IEEE Conference on Computer Vision and Pattern Recognition* [online], pp. 3431–3440 [visited on 2024-04-05] (cit. on p. 96).

LOOBY, S.; FLANDERS, A., 2011. Spine Trauma. *Radiologic Clinics of North America* [online]. Vol. 49, no. 1, pp. 129–163 [visited on 2023-05-11]. ISSN 00338389. Available from DOI: 10.1016/j.rcl.2010.07.019 (cit. on p. 40).

MA, J.; LU, L.; ZHAN, Y., et al., 2010. Hierarchical Segmentation and Identification of Thoracic Vertebra Using Learning-Based Edge Detection and Coarse-to-Fine Deformable Model. In: JIANG, T.; NAVAB, N.; PLUIM, J. P. W., et al. (eds.). *Medical Image Computing and Computer-Assisted Intervention – MICCAI 2010*. Berlin, Heidelberg: Springer, pp. 19–27. ISBN 978-3-642-15705-9. Available from DOI: 10.1007/978-3-642-15705-9_3 (cit. on p. 95).

MACCAURO, G.; SPINELLI, M. S.; MAURO, S., et al., 2011. Physiopathology of Spine Metastasis. *International Journal of Surgical Oncology*. Vol. 2011, p. 107969. ISSN 2090-1410. Available from DOI: 10.1155/2011/107969 (cit. on p. 49).

MAGERL, F. P., 1984. Stabilization of the Lower Thoracic and Lumbar Spine with External Skeletal Fixation. *Clinical Orthopaedics and Related Research*. Vol. 189, pp. 125–141. ISSN 0009921X. Available from DOI: 10.1097/00003086-198410000-00014 (cit. on pp. 53, 57, 58).

MAKARAM, H.; SWAMINATHAN, R., 2021. Influence of Bone Quality and Pedicle Screw Design on the Fixation Strength during Axial Pull-out Test: A 2D Axisymmetric FE Study. *Annual International Conference of the IEEE Engineering in Medicine and Biology Society. IEEE Engineering in Medicine and Biology Society. Annual International Conference*. Vol. 2021, pp. 4924–4927. ISSN 2694-0604. Available from DOI: 10.1109/EMBC46164.2021.9629484 (cit. on p. 134).

MALTER, A. D.; MCNENEY, B.; LOESER, J. D., et al., 1998. 5-Year Reoperation Rates After Different Types of Lumbar Spine Surgery. *Spine* [online]. Vol. 23, no. 7, p. 814 [visited on 2024-06-10]. ISSN 0362-2436 (cit. on p. 52).

MARTIN, B. I.; MIRZA, S. K.; COMSTOCK, B. A., et al., 2007. Reoperation Rates Following Lumbar Spine Surgery and the Influence of Spinal Fusion Procedures. *Spine* [online]. Vol. 32, no. 3, p. 382 [visited on 2024-06-10]. ISSN 0362-2436. Available from DOI: 10.1097/01.brs.0000254104.55716.46 (cit. on p. 52).

MARTIN, G. J. J.; HAID, R. W. J.; MACMILLAN, M., et al., 1999. Anterior Cervical Discectomy With Freeze-Dried Fibula Allograft: Overview of 317 Cases and Literature Review. *Spine* [online]. Vol. 24, no. 9, p. 852 [visited on 2024-06-10]. ISSN 0362-2436 (cit. on p. 52).

MASTMEYER, A.; ENGELKE, K.; FUCHS, C., et al., 2006. A Hierarchical 3D Segmentation Method and the Definition of Vertebral Body Coordinate Systems for QCT of the Lumbar Spine. *Medical Image Analysis* [online]. Vol. 10, no. 4, pp. 560–577 [visited on 2024-04-04]. ISSN 1361-8415. Available from DOI: 10.1016/j.media.2006.05.005 (cit. on p. 95).

MAURER, C.; QI, R.; RAGHAVAN, V., 2003. A Linear Time Algorithm for Computing Exact Euclidean Distance Transforms of Binary Images in Arbitrary Dimensions. *IEEE Transactions on Pattern Analysis and Machine Intelligence* [online]. Vol. 25, no. 2, pp. 265–270 [visited on 2024-03-29]. ISSN 1939-3539. Available from DOI: 10.1109/TPAMI.2003.1177156 (cit. on p. 92).

MCCORMICK, M.; LIU, X.; JOMIER, J., et al., 2014. ITK: Enabling Reproducible Research and Open Science. *Frontiers in Neuroinformatics*. Vol. 8. ISSN 1662-5196. Available from DOI: 10.3389/fninf.2014.00013 (cit. on p. 109).

MEHMANPARAST, H. N.; MAC-THIONG, J. M.; PETIT, Y., 2014. Estimation of Pedicle Screw Fixation Strength from Probe Indentation Force and Screw Insertion Torque: A Biomechanical Study on Bone Surrogates of Various Densities. In: *2014 36th Annual International Conference of the IEEE Engineering in Medicine and Biology Society* [online]. Chicago, IL: IEEE, pp. 4350–4353 [visited on 2024-02-23]. ISBN 978-1-4244-7929-0. Available from DOI: 10.1109/EMBC.2014.6944587 (cit. on p. 40).

MENG, F.; LI, H.; LIU, G., 2012. A New Co-Saliency Model via Pairwise Constraint Graph Matching. In: *2012 International Symposium on Intelligent Signal Processing and Communications Systems* [online], pp. 781–786 [visited on 2024-03-28]. Available from DOI: 10.1109/ISPACS.2012.6473597 (cit. on p. 184).

MESZAROS, J.; MINARI, J.; HUYS, I., 2022. The Future Regulation of Artificial Intelligence Systems in Healthcare Services and Medical Research in the European Union. *Frontiers in Genetics*. Vol. 13, p. 927721. ISSN 1664-8021. Available from DOI: 10.3389/fgene.2022.927721 (cit. on p. 69).

METROPOLIS, N.; ULAM, S., 1949. The Monte Carlo Method. *Journal of the American Statistical Association* [online]. Vol. 44, no. 247, pp. 335–341 [visited on 2024-03-28]. ISSN 0162-1459. Available from DOI: 10.2307/2280232 (cit. on p. 86).

METTLER, F. A.; BHARGAVAN, M.; FAULKNER, K., et al., 2009. Radiologic and Nuclear Medicine Studies in the United States and Worldwide: Frequency, Radiation Dose, and Comparison with Other Radiation Sources—1950–2007. *Radiology* [online]. Vol. 253, no. 2, pp. 520–531 [visited on 2024-05-29]. ISSN 0033-8419. Available from DOI: 10.1148/radiol.2532082010 (cit. on p. 47).

MIN, K.; SDZUY, C.; FARSHAD, M., 2013. Posterior Correction of Thoracic Adolescent Idiopathic Scoliosis with Pedicle Screw Instrumentation: Results of 48 Patients with Minimal 10-Year Follow-Up. *European Spine Journal: Official Publication of the European Spine Society, the European Spinal Deformity Society, and the European Section of the Cervical Spine Research Society*. Vol. 22, no. 2, pp. 345–354. ISSN 1432-0932. Available from DOI: 10.1007/s00586-012-2533-3 (cit. on p. 100).

MISENHIMER, G. R.; PEEK, R. D.; WILTSE, L. L., et al., 1989. Anatomic Analysis of Pedicle Cortical and Cancellous Diameter as Related to Screw Size. *Spine* [online]. Vol. 14, no. 4, p. 367 [visited on 2024-05-30]. ISSN 0362-2436 (cit. on p. 37).

MODI, H.; SUH, S. W.; SONG, H. R., et al., 2009. Accuracy of Thoracic Pedicle Screw Placement in Scoliosis Using the Ideal Pedicle Entry Point during the Freehand Technique. *International Orthopaedics*. Vol. 33, no. 2, pp. 469–475. ISSN 03412695. Available from DOI: 10.1007/s00264-008-0535-x (cit. on pp. 133, 134).

MODI, H. N.; SUH, S. W.; HONG, J. Y., et al., 2010. Accuracy of Thoracic Pedicle Screw Using Ideal Pedicle Entry Point in Severe Scoliosis. *Clinical Orthopaedics and Related Research*. Vol. 468, no. 7, pp. 1830–1837. ISSN 15281132. Available from DOI: 10.1007/s11999-010-1280-1 (cit. on p. 56).

MÖLLER, T.; TRUMBORE, B., 1997. Fast, Minimum Storage Ray-Triangle Intersection. *Journal of Graphics Tools*. Vol. 2, no. 1, pp. 21–28. ISSN 1086-7651. Available from DOI: 10.1080/10867651.1997.10487468 (cit. on pp. 111, 112).

MORGAN, E. F.; KEAVENY, T. M., 2001. Dependence of Yield Strain of Human Trabecular Bone on Anatomic Site. *Journal of Biomechanics*. Vol. 34, no. 5, pp. 569–577. ISSN 0021-9290. Available from DOI: 10.1016/s0021-9290(01)00011-2 (cit. on p. 134).

MORGAN, E. F.; BAYRAKTAR, H. H.; KEAVENY, T. M., 2003. Trabecular Bone Modulus-Density Relationships Depend on Anatomic Site. *Journal of Biomechanics*. Vol. 36, no. 7, pp. 897–904. ISSN 00219290. Available from DOI: 10.1016/S0021-9290(03)00071-X (cit. on p. 134).

MORGAN, E. F.; UNNIKRISNAN, G. U.; HUSSEIN, A. I., 2018. *Bone Mechanical Properties in Healthy and Diseased States*. Vol. 20. Annual Reviews Inc. ISSN 15454274. Available from DOI: 10.1146/annurev-bioeng-062117-121139 (cit. on pp. 32, 134, 145).

MOSHER, H. P., 1913. The Applied Anatomy and the Intra-nasal Surgery of the Ethmoidal Labyrinth. *The Laryngoscope* [online]. Vol. 23, no. 9, pp. 881–907 [visited on 2024-02-21]. ISSN 0023-852X, ISSN 1531-4995. Available from DOI: 10.1288/00005537-191309000-00001 (cit. on p. 61).

MOSTAFAPOUR, S.; GREUTER, M.; VAN SNICK, J. H., et al., 2024. Ultra-Low Dose CT Scanning for PET/CT. *Medical Physics* [online]. Vol. 51, no. 1, pp. 139–155 [visited on 2024-05-29]. ISSN 2473-4209. Available from DOI: 10.1002/mp.16862 (cit. on p. 47).

MUKHERJEE, L.; SINGH, V.; DYER, C. R., 2009. Half-Integrality Based Algorithms for Cosegmentation of Images. In: *2009 IEEE Conference on Computer Vision and Pattern Recognition* [online], pp. 2028–2035 [visited on 2024-03-22]. ISSN 1063-6919. Available from DOI: 10.1109/CVPR.2009.5206652 (cit. on p. 184).

MYS, K.; VARGA, P.; STOCKMANS, F., et al., 2021. High-Resolution Cone-Beam Computed Tomography Is a Fast and Promising Technique to Quantify Bone Microstructure and Mechanics of the Distal Radius. *Calcified Tissue International* [online]. Vol. 108, no. 3, pp. 314–323 [visited on 2024-05-29]. ISSN 1432-0827. Available from DOI: 10.1007/s00223-020-00773-5 (cit. on p. 44).

NAGARAJA, S.; PALEPU, V., 2016. Comparisons of Anterior Plate Screw Pullout Strength Between Polyurethane Foams and Thoracolumbar Cadaveric Vertebrae. *Journal of Biomechanical Engineering*. Vol. 138, no. 10. ISSN 1528-8951. Available from DOI: 10.1115/1.4034427 (cit. on p. 143).

NAIK, N.; HAMEED, B. M. Z.; SHETTY, D. K., et al., 2022. Legal and Ethical Consideration in Artificial Intelligence in Healthcare: Who Takes Responsibility? *Frontiers in Surgery*. Vol. 9, p. 862322. ISSN 2296-875X. Available from DOI: 10.3389/fsurg.2022.862322 (cit. on p. 69).

NGUYEN, V. A.; SUN, C.; XU, H., et al., 2021. *Characteristics of CT Hounsfield Unit Values in Lumbar Vertebrae and Lumbar Pedicle – A Comparative Study Based on CT Scans and Dual-Energy X-ray Absorptiometry (DEXA)* [online]. [visited on 2024-05-13]. ISSN 2693-5015. Available from DOI: 10.21203/rs.3.rs-287863/v1 (cit. on p. 114).

NIIMI, R.; KONO, T.; NISHIHARA, A., et al., 2015. Cortical Thickness of the Femur and Long-Term Bisphosphonate Use. *Journal of Bone and Mineral Research* [online]. Vol. 30, no. 2, pp. 225–231 [visited on 2024-01-24]. ISSN 0884-0431, ISSN 1523-4681. Available from DOI: 10.1002/jbmr.2345 (cit. on p. 32).

NOWAK, B., 2019. Experimental Study on the Loosening of Pedicle Screws Implanted to Synthetic Bone Vertebra Models and under Non-Pull-out Mechanical Loads. *Journal of the Mechanical Behavior of Biomedical Materials*. Vol. 98, pp. 200–204. ISSN 1878-0180. Available from DOI: 10.1016/j.jmbbm.2019.06.013 (cit. on p. 143).

ODEH, K.; ROSINSKI, A.; LEASURE, J., et al., 2021. Pedicle Screws Challenged: Lumbar Cortical Density and Thickness Are Greater in the Posterior Elements Than in the Pedicles. *Global Spine Journal* [online]. Vol. 11, no. 1, pp. 34–43 [visited on 2023-07-06]. ISSN 2192-5682, ISSN 2192-5690. Available from DOI: 10.1177/2192568219889361 (cit. on pp. 100, 120, 145).

OHTORI, S.; INOUE, G.; ORITA, S., et al., 2013. Comparison of Teriparatide and Bisphosphonate Treatment to Reduce Pedicle Screw Loosening after Lumbar Spinal Fusion Surgery in Postmenopausal Women with Osteoporosis from a Bone Quality Perspective. *Spine*. Vol. 38, no. 8, E487–492. ISSN 1528-1159. Available from DOI: 10.1097/BRS.0b013e31828826dd (cit. on p. 100).

OKUYAMA, K.; ABE, E.; SUZUKI, T., et al., 2001. Influence of Bone Mineral Density on Pedicle Screw Fixation: A Study of Pedicle Screw Fixation Augmenting Posterior Lumbar Interbody Fusion in Elderly Patients. *The Spine Journal: Official Journal of the North American Spine Society*. Vol. 1, no. 6, pp. 402–407. ISSN 1529-9430. Available from DOI: 10.1016/s1529-9430(01)00078-x (cit. on p. 100).

OROSZLÁNY, Á.; NAGY, P.; KOVÁCS, J. G., 2015. Compressive Properties of Commercially Available PVC Foams Intended for Use as Mechanical Models for Human Cancellous Bone. *Acta Polytechnica Hungarica* [online]. Vol. 12, no. 2 [visited on 2024-05-07]. ISSN 17858860. Available from DOI: 10.12700/APH.12.2.2015.2.6 (cit. on p. 144).

OTSU, N., 1979. A Threshold Selection Method from Gray-Level Histograms. *IEEE Transactions on Systems, Man, and Cybernetics* [online]. Vol. 9, no. 1, pp. 62–66 [visited on 2024-03-21]. ISSN 0018-9472, ISSN 2168-2909. Available from DOI: 10.1109/TSMC.1979.4310076 (cit. on p. 82).

PAL, G. P.; COSIO, L.; ROUTAL, R. V., 1988. Trajectory Architecture of the Trabecular Bone between the Body and the Neural Arch in Human Vertebrae. *The Anatomical Record*. Vol. 222, no. 4, pp. 418–425. ISSN 0003-276X. Available from DOI: 10.1002/ar.1092220414 (cit. on p. 28).

PANJABI, M. M.; CHEN, N. C.; SHIN, E. K., et al., 2001. The Cortical Shell Architecture of Human Cervical Vertebral Bodies. *Spine* [online]. Vol. 26, no. 22, p. 2478 [visited on 2024-05-13]. ISSN 0362-2436 (cit. on p. 107).

PARKER, S. L.; MCGIRT, M. J.; FARBER, S. H., et al., 2011. Accuracy of Free-Hand Pedicle Screws in the Thoracic and Lumbar Spine: Analysis of 6816 Consecutive Screws. *Neurosurgery*. Vol. 68, no. 1, pp. 170–178. ISSN 0148396X. Available from DOI: 10.1227/NEU.0b013e3181fdfaf4 (cit. on pp. 56, 57).

PASHKOV, V. M.; HARKUSHA, A. O.; HARKUSHA, Y. O., 2020. ARTIFICIAL INTELLIGENCE IN MEDICAL PRACTICE: REGULATIVE ISSUES AND PERSPECTIVES. *Wiadomosci Lekarskie (Warsaw, Poland: 1960)*. Vol. 73, no. 12 cz 2, pp. 2722–2727. ISSN 0043-5147 (cit. on p. 69).

PAVLIDIS, T., 1972. Segmentation of Pictures and Maps through Functional Approximation. *Computer Graphics and Image Processing* [online]. Vol. 1, no. 4, pp. 360–372 [visited on 2024-03-21]. ISSN 0146664X. Available from DOI: 10.1016/0146-664X(72)90021-4 (cit. on p. 78).

PAXINOS, O.; TSITSOPOULOS, P. P.; ZINDRICK, M. R., et al., 2010. Evaluation of Pull-out Strength and Failure Mechanism of Posterior Instrumentation in Normal and Osteopenic Thoracic Vertebrae: Laboratory Investigation. *Journal of Neurosurgery: Spine* [online]. Vol. 13, no. 4, pp. 469–476 [visited on 2024-05-07]. Available from DOI: 10.3171/2010.4.SPINE09764 (cit. on p. 161).

PEARSON, K., 1901. On Lines and Planes of Closest Fit to Systems of Points in Space. *The London, Edinburgh, and Dublin Philosophical Magazine and Journal of Science* [online]. Vol. 2, no. 11, pp. 559–572 [visited on 2024-03-28]. ISSN 1941-5982, ISSN 1941-5990. Available from DOI: 10.1080/14786440109462720 (cit. on p. 86).

PHILLIPS, F. M.; CARLSON, G.; EMERY, S. E., et al., 1997. Anterior Cervical Pseudarthrosis: Natural History and Treatment. *Spine* [online]. Vol. 22, no. 14, p. 1585 [visited on 2024-06-10]. ISSN 0362-2436 (cit. on p. 52).

PIETROBELLI, A.; FORMICA, C.; WANG, Z., et al., 1996. Dual-Energy X-ray Absorptiometry Body Composition Model: Review of Physical Concepts. *The American Journal of Physiology*. Vol. 271, no. 6 Pt 1, E941–951. ISSN 0002-9513. Available from DOI: 10.1152/ajpendo.1996.271.6.E941 (cit. on p. 46).

PLOMP, K.; VIÐARSDÓTTIR, U. S.; DOBNEY, K., et al., 2019. Potential Adaptations for Bipedalism in the Thoracic and Lumbar Vertebrae of *Homo Sapiens*: A 3D Comparative Analysis. *Journal of Human Evolution* [online]. Vol. 137, p. 102693 [visited on 2024-05-23]. ISSN 0047-2484. Available from DOI: 10.1016/j.jhevol.2019.102693 (cit. on p. 31).

PLOMP, K. A.; ROBERTS, C. A.; VIÐARSDÓTTIR, U. S., 2012. Vertebral Morphology Influences the Development of Schmorl's Nodes in the Lower Thoracic Vertebrae. *American Journal of Physical Anthropology* [online]. Vol. 149, no. 4, pp. 572–582 [visited on 2024-05-23]. ISSN 1096-8644. Available from DOI: 10.1002/ajpa.22168 (cit. on p. 31).

PRESCIUTTI, S. M.; KARUKANDA, T.; LEE, M., 2014. Management Decisions for Adolescent Idiopathic Scoliosis Significantly Affect Patient Radiation Exposure. *The Spine Journal: Official Journal of the North American Spine Society*. Vol. 14, no. 9, pp. 1984–1990. ISSN 1878-1632. Available from DOI: 10.1016/j.spinee.2013.11.055 (cit. on p. 129).

PREVRHAL, S.; ENGELKE, K.; KALENDER, W. A., 1999. Accuracy Limits for the Determination of Cortical Width and Density: The Influence of Object Size and CT Imaging Parameters. *Physics in Medicine and Biology* [online]. Vol. 44, no. 3, pp. 751–764 [visited on 2023-12-20]. ISSN 0031-9155, ISSN 1361-6560. Available from DOI: 10.1088/0031-9155/44/3/017 (cit. on pp. 100, 120).

PREVRHAL, S.; FOX, J. C.; SHEPHERD, J. A., et al., 2003. Accuracy of CT-based Thickness Measurement of Thin Structures: Modeling of Limited Spatial Resolution in All Three Dimensions. *Medical Physics* [online]. Vol. 30, no. 1, pp. 1–8 [visited on 2023-12-20]. ISSN 0094-2405, ISSN 2473-4209. Available from DOI: 10.1118/1.1521940 (cit. on pp. 100, 120, 121).

R CORE TEAM, 2021. *R: A Language and Environment for Statistical Computing* [R Foundation for Statistical Computing]. Vienna, Austria (cit. on p. 150).

RAJAEE, S. S.; KANIM, L. E. A.; BAE, H. W., 2014. National Trends in Revision Spinal Fusion in the USA: Patient Characteristics and Complications. *The Bone & Joint Journal* [online]. Vol. 96-B, no. 6, pp. 807–816 [visited on 2024-06-10]. ISSN 2049-4408. Available from DOI: 10.1302/0301-620x.96b6.31149 (cit. on p. 183).

RAMPERSAUD, Y. R.; SIMON, D. A.; FOLEY, K. T., 2001. Accuracy Requirements for Image-Guided Spinal Pedicle Screw Placement: *Spine* [online]. Vol. 26, no. 4, pp. 352–359 [visited on 2024-01-18]. ISSN 0362-2436. Available from DOI: 10.1097/00007632-200102150-00010 (cit. on pp. 131, 133).

RESNICK, D., 1985. Degenerative Diseases of the Vertebral Column. *Radiology* [online]. Vol. 156, no. 1, pp. 3–14 [visited on 2023-05-11]. ISSN 0033-8419, ISSN 1527-1315. Available from DOI: 10.1148/radiology.156.1.3923556 (cit. on p. 40).

REZNIKOV, N.; CHASE, H.; BEN ZVI, Y., et al., 2016. Inter-Trabecular Angle: A Parameter of Trabecular Bone Architecture in the Human Proximal Femur That Reveals Underlying Topological Motifs. *Acta Biomaterialia* [online]. Vol. 44, pp. 65–72 [visited on 2024-02-23]. ISSN 17427061. Available from DOI: 10.1016/j.actbio.2016.08.040 (cit. on p. 35).

RIECHERT, T., 1975. Development of Human Stereotactic Surgery. *Stereotactic and Functional Neurosurgery* [online]. Vol. 37, no. 4, pp. 399–409 [visited on 2024-02-21]. ISSN 1011-6125, ISSN 1423-0372. Available from DOI: 10.1159/000102774 (cit. on p. 61).

RILEY, L. H.; ROBINSON, R. A.; JOHNSON, K. A., et al., 1969. The Results of Anterior Interbody Fusion of the Cervical Spine: Review of Ninety-Three Consecutive Cases. *Journal of Neurosurgery* [online]. Vol. 30, no. 2, pp. 127–133 [visited on 2024-06-10]. Available from DOI: 10.3171/jns.1969.30.2.0127 (cit. on p. 52).

RITZEL, H.; AMLING, M.; PÖSL, M., et al., 1997. The Thickness of Human Vertebral Cortical Bone and Its Changes in Aging and Osteoporosis: A Histomorphometric Analysis of the Complete Spinal Column from Thirty-Seven Autopsy Specimens. *Journal of Bone and Mineral Research*. Vol. 12, no. 1, pp. 89–95. ISSN 08840431. Available from DOI: 10.1359/jbmr.1997.12.1.89 (cit. on pp. 107, 120).

RODT, T.; KÖPPEN, G.; LORENZ, M., et al., 2007. Placement of Intraventricular Catheters Using Flexible Electromagnetic Navigation and a Dynamic Reference Frame: A New Technique. *Stereotactic and Functional Neurosurgery* [online]. Vol. 85, no. 5, pp. 243–248 [visited on 2024-06-03]. ISSN 1011-6125. Available from DOI: 10.1159/000103263 (cit. on p. 63).

RONCKERS, C. M.; LAND, C. E.; MILLER, J. S., et al., 2010. Cancer Mortality among Women Frequently Exposed to Radiographic Examinations for Spinal Disorders. *Radiation Research*. Vol. 174, no. 1, pp. 83–90. ISSN 1938-5404. Available from DOI: 10.1667/RR2022.1 (cit. on p. 129).

RONNEBERGER, O.; FISCHER, P.; BROX, T., 2015. *U-Net: Convolutional Networks for Biomedical Image Segmentation* [online]. arXiv [visited on 2024-04-05]. No. arXiv:1505.04597. Available from DOI: 10.48550/arXiv.1505.04597 (cit. on pp. 96, 97).

ROSENFELD, A., 1979. Fuzzy Digital Topology. *Information and Control* [online]. Vol. 40, no. 1, pp. 76–87 [visited on 2024-03-21]. ISSN 00199958. Available from DOI: 10.1016/S0019-9958(79)90353-X (cit. on p. 78).

ROTHER, C.; MINKA, T.; BLAKE, A., et al., 2006. Cosegmentation of Image Pairs by Histogram Matching - Incorporating a Global Constraint into MRFs. In: *2006 IEEE Computer Society Conference on Computer Vision and Pattern Recognition (CVPR'06)* [online]. Vol. 1, pp. 993–1000 [visited on 2024-03-21]. ISSN 1063-6919. Available from DOI: 10.1109/CVPR.2006.91 (cit. on pp. 84, 184).

ROTHMAN, R. H.; SIMEONE, F. A.; HERKOWITZ, H. N. (eds.), 2018. *Rothman-Simeone and Herkowitz's, the Spine*. Seventh edition. Philadelphia, PA: Elsevier. ISBN 978-0-323-39397-3 978-99961-1-786-2 978-99961-1-792-3 (cit. on pp. 42–45).

ROUSSOULY, P.; PINHEIRO-FRANCO, J. L., 2011. Biomechanical Analysis of the Spino-Pelvic Organization and Adaptation in Pathology. *European Spine Journal* [online]. Vol. 20, no. S5, pp. 609–618 [visited on 2024-02-02]. ISSN 0940-6719, ISSN 1432-0932. Available from DOI: 10.1007/s00586-011-1928-x (cit. on p. 26).

ROY-CAMILLE, R.; SAILLANT, G.; MAZEL, C., 1986a. Plating of Thoracic, Thoracolumbar, and Lumbar Injuries with Pedicle Screw Plates. *The Orthopedic clinics of North America*. Vol. 17, no. 1, pp. 147–59. ISSN 0030-5898. Available from PMID: 3945476 (cit. on pp. 58, 59).

ROY-CAMILLE, R.; BERTEAUX, D.; SAILLANT, G., et al., 1977. Internal Fixation of Fractures of the Dorsal and Lumbar Spine Using Plates Screwed to the Vertebral Pedicles. *International Orthopaedics*. Vol. 1, no. 2, pp. 121–124. ISSN 0341-2695 (cit. on p. 52).

ROY-CAMILLE, R.; SAILLANT, G.; MAZEL, C., 1986b. Internal Fixation of the Lumbar Spine with Pedicle Screw Plating. *Clinical Orthopaedics and Related Research*. Vol. 203, pp. 7–17. ISSN 0009921X. Available from DOI: 10.1097/00003086-198602000-00003 (cit. on pp. 52, 58).

RUSSAKOVSKY, O.; DENG, J.; SU, H., et al., 2015. ImageNet Large Scale Visual Recognition Challenge. *International Journal of Computer Vision* [online]. Vol. 115, no. 3, pp. 211–252 [visited on 2024-04-05]. ISSN 1573-1405. Available from DOI: 10.1007/s11263-015-0816-y (cit. on p. 96).

SAARINEN, A. J.; SUOMINEN, E. N.; HELENIUS, L., et al., 2022. Intraoperative 3D Imaging Reduces Pedicle Screw Related Complications and Reoperations in Adolescents Undergoing Posterior Spinal Fusion for Idiopathic Scoliosis: A Retrospective Study. *Children (Basel, Switzerland)*. Vol. 9, no. 8, p. 1129. ISSN 2227-9067. Available from DOI: 10.3390/children9081129 (cit. on p. 129).

SANDERS, J. O.; DIAB, M.; RICHARDS, S. B., et al., 2011. Fixation Points within the Main Thoracic Curve: Does More Instrumentation Produce Greater Curve Correction and Improved Results? *Spine*. Vol. 36, no. 21, E1402–1406. ISSN 1528-1159. Available from DOI: 10.1097/BRS.0b013e31822815ff (cit. on p. 100).

SANDERSON, C.; CURTIN, R., 2016. Armadillo: A Template-Based C++ Library for Linear Algebra. *The Journal of Open Source Software*. Vol. 1, no. 2, p. 26. ISSN 2475-9066. Available from DOI: 10.21105/joss.00026 (cit. on p. 111).

SANDOR, T.; FELSENBERG, D.; KALENDER, W. A., et al., 1992. Compact and Trabecular Components of the Spine Using Quantitative Computed Tomography. *Calcified Tissue International*. Vol. 50, no. 6, pp. 502–506. ISSN 0171-967X. Available from DOI: 10.1007/BF00582162 (cit. on p. 100).

SCHLENK, R. P.; KOWALSKI, R. J.; BENZEL, E. C., 2003. Biomechanics of Spinal Deformity. *Neurosurgical Focus* [online]. Vol. 14, no. 1, pp. 1–15 [visited on 2023-05-22]. ISSN 1092-0684. Available from DOI: 10.3171/foc.2003.14.1.3 (cit. on p. 42).

SCHREIBER, J. J.; ANDERSON, P. A.; ROSAS, H. G., et al., 2011. Hounsfield Units for Assessing Bone Mineral Density and Strength: A Tool for Osteoporosis Management. *Journal of Bone and Joint Surgery* [online]. Vol. 93, no. 11, pp. 1057–1063 [visited on 2024-05-07]. ISSN 0021-9355, ISSN 1535-1386. Available from DOI: 10.2106/JBJS.J.00160 (cit. on p. 161).

SCHROEDER, W.; MARTIN, K.; LORENSEN, B., et al., 2006. *The Visualization Toolkit: An Object-oriented Approach to 3D Graphics*. Kitware. ISBN 978-1-930934-19-1 (cit. on p. 111).

SEEGER, L. L., 1989. Physical Principles of Magnetic Resonance Imaging. *Clinical Orthopaedics and Related Research*. No. 244, pp. 7–16. ISSN 0009-921X (cit. on p. 45).

SEKUBOYINA, A.; HUSSEINI, M. E.; BAYAT, A., et al., 2021. VerSe: A Vertebrae Labelling and Segmentation Benchmark for Multi-Detector CT Images. *Medical Image Analysis*. Vol. 73, p. 102166. ISSN 1361-8415. Available from DOI: 10.1016/J.MEDIA.2021.102166 (cit. on p. 106).

SERRURIER, A.; JOLIVET, E.; QUIJANO, S., et al., 2014. Distribution and Variability Study of the Femur Cortical Thickness from Computer Tomography. *Computer Methods in Biomechanics and Biomedical Engineering*. Vol. 17, no. 7, pp. 768–786. ISSN 1476-8259. Available from DOI: 10.1080/10255842.2012.715640 (cit. on p. 106).

SHEN, D.; WU, G.; SUK, H.-I., 2017. Deep Learning in Medical Image Analysis. *Annual review of biomedical engineering* [online]. Vol. 19, pp. 221–248 [visited on 2024-04-05]. ISSN 1523-9829. Available from DOI: 10.1146/annurev-bioeng-071516-044442 (cit. on p. 96).

SHENG, S. R.; WANG, X. Y.; XU, H. Z., et al., 2010. Anatomy of Large Animal Spines and Its Comparison to the Human Spine: A Systematic Review. *European Spine Journal*. Vol. 19, no. 1, pp. 46–56. ISSN 09406719. Available from DOI: 10.1007/s00586-009-1192-5 (cit. on p. 29).

SILVA, M.; WANG, C.; KEAVENY, T., et al., 1994. Direct and Computed Tomography Thickness Measurements of the Human, Lumbar Vertebral Shell and Endplate. *Bone* [online]. Vol. 15, no. 4, pp. 409–414 [visited on 2023-12-20]. ISSN 87563282. Available from DOI: 10.1016/8756-3282(94)90817-6 (cit. on pp. 100, 120, 121).

SIMONY, A.; HANSEN, E. J.; CHRISTENSEN, S. B., et al., 2016. Incidence of Cancer in Adolescent Idiopathic Scoliosis Patients Treated 25 Years Previously. *European Spine Journal: Official Publication of the European Spine Society, the European Spinal Deformity Society, and the European Section of the Cervical Spine Research Society*. Vol. 25, no. 10, pp. 3366–3370. ISSN 1432-0932. Available from DOI: 10.1007/s00586-016-4747-2 (cit. on p. 129).

SINGH, I., 1978. The Architecture of Cancellous Bone. *Journal of Anatomy* [online]. Vol. 127, no. Pt 2, p. 305 [visited on 2024-05-30] (cit. on pp. 33–35).

SIVASUBRAMANIAM, V.; PATEL, H. C.; OZDEMIR, B. A., et al., 2015. Trends in Hospital Admissions and Surgical Procedures for Degenerative Lumbar Spine Disease in England: A 15-Year Time-Series Study. *BMJ Open* [online]. Vol. 5, no. 12, e009011 [visited on 2024-06-10]. ISSN 2044-6055, ISSN 2044-6055. Available from DOI: 10.1136/bmjopen-2015-009011 (cit. on p. 52).

SKEDROS, J. G.; MASON, M. W.; BLOEBAUM, R. D., 1994. Differences in Osteonal Micromorphology between Tensile and Compressive Cortices of a Bending Skeletal System: Indications of Potential Strain-specific Differences in Bone Microstructure. *The Anatomical Record*. Vol. 239, no. 4, pp. 405–413. ISSN 10970185. Available from DOI: 10.1002/ar.1092390407 (cit. on p. 26).

SMORGICK, Y.; MILLGRAM, M. A.; ANEKSTEIN, Y., et al., 2005. Accuracy and Safety of Thoracic Pedicle Screw Placement in Spinal Deformities. *Journal of Spinal Disorders & Techniques*. Vol. 18, no. 6, pp. 522–526. ISSN 1536-0652. Available from DOI: 10.1097/01.bsd.0000154448.90707.a8 (cit. on p. 52).

SOBEL, I.; FELDMAN, G., 1973. A 3×3 Isotropic Gradient Operator for Image Processing. *Pattern Classification and Scene Analysis*, pp. 271–272 (cit. on p. 79).

SPIEGEL, E. A.; WYCIS, H. T.; MARKS, M., et al., 1947. Stereotaxic Apparatus for Operations on the Human Brain. *Science* [online]. Vol. 106, no. 2754, pp. 349–350 [visited on 2024-02-21]. ISSN 0036-8075, ISSN 1095-9203. Available from DOI: 10.1126/science.106.2754.349 (cit. on p. 61).

SUK, S.-I., 2011. Pedicle Screw Instrumentation for Adolescent Idiopathic Scoliosis: The Insertion Technique, the Fusion Levels and Direct Vertebral Rotation. *Clinics in Orthopedic Surgery*. Vol. 3, no. 2, pp. 89–100. ISSN 2005-4408. Available from DOI: 10.4055/cios.2011.3.2.89 (cit. on pp. 129, 133).

SWAMINATHAN, G.; MURALIDHARAN, V.; DEVAKUMAR, D., et al., 2020. Accuracy of the Freehand (Fennell) Technique Using a Uniform Entry Point and Sagittal Trajectory for Insertion of Thoracic Pedicle Screws: A Computed Tomography-Based Virtual Simulation Study. *Neurology India*. Vol. 68, no. 2, pp. 468–471. ISSN 1998-4022. Available from DOI: 10.4103/0028-3886.284379 (cit. on pp. 133, 134).

TALAIRACH, J.; TOURNOUX, P., 1988. *Co-Planar Stereotaxic Atlas of the Human Brain: 3-Dimensional Proportional System: An Approach to Cerebral Imaging*. Stuttgart ; New York: Georg Thieme. ISBN 978-0-86577-293-9 978-3-13-711701-8 (cit. on p. 61).

TOMI, F.; et al., 2024. Vertebral Cortical Thickness and Cortical Bone Density: An Automated CT Assessment - towards Enhanced Spine Segmentation. *Computer Methods in Biomechanics and Biomedical Engineering: Imaging & Visualization* [online]. Vol. 12, no. 1, p. 2412332 [visited on 2025-03-20]. ISSN 2168-1163. Available from DOI: 10.1080/21681163.2024.2412332 (cit. on pp. 3, 106).

TOMINAGA, T.; DICKMAN, C. A.; SONNTAG, V. K. H., et al., 1995. Comparative Anatomy of the Baboon and the Human Cervical Spine: *Spine* [online]. Vol. 20, no. 2, pp. 131–137 [visited on 2023-05-09]. ISSN 0362-2436. Available from DOI: 10.1097/00007632-199501150-00001 (cit. on p. 29).

TONETTI, J.; BOUDISSA, M.; KERSCHBAUMER, G., et al., 2020. Role of 3D Intraoperative Imaging in Orthopedic and Trauma Surgery. *Orthopaedics & traumatology, surgery & research: OTSR*. Vol. 106, no. 1S, S19–S25. ISSN 1877-0568. Available from DOI: 10.1016/j.otsr.2019.05.021 (cit. on pp. 46, 129).

TSUJI, M.; CROOKSHANK, M.; OLSEN, M., et al., 2013. The Biomechanical Effect of Artificial and Human Bone Density on Stopping and Stripping Torque during Screw Insertion. *Journal of the Mechanical Behavior of Biomedical Materials*. Vol. 22, pp. 146–156. ISSN 1878-0180. Available from DOI: 10.1016/j.jmbbm.2013.03.006 (cit. on p. 144).

TYRRELL, P. N. M.; CASSAR-PULLICINO, V. N.; MCCALL, I. W., 1999. Spinal Infection. *European Radiology* [online]. Vol. 9, no. 6, pp. 1066–1077 [visited on 2023-05-11]. ISSN 0938-7994, ISSN 1432-1084. Available from DOI: 10.1007/s003300050793 (cit. on pp. 41, 50).

VACCARO, A. R.; HARRIS, J. A.; HUSSAIN, M. M., et al., 2020. Assessment of Surgical Procedural Time, Pedicle Screw Accuracy, and Clinician Radiation Exposure of a Novel Robotic Navigation System Compared With Conventional Open and Percutaneous Freehand Techniques: A Cadaveric Investigation. *Global Spine Journal*. Vol. 10, no. 7, pp. 814–825. ISSN 2192-5682. Available from DOI: 10.1177/2192568219879083 (cit. on p. 133).

VACCARO, A. R.; ONER, C.; KEPLER, C. K., et al., 2013. AOSpine Thoracolumbar Spine Injury Classification System: Fracture Description, Neurological Status, and Key Modifiers. *Spine*. Vol. 38, no. 23, pp. 2028–2037. ISSN 1528-1159. Available from DOI: 10.1097/BRS.0b013e3182a8a381 (cit. on p. 49).

VALENTIN, J.; INTERNATIONAL COMMISSION ON RADIOLOGICAL PROTECTION (eds.), 2007. *The 2007 Recommendations of the International Commission on Radiological Protection*. Oxford: Elsevier. ICRP Publication, no. 103. ISBN 978-0-7020-3048-2 (cit. on p. 67).

VAN DER KOLK, B. (Y. M.; SLOTMAN, D. J. (; NIJHOLT, I. M., et al., 2022. Bone Visualization of the Cervical Spine with Deep Learning-Based Synthetic CT Compared to Conventional CT: A Single-Center Noninferiority Study on Image Quality. *European Journal of Radiology* [online]. Vol. 154, p. 110414 [visited on 2023-07-19]. ISSN 0720-048X. Available from DOI: 10.1016/j.ejrad.2022.110414 (cit. on p. 45).

VAN GOETHEM, J.; VAN DEN HAUWE, L.; ÖZSARLAK, Ö., et al., 2004. Spinal Tumors. *European Journal of Radiology* [online]. Vol. 50, no. 2, pp. 159–176 [visited on 2023-05-10]. ISSN 0720048X. Available from DOI: 10.1016/j.ejrad.2003.10.021 (cit. on p. 41).

VARGHESE, V.; KRISHNAN, V.; SARAVANA KUMAR, G., 2018. Testing Pullout Strength of Pedicle Screw Using Synthetic Bone Models: Is a Bilayer Foam Model a Better Representation of Vertebra? *Asian Spine Journal*. Vol. 12, no. 3, pp. 398–406. ISSN 1976-1902. Available from DOI: 10.4184/asj.2018.12.3.398 (cit. on p. 143).

VESTERBY, A.; MOSEKILDE, L.; GUNDERSEN, H. J., et al., 1991. Biologically Meaningful Determinants of the in Vitro Strength of Lumbar Vertebrae. *Bone*. Vol. 12, no. 3, pp. 219–224. ISSN 8756-3282. Available from DOI: 10.1016/8756-3282(91)90044-j (cit. on p. 100).

VIALLE, R.; ZELLER, R.; GAINES, R. W., 2014. The "Slide Technique": An Improvement on the "Funnel Technique" for Safe Pedicle Screw Placement in the Thoracic Spine. *European Spine Journal: Official Publication of the European Spine Society, the European Spinal Deformity Society, and the European Section of the Cervical Spine Research Society*. Vol. 23 Suppl 4, S452–456. ISSN 1432-0932. Available from DOI: 10.1007/s00586-014-3342-7 (cit. on pp. 131, 133).

VIAU, M.; TARBOX, B. B.; WONGLERTSIRI, S., et al., 2002. Thoracic Pedicle Screw Instrumentation Using the "Funnel Technique": Part 2. Clinical Experience. *Journal of Spinal Disorders & Techniques*. Vol. 15, no. 6, pp. 450–453. ISSN 1536-0652. Available from DOI: 10.1097/00024720-200212000-00002 (cit. on p. 131).

VICENTE, S.; KOLMOGOROV, V.; ROTHER, C., 2010. Cosegmentation Revisited: Models and Optimization. In: DANIILIDIS, K.; MARAGOS, P.; PARAGIOS, N. (eds.). *Computer Vision – ECCV 2010*. Berlin, Heidelberg: Springer, pp. 465–479. ISBN 978-3-642-15552-9. Available from DOI: 10.1007/978-3-642-15552-9_34 (cit. on p. 184).

VIRTANEN, P.; GOMMERS, R.; OLIPHANT, T. E., et al., 2020. SciPy 1.0: Fundamental Algorithms for Scientific Computing in Python. *Nature Methods* [online]. Vol. 17, no. 3, pp. 261–272 [visited on 2023-12-20]. ISSN 1548-7091, ISSN 1548-7105. Available from DOI: 10.1038/s41592-019-0686-2 (cit. on p. 115).

WADE, R.; YANG, H.; MCKENNA, C., et al., 2013. A Systematic Review of the Clinical Effectiveness of EOS 2D/3D X-ray Imaging System. *European Spine Journal* [online]. Vol. 22, no. 2, pp. 296–304 [visited on 2023-12-20]. ISSN 0940-6719, ISSN 1432-0932. Available from DOI: 10.1007/s00586-012-2469-7 (cit. on pp. 43, 120).

WAGNAC, E.; ARNOUX, P.-J.; GARO, A., et al., 2011. Calibration of Hyperelastic Material Properties of the Human Lumbar Intervertebral Disc under Fast Dynamic Compressive Loads. *Journal of Biomechanical Engineering* [online]. Vol. 133, no. 10, p. 101007 [visited on 2024-05-13]. ISSN 0148-0731, ISSN 1528-8951. Available from DOI: 10.1115/1.4005224 (cit. on pp. 107, 115).

WANG, F.; ZHENG, K.; LU, L., et al., 2020. Automatic Vertebra Localization and Identification in CT by Spine Rectification and Anatomically-constrained Optimization [online] [visited on 2024-05-06]. Available from DOI: 10.48550/ARXIV.2012.07947 (cit. on p. 158).

WANG, J. C.; MCDONOUGH, P. W.; KANIM, L. E. A., et al., 2001. Increased Fusion Rates With Cervical Plating for Three-Level Anterior Cervical Discectomy and Fusion. *Spine* [online]. Vol. 26, no. 6, p. 643 [visited on 2024-06-10]. ISSN 0362-2436 (cit. on p. 52).

WARD, J. H., 1963. Hierarchical Grouping to Optimize an Objective Function. *Journal of the American Statistical Association* [online]. Vol. 58, no. 301, pp. 236–244 [visited on 2024-03-28]. ISSN 0162-1459. Available from DOI: 10.2307/2282967 (cit. on p. 86).

WATANABE, E.; WATANABE, T.; MANAKA, S., et al., 1987. Three-Dimensional Digitizer (Neuronavigator): New Equipment for Computed Tomography-Guided Stereotaxic Surgery. *Surgical Neurology* [online]. Vol. 27, no. 6, pp. 543–547 [visited on 2024-02-21]. ISSN 00903019. Available from DOI: 10.1016/0090-3019(87)90152-2 (cit. on p. 62).

WEINSTEIN, J. N.; SPRATT, K. F.; SPENGLER, D., et al., 1988. *Spinal Pedicle Fixation: Reliability and Validity of Roentgenogram-Based Assessment and Surgical Factors on Successful Screw Placement*. Vol. 13. No. 9. ISSN 15281159. Available from DOI: 10.1097/00007632-198809000-00008 (cit. on pp. 58, 59).

WOOD, K. B.; KOS, P.; SCHENDEL, M., et al., 1996. Effect of Patient Position on the Sagittal-Plane Profile of the Thoracolumbar Spine. *Journal of spinal disorders*. Vol. 9, no. 2, pp. 165–9. ISSN 0895-0385. Available from PMID: 8793786 (cit. on p. 26).

WU, Z.-x.; GONG, F.-t.; LIU, L., et al., 2012. A Comparative Study on Screw Loosening in Osteoporotic Lumbar Spine Fusion between Expandable and Conventional Pedicle Screws. *Archives of Orthopaedic and Trauma Surgery*. Vol. 132, no. 4, pp. 471–476. ISSN 1434-3916. Available from DOI: 10.1007/s00402-011-1439-6 (cit. on p. 100).

XU, R.; BURGAR, A.; EBRAHEIM, N. A., et al., 1999. The Quantitative Anatomy of the Laminas of the Spine. *Spine*. Vol. 24, no. 2, pp. 107–113. ISSN 0362-2436. Available from DOI: 10.1097/00007632-199901150-00002 (cit. on p. 28).

YAO, J.; O'CONNOR, S.; SUMMERS, R., 2006. Automated Spinal Column Extraction and Partitioning. In: *3rd IEEE International Symposium on Biomedical Imaging: Nano to Macro, 2006.* [online], pp. 390–393 [visited on 2024-04-04]. ISSN 1945-8452. Available from DOI: 10.1109/ISBI.2006.1624935 (cit. on p. 94).

YASUDA, T.; HASEGAWA, T.; YAMATO, Y., et al., 2018. Effect of Position on Lumbar Lordosis in Patients with Adult Spinal Deformity. *Journal of Neurosurgery. Spine*. Vol. 29, no. 5, pp. 530–534. ISSN 1547-5646. Available from DOI: 10.3171/2018.3.SPINE1879 (cit. on p. 130).

YENI, Y. N.; DIX, M. R.; XIAO, A., et al., 2022. Measuring the Thickness of Vertebral Endplate and Shell Using Digital Tomosynthesis. *Bone* [online]. Vol. 157, p. 116341 [visited on 2024-01-24]. ISSN 87563282. Available from DOI: 10.1016/j.bone.2022.116341 (cit. on p. 32).

YINGSAKMONGKOL, W.; HANGSAPHUK, N.; LERDLAM, S., 2007. The Accuracy of Pedicle Screw Placement in Thoracic Spine Using the Funnel Technique in Idiopathic Scoliosis. *Journal of the Medical Association of Thailand = Chotmaihet Thangphaet*. Vol. 90, no. 1, pp. 96–105. ISSN 0125-2208 (cit. on p. 131).

YU, Y.; WANG, C.; FU, Q., et al., 2023. Techniques and Challenges of Image Segmentation: A Review. *Electronics* [online]. Vol. 12, no. 5, p. 1199 [visited on 2024-03-21]. ISSN 2079-9292. Available from DOI: 10.3390/electronics12051199 (cit. on p. 78).

ZHANG, J.; WU, C.; CAI, J., et al., 2010. Mesh Snapping: Robust Interactive Mesh Cutting Using Fast Geodesic Curvature Flow. *Computer Graphics Forum* [online]. Vol. 29, no. 2, pp. 517–526 [visited on 2024-03-21]. ISSN 0167-7055, ISSN 1467-8659. Available from DOI: 10.1111/j.1467-8659.2009.01621.x (cit. on p. 84).

ZHANG, T.; XIA, Y.; FENG, D. D., 2012. A Deformable Cosegmentation Algorithm for Brain MR Images. In: *2012 Annual International Conference of the IEEE Engineering in Medicine and Biology Society* [online], pp. 3215–3218 [visited on 2024-03-22]. ISSN 1558-4615. Available from DOI: 10.1109/EMBC.2012.6346649 (cit. on p. 184).

ZHANG, Y.; XIE, J.; WANG, Y., et al., 2014. Thoracic Pedicle Classification Determined by Inner Cortical Width of Pedicles on Computed Tomography Images: Its Clinical Significance for Posterior Vertebral Column Resection to Treat Rigid and Severe Spinal Deformities-a Retrospective Review of Cases. *BMC musculoskeletal disorders*. Vol. 15, p. 278. ISSN 1471-2474. Available from DOI: 10.1186/1471-2474-15-278 (cit. on pp. 134, 154).

ZHANG, Z.; LIU, X.; SOOMRO, N. Q., 2016. An Efficient Image Co-segmentation Algorithm Based on Active Contour and Image Saliency. *MATEC Web of Conferences* [online]. Vol. 54, p. 08004 [visited on 2024-03-22]. ISSN 2261-236X. Available from DOI: 10.1051/matecconf/20165408004 (cit. on p. 184).

ZHAO, J.; LONG, C.; XIONG, S., et al., 2014. A New K Nearest Neighbours Algorithm Using Cell Grids for 3D Scattered Point Cloud. *Elektronika ir Elektrotechnika* [online]. Vol. 20, no. 1, pp. 81–87 [visited on 2024-03-29]. ISSN 2029-5731. Available from DOI: 10.5755/j01.eee.20.1.3926 (cit. on p. 92).

ZHAO, S.; ARNOLD, M.; MA, S., et al., 2018. Standardizing Compression Testing for Measuring the Stiffness of Human Bone. *Bone & Joint Research* [online]. Vol. 7, no. 8, pp. 524–538 [visited on 2024-02-23]. ISSN 2046-3758. Available from DOI: 10.1302/2046-3758.78.BJR-2018-0025.R1 (cit. on p. 36).

ZHAO, X.; ZHAO, J.; XIE, Y., et al., 2016. The Utility of a Digital Virtual Template for Junior Surgeons in Pedicle Screw Placement in the Lumbar Spine. *BioMed Research International*. Vol. 2016, p. 3076025. ISSN 2314-6141. Available from DOI: 10.1155/2016/3076025 (cit. on p. 130).

ZHENG, T.; DUAN, Z.; WANG, J., et al., 2021. Research on Distance Transform and Neural Network Lidar Information Sampling Classification-Based Semantic Segmentation of 2D Indoor Room Maps. *Sensors* [online]. Vol. 21, no. 4, p. 1365 [visited on 2024-03-21]. ISSN 1424-8220. Available from DOI: 10.3390/s21041365 (cit. on p. 82).

ZIOUPOS, P.; CURREY, J. D., 1998. Changes in the Stiffness, Strength, and Toughness of Human Cortical Bone With Age. *Bone* [online]. Vol. 22, no. 1, pp. 57–66 [visited on 2024-05-30]. ISSN 8756-3282. Available from DOI: 10.1016/S8756-3282(97)00228-7 (cit. on p. 33).

ZYSSET, P. K., 2009. Indentation of Bone Tissue: A Short Review. *Osteoporosis International* [online]. Vol. 20, no. 6, pp. 1049–1055 [visited on 2024-07-09]. ISSN 0937-941X, ISSN 1433-2965. Available from DOI: 10.1007/s00198-009-0854-9 (cit. on p. 39).